THESE

En vue de l'obtention du

DOCTORAT DE L'UNIVERSITÉ DE TOULOUSE

Présentée et soutenue par *Jorge AMAYA*
Le *24 Juin 2010*

Titre :
*Unsteady coupled convection, conduction and radiation
simulations on parallel architectures for combustion applications*

JURY

François-Xavier ROUX	Prof. à l'Université Paris 6	Rapporteur
Olivier GICQUEL	Prof. à l'Ecole Centrale Paris	**Président du jury**
Mouna EL HAFI	Maître assist. à l'Ecole des Mines d'Albi	Examinateur
Pedro COELHO	Prof. à l'IST, Portugal	Examinateur
Denis LEMONNIER	Directeur de recherche au LET-ENSMA	Examinateur
Thomas LEDERLIN	Ing. de recherche à Turbomeca	Examinateur
Thierry POINSOT	Directeur de recherche à l'IMFT	Directeur

Contents

Abstract

In the aeronautical industry, energy generation relies almost exclusively in the combustion of hydro-carbons. The best way to improve the efficiency of such systems, while controlling their environmental impact, is to optimize the combustion process. With the continuous rise of computational power, simulations of complex combustion systems have become feasible, but until recently in industrial applications radiation and heat conduction were neglected. In the present work the numerical tools necessary for the coupled resolution of the three heat transfer modes have been developed and applied to the study of an helicopter combustion chamber. It is shown that the inclusion of all heat transfer modes can influence the temperature repartition in the domain. The numerical tools and the coupling methodology developed are now opening the way to a good number of scientific and engineering applications.

Resumé

Dans l'industrie aéronautique, la génération d'énergie dépend presque exclusivement de la combustion d'hydrocarbures. La meilleure façon d'améliorer le rendement de ces systèmes et de contrôler leur impact environnemental, est d'optimiser le processus de combustion. Avec la croissance continue du de la puissance des calculateurs, la simulation des systèmes complexes est devenue abordable. Jusqu'à très récemment dans les applications industrielles le rayonnement des gaz et la conduction de chaleur dans les solides ont été négligés. Dans ce travail les outils nécessaires à la résolution couplée des trois modes de transfert de chaleur ont été développés et ont été utilisés pour l'étude d'une chambre de combustion d'hélicoptère. On montre que l'inclusion de tous les modes de transfert de chaleur peut influencer la distribution de température dans le domaine. Les outils numériques et la méthodologie de couplage développés ouvrent maintenant la voie à un bon nombre d'applications tant scientifiques que technologiques.

Nomenclature

Accronyms

ACS   Asynchronous Coupled Simulations, page 146
DES   Detached Eddy Simulation, page 39
DNS   Direct Numerical Simulation, page 39
DOM   Discrete Ordinates Method, page 85
FSTI   Fluid-Solid Thermal Interactions, page 128
LBL   Line-by-line, page 81
LES   Large Eddy Simulations, page 38
MC   Monte Carlo method, page 84
MPC   Multi-Physics Coupling, page 162
PCS   Parallel Coupling Strategy, page 126
RANS   Reynolds-Averaged Navier-Stokes, page 38
RFTI   Radiation-Fluid Thermal Interactions, page 148
RTE   Radiative Transfer Equation, page 68
RTF   Radial Temperature Function, page 207
SCS   Sequential Coupling Strategy, page 126
SNB   Spectral Narrow-Band, page 81
SRTI   Solid-Radiation Thermal Interactions, page 160
TBL   Turbulent Boundary Layer, page 132
TRI   Turbulence-Radiation Interactions, page 208
WM   Wall-Modeled, page 130
WR   Wall-Resolved, page 130

Greek symbols

α	Absorptance , page 59	[-]
α	Nondimensional coupling factor, page 146	
α	Weighting factor for the mean flux spatial scheme , page 89	[-]
$\alpha_{\tilde{\nu}}$	Absorptivity , page 64	[-]
β_j	Temperature exponent of reaction j , page 29	[-]
$\beta_{\tilde{\nu}}$	Extinction coefficient , page 65	[m^{-1}]
$\Delta()$	Absolute difference, page 205	
$\delta()$	Relative difference, page 205	
$\Delta h_{f,k}^0$	Formation enthalpy of species k , page 24	[J/kg]

Δh_f^0 Formation enthalpy , page 27   [J]
Δt Time step , page 7   [s]
Δx Mesh size , page 7   [m]
Δ Stencil size / LES filter size, page 48
δ_L^0 Flame thickness , page 42   [m]
$\dot{\omega}_k$ Mass reaction rate of species k , page 29   [kg/(m^{-3}s)]
$\dot{\omega}_T$ Heat source term , page 30   [W/m^3]
$\epsilon()$ Normalized absolute error, page 194
ϵ Emittance , page 59   [-]
γ Polytropic coefficient , page 27   [-]
$\kappa_{\tilde{v}}$ Absorption coefficient , page 64   [m^{-1}]
λ Thermal conductivity , page 3   [W m^{-1} K^{-1}]
λ Wavelength , page 52   [m]
μ Dynamic viscosity , page 25   [kg.s^{-1}m^{-1}]
ν Frequency , page 52   [Hz]
ν'',ν',ν Stoichiometric coefficients , page 29   [-]
ν_t Turbulent viscosity , page 41   [m^2/s]
ω Angular ferquency , page 52   [s^{-1}]
ω_i^d Directional quadrature weight associated to direction i , page 87   [-]
$\omega_{\tilde{v}}$ Monochromatic scattering albedo , page 68   [-]
$\overline{\delta}$ Band average spectral line spacing, page 95
$\overline{\gamma}$ Band average of the Lorentz lines half-width, page 95
ϕ Equivalence ratio , page 31   [-]
ϕ_g Global equivalence ratio , page 31   [-]
$\phi_{\Delta\tilde{v}}$ Mean band line shape parameter, page 95
$\Phi_{\tilde{v}}$ Scattering phase function , page 66   [-]
$\boldsymbol{\lambda}$ Conductivity tensor , page 3   [Wm^{-1}K^{-1}]
ρ Density , page 3   [kg m^{-3}]
ρ Reflectance , page 59   [-]
ρ^s Specular reflectance , page 61   [-]
$\rho_{\tilde{v}}^d$ Diffuse reflectance , page 61   [-]
σ Stefan-Boltzmann constant , page 58   [Wm^{-2}K^{-4}]
$\sigma_{s\tilde{v}}$ Scattering coefficient , page 65   [m^{-1}]
τ Transmittance , page 59   [-]
$\tau_{\tilde{v}}$ Monochromatic optical thickness , page 69   [-]
τ_{ij} Viscous stress tensor , page 32   [Pa]
$\tilde{v}$ Wavenumber , page 52   [m^{-1}]

Subscripts and superscripts

0   Relative to the initial condition
τ Relative to the friction properties at the wall
ext   External/reference quantities
f Quantities related to the fluid domain

r	Quantities related to radiation	
s	Quantities related to the solid domain	
w	Wall/interface quantities	
$+$	Quantities in wall units	

Roman symbols

$\dot{m}$	Mass flow rate , page 31	[kg/s]
$\mathbf{n}_j$	Normal vector of face j , page 88	[-]
$\mathbf{q}$	Heat flux vector , page 3	[W/m^2]
$\mathbf{s}$	Direction vector, page 53	
$\mathscr{D}_k$	Diffusion coefficient of species k in the mixture , page 34	[m^2/s]
$\mathscr{D}_k^t$	Turbulent diffusion of species k , page 41	[-]
$\mathscr{E}$	Efficiency function , page 44	[-]
$\mathscr{F}$	Thickening factor , page 44	[-]
$\mathscr{S}_r$	Radiative source term , page 71	[W/m^3]
$\overline{\kappa}_P$	Planck mean absorption coefficient , page 106	[m^{-1}]
$\overline{A}$	Mean band absorption , page 93	[-]
$\overline{I_{\bar{v},in}}$	Averaged intensities crossing the entry faces of a control volume , page 89	[Wm^{-2}Hz^{-1}]
$\overline{I_{\bar{v},out}}$	Averaged intensities crossing the exit faces of a control volume , page 89	[Wm^{-2}Hz^{-1}]
$\overline{W}$	Mean band equivalent width , page 94	[-]
A	Dimensionless average absoption , page 93	[-]
a	Thermal difussivity , page 3	[m^2 s^{-1}]
A_j	Pre-exponential factor of reaction j , page 29	[s^{-1}]
b_N	Half-width of a Dopler broadened spectral line, page 77	
b_N	Half-width of a collision broadened spectral line, page 77	
b_N	Half-width of a natural broadened spectral line, page 76	
C	Specific heat capacity , page 3	[J K^{-1}kg^{-1}]
c_0	Speed of light in vacuum , page 51	299 792 458 [m/s]
C_p	Total heat capacity at constant pressure , page 27	[Jkg^{-1}K^{-1}]
C_v	Total heat capacity at constant volume , page 27	[Jkg^{-1}K^{-1}]
$C_{p,k}$	Heat capacity at constant pressure for species k , page 24	[J kg^{-1} K^{-1}]
$C_{v,k}$	Heat capacity at constant volume for species k , page 24	[J kg^{-1} K^{-1}]
D	Diffusion matrix , page 34	[m^2/s]
$d\Omega$	Infinitesimal solid angle , page 54	[sr]
D_j	Projection of the normal of face j on the beam direction j , page 88	[-]
D_l^k	Diffusion coefficient of species k in species l , page 34	[m^2/s]
D_l^k	Species diffusion coefficient , page 25	[m^2/s]
E	Total emissive power , page 56	[Wm^{-2}]
E	Total energy , page 32	[J]
e	Internal energy , page 27	[J]
E_v	Spectral emissive power , page 56	[Wm^{-2}Hz^{-1}]
E_b	Blackbody emissive power , page 58	[Wm^{-2}]

One day there was a storm, with much lighting and thunder and rain. The little ones are afraid of storms. And sometimes so am I. The secret of the storm is hidden. The thunder is deep and loud; the lighting is brief and bright. Maybe someone very powerful is very angry. It must be someone in the sky, I think.

After the storm there was a flickering and crackling in the forest nearby. We went to see. There was a bright, hot, leaping thing, yellow and red. We had never seen such a thing before. We now call it "flame".

One of us had the brave and fearful thought: to capture the flame, feed it a little, and make it our friend.

[...] The flame is ours. We take care of the flame. The flame takes care of us.

Cosmos, Carl Sagan

1

Preface

One of the most important achievements of mankind is his ability to control fire. And with such power we have been able to fly, take off from Earth and reach space. But the path that lead us to land on Saturn's biggest moon Titan (Fig. 1.1-a), began around the 15th century B.C. in Babylon, with the invention of the oil lamp (Fig. 1.1-b). At the time Fire was considered one of the four basic elements of nature which, with Water, Air and Earth, flowed through an invisible medium called the Aether. This was the prevailing vision in ancient Greece but it was one shared with Hindus, Buddhist and Chinese, and was first inscribed in the babylonian myth of Enûma Eliš, recovered by Austen Henry Layard in 1849 and published by George Smith in 1979 [239].

After a flourishing era of awakening in science, philosophy, literature, arts and exploration, the classical civilization, the root of our society, felt into an era of obscurantism, marked by the destruction of the last remnants of the Library of Alexandria in the IV century and the death of its last librarian, the mathematician, astronomer, physicist and philosopher, Hypatia, murdered by a Christian mob orchestrated by Cyril, who dragged her from her chariot, tore off her clothes and flayed her flesh from her bones. Her remains were burned and her name forgotten while Cyril was made a saint. Some of the knowledge of the greek scientific tradition of the Alexandrian era was forgotten for almost one millennium. But most of it was lost [223].

It was again, around the XV century, that some of the works of Aristotle, Socrates, Aristarchus, Pythagoras and other ancient philosophers were rediscovered by a new generation of thinkers in an era of renaissance. Between them two of the first theoretical physicist[1] Isaac Newton and Christiaan Huyguens,

---

[1]They are considered the first theoretical physicists as they used mathematics in order to explain nature.

(a)   (b)
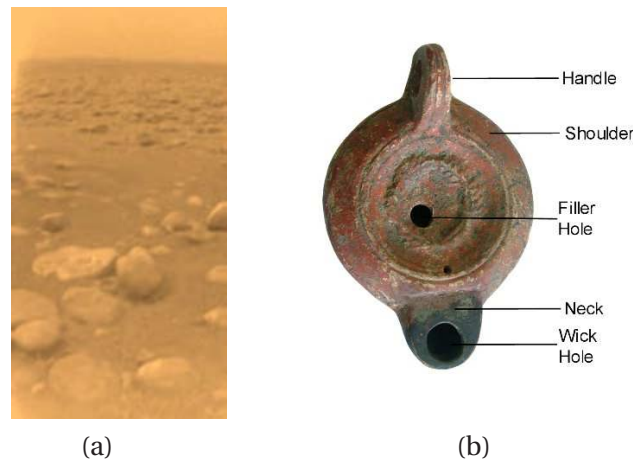
Figure 1.1: (a) View of the surface of Titan, Saturn's largest moon, taken by the ESA Huyguens probe on January 14, 2005. (b) Ceramic oil lamp and its components.

.

established at the end of the XVII century, the starting point in our modern understanding of fire, and in particular one of its most important aspects: light.

Each one had an explanation for light that seemed contradictory[2]: Newton fervently defended the corpuscular nature of light (which gave origin to one of its most important writings, *Opticks* [186]) against critics like Robert Hooke and Christiaan Huyguens, who promoted a wave theory of light. A clear mathematical foundation described very well light refraction as a consequence of wave propagation, and was more useful to explain the interference patterns observed in the double-stilt experiments carried out by Thomas Young [277]. It was Augustin-Jean Fresnel who, at the beginning of the XIX century, rediscovered Huyguens results and showed that the wave theory of light is not in contradiction with the linear propagation of light (one of Newton's arguments against the theory). Today the model that explains refraction and diffraction of light is called the Huyguens-Fresnel principle. However, the corpuscular/wave controversy remained open until the end of the XIX century.

To understand the origin light it is indispensable to understand electromagnetic theory. Michael Faraday was born in 1791 and from 1804 to 1811 he worked as a book binder in a library. There he became aware of the scientific literature and got versed in some specific topics while developing very good handicraft skills. At the age of 20 he became assistant of chemist Humphry Davy of the Royal Institution. He became a good laboratory employee, and eventually instruments supervisor, laboratory director and finally in 1833 professor of chemistry at the Royal Institution of Great Britain.

His great ability to setup precise and good experiments allowed him to understand the intricate relationship between electricity and magnetism. In particular he is at the origin of the induction of an electric current by the motion of a magnet, which finally derived in great technical advances, as the

---

[2]Most of the historical background presented here can be found in Sagan [223] and Ronan [219].

electrical engine, the electrical generator, public electricity and wire communications, but also lead to the concept of electric and magnetic fields, inspiring James Clerk Maxwell who in 1873 published his most famous work *A treatise on electricity and magnetism* [165].

Maxwell found a close link between the magnetic and the electric fields. Applying these results to the particular case of a linearly propagating harmonic electric wave, he deduced that there exists an associated perpendicular magnetic wave. In the vacuum the propagation speed of this coupled wave perfectly matches the speed of light. Light is an electromagnetic wave. Some years after Maxwell's death Heinrich Hertz showed that at some frequencies these waves become invisible but are still detectable using measuring instruments. Hertz is the father of VHF and UHF radio waves, and light is only one small part of a greater electromagnetic wave spectrum.

But still some experiments showed that light behave like a particle. It was only after the quantum revolution of the beginning of the XX century that the final answer came in the strangest form. Through the work of Max Planck, Albert Einstein, Louis de Broglie, Arthur Compton and Niels Bohr, the current scientific consensus holds that all particles (including light) have both wave and corpuscular properties.

Fire is also build on interacting particles. It is the energy stored inside the chemical compounds of a molecule of fuels that generates the necessary energy in the first place to produce heat and light. It was the medieval Arab and Persian scholars who first introduced a precise observation and controlled experimentation, which lead to the discovery of numerous chemical substances.

The most influential Muslim chemists were Jābir ibn Hayyān (d. 815), al-Kindi (d. 873), Al-Rāzī (d. 925), al-Bīrūnī (d. 1048) and Alhazen (d. 1039). The works of Jābir became more widely known in Europe through latin translations. The emergence of chemistry in Europe during the XV century was mainly motivated by the rise in the demand for medicines. Over time, the initial alchemy approach was replaced by a more strict and scientific method. Paracelsus in he XVI century rejected the 4-elemental theory and, with only a vague understanding of his chemicals and medicines, formed a hybrid of alchemy and science. The systematic and scientific revolution promoted by Sir Francis Bacon and René Descartes inspired philosophers like Robert Boyle to perform analytical scientific studies in domains like combustion, oxidation and respiration.

It was however Antoine Lavoisier, who developed the theory of conservation of mass in 1783, that advanced the oxygen theory of combustion ("the acid principle" or "the oxygen principle" derived from the greek *oxus*=acid). The detailed experimental analysis carried out by Levoisier, was completed by the work of Claude Berthollet, Guyton de Morveau and Antoine de Fourcroy who helped in the reformulation of a consistent chemical nomenclature. A complete compendium of such enterprise can be found in the 1787 *Traité élémentaire de chimie* by Levoisier, the father of modern chemistry.

Finally, the transport of the different chemical elements in a continuum medium is the subject of the fluid dynamics, which in the XVIII and XIV century was a subject of controversy among the physicists. In 1757 Leonhard Euler published his work on the general principles of fluid motion. Many modern applications still rely on Euler's mathematical model of inviscid flows. But during the decades that fol-

lowed Euler's discovery experiences and theoretical analysis showed that improvements of the model where necessary. Almost one century later Claude Navier published a mathematical derivation of the equations of motion of incompressible viscous fluids. His model, altough accurate, was obtained using a wrong analysis of the interaction forces between particles. It was Jean-Claude Barré de Saint-Venant who established a correct physical framework for the derivation of the modern Navier-Stokes equations, interpreting the multiplying factor of the velocity gradient as a viscous coefficient, and identifying such product as the viscous stresses acting within the fluid because of friction. It's still uncertain why the name of Saint-Venant has never been associated with the equations of motion of viscous fluids.

The equations were independently derived by George Stokes, who worked as the Lucasian chair of mathematics at Cambridge during most of the second half of the 19th century. His expertise on fluid mechanics was mainly inspired by his work on the properties of light, the searching for an explanation of it's movement within the ether and the study of the motion of pendulum. The monumental contributions of Stokes on the understanding of friction in viscous flows is still honored with the inclusion of his name in the Navier-Stokes equations of fluid motion.

Building a theory that explains how a candle works required the tireless work of the most prominent scientists, some of which, sometimes without knowing, became prolific scientists in all the areas related to combustion (chemistry, electromagnetism, fluid dynamics, heat transfer, etc.):

> Atom by atom, link by link, has the reasoning chain been forged. Some links too quickly and to slightly made have given way, and replaced by better work; but now the great phenomena are known, the outline is correctly and firmly drawn, cunning artists are filling the rest, and the child who masters these Lectures knows more of fire than Aristotle.
>
> *The chemical history of a candle*, Michael Faraday [77]

2
Introduction

La combustion est la science qui étudie, à l'aide de la chimie, la mécanique des fluides et le transfert de chaleur, les mécanismes impliqués dans le dégagement d'énergie due à l'oxydation exothermique de molécules de combustible. Dans des applications industrielles la combustion est communément utilisé pour le dimensionnement de machines pour la transformation efficace d'énergie chimique en travail mécanique en utilisant la théorie des cycles thermodynamiques.

Une bonne connaissance théorique des processus sous-jacents de la combustion a été développée dans les dernières décennies, néanmoins, pour des applications industrielles, les interactions non-linéaires entre les différents phénomènes physico-chimiques font presque impossible une étude analytique du processus de combustion qu'en générale incluent une géométrie complexe et un écoulement turbulent. Une réponse à ce problème a été présenté à la fin de la seconde guerre mondiale: pour résoudre les équations qui déterminent le comportement des bombes nucléaires, Stanislaw Ulman et John von Neumann ont eu recours à la simulation numérique et aux ordinateurs. Le laboratoire de Los Alamos en Californie a été le berceau de la plupart des méthodes numériques utilisés actuellement pour la résolution numérique du transfert de chaleur et de la dynamique des fluides.

Pendant la seconde moitié du 20ème siècle et le début du 21ème, les simulations par ordinateur ont été utilisées pour résoudre des problèmes extrêmement complexes et on permis d'étudier, des problèmes physiques fondamentaux comme la turbulence, le transfert de chaleur, les couches limites, la dynamique moléculaire, la chimie et le rayonnement entre autres. Aujourd'hui les simulations par ordinateur sont utilisés pour étudier et valider systèmes complexes comme celui visé par ce travail: les chambres de combustion aéronautiques.

Une forte augmentation de la puissance de calcul a été observée ces dernières années et elle est principalement due à la réduction dans la taille des transistors des processeurs et à la distribution des tâches sur plusieurs unités de calcul. Les simulations sur des architectures parallèles ont montré des résultats étonnants, comme ceux présentés par Wolf et al. [271] et Boileau et al. [17]. Ces simulations incluent plusieurs modèles avancés pour la turbulence, le changement de phase des hydrocarbures, la cinétique chimique et la stabilité numérique, mais elles n'ont pas tenu encore en compte quelques uns des phénomènes physiques les plus importants, car leur inclusion restait encore très coûteuse.

Dans une chambre de combustion la chaleur peut être transmise par rayonnement, par conduction et par convection. Les interactions thermiques entre le solide et le fluide sont très fortes: la température de la structure impose un flux thermique à l'interface entre les deux milieux. De l'énergie peut être rayonnée par ce même solide et par les zones chaudes du gaz quand ils se trouvent à haute température, et peuvent aussi absorber de l'énergie quand leur température est basse. De plus, les gradients de température dans le fluide imposent un flux de chaleur vers les parois. Finalement, les propriétés radiatives du fluide dépendent des propriétés thermochimiques du mélange. En bref, chaque mode de transfert encadre l'évolution des autres modes.

Dans ces dernières années, différents équipes de recherche ont aperçu la nécessité croissante d'inclure tous les modes de transfert de chaleur pour l'étude des applications en combustion. Concernant l'interaction entre le rayonnement et le fluide Schmitt et al. [230] et Gonçalves dos Santos et al. [64] ont montré que le rayonnement peut modifier la dynamique de flamme. Des simulations numériques sur l'interaction rayonnement-turbulence (Turbulence-Radiation Interaction: TRI) ont été réalisées (voir Coelho [45] pour avoir une synthèse des travaux réalisés dans ce domaine), les interactions entre la combustion et le rayonnement ont été étudiées par Kounalakis et al. [139], Adams et al. [3], Desjardin et Frankel [60], Giordano et Lentini [87], Wu et al. [272, 273] Deshmukh et al. [58, 59], Narayanan et Trouvé [185], et des analyses sur l'influence du rayonnement sur des systèmes de combustion aéronautiques ont gagné grande couverture par les travaux de Lefebvre [147], Mengüç et Viskanta [263], et plus récemment par Bialecki et Wecel [15] et Paul and Paul [194].

Concernant l'interaction Fluide-Solide pour des applications en combustion des travaux sur l'impact du transfert de chaleur entre les gaz de combustion et les vannes de guidage en sortie de chambre ont été réalisés par Grag [84], Wang et al. [266], Kassab et al. [129], Mazur et al [167], and Duchaine et al. [67]. Des méthodes pour les échanges entre ces deux milieux ont été largement étudiées par Errera et al. [74, 75], Chemin [40], Roux [221] et Châtelain [39].

La littérature au sujet des interactions entre le rayonnement et la combustion et entre la convection et la conduction, est récente. Dans ce travail un des objectifs est d'approfondir l'étude des effets combinés des trois modes de transfert de chaleur (convection, conduction, rayonnement) appliqués à une géométrie complexe tout en tenant en compte de la combustion turbulente. La puissance de calcul actuelle a atteint un point où un tel type de simulation parallèle peut être réalisée. Ce travail demande donc la connaissance de trois domaines de la physique et d'un travail de développement de nouveaux outils numériques. **Le principal objectif de cette thèse est d'explorer comment les architectures parallèles modernes et les outils de couplage peuvent être utilisés pour réaliser des**

simulations couplées instationnaires multi-physiques.

En se basant sur ces artchitectures parallèles, trois codes qui résolvent les trois modes de transfert de chaleur sont employés pour analyser les effets couplés en combustion. Le but est de ainsi de s'attaquer aux aspects *scientifiques et d'ingénierie* nécessaires pour un tel type d'étude. Dans le domaine scientifique, chaque phénomène de transfert doit être étudié et les outils numériques employés pour leur résolution spatio-temporelle doivent être évalués de façon indépendante.

Finalement, l'utilisation de simulations couplées doit montrer qu'il existe une amelioration de la prédiction du comportement du système par rapport aux simulations non couplées. En particulier il est important de déterminer dans quels aspects les simulations couplées présentent des prédictions plus exactes, et quand est-ce qu'un tel type de simulation n'est pas nécessaire.

Les simulations couplées peuvent être utilisées pour l'étude du transfert de chaleur dans les couches limites turbulentes, pour l'étude de la structure de flamme et son stabilité, pour l'étude de la dynamique du fluide et de la distribution de température dans le domaine de calcul.

Afin de satisfaire les besoins industriels une simulation couplée doit répondre aux exigences suivantes:

- **Géométries complexes:** pour des applications en aérodynamique interne les géométries communément étudiées sont très complexes. Elles peuvent inclure différentes zones d'injection de différentes tailles et dans le cas des chambres de combustion comportent une forme toroïdale caractéristique. Les codes doivent être capables de manipuler un tel type de mailles, qui pour la plupart sont composés d'éléments hybrides (tétraèdres, hexaèdres, pyramides, etc.).

- **Temps de restitution:** même si les Simulations aux Grandes Echèlles (SGE) ne sont pas la norme dans l'industrie, elles sont en train de devenir de plus en plus populaires grâce à leur efficacité pour prédire des phénomènes instationnaires. La croissance de la puissance de calcul et un accès plus aisé à des super calculateurs sont des arguments qui permettront aux industriels de se tourner dans les années à venir vers la SGE. Néanmoins, le temps de restitution de cette méthode est encore très grand et demande encore beaucoup d'heures de travail humain. Les simulations couplées doivent présenter des temps de restitution comparables à celles montrées par la SGE seule.

- **Portabilité:** les outils de simulation doivent être faciles à transporter d'un ordinateur à un autre, insouciant de l'architecture et du système d'exploitation. Les simulateurs doivent demander une intervention minimale quand ils sont installés sur des nouveaux systèmes. Dans le cas des simulations couplées cette tâche demande une politique de développement, car au lieu d'un seul code les applications multi-physiques font intervenir de plusieurs codes, unités de communication et logiciels de couplage qui doivent évoluer de façon simultanée.

- **Ergonomie:** un code qui présente une clarté de fonctionnement est plus facile à être pris en main, est plus fonctionnel, efficace et plus agréable utiliser. Un des problèmes majeurs de la

computation scientifique et de sa mise au service de l'industrie est la négligence des interactions entre l'utilisateur et le logiciel. Pour des applications dans lesquelles plusieurs codes doivent coexister il est essentiel de garder une interface consistante entre l'utilisateur et les différents codes.

Pour palier à ces besoins d'ingénierie, les outils numériques utilisés doivent être évalués et optimisés, et d'autres doivent être développés. Les objectifs particuliers de ce travail de thèse dans ce domaine concernent:

- l'évaluation des performances du code de conduction AVTP pour réaliser des simulations transitoires,

- le développement et optimisation du code radiatif PRISSMA pour des applications couplées,

- la mise en place du software permettant la distribution de ressources et la synchronisation des trois codes de calcul AVBP (pour la SGE), AVTP (pour la conduction) et PRISSMA (pour le rayonnement) à l'aide du coupleur PALM,

- la réalisation d'une simulation couplée d'une chambre de combustion aéronautique, incluant les phénomènes instationnaires de la combustion turbulente, la conduction de chaleur dans la structure et des modèles détaillés de rayonnement électromagnétique.

Ce document est divisé en trois parties majeures: dans la première partie une introduction à chacun des modes de transfert est présentée. Une attention particulière est donnée à la théorie du rayonnement électromagnétique et aux méthodes numériques employés pour résoudre l'équation de transfert radiatif sur des architectures parallèles. Dans la deuxième partie une description des effets thermiques couplés et des méthodes développées pour résoudre leurs interactions instationnaires sont présentés. Finalement, dans la troisième partie, les outils développés dans les sections précédentes sont utilisés pour réaliser le couplage instationnaire d'une chambre de combustion d'hélicoptère et pour étudier les effets des interactions thermiques Fluide-Rayonnement, Solide-Fluide et Multi-Physiques.

3

Introduction

Combustion is the science that combines chemistry, fluid dynamics and heat transfer in order to explain the mechanisms of energy release due to the exothermal oxidation of fuel molecules. In industrial applications combustion is used to design efficient tools that transform chemical energy into mechanical work using a thermodynamic cycle.

A good understanding of all the underlying processes in combustion has been acquired over the last decades. However, in industrial applications there are non-linear interactions between the different physicochemical phenomena, making almost impossible to develop an analytical study of a combustion process involving a complex geometry and a turbulent flow. One answer to this problem was given by the time of World War II, when the resolution of the equations describing a complex system as the explosion of a nuclear bomb was carried out by Stanislaw Ulman using simulations with John von Neumann digital computers. Los Alamos Laboratory was the birth place of many of the modern numerical methods used in heat transfer and fluid dynamics.

During the second half of the XX and the beginning of the XXI centuries, computer simulations have been used to resolve extremely complex problems and gave the opportunity to study, from a new point of view, fundamental scientific problems such as turbulence, heat transfer, boundary layer theory, molecular dynamics, molecular chemistry and radiation among others. Today computer simulations are used to study and validate complex systems as the one targeted in this work: the unsteady simulation of an aeronautical combustion chamber.

The increment in computational power has been mainly achieved by reduction in the transistor size and by the distribution of the tasks over many different process units, what is called parallel com-

puting. Simulations of combustion on parallel architectures have shown incredible results, as in the case of Wolf et al. [271] and Boileau et al. [17]. Such simulations include many complex models for turbulence, phase change, chemistry and numerical stability, but still do not take into account some important physical phenomena, as the simulation of such systems may be very expensive.

In a combustion chamber heat can be transfered by radiation, conduction and convection. The thermal interactions between the solid and the fluid are closely related: the temperature of the solid structure imposes a heat flux to the fluid, while radiation emitted by the solid wall and by the hot spots in the gas is absorbed by cold zones in the fluid and the structure. In addition, the temperature gradients in the fluid impose a heat flux to the walls and finally the radiative properties of the fluid depend on the thermochemical properties of the mixture. In summary each transfer mode bounds the evolution of the others.

In the last years however, different scientific teams have acknowledged the necessity to include different heat transfer modes for the study of combustion applications. Concerning the Fluid-Radiation interaction Schmitt et al. [230] and Gonçalves dos Santos et al. [64] showed that radiation can modify the flame dynamics. Advances in numerical simulation include the study of the Turbulence-Radiation Interactions (Coelho [45] gives a good synthesis of the state of the art in TRI), the interactions between combustion and radiation of Kounalakis et al. [139], Adams et al. [3], Desjardin et Frankel [60], Giordano et Lentini [87], Wu et al. [272, 273] Deshmukh et al. [58, 59], Narayanan et Trouvé [185], and the analysis of radiation effects on aeronautical combustion systems which have receive wide coverage by Lefebvre [147], Mengüç et Viskanta [263], and more recently by Bialecki et Wecel [15] and Paul et Paul [194].

In the complementary field of Fluid-Solid interaction, work has been done on the impact of hot combustion gases on the guiding vanes at the exit of the combustion chamber by Grag [84], Wang et al. [266], Kassab et al. [129], Mazur et al [167], and Duchaine et al. [67]. Other fundamental principles on Fluid-Solid Thermal Interactions (FSTI) have been studied by Errera et al. [74, 75], Chemin [40], Roux [221] and Châtelain [39].

Scientific literature on the interaction between radiation and combustion (Radiation-Fluid) and between convection and conduction (Fluid-Solid) is recent. In the present work our aim is to go one step further and study the combined effect of the three heat transfer modes, conduction, convection and radiation applied to an industrial complex geometry, while resolving the unsteady turbulent combustion. The current available computational power has reached a point where such parallel simulations can be performed. This task demands the knowledge of three different areas of physics and involves the development of new numerical tools. **The main objective of the present work is to explore the possibilities of modern parallel architectures and coupling methods to achieve unsteady Multi-Physics Coupled (MPC) simulations**.

Taking advantage of the parallel architectures, three codes that solve the three heat transfer modes are employed to analyze the coupled effects in combustion. The goal is then to tackle both the *scientific and the engineering* aspects of the interaction between the different heat transfer modes.

In the scientific area, each independent heat transfer mode must be understood, and the numerical tools developed must show a good prediction of the spatial and temporal evolution of each independent system. Next, the interactions between the different transfer modes must be analyzed, and the effects of one subsystem on the other must be presented (how does radiation affect convection for example).

Finally, the use of coupled simulations must show that there exists an advantage in the prediction of the system's behavior against uncoupled simulations. In particular it is important to determine in which aspects coupled simulations can provide more accurate predictions, and when they are not necessary. Coupled simulations can be used to study the effects on the heat transfer in the turbulent boundary layer, the flame structure and its stability, the flow dynamics and the temperature distribution in the studied domain.

In order to meet industrial needs, it was identified that a coupled simulation must respond to a series of requirements:

- **Complex geometries:** in aeronautical applications the geometries are very complex. They can include different flow entries of different sizes, complex injector geometries and a general annular shape. Each simulation code must be able to handle complex meshes, often composed of hybrid elements.

- **Restitution time:** even though unsteady LES are not the norm in industrial design, they are becoming more and more popular due to their ability to predict unsteady phenomena. The fast growth in computer power and the increased access to supercomputers provide a good argument for industrials to turn towards LES. However the restitution time for one LES is often very large and involve many human hours of specialized workforce. Coupled simulations must look up for restitution times close to the ones proposed by the LES applications alone.

- **Portability:** simulation tools must be easy to transport from one computer to another, regardless of the hardware or the operating system. Simulation codes must require minimal intervention when installed in a new system. In the case of coupled simulations this task requires a development policy, because instead of one simulation code, multi-physics applications consist of several codes, communication units and a coupling software evolving simultaneously.

- **Usability:** refers to the clarity of interaction with a computer program. A well designed software is easier to learn, is more functional, efficient and is more satisfying to be used. One of the major drawbacks of scientific computation and its transfer to the industry comes from the fact that human interaction with the software is often neglected. In applications where many different simulation codes coexist it is essential to have a consistent interface between the user and the different codes.

To tackle these engineering requirements the available numerical tools must be evaluated and optimized, while new tools must be developed. To this respect, the specific objectives of the present work can be summarized as follows:

- To evaluate the heat conduction code AVTP and its ability to perform transient simulations.

- To develop and optimize the software PRISSMA that resolves the Radiative Transfer Equation (RTE) in parallel architectures and can be used for coupled simulations.

- To develop the numerical tools necessary to perform coupled simulations in parallel architectures using the codes AVBP (Large Eddy Simulation), AVTP (heat conduction) and PRISSMA (radiation), and the coupler PALM.

- To perform coupled simulations of an aeronautical combustion chamber, using LES, heat conduction and realistic gas radiation.

The document is divided in three main parts: in the first an introduction to each one of the three heat transfer modes is presented. A particular interest is given to electromagnetic radiation theory and to the numerical methods employed to resolve the Radiative Transfer Equation (RTE) on parallel architectures. In the second part a description of the coupled thermal effects and the methods developed to resolve the unsteady interaction between the heat transfer modes is presented. Finally, in the third part, the tools presented in the first and the second part are used to perform Radiation-Fluid Thermal Interaction (RFTI), Fluid-Solid Thermal Interaction (FSTI) and Multi-Physics Coupled (MPC) simulations of an helicopter combustion chamber.

Part I

Heat and mass transfers in fluids and solids

4

Heat transfer in solids

Contents

Heat conduction is a process carried out at a molecular level, in which energy is transfered from one point of the space to another through a continuous support (this heat transfer process can not be done in vacuum). The transfer is done from highly energetic molecules to molecules with less energy (from the second law of thermodynamics), i.e. from high temperature to low temperature regions. There is no associated mass transfer.

2

4.1   The Fourier law

As most transfer processes, conduction is driven by a gradient law, known as the Fourier law of heat transfer (4.1).

$$\mathbf{q} = -\boldsymbol{\lambda}\nabla T \tag{4.1}$$

where the heat flux $\mathbf{q}$ is considered positive when energy flows from hot to cold zones. $\boldsymbol{\lambda}$ is the conductivity tensor, which is generally considered isotropic for most solids and described using eq.(4.2), where λ is the thermal conductivity:

$$\boldsymbol{\lambda} = \lambda \begin{pmatrix} 1 & 0 & 0 \\ 0 & 1 & 0 \\ 0 & 0 & 1 \end{pmatrix} \tag{4.2}$$

4.2   Physical properties of solids

In a heat transfer problem, the velocity and reactivity of the system depend on four main properties of the solids:

- **The density of the material,** ρ [kg m^{-3}]: is the total amount of mass in the solid per unit volume.

- **The specific heat capacity,** C [J K^{-1}kg^{-1}]: reflects the ability of an object to stock energy.

- **The thermal conductivity,** λ [W m^{-1} K^{-1}]: represents the ability of the object to conduct heat. Typical values of the thermal conductivity lay between 10^2 for some metals to 10^{-2} in most gases.

- **Thermal difussivity,** a [m^2 s^{-1}]: appears in transitory regimesand evaluates the time required by a solid to change temperature under the influence of an external or internal source. It is defined by:

$$a = \frac{\lambda}{\rho C} \tag{4.3}$$

The knowledge of three of these properties gives access to the fourth.

4.3   The heat equation

The derivation of the heat equation is obtained from the first principle of thermodynamics. Consider a volume V bounded by a non-deformable surface S, i.e. without any work from a compression or dilatation of the volume. During the time dt the variation of temperature at any point M can be expressed using eq. (4.4):

$$dT = T(M, t + dt) - T(M, t) = \frac{\partial T}{\partial t} dt \tag{4.4}$$

The variation of the internal energy per unit volume e is expressed as:

$$de = \rho C dT = \rho C \frac{\partial T}{\partial t} dt \tag{4.5}$$

Integrating on the total volume gives:

$$dE = dt \iiint_V \rho C \frac{\partial T}{\partial t} dV \tag{4.6}$$

From the first principle of thermodynamics, this energy variation is equal to the sum of the heat flux trough the surface S and the internal energy sources. During the time dt the heat flux trough S can be expressed:

$$Q_s = -dt \iint_S \mathbf{q} \cdot \mathbf{n} dS \tag{4.7}$$

The heat Q_v produced by the internal sources $P(M, t)$ is obtained by integration over the volume V:

$$Q_v = dt \iiint_V P(M, t) dV \tag{4.8}$$

The first principle of thermodynamics gives then:

$$dE = \delta Q + \delta W = (\delta Q_s + \delta Q_v) + 0 \tag{4.9}$$

where the work δW is supposed equal to zero in the present case. This expression can be expanded:

$$\iiint_V \rho C \frac{\partial T}{\partial t} dV = - \iiint_V \nabla . \mathbf{q} dV \iiint_V P(M, t) dV \tag{4.10}$$

Using eq.(4.1) and taking the limit when $V \rightarrow 0$ gives:

$$\rho C \frac{\partial T}{\partial t} = -\nabla.(-\lambda \nabla T) + P \tag{4.11}$$

which is known as the heat equation for an non-homogeneous non-isotropic medium.

Many different forms of the heat equation can be found, depending on the different possible assumptions that are made to simplify the problem. At the first order, considering that the physical properties of the isotropic medium do not depend on temperature reduces the heat equation to:

$$\frac{\partial T}{\partial t} = a \nabla^2 T + P \tag{4.12}$$

A summary of usual simplified heat equations is given in Table 4.1.

Table 4.1: Commonly used simplifications of the heat equation.

Description	Equation
Permanent regime without energy sources:	$\nabla^2 T = 0$
Permanent regime with energy sources:	$\nabla^2 T = P$
Transitory regime without energy sources:	$\frac{\partial T}{\partial t} = a \nabla^2 T$

4.3.1 Initial and boundary conditions

A partial differential equation admits an infinite number of solutions. To bound the problem, a set of initial and boundary conditions must be used.

Initial conditions

They are defined at the initial time t_0 and for the whole domain as:

$$T(x, y, z, t_0) = T_0(x, y, z) \tag{4.13}$$

Boundary conditions

These conditions define the state at all points of the limiting surface S of the domain V, for any given time $t > t_0$. Boundary conditions can be of three kinds:

- **Dirichlet boundary conditions:** the value of the temperature is fixed in a hard way by imposing: $T(x_w, y_w, z_w, t) = T_0$, where w sub-scripted quantities refer to quantities imposed at the limiting surface S.

- **Neumann boundary conditions:** the temperature is not fixed, only the heat flux is imposed at the surface S:

$$-\lambda \left(\frac{\partial T}{\partial \mathbf{n}} \right)_w = f(x_w, y_w, z_w, t) = q_w^s \tag{4.14}$$

For example, imposing $q_w^s = 0$ corresponds to an adiabatic condition. Note that in a closed system where only a Neumann boundary condition with positive sign is applied on all the surface S, the temperature of the solid will diverge as the energy will be constantly added to the solid.

- **Convective flux boundary conditions:** the heat flux is imposed from the convective flux at the surface of the wall S limiting with an external fluid flow. It is written as:

$$-\lambda \left(\frac{\partial T^s}{\partial \mathbf{n}} \right)_w = q_w^s = h(T^{\text{ext}} - T_w^s) \tag{4.15}$$

where T^{ext} is the mean temperature of the external flow, the s index is used to distinguish the variables describing the solid, and h is the convective heat transfer coefficient, which depends on the nature of the external flow. These expression links the three variables q_w^s, T^{ext} and T_w. There are then three different ways of imposing this boundary condition. The most commonly is to impose $T_w^s = f(q_w^s, T^{\text{ext}}, h)$. But it is also possible to impose the flux $q_w^s = f(T_w^s, T^{\text{ext}}, h)$, or the external flow temperature $T^{\text{ext}} = f(q_w^s, T_w^s, h)$.

4.4   The code AVTP

AVTP is a parallel numerical code that solves the heat equation (4.11) on unstructured hybrid meshes. The data structure and the numerical methods are inherited from the LES solver AVBP. The motivation for AVTP is to have access to a reliable and fast solver of the heat equation in solid components in a combustion system compatible with the LES solver AVBP. The main targeted applications are aerothermal unsteady coupled simulations with both AVTP and AVBP.

The numerical solver is based on a cell-vertex approach of a finite element discretization of the heat equation. The temporal integration is accomplished using a simple explicit numerical scheme:

$$\frac{\partial T}{\partial t} \approx \frac{T^{n+1} - T^n}{\Delta t} = a\nabla^2 T \tag{4.16}$$

where T^n and T^{n+1} are the temperatures at iterations n and $n+1$, which leads to:

$$T^{n+1} = T^n + \Delta t(a\nabla.\boldsymbol{\nabla}T^n) \tag{4.17}$$

The time step Δt is based on the diffusion velocity of the temperature from one cell to the next, and is based on the Fourier condition:

$$Fo = \frac{a\Delta t}{\Delta x_{min}^2} < 0.5 \tag{4.18}$$

where $\Delta x_{min} = \sqrt[3]{\text{Vol}_{min}}$ is the length of the smallest cell in the domain.

The diffusion term $(a\nabla.\boldsymbol{\nabla}T^n)$ can be solved using two methods. The first is derived from the cell-vertex discretization where a stencil of size 4Δ is used: the construction of the diffusion operator at one node requires the knowledge of the information of the two neighboring layers of cells (and nodes) as shown in Fig. 4.1-a. The second formulation is derived from a finite-element method with a vertex-centered discretization [101] that uses a smaller stencil of size 2Δ: to construct the diffusion operator this method only needs the information of the closest layer of cells and nodes (Fig. 4.1-b). Details on the diffusion operators used in AVTP are presented by Lamarque [143].

(a) *Cell-vertex* discretization   (b) *Vertex-centered* discretization
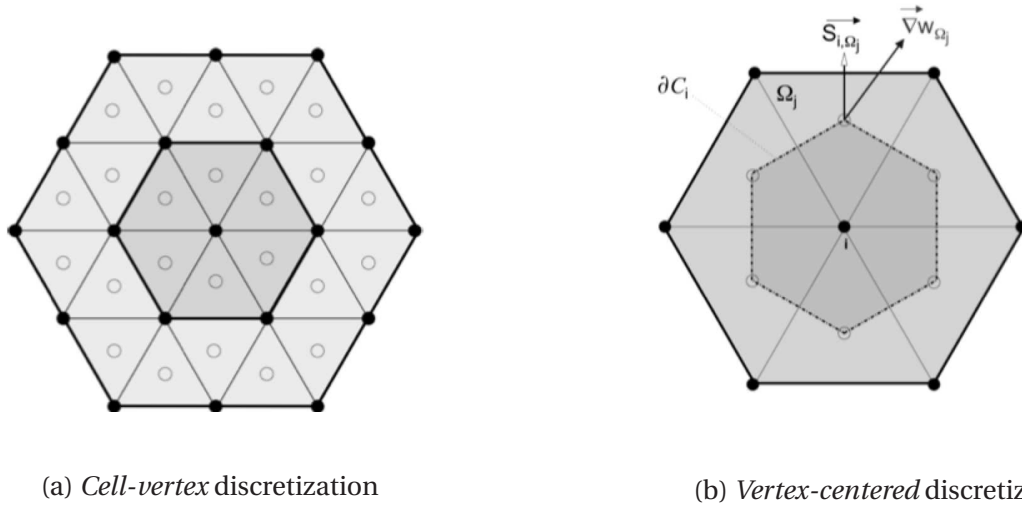
Figure 4.1: Nodes and cells used in the computation of the diffusion operator on the central node.

Four types of boundary conditions are available in AVTP:

1. **Isothermal wall (Dirichelt B.C.):** the temperature of the boundary surfaces are imposed.

2. **Heat loss wall (Neumann B.C.):** the temperature evolution of the boundary surface depends on the heat flux imposed through the knowledge of an external reference temperature T^{ref} and a covective heat transfer coefficient h.

3. **Adiabatic wall (Neumann B.C.):** is the same as the previous B.C. but the heat flux imposed is equal to zero.

4. **Flux-Temperature wall (Mixed B.C.):** mainly developed for coupled Fluid-Solit Thermal Interaction (FSTI) applications, in this boundary condition a heat flux is imposed and a reference temperature is added in order to help to code to converge to the target imposed: $q_w^s = q_w^{ref} + k(T - T^{\text{ref}})$.

4.5   Analytical and numerical solutions for the transient heat equation

Textbooks on heat transfer cover the most basic methods for the resolution of the heat transfer equation [152, 114, 110, 173, 251, 11], from the classical one-dimensional steady heat conduction problem to complex geometries like fins [152].

Among them, three resolution methods are discussed here and will be used as analytical references in four test cases to validate the simulations of the transient heat transfer problem. They are:

- **Test case 1:** the case of a small and highly conducting object plunged into a fluid at different temperature. The *Low-Biot approximation* is employed to determine its temperature evolution.

- **Test case 2:** the computation of the temperature evolution on an one-dimensional externally heated solid slab subject to Dirichlet boundary conditions on both ends. The heat conduction equation is solved using the *Fourier method*.

- **Test case 3:** the computation of the temperature evolution on the same one-dimensional but this time cooled using Dirichlet boundary conditions on both ends. The *Fourier method* is also employed.

- **Test case 4:** the determination of the transient temperature of a solid wall subject to a Dirichlet boundary condition in one end and a Neumann boundary condition in the other. The *Laplace transform* is used to solve the heat conduction equation in this case.

4.5.1 The Low-Biot approximation

Analytic solution

When the internal or external conditions of an originally stable medium are abruptly modified the system has to transit to a new stable state to achieve energy equilibrium. The time-evolution of the temperature in the solid is characterized by the Biot number Bi, which is proportional to the ratio between the convective heat transfer between the solid and the external flow and the conductive heat transfer within the solid:

$$Bi = \frac{hL}{\lambda} \tag{4.19}$$

where L is a characteristic length scale of the solid.

If $Bi \ll 1$ the main heat transfer process is conduction (low resistance of the solid). For a small and highly conductive sphere plunged into a fluid at different temperature ($Bi \ll 1$), it has been shown that the temperature of the sphere evolves following expression (4.20) [152].

$$\frac{T - T^{\text{ext}}}{T_0 - T^{\text{ext}}} = \exp\left(-\frac{hS}{\rho C V} t\right) \tag{4.20}$$

where t is the time, T^{ext} is the temperature of the external flow, T_0 is the initial temperature of the solid, S is the surface and V is the total volume of the solid. This analytical solution is the simplest version of the transient heat conduction equation. Diffusion of heat inside the solid is very fast. This analytical solution can be used to test the temporal integration of a heat conduction code and the reliability of the diffusion operator.

Furthermore, in real aeronautical applications this approximation can be useful to study the unsteady nature of the heat conduction, particularly in the thin layers of the combustion chamber liner and the walls of cane injectors.

Numerical simulation: test case 1

A benchmark case has been carried up in order to test AVTP under the Low-Biot approximation. In this case a 2D square of side length $L = 0.001$ [m], initially at the temperature $T(t = 0) = T_0 = 400$K, is plunged into a fluid which is at a higher temperature $T^{\text{ext}} = 600$K. The total surface of the solid is given by $S = 4L$, and the volume[1] $V = L \times L = 1\,10^{-6}$[m^2]. Given the heat conduction coefficient $h = 100$ [W m^{-2} K^{-1}], the density of the solid[2] $\rho = 7900$ [kg m^{-3}], the conductivity $\lambda = 68.203929$ [W m^{-1} K^{-1}] and the heat capacity $C = 450$ [J K^{-1} kg^{-1}], the solution of eq.(4.20) can be written and is plotted in Fig. 4.2.

---

[1] Here the volume of the 2D solid must be considered equal to the area of the square.
[2] The properties of the solid presented in this paragraph correspond to the properties of iron.
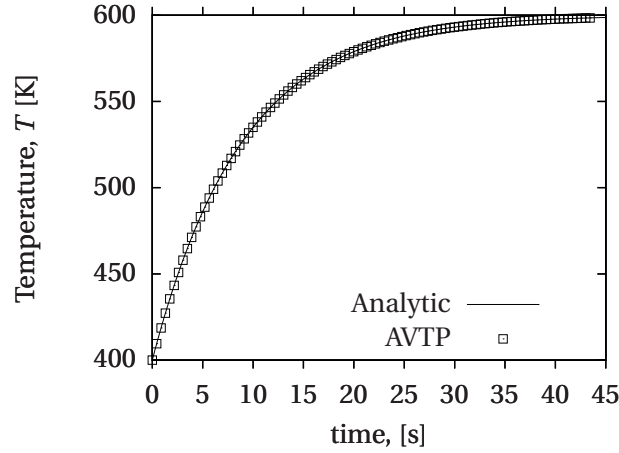
Figure 4.2: Temporal evolution of the solid temperature of test case 1.

In this case the Biot number is equal to $Bi = 0.0001466 \ll 1$, and the highly conducting solid approximation can be applied. The characteristic conductive time is equal to $\tau_{\text{cond}} = L^2/a \approx 4.335\,10^{-2}$ [s]. This characteristic time has an order of magnitude comparable with the characteristic times of some LES applications.

The simulation was carried out using a 30 x 30 cell mesh, and a convective flux boundary condition at all four limiting surfaces. The time evolution of the solid temperature is also plotted in Fig. 4.2 (symbols). The time step of such a simulation depends on the Fourier condition presented in eq.(4.18). In the present case this condition imposes a time step of $\Delta t = 2.8957\,10^{-5}$ [s]. This small time step is comparable to the time steps observed the simulation of compressible flows using implicit numerical schemes.

4.5.2 Resolution by the Fourier method

Analytic solution

Simulations of quasi-1D wall offer a more complete benchmark case for heat conduction codes. Fig. 4.3 shows the studied geometry. It is a simple slab at an initial uniform temperature T_0. A sudden change of the temperature of the surfaces ($T_w^s = 0$) modifies the temperature field inside the slab in space and time. The corresponding heat conduction equation writes:

$$\frac{\partial^2 T}{\partial x^2} = \frac{1}{a} \frac{\partial T}{\partial t} \tag{4.21}$$

with the conditions:

Initial condition: $\quad T(x, t = 0) = T_0$

Boundary conditions: $\quad \begin{cases} T(x = 0, t > 0) & = & T_w^s = 0 \\ T(x = L, t > 0) & = & T_w^s = 0 \end{cases}$
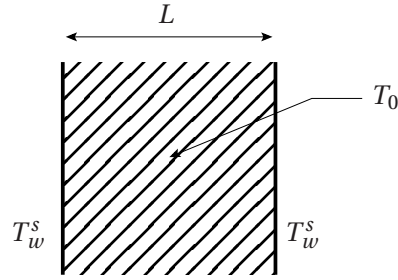
Figure 4.3: Quasi one-dimensional slab. Test case 2.

The simplest way to solve the problem is using Fourier's method: the temperature field is searched in the form of a linear combination of independent orthogonal functions: $T(x, t) = \sum_{k=0}^{\infty} F_k(x) G_k(t)$, where $F_k(x)$ and $G_k(t)$ are functions that depend only on the space and the time variable respectively. The functions depending only on one variable, the prime represents one differentiation of the function with respect of that variable, i.e. $F_k' = dF_k/dx$, $G_k' = dG_k/dt$, $F_k'' = d^2F_k/dx^2$ and $G_k'' = d^2G_k/dt^2$. Replacing T with this linear combination, each elementary solution $F_k(x) G_k(t)$ must verify:

$$F_k(x) \frac{dG_k(t)}{dt} = a G_k(t) \frac{d^2 F(x)}{dx^2} \tag{4.22}$$

which can be written:

$$\frac{G_k'}{G_k} = \frac{a}{F_k} F_k'' \tag{4.23}$$

The Left-Hand Side (LHS) and the Right-Hand Side (RHS) of this equation are functions of different independent variables. This happens only when both sides are equal to a constant:

$$\frac{G_k'}{G_k} = \frac{a}{F_k} F_k'' = -m_k \tag{4.24}$$

Integrating eq.(4.24) for the function G_k gives:

$$G_k' \quad = \quad -m_k G_k \tag{4.25}$$
$$G_k(t) \quad = \quad K_0 \exp(-m_k t) \tag{4.26}$$

In a similar way integrating eq.(4.24) for F_k gives:

$$\frac{d^2 F_k}{dx^2} = \frac{-m_k}{a} F_k \tag{4.27}$$

$$F_k(x) = K_1 \cos\left(\sqrt{m_k/a}\, x\right) + K_2 \sin\left(\sqrt{m_k/a}\, x\right) \tag{4.28}$$

Eq. (4.28) represents an infinite number of solutions of the differential system where K_1 and K_2 are integration constants. From the boundary conditions the particular solution of the heat conduction problem presented in this section can be deduced:

$$\begin{aligned} x = 0 &\quad \rightarrow \quad K_1 = 0 \\ x = L &\quad \rightarrow \quad \sin(\sqrt{m_k/a}\, L) = 0 \end{aligned}$$

where the second condition implies $\sqrt{m_k/a}\, L = k\pi$.

The full solution to the heat conduction equation is then:

$$T(x, t) = \sum_{k}^{\infty} B_k \sin(k\pi x/L) \exp(-k^2 t/\tau) \tag{4.29}$$

The orthogonality property of F_k, leads to the following expression for B_k:

$$B_k = \frac{\int_0^L T_0 \sin(k\pi x/L)\, dx}{\int_0^L \sin^2(k\pi x/L)\, dx} \tag{4.30}$$

which is equal to zero for pair values of k and gives $B_k = 4T_0/\pi k$ for odd values of k. We finally get:

$$T(x, t) = \frac{4T_0}{\pi}\left\{ \sin(\pi x/L)\exp(-t/\tau) + \frac{1}{3}\sin(3\pi x/L)\exp(-9t/\tau) + \frac{1}{5}\sin(5\pi x/L)\exp(-25t/\tau) + ... \right\} \tag{4.31}$$

Eq. (4.31) represents the spatial and temporal evolution of a 1D slab that cools down from an initial temperature to zero. For an arbitrary boundary temperature T_w^s, expression (4.31) can be generalized, giving:

$$T(x, t) = T_x^s - \frac{4(T_0 - T_w^s)}{\pi} \sum_{k}^{\infty} \frac{1}{2k+1} \sin\left(\frac{(2k+1)\pi x}{H}\right) \exp\left(\frac{-(2k+1)t}{\tau}\right) \tag{4.32}$$

Numerical solution: the heating wall - test case 2

In this second test case, a 2D solid of length L is considered, with an infinite transverse size so that the thermal problem is can be considered one-dimensional. A uniform temperature of $T_0 = 300$K is

imposed as initial condition. A temperature $T_w^s = 400K$ is suddenly imposed at both ends through a Dirichlet boundary condition. For a length $L = 1$[m] and using the same properties as in section 4.5.1, the temporal and spatial evolution of the temperature is described using eq.(4.32).
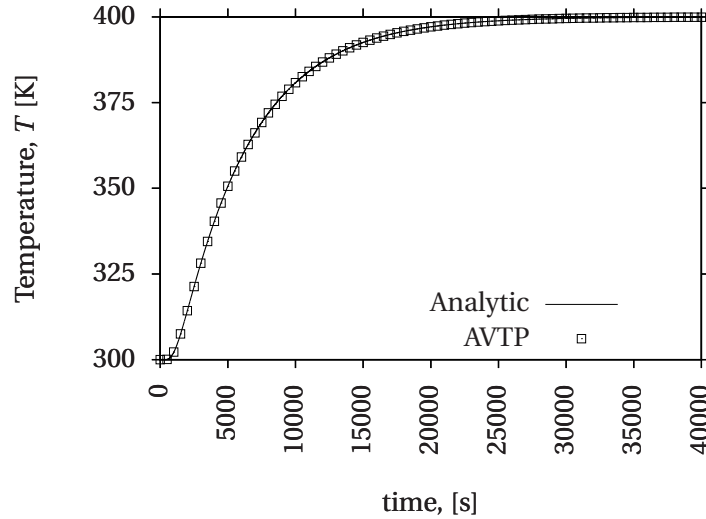
Figure 4.4: Temporal evolution of the temperature at $x = L/2$ for test case 2.

The mesh is a 30 x 30 cell domain, and isothermal surfaces (Dirichlet boundary conditions) are imposed along the axial direction, while periodic conditions are imposed in the transversal direction. The analytical and numerical solutions and the simulations are plotted vs. the time on in Fig. 4.4 at $x = L/2 = 0.5$[m]. In this case the characteristic conduction time is $\tau_{\mathrm{cond}} \approx 52000$[s] and the numerical time step is $\Delta t \approx 870$[s] (the time step is enormous in this case, mainly because each mesh has a length of $\Delta x = 33.33$ [cm]).

Figure 4.5 shows the spatial temperature profiles at different times obtained from theory and simulation. It can be seen that heating an iron[3] solid cube one meter high and one meter long takes a very long time. In general, cases of large sized solids with a low conductivity or cases of large sizes have a slow temperature evolution[4] compared to any convective phenomena of a fluid flow. During a small time interval the solid can then be considered isothermal.

Numerical solution: The cooling wall - test case 3

Inverting the initial and the boundary temperatures as $T_w^s = 300K$ and $T_0 = 400$K the solutions of figs. 4.6 and 4.7 are obtained. Characteristic times and numerical parameters do not change, and the same comments hold.

---

[3]The solid properties used in this examples are those of iron.

[4]In an electrical circuit analogy this means that the resistance of the circuit is high.

Figure 4.5: Evolution of the temperature profile test case 2. The profiles correspond to times (a) $t = 100$ [s] to (i) $t = 25600$ [s], with intermediary times (not explicitly labeled in the figure) (b) $t = 200$, (c) $t = 400$, (d) $t = 800$, (e) $t = 1600$, (f) $t = 3200$, (g) $t = 6400$, (h) $t = 12800$. Solutions in the AVTP simulation were stored only every $\Delta_{rec} t = 1600$ [s]

4.5.3   Resolution using the Laplace transform

Analytic solution

Another methodology to solve eq.(4.21) is to apply the Laplace transform, defined by:

$$\mathscr{L}\{f(t)\} = F(p) = \int_0^\infty e^t f(t) dt \tag{4.33}$$

This leads to to the second order ordinary differential equation:

$$\frac{\partial^2 F}{\partial x^2} - \frac{1}{a}\left[pF(p) - T_0\right] = 0$$

or,

$$F'' - \frac{p}{a}F = -\frac{T_0}{a} \tag{4.34}$$

where T_0 is the initial temperature of the slab.

The solution to this system can be written as:
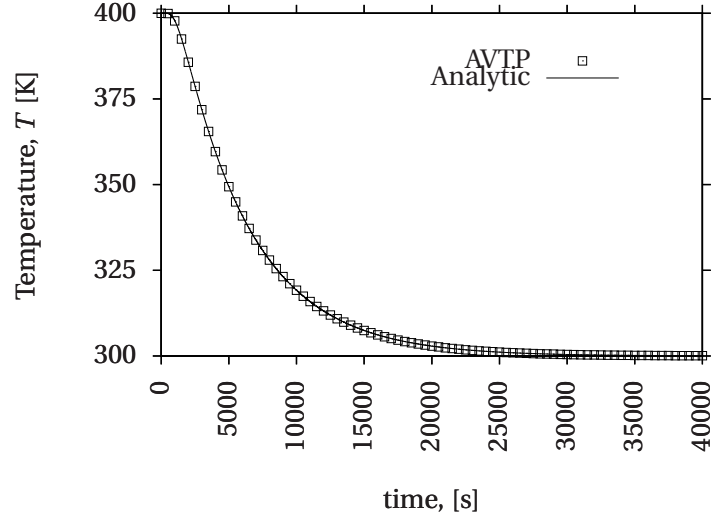
Figure 4.6: Temporal evolution of the temperature at the position $L/2$ for a cooling 1D wall of length $L = 1$m.

$$F(x, p) = \underbrace{A\exp(-qx) + B\exp(qx)}_{\text{Homogeneous solution}} + \underbrace{T_0/p}_{\text{particular solution}} \tag{4.35}$$

where $q = \sqrt{p/a}$.

We now consider the test case where, at the time $t = 0$, the temperature of one of the faces is instantly raised to T_w^s, while the second face is maintained adiabatic. Proceeding in the same way as before, it can be shown that the solution to the problem in the Laplacian space can be written:

$$f(x, p) = \frac{\theta_0}{p} - \frac{\theta_0}{p}\frac{\exp(-qx)}{1 + \exp(-2qL)} + \frac{\theta_0}{p}\frac{\exp(qx)}{1 + \exp(-2qL)} - \frac{\theta_0}{p}\exp(qx) \tag{4.36}$$

where $\theta_0 = T_0 - T_w^s$.

To apply the inverse Laplace transform, the dividend exponential terms are expressed using a series expansion:

$$\frac{1}{1 + \exp(-2qL)} = \sum_{n=0}^{\infty}(-1)^n\exp(-q(2nL + x)) = 1 + \sum_{n=1}^{\infty}(-1)^n\exp(-q(2nL + x)) \tag{4.37}$$

The inverse transform of expression (4.36) gives an expanded formulation of the solution:
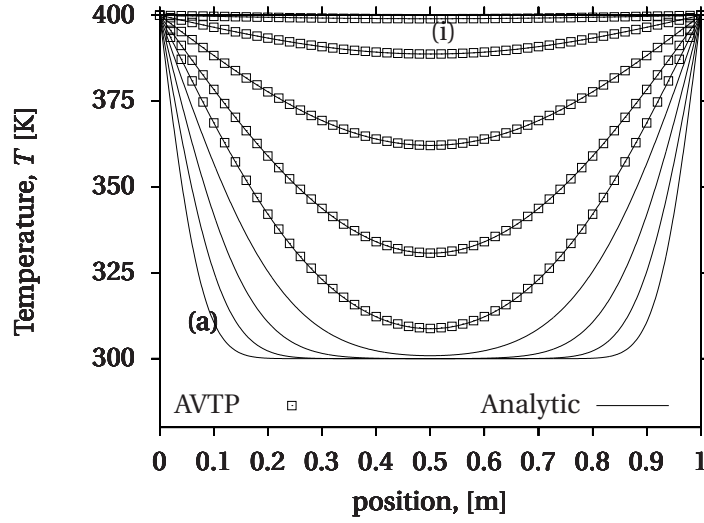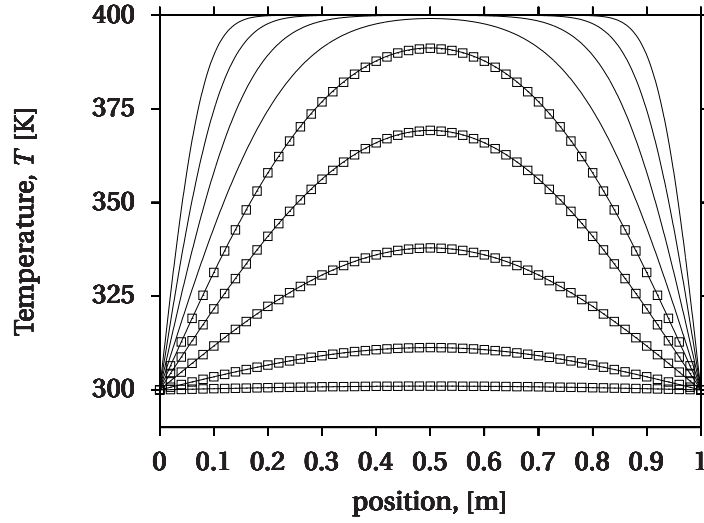
Figure 4.7: Evolution of the temperature profile test case 3. The profiles correspond to times $t = 100$, $t = 200$, $t = 400$, $t = 800$, $t = 1600$, $t = 3200$, $t = 6400$, $t = 12800$, $t = 25600$ [s]. Solutions in the AVTP simulation were stored only every $\Delta_{\text{rec}} t = 1600$ [s].

$$T(x,t) = T_w^s + \theta_0 \operatorname{erf}\left(\frac{x}{2\sqrt{at}}\right) + \theta_0 \sum_{n=0}^{\infty} (-1)^n \left[\operatorname{erfc}\left(\frac{2nL-x}{2\sqrt{at}}\right) - \operatorname{erfc}\left(\frac{2nL+x}{2\sqrt{at}}\right)\right] \qquad (4.38)$$

Numerical solution: test case 4

In this case, boundary conditions include an isothermal surface (Dirichlet B.C) at $x = 0$, periodic boundary conditions in the transverse direction and an adiabatic surface (Neumann B.C.) at $x = L$. The initial temperature of the wall is $T_0 = 400$K and the imposed wall temperature at the isothermal surface is $T_w^s = 600$K.

The space and time evolution of the problem are obtained from eq. (4.38). Results are compared in Fig. 4.8 at three different points inside the domain and show excellent agreement.

Figure 4.9 shows the spatial variation of the temperature at different times. It can be seen that the Neumann boundary condition (at $x = L$) is always satisfied and the heat flux at this surface remains zero.
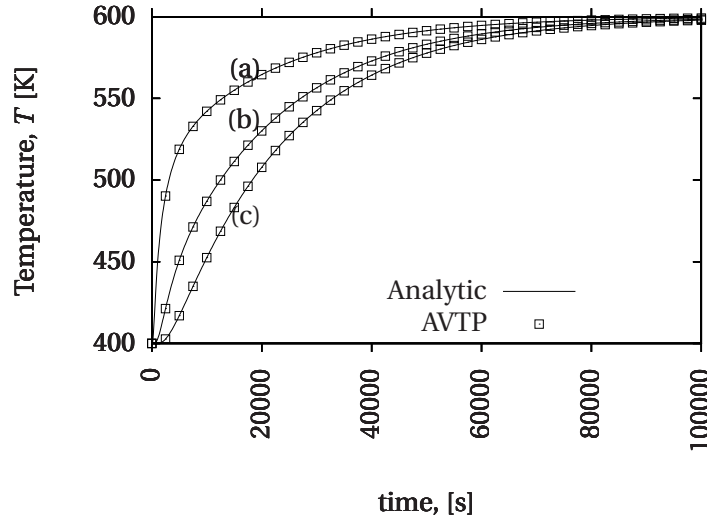
Figure 4.8: Temporal evolution of the temperature at three different positions: (a) $x = 0.25L$, (b) $x = 0.5L$ and $x = 0.75L$. Test case 4.

4.6 Temperature dependence of the solid properties

In the previous cases the properties of the solid were considered constant. However, the thermal conductivity $\lambda(T)$ and the heat capacity $C(T)$ both depend on the temperature of the solid. Figure 4.10 illustrates how $\lambda(T)$ changes with the temperature for different materials. In AVTP the temperature dependence are accounted for by using polynomial approximations:

$$C(T) = \sum_{k}^{K} C_k T^k \tag{4.39}$$

$$\lambda(T) = \sum_{k}^{K} \lambda_k T^k \tag{4.40}$$

Table 4.2 gives the values of the polynomial constants for iron. Such tables are given as input values to the code. When the properties of the material are considered invariant with the temperature, all the constants but the first are set to zero.
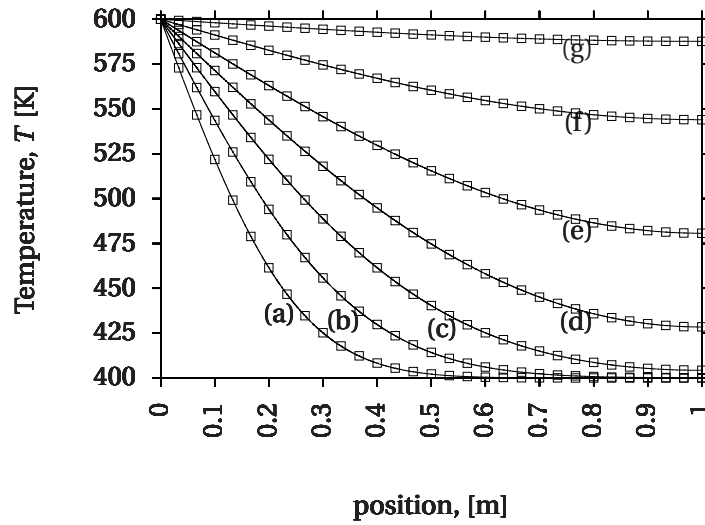
Figure 4.9: Spatial temperature profiles for seven different times (units, seconds [s]): (a) $t = 1000$, (b) $t = 2000$, (c) $t = 4000$, (d) $t = 8000$, (e) $t = 16000$, (f) $t = 32000$, (g) $t = 64000$. Test case 4.

Table 4.2: Constants for the heat conductivity and heat capacity polynomial dependence on temperature for the iron.

k	0	1	2	3	4	5	6
C_k	255.3757	1.6156	-0.00462	$0.6038 \ 10^{-5}$	$-0.4096 \ 10^{-8}$	$0.1405 \ 10^{-11}$	$-0.1924 \ 10^{-15}$
λ_k	68.2039	0.01698	$-0.2783 \ 10^{-3}$	$0.3836 \ 10^{-6}$	$-0.1989 \ 10^{-9}$	$0.38666 \ 10^{-13}$	$-0.1097 \ 10^{-17}$

4.7   Heat transfer in a 3D geometry

In this section a 3D geometry is simulated. The main goal is to evaluate the performances of the code in a realistic configuration. The studied geometry is the "T" shaped cane injector of a combustion chamber (Fig. 4.11). Cold fuel is injected in the central cylinder, and is expelled to the chamber through two lateral pipes (cane tips). Outside the cane (in the combustion chamber) the combustion products are raised to very high temperatures. The cane is subjected to strong thermal stresses, with a relatively cold flow at the interior and a hot flow at the exterior. Moreover, the thickness of the wall is small (of the order of one millimeter) so that temperature gradients are strong.

Four different boundary zones (boundary patches) have been defined in the geometry: the cane fixation (Fig. 4.11-A), the cane base (Fig. 4.11-B), the interior of the pipe (Fig. 4.11-C) and the exterior of the pipe (Fig. 4.11-D). The solid is composed by iron, which has the same properties described in section 4.5.1

In the interior, exterior and base zones a convective flux boundary condition was used. The values for h, T_w^s imposed in this zones are summarized in Table 4.3 and were taken arbitrarily to mimic reheat by hot gas of the external flow. The boundary condition applied to the fixation corresponds to an isothermal surface.

Table 4.3: Boundary conditions for the 3D test case.

Boundary patch	h [W m^{-2} K^{-1}]	T_{ref} [K]	Surface area [m^2]
Interior	3000	600	$1.84\ 10^{-3}$
Exterior	850	2000	$2.25\ 10^{-3}$
Base	850	2000	$3.74\ 10^{-4}$
Fixation (isothermal)	-	800	$1.25\ 10^{-4}$

The initial condition has been set up in order to test the code capacity to respond to a rapid variation in boundary conditions. The solid was initialized with a temperature field at a constant temperature $T_0 = 600$K. The heat flux imposed at the exterior of the cane rises the temperature. The cooling flux at the interior counterbalances the heating effect, but the cooling heat flux is lower than the heating flux. The expected behavior for the solid is then to rise its temperature up to the point of balance between the internal and external energy fluxes.

Figure 4.12 shows the temporal evolution of the mean, maximum and minimum temperatures in the solid. The minimal temperature rises from the initial value $T_0 = 600$K up to the value of the isothermal wall $T_w^s = 800$K.

The variation of the temperature at the boundary surfaces produces a variation of the heat fluxes through the patches. The problem is therefore a closed loop. The solid is considered at equilibrium when the energy budget[5] is zero. Figure 4.13 shows the evolution of all heat fluxes and the heat flux budget. Equilibrium is reached after 6 seconds.

The initial temperature in the domain is uniform. Using a Dirichlet boundary condition in the fixation of the cane with a temperature 200K higher than the domain produces an initial jump in the heat flux at this surface which is reflected in the budget profile of Fig. 4.13. With the evolution of the temperature field in the solid the heat flux on each surface adapts in order to respond to the boundary condition. The heat flux levels observed in the internal surface are very close to the levels observed in the external surfaces, but with an inverted sign.

---

[5]The sum of the energy fluxes through all the surfaces plus the internal volume sources.
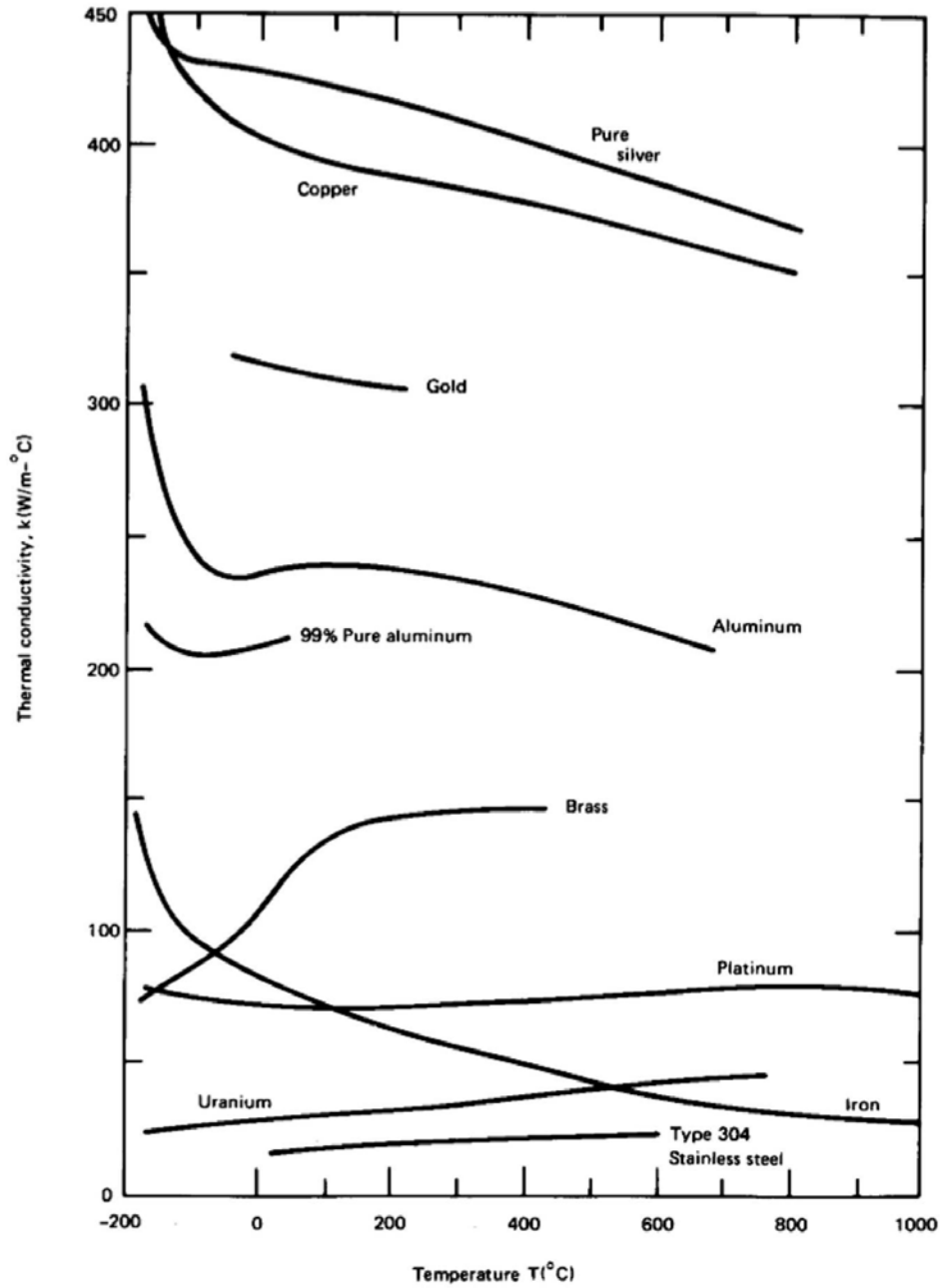
Figure 4.10: Temperature dependence of the thermal conductivity for different materials. extracted from [152].
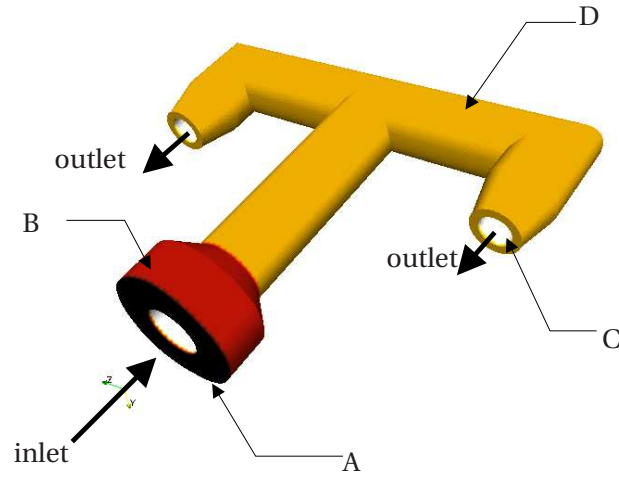
Figure 4.11: Geometry of the 3D case and boundary zones. The interior pipe is colored in withe. (A) Fixation of the cane to the chamber wall. (B) Base of the cane. (C) Internal wall of the vaporizer. (D) External wall of the vaporizer. The inlet and outlet arrows point in the direction of the fuel flow.
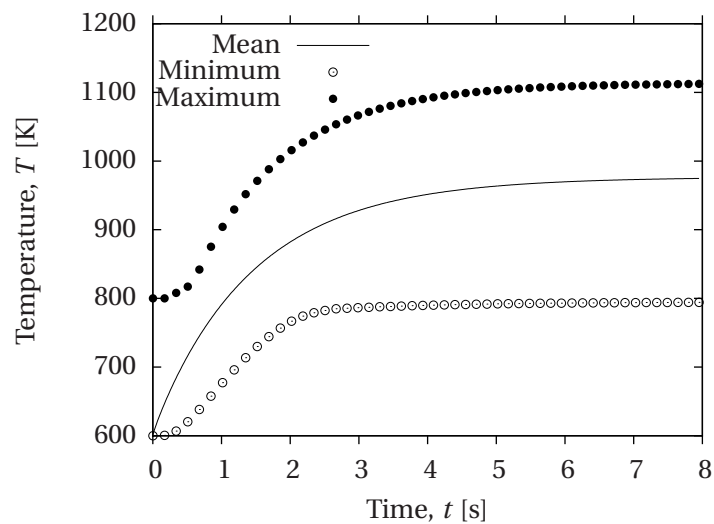
Figure 4.12: Temporal evolution of the mean, maximum and minimum temperatures in the solid for the 3D case.
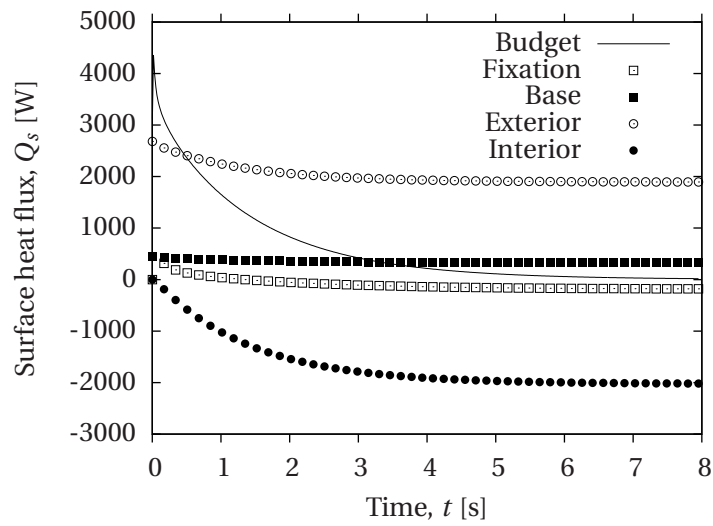
Figure 4.13: Temporal evolution of the surface heat fluxes Q_s through the boundary patches in symbols, and their summation (energy budget) in a continuous line.

5

Heat and mass transfer in fluid flows

Contents

5.1 Thermochemistry of multicomponent mixtures

Thermochemistry is the study of the physical transformations involved in a system where chemical elements evolve. Multicomponent mixtures of chemical elements are subject to thermochemical processes such as heat exchange, mixing, phase transitions and chemical reactions. This science sets the bases for the study of combustion processes.

When a combustible gas and an oxigen-rich gas are mixed together an exothermic chemical reaction[1] can be triggered. The chemical components are transformed into new chemical species and a certain amount of energy is released.

To understand how much energy is created in such a reaction the basic elements and processes in the combustion phenomena are presented in the next sections.

5.1.1 Primitive variables

In an isolated thermodynamic system, lets consider a mixture of k different species, called $\mathscr{M}_k$, characterized by their chemical, thermodynamic and transport properties.

An elemental *chemical property* of species $\mathscr{M}_k$ is the number of atoms z_i of each element $\mathscr{N}_i$ that compose the molecule $\mathscr{M}_k$. Knowing the atomic composition of a substance, its mean molar mass W_k can be obtained by simple addition of the molar masses $M_{\mathscr{N}_i}$ of each element: $W_k = \sum_i z_i M_{\mathscr{N}_i}$ [kg/mol].

The *thermodynamic properties* of the k-th species are:

- The quantity of matter, i.e. the number of moles n_k, of species k in the volume V, [mol/m^3].

- The heat capacities at constant volume $C_{v,k}$ and constant pressure $C_{p,k}$: amount of energy required to increase the temperature of a unit quantity of the substance k by a unit of temperature, [J kg^{-1} K^{-1}].

- The formation enthalpy $\Delta h_{f,k}^0$ of $\mathscr{M}_k$: energy absorbed in the formation of the chemical bonds of the molecule from its constituent elements $\mathscr{N}_i$ and their standard states (commonly measured at room conditions, i.e. at 1 bar and 298.15 K), [J/kg].

The *transport properties* permit to calculate the displacement of species k in a flow, i.e., the mean velocity of the molecules of species k within the system. The transport of molecules depend on the intermolecular interactions. They are:

- thermal conductivity, λ [W.m^{-1}K^{-1}], indicates the ability of the fluid to transport heat.

- species diffusion, D_l^k [m^2/s], represents the speed at which species k diffuses into species l.

- shear viscosity, μ [kg.s^{-1}m^{-1}], is a measure of the resistance of a fluid deformed by stress.

---

[1] Exothermic reactions refer to chemical reactions where heat is a result of the chemical process. The opposite of exothermic reaction is endothermic reaction.

Data concerning the chemical, thermodynamic and transport properties of molecules can be found in databases (JANAF [248] and the NASA database [168]) and are obtained by experimental measurements or by a detailed simulation of the interactions between particles at the atomic level. Using these properties mixing laws allow to derive all thermochemical properties of any mixture.

The mass m_k of species k is equal to the number of moles multiplied by the molar weight of the particle as shown by eq.(5.1). The total mass m (eq. 5.2) and the total number n of moles in the system (eq. 5.3) are the result of a somation over all species ($k = 1, N$):

$$m_k = n_k W_k \tag{5.1}$$

$$m = \sum_{k=1}^{N} m_k \tag{5.2}$$

$$n = \sum_{k=1}^{N} n_k \tag{5.3}$$

The mixture can be described either with the quantity of matter or the quantity of mass. In the first case the quantities used are the molar concentration $[X_k]$ of species k, the concentration $[X]$ of the mixture and the mole fraction X_k of species k. The quantities associated to mass are the density ρ_k of species k, the density of the mixture ρ and the mass fraction Y_k. Definitions of these quantities are given in Table 5.1.

Table 5.1: Definitions.

using molar quantities	using mass quantities
$[X_k] = \frac{n_k}{V}$	$\rho_k = \frac{m_k}{V}$
$[X] = \sum_{k=1}^{N} [X_k] = \frac{n}{V}$	$\rho = \sum_{k=1}^{N} \rho_k = \frac{m}{V}$
$X_k = \frac{n_k}{n} = \frac{[X_k]}{[X]}$	$Y_k = \frac{m_k}{m} = \frac{\rho_k}{\rho}$

The link between these descriptions is expressed by eq.(5.4), where W represents the mean molar mass of the mixture and is defined by (5.5):

$$Y_k = X_k \frac{W_k}{W} \tag{5.4}$$

$$W = \frac{m}{n} = \sum_{k=1}^{N} X_k W_k = \left(\sum_{k=1}^{N} \frac{Y_k}{W_k} \right)^{-1} \tag{5.5}$$

By definition, the sum of the N species mass fractions (mole fractions) found in the mixture must be equal to 1: $\sum_{k=1}^{N} Y_k = 1$ ($\sum_{k=1}^{N} X_k = 1$).

The ideal equation of state is used for the mixture and is given in eq. (5.6), where the pressure p is equal to the sum of the partial pressures p_k of each species. It is possible to write an equation of state for each of the species as shown in eq. (5.9):

$$pV = nRT \tag{5.6}$$

$$p_k = pX_k \tag{5.7}$$

$$p = \sum_{k=1}^{N} p_k \tag{5.8}$$

$$p_k V = n_k RT \tag{5.9}$$

Eq. (5.6) and (5.9) can be also written as:

$$p = \rho r T \tag{5.10}$$

$$p_k = \rho_k r_k T \tag{5.11}$$

The quantities r and r_k are the gas constant of the mixture and the gas constant of species k respectively, defined in eq. (5.12) and eq. (5.13), where $R = 8.314$ [JK^{-1}mole^{-1}] is the universal gas constant:

$$r \quad = \quad \frac{R}{W} = \sum_{k=1}^{N} Y_k r_k \tag{5.12}$$

$$r_k \quad = \quad \frac{R}{W_k} \tag{5.13}$$

The energy contained in the mixture can be represented by the value of the internal energy e or by the specific enthalpy h. The two variables are related through $e = h - p/\rho$. These variables are used for the energetic analysis of reacting flows. The total heat capacity at constant pressure C_p and volume C_v are defined in Table 5.2. The same definitions hold for the partial heat capacities of species k at constant pressure $C_{p,k}$ and volume $C_{v,k}$, so that the sum of the partial heat capacities is equal to the total heat capacity (eq. 5.14 and 5.15).

Table 5.2: Calorific capacities

	Constant pressure	Constant volume
Total (mixture)	$C_p = \left(\frac{\partial h}{\partial T}\right)_p$	$C_v = \left(\frac{\partial e}{\partial T}\right)_v$
Partial (species k)	$C_{p,k} = \left(\frac{\partial h_k}{\partial T}\right)_p$	$C_{v,k} = \left(\frac{\partial e_k}{\partial T}\right)_v$

$$C_p = \sum_{k=1}^{N} Y_k C_{p,k} \tag{5.14}$$

$$C_v = \sum_{k=1}^{N} Y_k C_{v,k} \tag{5.15}$$

The ratio C_p/C_v is known as the polytropic coefficient, γ. Moreover a simple relation exists between the heat capacities (eqs. 5.16 and 5.17), so that the gas mixture is fully described by γ, C_p and r only:

$$C_p - C_v \;\; = \;\; r \tag{5.16}$$

$$C_{pk} - C_{vk} \;\; = \;\; \frac{R}{W_k} \tag{5.17}$$

As shown in eq. (5.18), enthalpy is composed by two terms, one varying with temperature, called sensible enthalphy h_{sk} and the other constant, called formation enthalpy $\Delta h^0_{f,k}$, that can be read from databases [248, 168]. Integrating the partial heat capacity $C_{p,k}$ gives the sensible enthalpy h_{sk} of species k. In a similar way the internal energy e_k is the sum of a constant and a sensible part $e_{s,k}$, which results from the integration of $C_{v,k}$:

$$h_k = \int_{T_0}^{T} C_{pk} dT + \Delta h^0_{f,k} = h_{sk} + \Delta h^0_{f,k} \tag{5.18}$$

$$e_k = \int_{T_0}^{T} C_{vk} dT - \frac{RT_0}{Wk} + \Delta h^0_{f,k} = e_{sk} - \frac{RT_0}{W_k} + \Delta h^0_{f,k} \tag{5.19}$$

The mass enthalpy of the mixture is obtained by the sum of the enthalpy of each species weighted by mass fractions, as shown in eq.(5.20). The same is true for the total internal energy of the system in eq.(5.21):

$$
\begin{aligned}
h = \sum_{k=1}^{N} h_k Y_k &= \sum_{k=1}^{N} \left(\int_{T_0}^{T} C_{pk} \, dT + \Delta h_{f,k}^0 \right) Y_k \\
&= \int_{T_0}^{T} C_p \, dT + \sum_{k=1}^{N} \Delta h_{f,k}^0 Y_k \\
&= h_s + \sum_{k=1}^{N} \Delta h_{f,k}^0 Y_k
\end{aligned}
\tag{5.20}
$$

$$
\begin{aligned}
e = \sum_{k=1}^{N} e_k Y_k &= \sum_{k=1}^{N} \left(\int_{T_0}^{T} C_{vk} \, dT - \frac{RT_0}{W_k} + \Delta h_{f,k}^0 \right) Y_k \\
&= \int_{T_0}^{T} C_v \, dT - \frac{RT_0}{W} + \sum_{k=1}^{N} \Delta h_{f,k}^0 Y_k \\
&= e_s - \frac{RT_0}{W} + \sum_{k=1}^{N} \Delta h_{f,k}^0 Y_k
\end{aligned}
\tag{5.21}
$$

5.1.2 Chemical kinetics

In combustion science the oxidation of fuel involves a chemical kinetic mechanism, globally represented by the scheme $F + O \rightarrow P$, where F is the fuel, O is an oxidizing molecule like air or oxygen, and P are the products of the reaction. A combustion reaction can be triggered for a large range of $(F + O)$ mixture compositions.

Chemical reactions

When two reactants enter in contact at a sufficiently high temperature, they react to produce new molecules and release energy. The newly created molecules may in turn interact and release more energy, producing other new molecules. This process is repeated until chemical equilibrium is reached. This makes the oxidation of hydrocarbons complex and difficult to solve, with a complexity increasing with the length of the carbon chain.

In the present work the kinetic mechanism is simplified. Consider a mixture of N species that can interact thanks to the action of M reactions:

$$\sum_{k=1}^{N} v'_{kj} \mathcal{M}_k \rightleftharpoons \sum_{k=1}^{N} v''_{kj} \mathcal{M}_k \qquad j = 1, M \tag{5.22}$$

where the stoichiometric coefficients v'_{kj} and v''_{kj} guarantee mass conservation, and verify:

$$\sum_{k=1}^{N} v_{kj} W_k = 0 \tag{5.23}$$

where,

$$v_{kj} = v''_{kj} - v'_{kj} \tag{5.24}$$

The mass (mol) variation of any species k due to the reactions is described by the mass reaction rate $\dot{\omega}_k$ shown in eq. (5.25), where $\mathcal{Q}_j$ is known as the progress rate of reaction j and is defined by expression (5.26):

$$\dot{\omega}_k = \sum_{j=1}^{M} \dot{\omega}_{kj} = W_k \sum_{j=1}^{M} v_{kj} \mathcal{Q}_j \tag{5.25}$$

$$\mathcal{Q}_j = \frac{\dot{\omega}_{kj}}{W_k v_{kj}} \tag{5.26}$$

The progress rate of reaction j is:

$$\mathcal{Q}_j = K_{fj} \prod_{k=1}^{N} \left(\frac{\rho Y_k}{W_k} \right)^{v'_{kj}} - K_{rj} \prod_{k=1}^{N} \left(\frac{\rho Y_k}{W_k} \right)^{v''_{kj}} \tag{5.27}$$

where K_{fj} and K_{rj}, are the forward and reverse reaction rates. It is generally accepted that these coefficients can be modeled with an empirical Arrhenius law:

$$K_{fj} = A_{fj} T^{\beta_j} \exp\left(-\frac{E_{aj}}{RT} \right) = A_{fj} T^{\beta_j} \exp\left(-\frac{T_{aj}}{T} \right) \tag{5.28}$$

where A, β_j and E_{aj} are respectively the pre-exponential factor, the temperature exponent and the activation energy of the reaction. These parameters are determined through measurements or specific calculations when developing detailed chemical schemes. They are adjusted by comparison with detailed chemistry when developing simplified chemistry. In a simplified chemical scheme the stoichiometric exponents v'_{kj} and v''_{kj} are also considered adjustable parameters. In this case they are noted n'_{kj} and n''_{kj}, and preserve mass conservation:

$$v_{kj} = v''_{kj} - v'_{kj} = n''_{kj} - n'_{kj} \tag{5.29}$$

The reverse reaction rate is obtained through the equilibrium condition:

$$K_{rj} = \frac{K_{fj}}{\left(\frac{p_a}{RT}\right)^{\sum_{k=1}^{N} \nu_{kj}} \exp\left(\frac{\Delta S_j^0}{R} - \frac{\Delta H_j^0}{RT}\right)} \tag{5.30}$$

where $p_a = 1$ bar. The Δ symbols refer to changes occurring when passing from reactants to products in the j-th reaction: ΔH_j^0 and ΔS_j^0 are respectively enthalpy and entropy changes for reaction j. These quantities are obtained from tabulations.

The associated heat source term is defined as:

$$\dot{\omega}_T = -\sum_{k=1}^{N} \Delta h_{f,k}^0 \dot{\omega}_k \tag{5.31}$$

Stoichiometry

When fuel and oxidizer are mixed in optimal proportions, they are completely transformed into products. In this case the combustion is said to be stoichiometric. The ratio between the mass fractions of oxidizer and fuel at stoichiometric conditions is known as the stoichiometric coefficient s defined by:

$$\left(\frac{Y_O}{Y_F}\right)_{st} = \frac{\nu_O' W_O}{\nu_F' W_F} = s \tag{5.32}$$

However, in most applications the fuel/oxidizer mixture is not stoechiometric: exces of oxidant corresponds to lean mixtures, while excess of fuel corresponds to rich mixtures. In hydrocarbon combustion a stoechiometric mixture leads to a maximum production of energy, however high temperatures are associated with production of toxic species as nitrogen oxides (NO_x). Low combustion temperatures on the other hand are obtained using lean combustion, but are also associated with a high production of another toxic gas: carbon monoxide (CO). Combustion processes are then often placed in between the lean and stoeichiometric limits.

The equivalence ratio ϕ, defined in eq.(5.33), is used to determine the combustion regime ($\phi < 1$ for lean combustion; $\phi > 1$ for rich combustion):

$$\phi = s\frac{Y_F}{Y_O} = \frac{Y_F/Y_O}{(Y_F/Y_O)_{st}} \tag{5.33}$$

Premixed and non-premixed combustion

From a practical point of view, fuel and oxidizer can enter into contact in two different ways:

- premixed combustion: both reactants are mixed previously to their injection in the combustion chamber.

- non-premixed combustion: the reactants are independently injected through different injectors in the combustion chamber.

These two situations correspond to different flame structures and properties. In premixed flames the local equivalence ratio has an homogeneous spatial distribution which can be associated to the mass flow rates of fuel and oxidizer:

$$\phi = s\frac{Y_F^0}{Y_O^0} = s\frac{\dot{m}_F}{\dot{m}_O} \tag{5.34}$$

where Y_F^0 and Y_O^0 are the fuel and oxidizer mass fractions respectively at the injection.

In non-premixed flames (also called diffusion flames), where the fuel and the oxidizer are injected separately, the equivalence ratio is:

$$\phi = s\frac{Y_F^1}{Y_O^2} \tag{5.35}$$

where Y_F^1 is the fuel mass fraction at the fuel injector, and Y_O^2 is the oxidizer mass fraction at the oxidizer injector. This definition characterizes the local structure of the flame but does not represent the combustor overall behavior. A global equivalence ratio is then also defined as:

$$\phi_g = s\frac{\dot{m}_F}{\dot{m}_O} \tag{5.36}$$

where $\dot{m}_F$ and $\dot{m}_O$ are the fuel and the oxidizer flow rates. The global and the local equivalence ratios are related via:

$$\phi_g = \phi\frac{\dot{m}^1}{\dot{m}^2} \tag{5.37}$$

where $\dot{m}^1$ and $\dot{m}^2$ are the total flow rates through the two injectors. In premixed flames $\dot{m}^1 = \dot{m}^2$ so that $\phi_g = \phi$.

It is often useful to define a passive scalar that is not affected by combustion. The mixture fraction is defined as [148]:

$$z = \frac{sY_F - Y_O + Y_O^0}{sY_F^0 + Y_O^0} \tag{5.38}$$

where Y_F^0 and Y_O^0 are the fuel and oxidizer mass fractions at injection. For stoichiometric combustion $sY_F - Y_O = 0$ and expression (5.38) reduces to the stoichiometric mixture fraction:

$$z_{st} = \frac{Y_O^0}{sY_F^0 + Y_O^0} = \frac{1}{\phi + 1} \tag{5.39}$$

5.2   The multicomponent Navier-Stokes equations

The equations of fluid motion

Eq. (5.40)-(5.42) are the conservative form of the Navier-Stokes equations for mass, momentum and energy (Einstein summation convention is used). In these equations u_i is the i-th component of velocity, ρ is the density as defined in Table 5.1, τ_{ij} is the viscous stress tensor (defined in eq. 5.43), f_i is a volume force, p is the pressure, E is the total energy defined as $E = e_s + \frac{1}{2}u_i u_i$ and q_j is the j-th component of the heat flux vector.

$$\frac{\partial \rho}{\partial t} + \frac{\partial \rho u_j}{\partial x_j} = 0 \tag{5.40}$$

$$\frac{\partial \rho u_i}{\partial t} + \frac{\partial \rho u_i u_j}{\partial x_j} = -\frac{\partial p}{\partial x_j} + \frac{\partial \tau_{ij}}{\partial x_j} + \rho f_i \tag{5.41}$$

$$\frac{\partial \rho E}{\partial t} + \frac{\partial \rho E u_j}{\partial x_j} = -\frac{\partial u_i p}{\partial x_j} + \frac{\partial q_j}{\partial x_j} + \frac{\partial u_i \tau_{ij}}{\partial x_j} + u_i \rho f_i \tag{5.42}$$

with,

$$\tau_{ij} = \left[\mu \left(\frac{\partial u_j}{\partial x_i} + \frac{\partial u_i}{\partial x_j} \right) + \mu'' \frac{\partial u_i}{\partial x_i} \right] \tag{5.43}$$

For a Newtonian fluid, both viscosity coefficients μ and μ'' are related via the Stokes relation: $2\mu + 3\mu'' = 0$, which leads to:

$$\tau_{ij} = \mu \left[\left(\frac{\partial u_j}{\partial x_i} + \frac{\partial u_i}{\partial x_j} \right) - \frac{2}{3} \frac{\partial u_i}{\partial x_i} \right] \tag{5.44}$$

The conservation equations for multicomponent reacting mixtures

Introducing multiple species into the system (5.40)-(5.42), mass conservation is split into mass fraction conservation equations for each species, with new terms arising from chemical reactions and species diffusion:

$$\frac{\partial \rho Y_k}{\partial t} + \frac{\partial}{\partial x_i}\left(\rho(u_i + V_i^k)Y_k\right) = \dot{\omega}_k \tag{5.45}$$

where V_i^k is the i-th component of the diffusion velocity of the k-th species and $\dot{\omega}_k$ is the reaction rate of species k (as defined in eq. 5.27).

Additionally a heat source term $\dot{\omega}_T$ appears in the energy equation:

$$\frac{\partial \rho E}{\partial t} + \frac{\partial \rho E u_j}{\partial x_j} = -\frac{\partial u_i p}{\partial x_j} + \frac{\partial q_j}{\partial x_j} + \frac{\partial u_i \tau_{ij}}{\partial x_j} + u_i \rho f_i + \dot{\omega}_T \tag{5.46}$$

Mass conservation imposes:

$$\sum_{k=1}^{N} Y_k V_i^k \quad = \quad 0 \tag{5.47}$$

$$\sum_{k=1}^{N} \dot{\omega}_k \quad = \quad 0 \tag{5.48}$$

These equations include terms relating to the velocity of diffusion of heat and mass in the fluid. Commonly used approximations of these terms are presented here:

- **Diffusion velocities**

  Involve multiple transport processes:

  $$V_i^k = -\underbrace{\sum_{l=1}^{N} D_l^k \frac{\partial X_l}{\partial x_i}}_{\text{mixture effect}} - \underbrace{\sum_{l=1}^{N} D_l^k (X_l - Y_l)\frac{1}{p}\frac{\partial p}{\partial x_i}}_{\text{pressure gradient effect}} - \underbrace{\sum_{l=1}^{N} D_l^k \chi_l \frac{\partial \ln(T)}{\partial x_i}}_{\text{Soret effect}} \tag{5.49}$$

  Species diffusion is mainly driven by three terms: the gradient of species concentration, the pressure differential and the Soret effect, where the gradient of the logarithm of the temperature is involved. In most applications where molecules are very small the Soret effect can be neglected[2] [32, 73, 88]. In addition the pressure gradient is usually small enough to also neglect the second terms.

---

[2]In systems where particles are big enough, as for example with sooting flames or coal combustion, the Soret effect might be important.

The term D_l^k represents the diffusion coefficient of species k with species l. The matrix $D = [D_l^k]$ is symmetric but its calculation is quite complex. A first order approximation is used instead, following the Hirschfelder-Curtis relation [102]:

$$Y_k V_i^k = -\mathscr{D}_k \frac{W_k}{W} \frac{\partial X_k}{\partial x_i} \tag{5.50}$$

with

$$\mathscr{D}_k = \frac{1 - Y_k}{\sum_{j \neq k}^{N} X_j / D_j^k} \tag{5.51}$$

The coefficient $\mathscr{D}_k$ corresponds to the diffusion of species k in the mixture. This approximation however does not guarantee mass conservation, thus a correction velocity V^c is added:

$$V_i^c = \sum_{k=1}^{N} \mathscr{D}_k \frac{W_k}{W} \frac{\partial X_k}{\partial x_i} \tag{5.52}$$

Computing the values for the diffusion coefficients $\mathscr{D}_k$ can be long, and unnecessary. Indeed, for combustion applications where reduced chemical schemes are employed, involving a limited number of reactions and species, a detailed representation of the transport properties would not necessarily improve the accuracy of the results. An useful simplification is to consider that the Schmidt number of each species Sc_k does not change in space and time, so that the diffusion coefficient for each species can be obtained as:

$$\mathscr{D}_k = \frac{\mu}{\rho Sc_k} \tag{5.53}$$

where the species Schmidt number is defined as the ratio between the momentum diffusivity and the mass diffusivity of species k.

- **Viscosity**

Depends on the species concentration. However in most CFD codes the dynamic viscosity μ is considered independent of the mixture and only dependent on temperature, as the error induced by such approximation is small [203]. These dependence can be characterized by the Sutherland law (eq. 5.54), or a power law of (eq. 5.55):

$$\mu = c_1 \frac{T^{2/3}}{T + c_2} \frac{T_{\text{ref}} + c_2}{T_{\text{ref}}^{3/2}} \tag{5.54}$$

$$\mu = \mu_0 \left(\frac{T}{T_{\text{ref}}} \right)^b \tag{5.55}$$

where $c_1 = 1.71\,10^{-5}$ kg/m.s, $c_2 = 110.4$ K and $b = 0.76$ for air at room conditions. The reference molecular viscosity of the power law for air is $\mu_0 = 1.788\,10^{-5}$ [kg m^{-1} s^{-1}]. Values for other mixtures can be easily retrieved from databases by using softwares like CHEMKIN for example.

- **The heat flux vector**

  For single component mixtures the heat flux vector only contains the contribution of conduction and radiation. In a multi-component gas mixture additional terms arise due to the transport of energy by species diffusion. This gives:

$$q_i = \underbrace{-\lambda \frac{\partial T}{\partial x_i}}_{\text{Fourier flux}} + \underbrace{\rho \sum_{k=1}^{N} \left(\mathscr{D}_k \frac{W_k}{W} \frac{\partial X_k}{\partial x_i} - Y_k V_i^c \right) h_{s,k}}_{\text{Species diffusion}} + \underbrace{p \sum_{k=1}^{N} \chi_k V_{k,i}}_{\text{Dufour effect}} + \underbrace{q_i^r}_{\text{Radiation}} \tag{5.56}$$

  where λ is the thermal conductivity of the mixture and q_i^r is the radiative heat flux in the i-th coordinate. Species diffusion introduces two terms, one of which is dependent on the mass fraction gradient (causing the Dufour effect) and often neglected.

  The conductivity is calculated from the Prandtl number:

$$\lambda = \frac{\mu C_p}{Pr} \tag{5.57}$$

  where $Pr = C_p \mu / \lambda$ is the ratio between the viscous and the thermal diffusion rates, and is taken constant.

  For a given species mass and heat diffusion rates are linked through the species Lewis number:

$$Le_k = \frac{Sc_k}{Pr} = \frac{a}{\mathscr{D}_k} = \frac{\lambda}{\rho C_p \mathscr{D}_k} \tag{5.58}$$

5.2.1 Turbulent flows

In most practical systems the flow enters in a turbulent regime as the Reynolds number increase. This turbulent nature of the flow requires an improved analysis of the system and introduces important difficulties in its description and understanding [100, 149, 199, 209]. Table 5.3 shows the different combustion regimes. In the present section the most relevant aspects of turbulence and its interaction with combustion are highlighted.
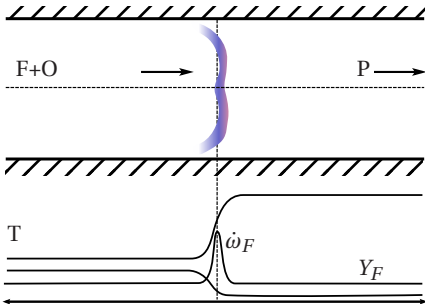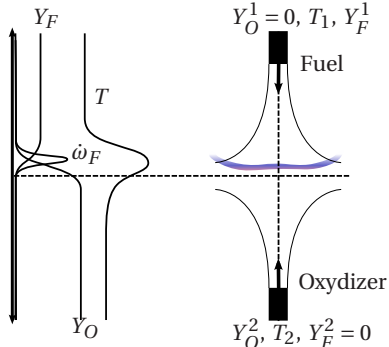
Turbulence

In a turbulent flow any quantity f is described as the composition of a mean[3] value $\overline{f}$ and a fluctuating contribution f':

$$f = \overline{f} + f' \tag{5.59}$$

---

[3]This mean represents an ensemble averaging over many realizations of the same phenomena. In an ergodic process this mean is replaced by a time average of the quantity over a long period of time.

Table 5.3: Combustion regimes

Schematic	**Low Reynolds number**	**High Reynolds number**
Premixed combustion	Laminar premixed	Turbulent premixed
Non-premixed combustion	Laminar non-premixed or diffusion	turbulent non-premixed or diffusion

$$\overline{\overline{f}} = \overline{f}$$
$$\overline{f'} = 0$$

For variable density flows, it is useful to introduce a mass-weighted average, called the Favre average to avoid the rise of additional unclosed correlations:

$$\widetilde{f} = \frac{\overline{\rho f}}{\overline{\rho}} \tag{5.60}$$

with a similar decomposition into a mean and a flutuating component:

$$f = \widetilde{f} + f'' \tag{5.61}$$

$$\widetilde{f''} = 0$$
$$\overline{f''} \neq 0$$

The turbulent intensity I of a quantity is the ratio between the root mean square (RMS[4]) and the mean value:

$$I = \frac{\sqrt{\overline{f'^2}}}{\overline{f}} \tag{5.62}$$

The turbulence intensity goes from 0 in laminar flows to a few tens of percent in highly turbulent wall-bounded flows. One important aspect of turbulence is that the flow energy is differently distributed along a wide range of length scales from the integral length scale l_t to the Kolmogorov length scale η_k. It has been shown that at the large scales, the flow is mainly controlled by inertia and is little affected by viscous dissipation.

In homogeneous isotropic turbulence the energy flows from the large scales to the small scales through the Kolmogorov energy cascade [137]. Reynolds number at the smallest scale becomes close to unity, as inertia and viscous forces balance. Such energy cascade is represented Fig. 5.1, where the turbulence energy is plotted as a function of wave numbers.

---

[4]Also known in statistics as the standard deviation, it represents the overall deviation of the quantity from the mean value.
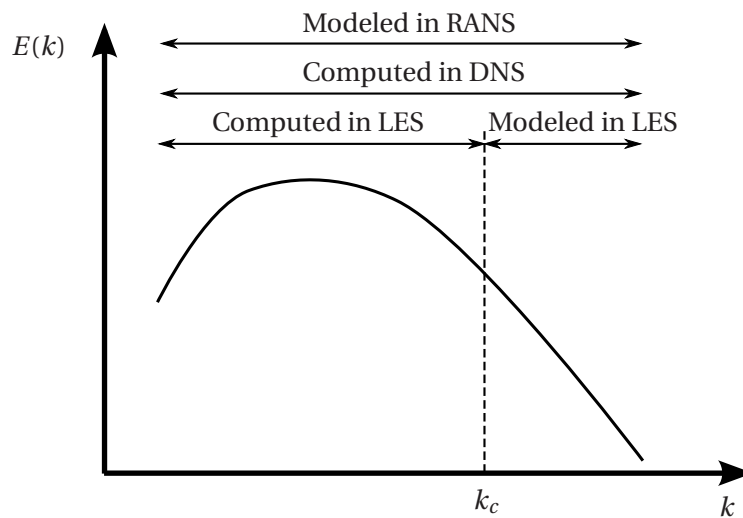
Figure 5.1: Typical energy spectrum of turbulence. RANS, LES and DNS spatial frequency ranges are plotted. k_c is the cut-off wavenumber used in LES.

Turbulence modeling approaches

A numerical description of the turbulent phenomena can be achieved using different statistical approaches:

- **RANS**

  An initial step into the modeling of turbulence was taken with the Reynolds-Averaged Navier Stokes equations (RANS), where a temporal averaging of the Navier-Stokes equation is applied. Non-linearities are modeled, so the Kolmogorov energy cascade is not explicitly resolved, and the result gives only access to the mean flow.

- **LES**

  In the Large Eddy Simulations (LES) the large scales of turbulence are explicitly resolved, while small turbulent scales are modeled using subgrid closing rules. The differentiation between the large scales and the small scales is obtained by statistical filtering of the instantaneous balance equations (see section 5.2.1).

- **DES**

  The difficulty to model all the closing terms of the LES approach and the near-wall phenomena inspired the creation of an alternative method which combines the best aspects of RANS and

LES simulations. Such approach is called Detached Eddy Simulation (DES). The principle resides in the resolution of near-wall flow using the RANS approach and the LES equations away from the walls.

- **DNS**

  In the Direct Numerical Simulations (DNS) all the scales of turbulence are resolved without using any subgrid turbulence model. All the temporal and spatial scales of the turbulence are resolved in the computational mesh. These explicit resolution of the Navier-Stokes equations gives access to the real behavior of the flow but the computational cost of such method is extremely high for industrial applications.

Filtering

In the Large Eddy Simulations (LES) approach, variables are filtered in the spectral or in the physical space. Applying a spatial filter F of size Δ to a quantity f leads to:

$$\overline{f} = \int f(y)F(x-y)dy \tag{5.63}$$

A mass-weighted Favre filter is also introduced when the flow density is not constant:

$$\overline{\rho}\widetilde{f} = \int \rho f(y)F(x-y)dy \tag{5.64}$$

The filtering operator allows to decouple the large scales from the small scales of turbulence, where the large scales are explicitly represented while the small scales must be modeled. Here $\overline{f}$ is the quantity explicitly resolved and $f' = f - \overline{f}$ corresponds to the unresolved part.

Filtered equations for reactive flows

Applying the filter operator to eq. (5.45)-(5.46) leads to equations (5.65)-(5.67):

$$\frac{\partial \overline{\rho}\widetilde{Y_k}}{\partial t} + \frac{\partial \overline{\rho}\widetilde{u_j}\widetilde{Y_k}}{\partial x_i} = \frac{\partial}{\partial x_i}\left[\overline{Y_k V_i^k} - \overline{\rho}\left(\widetilde{u_i Y_k} - \widetilde{u_i}\widetilde{Y_k}\right)\right] + \overline{\dot{\omega}_k} \tag{5.65}$$

$$\frac{\partial \overline{\rho}\widetilde{u_i}}{\partial t} + \frac{\partial \overline{\rho}\widetilde{u_i}\widetilde{u_j}}{\partial x_j} = -\frac{\partial \overline{p}\delta_{ij}}{\partial x_j} + \frac{\partial}{\partial x_j}\left[\overline{\tau_{ij}} - \overline{\rho}(\widetilde{u_i u_j} - \widetilde{u_i}\widetilde{u_j})\right] + \overline{\rho}\widetilde{f_i} \tag{5.66}$$

$$\frac{\partial \overline{\rho}\widetilde{E}}{\partial t} + \frac{\partial}{\partial x_j}\left(\overline{\rho}\widetilde{E}\widetilde{u_j}\right) = -\frac{\partial}{\partial x_j}\left(\overline{u_i p \delta_{ij}} - \overline{\tau_{ij}} + \overline{q_j} + \overline{\rho}(\widetilde{u_i E} - \widetilde{u_i}\widetilde{E})\right) + \overline{\dot{\omega}_T} + \overline{\rho}\widetilde{u_i f_i} \tag{5.67}$$

In these equations a number of simplifications were made and are presented in Table 5.4. Important non-linear terms remain unclosed and must be modeled.

Table 5.4: Simplification hypothesis for the filtered transport equations.

Quantity	Approximation
Laminar viscous stress tensor:	$\overline{\tau}_{ij} = \overline{2\mu(S_{ij} - 1/3\delta_{ij}S_{ll})} \approx 2\overline{\mu}(\widetilde{S}_{ij} - 1/3\delta_{ij}\widetilde{S}_{ll})$
Shear stress:	$\widetilde{S}_{ij} = \frac{1}{2}\left(\frac{\partial \widetilde{u}_j}{\partial x_i} + \frac{\partial \widetilde{u}_i}{\partial x_j}\right) - \frac{1}{3}\frac{\partial \widetilde{u}_k}{\partial x_k}\delta_{ij}$
Laminar species flux:	$\overline{Y_k V_i^k} \approx -\overline{\rho}\left(\overline{\mathscr{D}_k \frac{W_k}{W}\frac{\partial \widetilde{X}_k}{\partial x_i}} - \widetilde{Y}_k \widetilde{V}_i^c\right)$
Filtered heat flux:	$\overline{q_j} \approx \overline{\lambda}\frac{\partial \widetilde{T}}{\partial x_i} + \sum_{k=1}^N \overline{Y_k V_i^k}\widetilde{h}_s^k + \overline{q_j^r}$
Pressure velocity term:	$\overline{u_i p \delta_{ij}} \approx \widetilde{u_i}\overline{p}\delta_{ij}$
Filtered reaction rate:	$\overline{\dot{\omega}_k(Y_k, T)} \approx \dot{\omega}_k(\widetilde{Y}_k, \widetilde{T})$
Filtered heat release:	$\overline{\dot{\omega}_T(Y_k, T)} \approx \dot{\omega}_T(\widetilde{Y}_k, \widetilde{T})$

Sub-grid Scale (SGS) models for LES

- **The Reynolds SGS stress tensor**

  The general approach to model this term is to consider the Boussinesq approximation:

  $$-\overline{\rho}\left(\widetilde{u_i u_j} - \widetilde{u_i}\widetilde{u_j}\right) \approx 2\overline{\rho}\nu_t \widetilde{S}_{ij} - \frac{1}{3}\overline{\tau_{ll}}^t\delta_{ij} \tag{5.68}$$

  where ν_t is the so called turbulent viscosity. The turbulent viscosity can be written as the product of a velocity u^* and a lenght l^*: $\nu_t = u^* l^*$. These quantities are classicaly expressed using

three approximations: an algebraic model, a one-equation closure (most frequently using the kinetic energy, k) or a two-equation closure (including $k - \epsilon$ and the $k - \omega$ models).

For LES applications algebraic models are often used and include: the mixing length model [214], the Smagorinsky model [238], the filtered Smagorinsky model, the Wall-Adapting Local-Eddy-viscosity model [187], and Germano (dynamic Smagorinsky) model [85] [153].

- **The turbulent SGS species flux**

Accounts for the transport of species by the fluctuating velocity. It is modeled thorough a classical gradient approximation, where the turbulent Schmidt number is introduced:

$$\overline{\rho}\left(\widetilde{u_i Y_k} - \widetilde{u_i}\widetilde{Y_k}\right) \approx -\rho\left(\mathscr{D}_k^t \frac{W_k}{W}\frac{\partial \widetilde{X_k}}{\partial x_i} - \widetilde{Y_k}\widetilde{V_i}^{c,t}\right) \tag{5.69}$$

$$\mathscr{D}_k^t = \frac{\nu_t}{Sc_k^t} \tag{5.70}$$

Diffusion correction velocities are again obtained from mass conservation:

$$\widetilde{V_i}^c + \widetilde{V_i}^{c,t} = \sum_{k=1}^N \left(\frac{\overline{\mu}}{\overline{\rho}Sc_k} + \frac{\mu_t}{\overline{\rho}Sc_k^t}\right)\frac{W_k}{W}\frac{\partial \widetilde{X_k}}{\partial x_i} \tag{5.71}$$

- **The turbulent SGS heat flux**

This term is similarly modeled with a turbulent Prandtl number, Pr_t:

$$\overline{\rho}(\widetilde{u_i E} - \widetilde{u_i}\widetilde{E}) \approx -\lambda_t \frac{\partial \widetilde{T}}{\partial x_i} + \sum_{k=1}^N \overline{\rho}\left(\widetilde{u_i Y_k} - \widetilde{u_i}\widetilde{Y_k}\right)\widetilde{h_s^k} \tag{5.72}$$

with:

$$\lambda_t = \frac{\mu_t \overline{Cp}}{Pr_t} \tag{5.73}$$

The choice of the turbulent Prandtl number depends on the type of flow. Typical values vary from 0.5 [181] for HIT to 0.9 in some industrial applications [131].

5.2.2 Combustion models

The thickness of a flame δ_L^0 is usually smaller than the filter size and therefore can not be explicitly resolved. The sub-grid scale interaction between the chemical source term and turbulence can not be neglected. Turbulent combustion models are designed to close the filtered heat release term $\overline{\dot{\omega}_T}$ that represents this interaction. These models are commonly classified in three groups [261]: geometrical models, turbulent mixing models and one-point statistical models.

Geometrical models

The flame is considered as a geometrical surface evolving in the turbulent flow. The geometrical flame is related to an iso-surface of mixture fraction, and the mean reaction rate is estimated from the available flame surface area per unit volume multiplied by the theoretical mean reaction rate per unit of flame area [262]. The flame front propagation can be described by a "G-equation" [133, 127]:

$$\overline{\rho}\frac{\partial G}{\partial t} + \overline{\rho \widetilde{u_i}}\frac{\partial G}{\partial x_i} = \rho_0 s_T |\nabla G| \qquad (5.74)$$

where ρ_0 is the density in the fresh gases and the flame front is associated with a iso-surface level G^*. Although it is a good method to avoid resolving the subgrid scale resolution of the flame front, it requires the knowledge of the turbulent flame displacement speed s_T, a quantity depending on turbulent, chemical and thermal properties that can not be well defined [93]. The classical model of the turbulent flame speed relies on experimental [98, 1, 2] and analytical [274] data and writes:

$$\frac{s_T}{s_L} = \alpha + \left(\frac{u'}{s_L}\right)^n \qquad (5.75)$$

where α and n are model constants, s_L is the laminar flame speed and u' is the turbulent velocity.

The flame surface density model [163, 53, 207, 33, 257, 259] can also be considered part of the available geometrical models.

Turbulent mixing models

When the characteristic chemical time scales of the combustion process is shorter than the turbulent time scales the reaction rates are considered dependent on the turbulent mixing rates. The objective of the turbulent combustion model is then to express the mixing rates, expressed in general using a scalar dissipation rate. Two common implementations of this approach are the Eddy Break-Up [244, 245, 142]and the Eddy-Disipation Concept (EDC) models [160].

Statistical models

In this approach the objectif is to describe the flame properties by using a local statistical description of the combustion phenomena. The probability density function (pdf) $\overline{P}(Y^*; \mathbf{x}, t) dY$ describes the mass fraction Y at the possition $\mathbf{x}$ the time t in the interval dY around the random variable Y^*. The pdf must verify:

$$\int_Y \overline{P}(Y^*; \mathbf{x}, t) dY = 1 \tag{5.76}$$

$$\int_Y Y^* \overline{P}(Y^*; \mathbf{x}, t) dY = Y(\mathbf{x}, t) \tag{5.77}$$

$$\int_Y (Y^* - \overline{Y})^2 \overline{P}(Y^*; \mathbf{x}, t) dY = Y^2(\mathbf{x}, t) \tag{5.78}$$

In a multi-component anisothermal mixture, the statistical description of the combustion process must include an expression of the different species and the temperature. This is acheived using a "joint pdf" $\overline{P}(Y_1^*, Y_2^*, .., Y_N^*, T; \mathbf{x}, t)$. The mean value of any given function is obtained using:

$$\overline{f(\mathbf{x}, t)} = \int_{Y_1} ... \int_{Y_N} \int_T f(\mathbf{x}, t) \overline{P}(Y_1^*, Y_2^*, .., Y_N^*, T; \mathbf{x}, t) dY_1 ... dY_N dT \tag{5.79}$$

Two classes of statistical models are generally used:

- **Presumed pdf:** in this models the shape of the pdf of the mixture fraction is supposed known [270, 18, 25]. The most used shape is constructed using a β-function.

- **Transported pdf:** using a progress variable a transport equation for the joint pdf is constructed [208, 63]. The advantage of this model is that in the pdf balance equation the chemical reaction only depends on the chemical variables and do not require modeling. However a molecular diffusion term arises which is difficult to model [203].

Thickened flame model

The Thickened Flame model (TF model) initially developed by Butler and O'Rourke [31], is based on the flame speed s_L, flame thickness δ_L^0 their dependence on the thermal diffusivity D_{th} and the preexponential constant A as shown below:

$$s_L^0 \propto \sqrt{D_{th} A} \quad ; \quad \delta_L^0 \propto \frac{D_{th}}{s_L^0} = \sqrt{\frac{D_{th}}{A}} \tag{5.80}$$

Increasing the thermal diffusivity by a factor $\mathscr{F}$ while decreasing the preexponential constant by the same factor $\mathscr{F}$ leads to a flame thickness multiplied by $\mathscr{F}$ while the flame speed is unchanged. The flame structure can then be resolved on the LES mesh, with the correct propagation velocity. In practice the molecular and thermal diffusivities are replaced by $\mathscr{F} D_{th}$ and $\mathscr{F} \mathscr{D}_k$ respectively, and the reaction rates for each species are divided by $\mathscr{F}$.

The process of flow thickening alters the interaction between chemistry and the flow: motion scales below $\mathscr{F}\delta_L^0$ do not interact anymore with the flame, so that the flame wrinkling is reduced, leading to an underestimation of the total reaction rate.

The SGS wrinkling is modeled with the efficiency function $\mathscr{E}$ developed and studied by Angelberger et al. [9] and Colin et al. [49]. This function varies between $\mathscr{E} = 1$ (weak turbulence) and $\mathscr{E}_{\max} = \mathscr{F}^{2/3}$ (highly turbulent flow with strong sub-grid flame wrinkling), and is applied to the diffusion coefficient and the source terms.

To avoid the modification of the flow properties outside the flame front, the Dynamic Thickened flame model (DTF) has been developed: it applies the thickening factor only in the flame zone. The flame front is detected with a sensor. The thickening factor $\mathscr{F}$ varies from 1 outside the flame to $\mathscr{F}_{\max}$ in the reactive zones:

$$\mathscr{F} = 1 + (\mathscr{F}_{\max} - 1)\mathscr{S} \tag{5.81}$$

where:

$$\mathscr{S} = \tanh\left(\beta'\frac{\Omega}{\Omega_0}\right) \tag{5.82}$$

In this expression Ω is a function indicating the presence of the flame. It is constructed by using some parameters of the chemical kinetic scheme:

$$\Omega = Y_F^{n'_F} Y_O^{n'_O} \exp\left(-\Gamma_T\frac{E_a}{RT}\right) \tag{5.83}$$

The constants Γ_T and β' take the values of 0.5 and 50 respectively, and control the thickness of the detected zone.

5.2.3   Near-wall flow modeling

A critical aspect of LES simulations is the description of the turbulent boundary layer that build on solid walls. The level of mesh refinement required to explicitly resolve the near-wall flow is too high. Moreover, heat exchange problems require a correct prediction of the thermal and dynamic boundary layers, in order to capture the heat fluxes entering the solid walls q_w^s. The chosen approach is to model the turbulent boundary layers through the so-called law of the wall models, based on boundary layer theory.

In these models, quantities are generally expressed in wall units, using a scaling based on the friction properties at the wall. The friction velocity is:

$$u_\tau = \sqrt{\frac{\tau_w}{\rho_w}} \tag{5.84}$$

where τ_w is the wall shear stress and ρ_w is the density of the flow at the wall. A characteristic length scale y_τ can be defined using the kinematic viscosity at the wall $\nu_w = \mu_w / \rho_w$ and the friction velocity:

$$y_\tau = \frac{\nu_w}{u_\tau} \tag{5.85}$$

In a similar way, the friction temperature T_τ is defined using the heat capacity near the wall $C_{p,w}$ and the fluid heat flux near the wall q_w^f:

$$T_\tau = \frac{q_w^f}{\rho_w C_{p,w} u_\tau} \tag{5.86}$$

Another useful quantity, called the friction Reynolds number, is defined from h a characteristic length of the problem, u_τ and ν_w:

$$Re_\tau = \frac{h u_\tau}{\nu_w} \tag{5.87}$$

Non-dimensional variables (Table 5.5) are constructed from these characteristic quantities and commonly used in the study of turbulent boundary layers.

Table 5.5: Wall unit scaled variables

y^+	$=$	$\frac{y}{y_\tau}$	dimensionless wall distance
u^+	$=$	$\frac{u}{u_\tau}$	dimensionless velocity
T^+	$=$	$\frac{T_w - T}{T_\tau}$	dimensionless temperature

Simulations and experiments have shown that the dynamic turbulent boundary layer can be divided in three zones: a viscous sub-layer, a buffer layer and an inertial logarithmic layer. Figure 5.2 shows in dimensionless units the typical profiles of velocity and temperature across the boundary layer.

The viscous sub-layer

It has been shown by different authors [119, 36, 38] that the viscous sub-layer has a linear behavior:
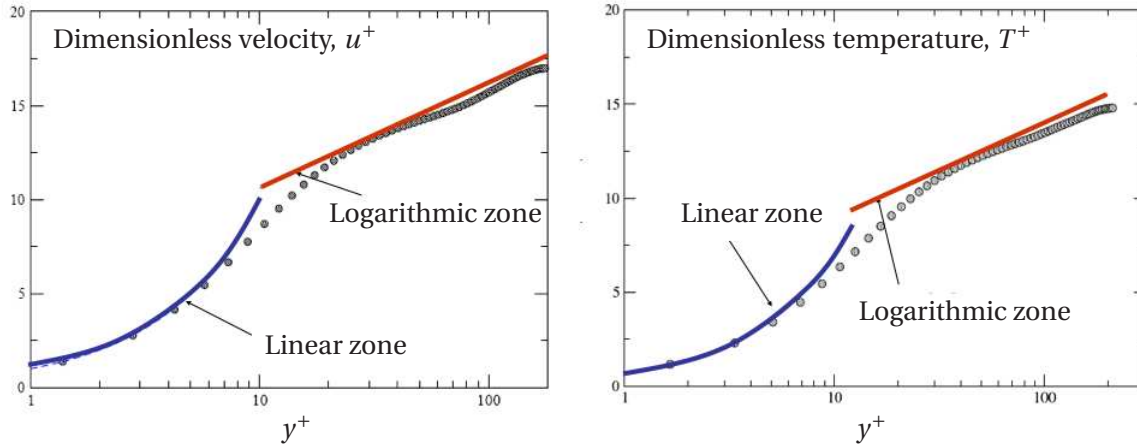
Figure 5.2: Velocity and temperature in wall units. Data obtained by Direct Numerical Simulation (DNS)

$$u^+ = y^+ \tag{5.88}$$
$$T^+ = Pr\, y^+ \tag{5.89}$$

where Pr represents the Prandtl number. Such behavior is normally detected at wall distances inferior to $y^+ = 5$.

The inertial sub-layer

In the inertial sub-layer, for values of y^+ typically larger than 10, the velocity and temperature evolve proportionally to the logarithm of the distance [227]:

$$u^+ = \kappa^{-1} \ln y^+ + C_u \tag{5.90}$$
$$T^+ = Pr_t \kappa^{-1} \ln y^+ + C_T \tag{5.91}$$

where κ is the Von-Kàrmàn constant and C_u and C_T are integration constants. Classical values for these three constants on wall-bounded flows are: $\kappa = 0.41$, $C_u = 5.5$ and $C_T = 3.9$ [125].

Coupled wall model

Recently Cabrit and Nicoud [32], have developed a law of the wall model for anisothermal reactive low-Mach turbulent boundary layers, where the computation of the shear stress and the heat fluxes

leads to a coupled expression for the dynamic (5.92) and the thermal (5.93) boundary models, that also takes into account the multicomponent nature of combustion gases. This model writes:

$$\frac{2}{\alpha}\left(\sqrt{D} - \sqrt{D - \alpha u^+}\right) \quad = \quad \frac{1}{\kappa}\ln y^+ + C \tag{5.92}$$

$$T^+ \quad = \quad \frac{1-D}{B_q} + \frac{\alpha}{B_q}u^+ \tag{5.93}$$

where

$$\alpha \quad = \quad \frac{C_p B_q}{\frac{C_p}{Pr_t} + \frac{1}{Sc_{t,k}}\sum_{k=1}^{N}\frac{d\overline{X_k}}{d\overline{T}}\Big|_{\mathrm{eq}}\Delta h_{f,k}^0}$$

$$B_q \quad = \quad \frac{T_\tau}{T_w} = \frac{\overline{q_w}}{\overline{\rho_w}C_p u_\tau T_w}$$

with integration constants taking the values:

$$C \quad = \quad 5.5 \tag{5.94}$$

$$\frac{1-D}{B_q} = K(Pr) \quad = \quad \beta(Pr) - Pr_t C + \left(\frac{Pr_t}{\kappa} + 2.12(1 - 2\ln(20))\right) \tag{5.95}$$

$$\beta(Pr) \quad = \quad (3.85 Pr^{1/3} - 1.3)^2 + 2.12\ln Pr \tag{5.96}$$

5.3 The code AVBP

5.3.1 Introduction

AVBP has originally been developed by the Oxford University Computing Laboratory (OUCL) and the CERFACS in 1993. Currently the code is property of the CERFACS and the Institut Français du Petrole (IFP). The most basic principle behind the code was to use arbitrary hybrid meshes for the resolution of the Navier-Stokes equations. From the beginning of the designing phase, the code was conceived in order to work on parallel architectures.

The original numerical methods where implemented by M. Rudgyard and T. Schönfeld following the cell-vertex methods developed at Oxford [222, 159, 52, 51]. A detailed presentation of the numerical methods currently implemented in the code is given by N. Lamarque [143]. In this section a short introduction of the numerical methods employed in AVBP are presented.

5.3.2   Overview of the numerical methods in AVBP

The precision of the simulations performed using a the LES solver depend on the numerical scheme employed. The resolved turbulent structures must not be dissipated of deformed by the spatial or temporal resolution of the problem. In a LES, turbulent structures of different characteristic times and lengths are resolved, this makes of the LES a computationally expensive resolution method. Thus the software data structure of AVBP has been designed in order to be ported on massively parallel architectures.

The algorithm uses a master-slave parallel architecture based on the MPI communications library. Parallelism is achieved by sub-domain decomposition of the problem using different partitioning algorithms [83]. The mesh employed for the simulations is unstructured and can be composed of hybrid elements (tetrahedral, hexahedral, pyramid, prism, etc.).

The numerical solver uses a cell-vertex technique, where the unknown variables are stocked at the nodes of the mesh [101], and the conservation budget is established at the faces of the associated primary cells. LES spatial filtering is implicitly assumed by the resolution of the Navier-Stokes equation on these cells. Different convection schemes have been implemented in AVBP. In the present work the Lax-Wendroff (LW) scheme has been primarily used. It is a one-step, centered, second order in space and time scheme with an explicit time advancement, however higher order schemes are available, like the two-step Taylor-Galerkin schemes.

The diffusion terms of the Navier-Stokes equations can be solved using two methods. The first is derived from the cell-vertex discretization where a stencil of size 4Δ is used: the construction of the diffusion operator at one node requires the knowledge of the information of the two neighboring layers of cells (and nodes) as shown in the left image of Fig. 5.3. The second formulation is derived from a finite-element method with a vertex-centered discretization [101] that uses a smaller stencil of size 2Δ: to construct the diffusion operator this method only needs the information of the closest layer of cells and nodes.

The different source terms of the transport equations can be directly calculated at the nodes of the mesh. However Lamarque shows [143] that in a cell-vertex formulation the source terms must be calculated at the center of the primary cell and then distributed to the nodes. In the present work this approach has been employed, in particular for the inclusion of the radiative power source term into the energy equation.

The code AVBP presents an excellent scalability as shown by Staffelbach et al. [246] who has ported the code to massively parallel computers with several thousand processors.

(a) *Cell-vertex* discretization

(b) *Vertex-centered* discretization
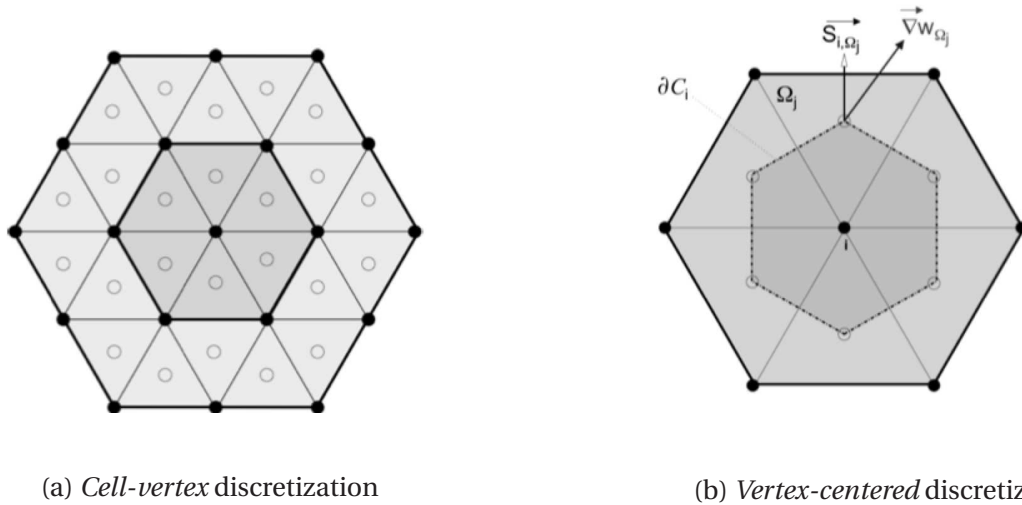
Figure 5.3: Nodes and cells used in the computation of the diffusion operator on the central node.

5.3.3 Boundary conditions

In LES of compressible flows, where acoustics play a major role, boundary conditions constitute a critical element of the code [252, 201, 231]. At each step of the numerical integration a correction of the boundary nodes is applied in order to impose the boundary conditions at the inlet, outlet and walls of the domain. Acoustic energy is not properly evacuated from the computational domain using a classical Dirichlet boundary condition. In AVBP the NSCBC characteristic treatment developed by Poinsot and Lele [202] was implemented to overcome this problem.

Solid walls are managed using different approaches depending on the boundary treatment required: isothermal, adiabatic, multiperforated, heat loss, slip and non-slip walls are a small list of the available wall treatments. A detailed study of the boundary conditions in AVBP can be found in [211].

6

Radiative heat transfer

Contents

6.1 Introduction

Radiation is defined as the transport of energy by means of electromagnetic waves. Radiation is present everywhere: the light illuminating the room, the radio and television waves transporting images and sounds, the microwaves transmitting information to sattelites in orbit around the planet and the gamma ray burst of distant galaxies are all crossing by millions per second through the space between your eyes and this sheet.

The omnipresence of radiation is due to its origins. In nature only four forces exist: the weak force, the strong force, gravity and the electromagnetic force. Outside the nuclear scales every object is only subject to gravity and the electromagnetic force. The chemical interactions between atoms and molecules have an electromagnetic origin. In a strict sense combustion is one of the macroscopic manifestations of the electromagnetic force acting on chemical molecules, and radiation is the interaction between those molecules and the electromagnetic field.

Radiation can be conceptualized as a stream of photons which carry energy. Photons are massless particles that travel in the vacuum at the constant speed of $c_0 = 299\,792\,458$ m/s. If not disturbed by external forces, photons travel in a linear path through space. The optical properties of light are obtained by studying this linear propagation. This *corpuscular* nature of light was extensibly studied by Newton [186].

However, Robert Hooke, Christian Huygens and Augustin-Jean Fresnel (contemporaries with Newton) developed a mathematical model showing that light propagation can be explained using a wave theory [109]. Such approximation explains the refraction of light and was used in the development of the Huygens-Fresnel principle of light propagation [158]. It also explained the odd results obtained by the double-stilt experiment carried by Thomas Young [277], where light photons crossing two stilts showed a wave interference pattern behind the obstacle.

While the relationship between electricity and magnetism was experimentally demonstrated by Faraday [76], it was the theoretical analysis of Maxwell that pointed out to the electromagnetic nature of light [166]. With the advent of quantum mechanics it was shown that the corpuscular and the wave nature of light are two separate expressions of the same phenomena. This is known as the wave-particle duality of light.

From our dilly experience we can observe that a correlation exists between heat and light: the red color produced by an oven, the heat from the Sun and the the yellow light of a candle are three examples where heat and radiation are associated. It will be shown in the present chapter that energy transfer by radiation is proportional to the fourth power of the temperature: $q_r \propto T^4 - T_{ref}^4$. In a system where the temperature rises to high levels, radiation can become dominant over other heat transfer modes. As a consequence, radiation becomes important in combustion, astrophysics, meteorology and nuclear physics. For applications such as combustion chambers, fusion reactors, space reentry vehicles, solar energy panels, radiation effects must take into account.

The length scales involved in radiation can be very wide, evolving from millimetric-sized exchangers to astronomical scale systems. Energy exchanges can occur between points in space separated by very long distances, and the energy variation of an object depend on the interactions with all the other elements in the system.

For non astronomical applications, heat transfer by radiation is almost an instantaneous phenomenon. The time that takes for light to reach from this paper sheet to your eyes is around 2 [ns]. In the same way in a combustion chamber every element exchanges heat by radiation almost instantaneously.

Radiation is a process that depends also on the direction of propagation of photons and their wavelength. In the same way that the human eye can discern the angular location and the color of a luminous source, interaction by radiation between two objects depend on their relative positions and on the wavelengths at which energy is emitted and absorbed.

Radiation requires a different set of tools and methods to the ones used in combustion. The non-local, instantaneous, directional and spectral aspects of radiation makes of this heat transfer mode a complex phenomenon to be modeled.

In section 6.2 the basic concepts of radiant energy are presented. It will be shown that in combustion applications, where temperatures range from 300K to 3000K, only the near infra-red zone of the electromagnetic spectrum needs to be considered. Transfer of energy between two zones is described by the Radiative Transfer Equation presented in section 6.3. In section 6.4 the absorpsion/emission properties of gases are introduced and sections 6.5 and 6.6 show how to solve the radiative problem using a numerical algorithm.

6.2   Basic concepts

The energy carried by electromagnetic waves is equal to $e = h\nu$, were $h = 6,626 10^{-34}$ [J.s] is the Planck constant, and ν [cycles/sec = s^{-1} = Hz] is the frequency of the wave. As any ossilatory phenomena frequency, wavelength, wavenumber or angular frequency of radiation can be described with any of the quantities presented on Table 6.1.

From the expression of electromagnetic energy, it is clear that high frequency (low wavelength) waves,

Table 6.1: Spectral variables used in radiation

Name	Symbol	Unit	I.S. unit
frequency	ν	Hz	Hz
wavelength	$\lambda = c/\nu$	$\mu\,\mathrm{m} = 10^{-6}\mathrm{m}$	m
wavenumber	$\tilde{\nu} = \nu/c$	cm^{-1}	m^{-1}
angular frequency	$\omega = 2\pi\nu$	$radians/s = s^{-1}$	s^{-1}

like gamma and X-rays, carry much more energy than low frequency (high wavelength) waves, like microwaves and radio waves. Visible light represents only a small part of the electromagnetic spectrum, as shown on Fig. 6.1 where the common classification of the different kinds of radiation is reproduced. Heat transfer by thermal radiation takes place between $\lambda \approx 0,1\mu m$ (ultraviolet) and $\lambda = 100 \approx m$ (mid-infrared).

6.2.1 Principles and definitions

Definitions

- **Transparent media**

  Refers to media where no attenuation of energy is measured on the transported photon. The media is also said to be non participative. The best example of such media is vacuum.

- **Participative media**

  In some cases there is an interaction between the photons and the molecules of the media, provoking a deflection of the beams, an absorption of the energy or an emission of new photons from the molecules, in this case the media is called participative, as it participates in the propagation of energy by radiative transfer.

- **Total quantities**

  Are quantities associated with the full electromagnetic spectrum. In general they are obtained by integration of the correspondent spectral quantity over the whole spectrum.

- **Spectral quantities**
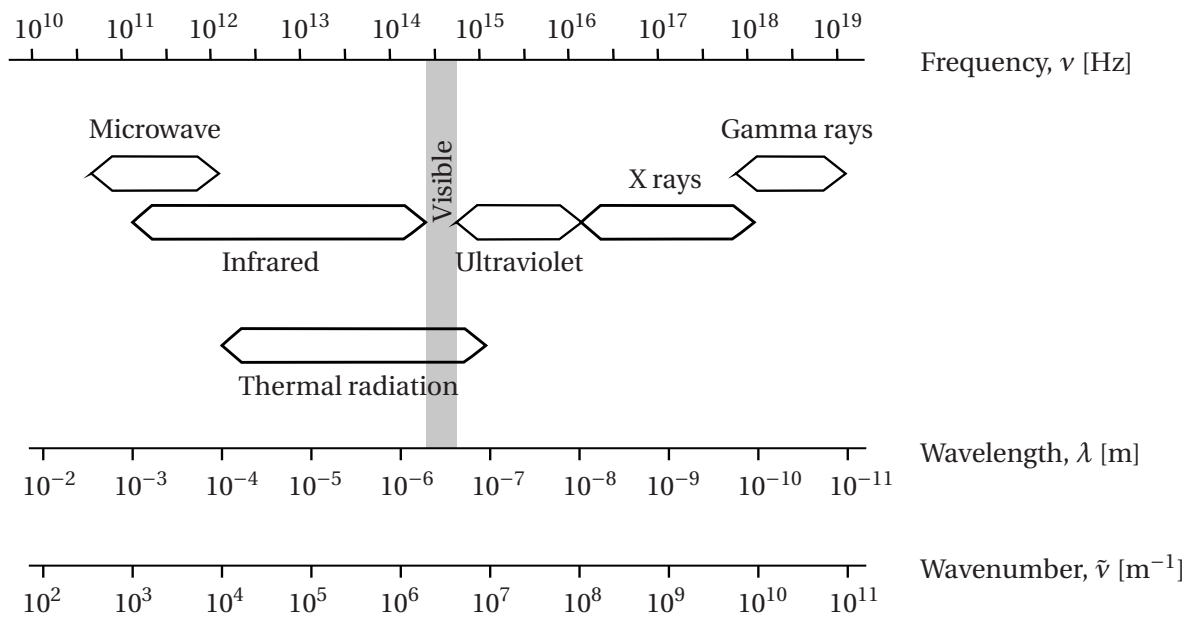
Figure 6.1: Electromagnetic wave spectrum

Are quantities relative to a narrow spectral zone around a given frequency. They are also called monochromatic quantities.

- **Solid angles**

At any point in space, at the position **r**, where a surface dA (with normal **n**) is located, looking in the direction **s** the apparent size of the surface dA_j, situated at a distance R, occupies a two-dimensional angle of the observable hemisphere called solid angle (Fig. 6.2). Such angle can be defined as the projection of the surface dA_j over the unity sphere around **r**. It can be obtained by projection of dA_j perpendicular to **s**, creating the surface $dA_j^p = \cos\theta_j dA_j$, where θ_j is the angle between the normal $\mathbf{n}_j$ of the surface dA_j and the direction vector **s**. Then projecting on the unity sphere gives:

$$d\Omega = \frac{dA_j^p}{R^2} = \frac{\cos\theta_j dA_j}{R^2} \tag{6.1}$$
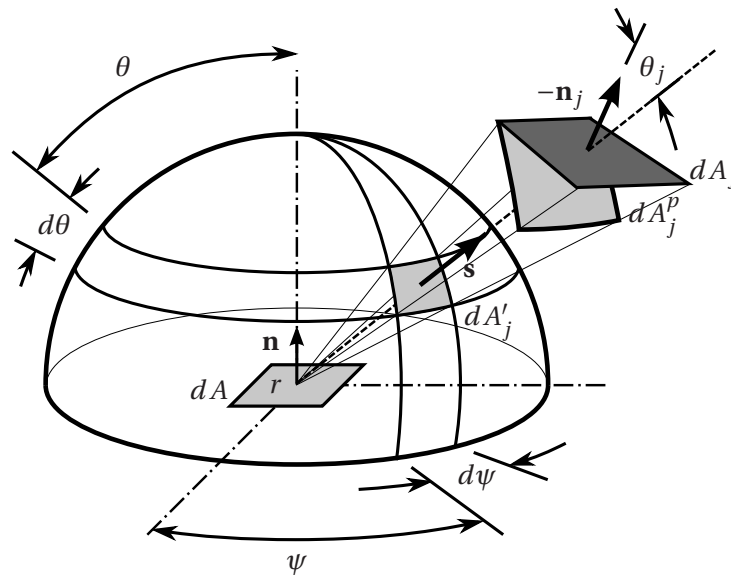
Figure 6.2: Solid angle

The total surface of the hemisphere is called the total solid angle, and covers an area equal to 2π. The infinitesimal solid angle $d\Omega$ is no more than an infinitesimal area on the unit sphere, which can be expressed:

$$d\Omega = dA'_j = \sin\theta\, d\theta\, d\psi \qquad (6.2)$$

where ψ and θ are the angular components of the direction vector, the first measured from the normal to dA and the second usually measured from the x-axis.

Solid angles can be considered as a two-dimensional equivalent of one-dimensional angles. Where the latter can vary between 0 and π for a semicircle (measured in dimensionless radians) the former can vary between 0 and 2π for a hemisphere (measured in dimensionless steradians).

- **Closed isothermal cavity**

Inside a closed isolated isothermal cavity radiation intensity in every point is homogeneous and isothrope. The analysis of the energy content of the cavity is similar to the analysis of the acoustic modes of an enclosure: from the electromagnetic theory radiation is the self-propagating wave of two orthogonal oscillating electric and magnetic fields. At the walls the parallel component of the electric field and the orthogonal component of the magnetic field vanish, and the fields inside the enclosure are the superposition of periodic functions [27]. The wavelengths

that can exist in the cavity and their energy content can be derived from the quantum mechanic theory [200].

- **Local thermodynamic equilibrium**

  It is considered that the local radiative properties of the media are independent from the environment, i.e. for any element of the media at temperature T its radiation properties are the same as if it was plunged inside a closed isolated isothermal cavity at the same temperature T.

- **Blackbody**

  Any media (in particular solids) that do not reflect radiation is known as a perfect absorber (as it absorbs all incident radiation) but is most commonly called a blackbody. More specifically a blackbody is a system Ω delimited by a surface $\partial\Omega$ on which any crossing photon can not cross back and suffers a complete absorption by Ω. The reflection of the photon on the internal walls of Ω, the absorption and remission of electromagnetic energy modifies the system until thermal equilibrium is achieved.

- **Emissive power**

  The energy emitted from a surface by radiation is called the emissive power E. A distinction is made between spectral (E_ν) and total emissive power (E). The latter is associated with the total energy emitted during a given time by a given surface (eq. 6.4). The former is the fraction of that energy emitted only at a given frequency (eq. 6.3). The integration of the spectral emissive power over the whole spectrum is equal to the total emissive power eq. (6.5):

$$E_\nu = \frac{\text{emitted energy}}{\text{time} \cdot \text{surface area} \cdot \text{frequency}} \tag{6.3}$$

$$E = \frac{\text{emitted energy}}{\text{time} \cdot \text{surface area}} \tag{6.4}$$

$$E = \int_0^\infty E_\nu(T,\nu)\,d\nu \tag{6.5}$$

The laws of radiation

- **Planck's law**

  In 1901 Max Planck published the results of his research on quantum statistics, in which he explained that a molecule can only emit energy at distinct levels [200]. He obtained a distribution of the spectral emissive power of a blackbody, known as Planck's law: any black surface bounded by a transparent medium with refractive index n has an emissive power described by:

$$E_{b\nu}(T,\nu) = \frac{2\pi h \nu^3 n^2}{c_0^2 [e^{h\nu/kT} - 1]} \tag{6.6}$$

where $k = 1.3807\,10^{-23}$ [J/K] is known as the Boltzmann's constant.

Eq. (6.6) can be also expressed in terms of the different variables of Table 6.1. Considering a constant refraction index n, eqs. (6.7) and (6.8) are obtained:

$$E_{b\lambda}(T,\lambda) \quad = \quad \frac{2\pi h c_0^2}{n^2 \lambda^5 [e^{hc_0/n\lambda kT} - 1]} \tag{6.7}$$

$$E_{b\tilde{\nu}}(T,\eta) \quad = \quad \frac{2\pi h c_0^2 \tilde{\nu}^3}{n^2 [e^{hc_0 \tilde{\nu}/nkT} - 1]} \tag{6.8}$$

To simplify the visibility of formulas, the following abbreviations are introduced:

$$C_1 = 2\pi h c_0^2 = 3.7418\,10^{-16}\ [W\,m^2] \tag{6.9}$$

$$C_2 = hc_0/k = 0.014388\ [m\,K] \tag{6.10}$$

which permits to rewrite expression (6.7) as:

$$\frac{E_{b\lambda}}{n^3 T^5} = \frac{C_1}{(n\lambda T)^5 [e^{C_2/(n\lambda T)} - 1]} \tag{6.11}$$

- **Wien's law**

Expression (6.11) depends on the variable $(n\lambda T)$ and presents a maximum value, determined by derivation of the function:

$$\frac{d}{d(n\lambda T)}\left(\frac{E_{b\lambda}}{n^3 T^5}\right) = 0 \tag{6.12}$$

which leads to Wien's displacement law:

$$(n\lambda T)_{\max} = C_3 = 2898\ [\mu m\,K] \tag{6.13}$$

In the case of a combustion application, temperatures range from $T = 300$K to $T = 3000$K. The wavelength at which the maximum energy is observed for each one of these values are: $\lambda_{\max}(T = 300) \approx 1\,10^{-5}$ [m] and $\lambda_{\max}(T = 3000) \approx 1\,10^{-6}$ [m]. In another example of the application of Wien's law, the temperature of the surface of the sun is $T = 5778$K, and the associated maximum energy can be found at a wavelength $\lambda_{\max}(T_{\text{sun}}) \approx 5\,10^{-7}$ [m], which is located right in the middle of the visible range of the spectrum. Humans have evolved a sensor system that detects the more energetic frequencies of the Sun.

- **Stefan-Boltzmann's law**

    The total emissive power of a blackbody can be determined by integration of eq. (6.7) over the whole spectrum:

    $$E_b(T) = \int_0^\infty E_{b\lambda}(T,\lambda)d\lambda = C_1 n^2 T^4 \int_0^\infty \frac{d(n\lambda T)}{(n\lambda T)^5[e^{C_2/(n\lambda T)} - 1]} = \left[\frac{C_1}{C_2^4}\int_0^\infty \frac{\xi^3 d\xi}{e^\xi - 1}\right] n^2 T^4 \quad (6.14)$$

    where n is considered constant. The result is known as the Stefan-Boltzmann law:

    $$E_b(T) = n^2 \sigma T^4 \tag{6.15}$$

    where σ is the Stefan-Boltzmann constant and is equal to:

    $$\sigma = \frac{\pi^4 C_1}{15 C_2^4} = 5.670\,10^{-8}\,[W/(m^2\,K^4)] \tag{6.16}$$

Derived quantities

- **Radiative Intensity**

    The emissive power seems to be a first choice for the description of the radiative phenomena. However this quantity is not enough to describe the directional dependence of radiation. Another quantity is thus defined: the radiative intensity I is the energy flow per unit solid angle and unit area normal to the rays, either at a given frequency (I_ν) or for the whole spectrum (I):

    $$I_\nu = \frac{\text{emitted energy}}{\text{time} \cdot \text{surface area normal to rays} \cdot \text{frequency} \cdot \text{solid angle}} \tag{6.17}$$

    $$I = \frac{\text{emitted energy}}{\text{time} \cdot \text{surface area normal to rays} \cdot \text{solid angle}} \tag{6.18}$$

    $$I(\mathbf{r},\mathbf{s}) = \int_0^\infty I_\nu(\mathbf{r},\mathbf{s},\nu)d\nu \tag{6.19}$$

    where $\mathbf{r}$ is a position vector and $\mathbf{s}$ is the vector of the propagation direction of the photons.

    Integration of the radiative intensity over the hemisphere gives the emissive power of a surface placed at $\mathbf{r}$ with normal $\mathbf{n}$, :

    $$E_\nu(\mathbf{r}) = \int_0^{2\pi}\int_0^{\pi/2} I_\nu(\mathbf{r},\theta,\psi)\cos\theta\sin\theta\,d\theta\,d\psi = \int_{2\pi} I_\nu(\mathbf{r},\mathbf{s})\mathbf{n}\cdot\mathbf{s}\,d\Omega \tag{6.20}$$

    If the intensity is considered independent of the directions, a simple relation between the spectral emissive power and the spectral intensity is found:

$$I_v(r, v) = \frac{E_v(r, v)}{\pi} \tag{6.21}$$

- **Luminance**

  Is the portion of the electromagnetic wave of spectral intensity I_v that falls into the human eye. It can be calculated as:

  $$L_v = K_v I_v \tag{6.22}$$

  where K_v is a function called luminous efficacy, generally described by a Gaussian distribution, and takes non-zero values for wavelengths from $0.4\,\mu m$ to $0.7\,\mu m$ (visible part of the spectrum). The unit of the luminance is the candela (cd), the lux (lx) or the lambert (L). It is a quantity mostly used in illuminating engineering [182] and computer animation. Note that in many textbooks (mainly in french speaking countries) the term *luminance* also used to designate the radiative intensity.

- **Radiative energy flux**

  The total energy crossing a small area is equal to the projection on the normal to the surface of the radiative intensities impinging the surface and coming from all the directions of space. The mathematical formulation of the spectral radiative energy flux is:

  $$q_v^r = \mathbf{q_v^r} \cdot \mathbf{n} = \int_{4\pi} I_v(\mathbf{s}) \mathbf{n} \cdot \mathbf{s} \, d\Omega \tag{6.23}$$

  and the total radiative energy flux at the surface is:

  $$q^r = \mathbf{q^r} \cdot \mathbf{n} = \int_0^\infty \mathbf{q_v^r} \cdot \mathbf{n} dv = \int_0^\infty \int_{4\pi} I_v(\mathbf{s}) \mathbf{n} \cdot \mathbf{s} \, d\Omega dv \tag{6.24}$$

6.2.2 Radiative properties of surfaces

In general, real surfaces do not behave like blackbodies, i.e. perfectly absorbing all incident radiation. On solid materials the total irradiation (radiation impinging on the surface) can be divided into three different parts (Fig. 6.3): one part of the radiation is reflected back into the medium, another is absorbed by the solid, and the remaining part is transmitted through the slab. Three quantities are associated to these three parts, as defined in Table 6.2.

Conservation of energy leads to:

$$\rho + \alpha + \tau = 1 \tag{6.25}$$

If the solid is thick enough to fully absorb the incoming radiation, there is no transmittion of radiation and eq. (6.25) reduces to:

$$\rho + \alpha = 1 \tag{6.26}$$
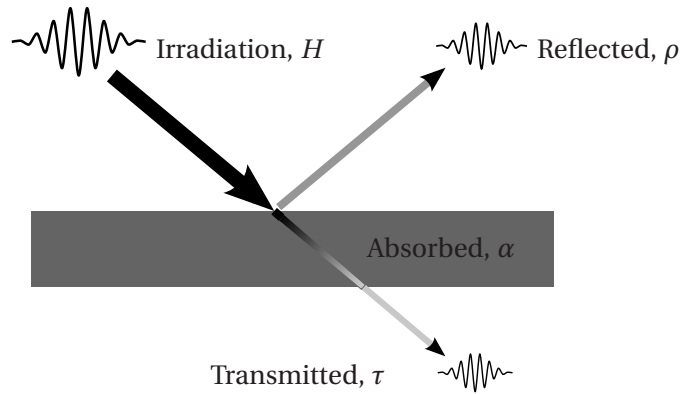
Figure 6.3: Radiation on a solid surface.

The solid surface is not cold (0 Kelvin), as a consequence a thermal radiation is associated to its temperature. As shown before, the energy produced by any surface is described by the Planck function (eq. 6.21). The quantity relating the emission of a real surface to the blackbody emission is emittance ϵ and is defined in in Table 6.2.

All these four properties are nondimensional and vary between 0 and 1. For example, the radiative properties of a black surface are simply: $\alpha = 1$, $\rho = 0$, $\tau = 0$, $\epsilon = 1$. In real configurations the properties depend on the direction, the spectral frequency considered and the temperature of the solid. However, such dependency is often neglected.

Note that the reflectivity, absorptivity, transmitivity and emissivity correspond to the same radiative properties defined in this section, but related to pure, perfectly smooth materials [177].

The total intensity leaving a solid wall is equal to the difference between the incident intensities on the wall and the emitted and reflected radiation.

Emission by solid surfaces

All materials emit a fraction of the blackbody intensity. The ratio between the blackbody intensity and the emitted intensity of a solid object is its emissivity ϵ. For some materials an spectral dependency exists and is characterized by the nature of the emissivity: $\epsilon = f(\tilde{\nu}) = \epsilon_{\tilde{\nu}}$. Angular dependency can also

Table 6.2: Radiative properties of solid surfaces

Name	Symbol	Definition
Reflectance	ρ	$\dfrac{\text{Reflected radiation}}{\text{Total irradiation}}$
Absorptance	α	$\dfrac{\text{Absorbed radiation}}{\text{Total irradiation}}$
Transmittance	τ	$\dfrac{\text{Transmitted radiation}}{\text{Total irradiation}}$
Emittance	ϵ	$\dfrac{\text{Emitted radiation from a surface}}{\text{Emitted radiation by a blackbody at the same temperature}}$

be observed in some materials. However in most practical applications (and in particular in combustion systems) such dependency is neglected, and objects emit equally in all directions (diffusely emitting body).

Reflection by solid surfaces

Photons colliding with a solid surface can be absorbed, transmitted or reflected. In materials like glass or plexiglas, the transmission of photons is high. However most materials involved in combustion systems are non transmissive. In that case the solid is called opaque and incident photons can only be absorbed or reflected by the solid surface.

Reflection can be diffuse or specular (Fig. 6.4). In the first case a fraction $\rho_{\tilde{v}}$ of the monochromatic incident intensity $H_{\tilde{v}}(\mathbf{r}_w)$ is reflected back to the medium in a uniform distribution over all directions. The reflected intensity in one direction is then:

$$\rho^d(\mathbf{r}_w)\frac{H_{\tilde{v}}(\mathbf{r}_w)}{\pi} \tag{6.27}$$

 where the hemispherical monochromatic irradiation of the wall (where $\mathbf{n}_w$ is the surface normal) is defined by:

$$H_{\tilde{v}}(\mathbf{r}_w) = \int_{\mathbf{n}\cdot\mathbf{s}'<0} I_{\tilde{v}}(\mathbf{r}_w,\mathbf{s}')|\mathbf{n}_w\cdot\mathbf{s}'|d\Omega' \tag{6.28}$$

In the second case, when the reflection is considered specular, photons arriving in the direction $\mathbf{s}_s$ will be reflected in the direction $\mathbf{s}$ following the relation:

(a) Specular reflection   (b) Diffuse reflection
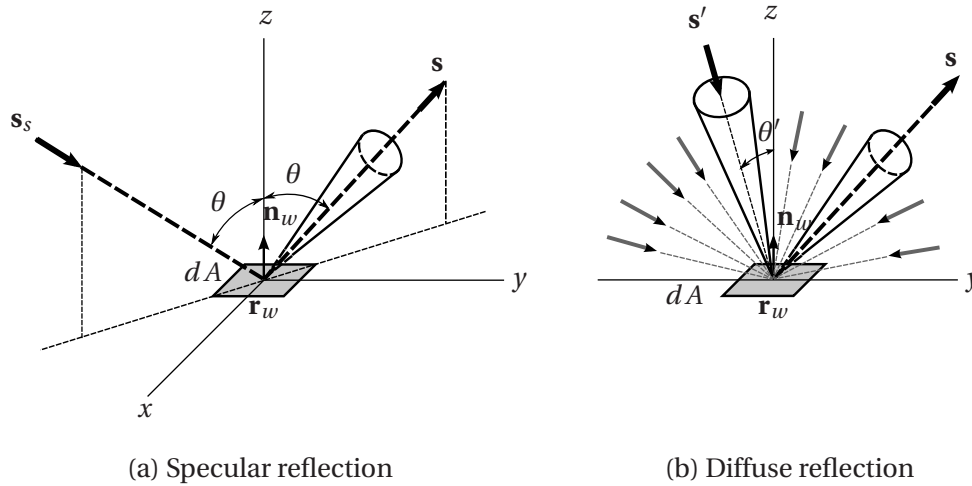
Figure 6.4: Reflection.

$$\mathbf{s}_s = \mathbf{s} - 2(\mathbf{s} \cdot \mathbf{n}_w)\mathbf{n}_w \qquad (6.29)$$

The specularly reflected intensity is written $\rho_{\tilde{\nu}}^s(\mathbf{r}_w) I_{\tilde{\nu}}(\mathbf{r}_w, \mathbf{s}_s)$ where $\rho_{\tilde{\nu}}^s$ is the fraction of the monochromatic intensity reflected back to te medium.

Finally the spectral intensity leaving the surface is:

$$I_{\tilde{\nu}}(\mathbf{r}_w, s) = \epsilon(\mathbf{r}_w) I_{b\tilde{\nu}}(\mathbf{r}_w) + \rho_{\tilde{\nu}}^d(\mathbf{r}_w) \frac{H_{\tilde{\nu}}(\mathbf{r}_w)}{\pi} + \rho_{\tilde{\nu}}^s(\mathbf{r}_w) I_{\tilde{\nu}}(\mathbf{r}_w, \mathbf{s}_s) \qquad (6.30)$$

The absorption of incident photons depend directly on the emissivity of the wall. For $\epsilon = 1$ (black-body) all incident photons are absorbed ($\alpha = 1$ and $\tau = 0$). In the same way, if the wall does not absorb any incident photon ($\alpha = 0$) all photons are reflected back to the medium. The relation between the emitted and the absorbed abilities of a body is called Kirchoff's law. When the properties of the solid are constant trough the spectrum, this law can be written: $\epsilon(\mathbf{r}_w) = \alpha(\mathbf{r}_w)$, and all the quantities are called "gray". This expression leads directly to a relation between the gray emissivity and the gray reflectivity of the opaque surface: $\rho(\mathbf{r}_w) = 1 - \epsilon(\mathbf{r}_w)$.

6.2.3   Radiative flux at the walls

The radiative flux that crosses a boundary (i.e. the radiation received by the solid) is the difference between the normal (to the surface) components of the emitted and the incident intensities integrated over the hemisphere above the surface. For an opaque surface with diffuse emissivity and diffuse reflectivity:

$$q_w^r = \text{emitted}_n - \text{incident}_n = \int_{2\pi} \left(\epsilon(\mathbf{r}_w) I_{b\tilde{v}}(\mathbf{r}_w) + \rho^d(\mathbf{r}_w) \frac{H_{\tilde{v}}(\mathbf{r}_w)}{\pi} \right) \mathbf{n} \cdot \mathbf{s} d\Omega - H_{\tilde{v}}(\mathbf{r}_w) \tag{6.31}$$

The total wall radiative flux is:

$$q_w^r = \epsilon(\mathbf{r}_w) [\pi I_{b\tilde{v}}(\mathbf{r}_w) - H_{\tilde{v}}(\mathbf{r}_w)] \tag{6.32}$$

It is clear that this flux must be equal to the normal component of the heat flux defined in eq (6.24):

$$q_w^r = \mathbf{q^r}(\mathbf{r}_w) \cdot \mathbf{n}_w \tag{6.33}$$

6.3   The Radiative Transfer Equation (RTE)

If the medium is transparent, the radiative energy transfer involves only the radiative properties of the surfaces and the geometrical description of the domain. The use of view factors, which describe the lines of sight between all the surfaces, is sufficient to calculate the heat transfer by radiation. This technique is used for satellite thermal control, thermal insulation, solar energy generation, heat dissipation in electronic components and for light distribution in computer animations where the effects of the gas can be neglected.

In the domain of energy production the impact of non-transparent media can not be neglected: the fluid can emit, diffuse and absorb radiative energy, modifying in consequence the radiative fluxes to the walls. In the present section the equations that govern radiation in the presence of a non-transparent medium are presented [91].

6.3.1   Intensity attenuation

In the present work it is considered that the refractive index of the medium n is uniform and constant. As a consequence the direction of propagation of the photons is not modified through the medium. The medium is also considered stationary compared with the speed of light, it is considered non-polarizing and in local thermodynamic equilibrium.

Absorption
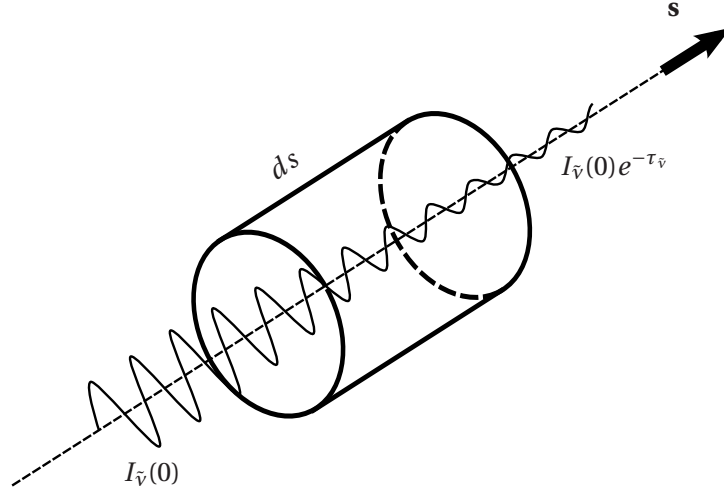
Figure 6.5: Absorption of energy at a given wavenumber.

Consider an elementary cylindrical control volume axed along the propagation direction of one electromagnetic wave (photon) as shown in Fig. 6.5. The variation of the radiation intensity between the entrance and the exit of the control volume, caused by energy absorption, is directly proportional to the magnitude of the entering intensity and the distance traveled by the beam. This variation can be described by:

$$(dI_{\tilde{v}})_{\text{abs}} = -\kappa_{\tilde{v}} I_{\tilde{v}} ds \tag{6.34}$$

where $\kappa_{\tilde{v}}$ [m^{-1}] is the proportionality constant known as the linear absorption coefficient[1]. $\kappa_{\tilde{v}}$ being a positive constant, a negative sign is introduced to express the diminution of intensity.

Integrating along the direction of propagation gives:

$$I_{\tilde{v}}(s) = I_{\tilde{v}}(0) \exp\left(-\int_0^s \kappa_{\tilde{v}} ds\right) = I_{\tilde{v}}(0) e^{-\tau_{\tilde{v}}} \tag{6.35}$$

where $I_{\tilde{v}}(0)$ is the intensity at the entrance of the domain, and $\tau_{\tilde{v}}$ is the optical thickness of the path. The absorbed fraction of the initial intensity (absorptivity) is:

---

[1]In the present section the spectral variable used is the wavenumber $\tilde{v}$ to conform with the majority of other publications.

$$\alpha_{\tilde{v}} = \frac{I_{\tilde{v}}(0) - I_{\tilde{v}}(s)}{I_{\tilde{v}}(0)} = 1 - e^{-\tau_{\tilde{v}}} \tag{6.36}$$

Out-scattering (Diffusion)

It is the deviation of the beam from the original propagation direction **s**. It reduces the energy content of the beam in the direction **s** in a similar way as absorption, with the difference that absorption transforms the photons into internal energy in the gas, while scattering redistributes it to another direction. For the considered direction energy diffusion (out-scattering) is expressed as:

$$(dI_{\tilde{v}})_{\text{sca}} = -\sigma_{s\tilde{v}} I_{\tilde{v}} ds \tag{6.37}$$

where $\sigma_{s\tilde{v}}$ [m^{-1}] is called the linear scattering coefficient.

The incident intensity suffers an attenuation caused simultaneously by absorption and diffusion: the combined effect is called extinction, characterized by the extinction coefficient $\beta_{\tilde{v}}$:

$$\beta_{\tilde{v}} = \kappa_{\tilde{v}} + \sigma_{s\tilde{v}} \tag{6.38}$$

6.3.2 Augmentation

Radiation intensity can be augmented through the control volume by two main processes: energy emission of the gas and capture of scattered radiation coming from other directions.

Emission

The emitted intensity is proportional to the volume of the gas. In the case of a cylindrical control volume, the emitted intensity depends only on the length of the path. Local thermodynamic equilibrium implies that the intensity is emitted as from a blackbody [236], leading to:

$$(dI_{\tilde{v}})_{\text{emi}} = \kappa_{\tilde{v}} I_{b\tilde{v}} ds \tag{6.39}$$

where the proportionality constant $\kappa_{\tilde{v}}$, based on the local thermodynamic equilibrium, follows Kirchhoff's law [135]: $\kappa_{\tilde{v}}^{\text{abs}} = \kappa_{\tilde{v}}^{\text{emi}} = \kappa_{\tilde{v}}$.

In-scattering

An amplification of the radiative intensity in the direction **s** can be also caused by deviation of beams from other directions (out-scattering). An integral evaluation over all solid angles and for each direction **s** is then necessary to acknowledge the in-scattering phenomena.
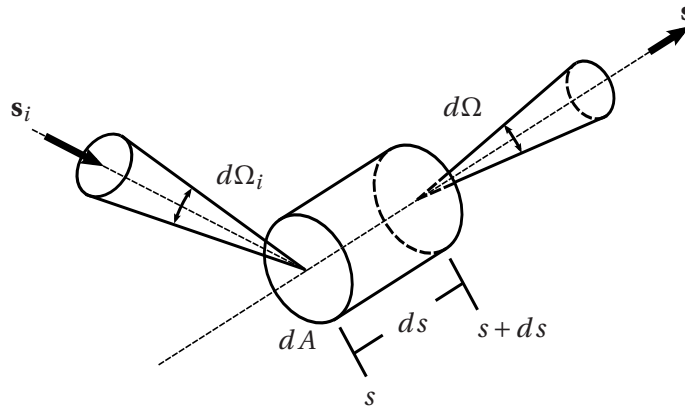
Figure 6.6: Scattered beam.

As shown in Fig. 6.6, the radiative flux impinging the entrance surface of the control volume $dV = dA\,ds$, along the direction $\mathbf{s}_i$ over a solid angle $d\Omega_i$ and with the intensity $I_{\tilde{v}}(\mathbf{s}_i)$, can be expressed as:

$$I_{\tilde{v}}(\mathbf{s}_i)(dA\mathbf{s}_i \cdot \mathbf{s})d\Omega_i d\tilde{v} \tag{6.40}$$

The distance traveled inside the volume dV by the incident beam of photons is equal to $ds/\mathbf{s}_i \cdot \mathbf{s}$. The energy loss of this beam by out-scattering is:

$$\sigma_{s\tilde{v}}I_{\tilde{v}}(\mathbf{s}_i)(dA\mathbf{s}_i \cdot \mathbf{s})d\Omega_i d\tilde{v}\left(\frac{ds}{\mathbf{s}_i \cdot \mathbf{s}}\right) = \sigma_{s\tilde{v}}I_{\tilde{v}}(\mathbf{s}_i)dAd\Omega_i d\tilde{v}ds \tag{6.41}$$

Of this total scattered intensity only a fraction is diffused in the solid angle $d\Omega$ around the direction **s**. This fraction can be calculated using $\Phi_{\tilde{v}}(\mathbf{s}, \mathbf{s}_i)d\Omega/4\pi$, where $\Phi_{\tilde{v}}$ is the so-called scattering phase function, which gives the probability that a beam coming along the direction $\mathbf{s}_i$ is scattered in the direction **s**.

Finally, the intensity coming from $d\Omega_i$ around $\mathbf{s}_i$ and scattered into $d\Omega$ around $\mathbf{s}$ is:

$$\sigma_{s\tilde{v}}I_{\tilde{v}}(\mathbf{s}_i)dAd\Omega_i d\tilde{v}ds\frac{\Phi_{\tilde{v}}(\mathbf{s},\mathbf{s}_i)}{4\pi}d\Omega \tag{6.42}$$

Summing over all scattered directions the total intensity gain by in-scattering writes:

$$(dI_{\tilde{v}})_{\mathrm{sca}}(\mathbf{s}) = ds\frac{\sigma_{s\tilde{v}}}{4\pi}\int_{4\pi}I_{\tilde{v}}(\mathbf{s}_i)\Phi_{\tilde{v}}(\mathbf{s},\mathbf{s}_i)d\Omega_i \tag{6.43}$$

The value of $\Phi_{\tilde{v}}$ is given by the properties of the media. However this function must verify the conservation of energy between the scattered beams: the total out-scattered radiation from $d\Omega_i$ around $\mathbf{s}_i$ into all directions is:

$$\sigma_{s\tilde{v}}I_{\tilde{v}}(\mathbf{s})dAd\Omega_i d\tilde{v}ds\frac{1}{4\pi}\int_{4\pi}\Phi_{\tilde{v}}(\mathbf{s}_i,\mathbf{s})d\Omega \tag{6.44}$$

which must be equal to the energy loss by this beam, (eq. 6.41), leading to:

$$\frac{1}{4\pi}\int_{4\pi}\Phi_{\tilde{v}}(\mathbf{s},\mathbf{s}_i)d\Omega = 1 \tag{6.45}$$

If scattering does not depend on the direction, i.e. energy is equally re-distributed among all directions, the probability $\Phi_{\tilde{v}}$ is constant. The normalization of eq. (6.45) leads to $\Phi_{\tilde{v}} = 1$.

6.3.3 The equation of transfer

A balance of the radiative energy for the control volume in the direction $\mathbf{s}$ is written by summing the attenuation and augmentation contributions defined in the previous sections (Fig. 6.7). The change of intensity in the direction $\mathbf{s}$ through the control volume is then:

$$
\begin{aligned}
I_{\tilde{v}}(s+ds,\mathbf{s},t+dt) - I_{\tilde{v}}(s,\mathbf{s},t) &= \kappa_{\tilde{v}}I_{b\tilde{v}}(s,t)ds - \kappa_{\tilde{v}}I_{\tilde{v}}(s,\mathbf{s},t)ds - \sigma_{s\tilde{v}}I_{\tilde{v}}(s,\mathbf{s},t)ds \\
&+ \frac{\sigma_{s\tilde{v}}}{4\pi}\int_{4\pi}I_{\tilde{v}}(\mathbf{s}_i)\Phi_{\tilde{v}}(\mathbf{s},\mathbf{s}_i)d\Omega_i ds
\end{aligned} \tag{6.46}
$$

The exiting intensity can be developed by the use of a partial derivatives, using also the relation between distance and time: $ds = cdt$. This leads to the expression:

$$I_{\tilde{v}}(s+ds,\mathbf{s},t+dt) = I_{\tilde{v}}(s,\mathbf{s},t) + dt\frac{\partial I_{\tilde{v}}}{\partial t} + ds\frac{\partial I_{\tilde{v}}}{\partial s} \tag{6.47}$$
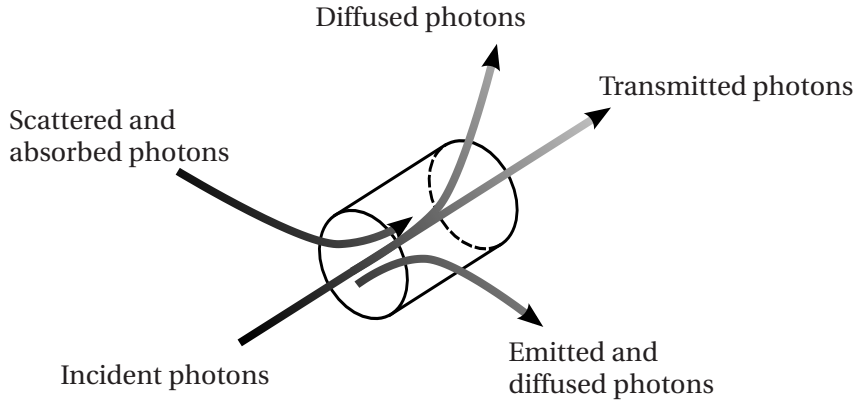
Figure 6.7: Possible interactions between a photon beam and a volume of gas.

Eq. (6.46) can now be expressed as:

$$\frac{1}{c}\frac{\partial I_{\tilde{v}}}{\partial t} + \frac{\partial I_{\tilde{v}}}{\partial s} = \kappa_{\tilde{v}} I_{b\tilde{v}} - \kappa_{\tilde{v}} I_{\tilde{v}} - \sigma_{s\tilde{v}} I_{\tilde{v}} + \frac{\sigma_{s\tilde{v}}}{4\pi} \int_{4\pi} I_{\tilde{v}}(\mathbf{s}_i)\Phi_{\tilde{v}}(\mathbf{s}, \mathbf{s}_i)d\Omega_i \qquad (6.48)$$

which is known as the Radiative Transfer Equation (RTE). This local formulation of the RTE contains terms which depend on the space location, the time, the wavenumber and the direction, but for simplicity reasons only the frequential and directional dependency are explicitly shown [263].

For the majority of engineering applications (except for short-pulsed lasers [141]) the first term of the LHS of equation (6.48) can be neglected, as the speed of light is many order of magnitudes superior to any other velocity scale in the problem. Introducing the extinction coefficient of eq. (6.38), the quasi-steady form of the RTE writes:

$$\frac{dI_{\tilde{v}}}{ds} = \mathbf{s} \cdot \boldsymbol{\nabla} I_{\tilde{v}} = \kappa_{\tilde{v}} I_{b\tilde{v}} - \beta_{\tilde{v}} I_{\tilde{v}} + \frac{\sigma_{s\tilde{v}}}{4\pi} \int_{4\pi} I_{\tilde{v}}(\mathbf{s}_i)\Phi_{\tilde{v}}(\mathbf{s}, \mathbf{s}_i)d\Omega_i \qquad (6.49)$$

with boundary conditions given by eq. (6.30).

Introducing the single scattering albedo $\omega_{\tilde{v}}$ (eq. 6.50), the RTE can be written in the even more simple form:

$$\omega_{\tilde{v}} = \frac{\sigma_{s\tilde{v}}}{\kappa_{\tilde{v}} + \sigma_{s\tilde{v}}} = \frac{\sigma_{s\tilde{v}}}{\beta_{\tilde{v}}} \qquad (6.50)$$

$$\frac{dI_{\tilde{v}}}{d\tau_{\tilde{v}}} + I_{\tilde{v}} = S_{\tilde{v}}(\tau_{\tilde{v}}, \mathbf{s}) \qquad (6.51)$$

where $\tau_{\tilde{\nu}}$ is the non-dimensional optical thickness:

$$\tau_{\tilde{\nu}} = \int_0^s (\kappa_{\tilde{\nu}} + \sigma_{s\tilde{\nu}})ds = \int_0^s \beta_{\tilde{\nu}}ds \tag{6.52}$$

and $S_{\tilde{\nu}}$ is the so-called source function, equal to:

$$S_{\tilde{\nu}}(\tau_{\tilde{\nu}}, \mathbf{s}) = (1 - \omega_{\tilde{\nu}})I_{b\tilde{\nu}} + \frac{\omega_{\tilde{\nu}}}{4\pi}\int_{4\pi} I_{\tilde{\nu}}(\mathbf{s}_i)\Phi_{\tilde{\nu}}(\mathbf{s}, \mathbf{s}_i)d\Omega_i \tag{6.53}$$

6.3.4 Integral formulation of the RTE

Integration of eq. (6.51) can be achieved by multiplying by the integration factor $e^{\tau_{\tilde{\nu}}}$:

$$\frac{d}{d\tau_{\tilde{\nu}}}\left(I_{\tilde{\nu}}e^{\tau_{\tilde{\nu}}}\right) = S_{\tilde{\nu}}(\tau_{\tilde{\nu}}, \mathbf{s})e^{\tau_{\tilde{\nu}}} \tag{6.54}$$

where it is supposed that the source function is known. Integration between points $s' = 0$ and $s' = s$ gives rise to:

$$I_{\tilde{\nu}}(\tau_{\tilde{\nu}}) = I_{\tilde{\nu}}(0)e^{-\tau_{\tilde{\nu}}} + \int_0^{\tau_{\tilde{\nu}}} S_{\tilde{\nu}}(\tau'_{\tilde{\nu}}, \mathbf{s})e^{-(\tau_{\tilde{\nu}} - \tau'_{\tilde{\nu}})}d\tau'_{\tilde{\nu}} \tag{6.55}$$

where the first term of the Right-Hand-Side (RHS) traduces the exponential attenuation of the intensity emitted at $s = 0$ and the integrand of the second term is the contribution of each point of the medium, attenuated over the distance $\tau_{\tilde{\nu}} - \tau'_{\tilde{\nu}}$.

Special case: non-scattering medium

In the case of a non-scattering medium, the source function reduces to the blackbody intensity and the solution can be written:

$$I_{\tilde{\nu}}(\tau_{\tilde{\nu}}) = I_{\tilde{\nu}}(0)e^{-\tau_{\tilde{\nu}}} + \int_0^{\tau_{\tilde{\nu}}} I_{b\tilde{\nu}}(\tau'_{\tilde{\nu}})e^{-(\tau_{\tilde{\nu}} - \tau'_{\tilde{\nu}})}d\tau'_{\tilde{\nu}} \tag{6.56}$$

In such case, knowing the temperature field is sufficient to resolve eq. (6.56). Notice that in such case, $\tau_{\tilde{\nu}}$ is a quantity that depends only on the absorption coefficient $\kappa_{\tilde{\nu}}$.

Many other simplifications of the RTE exist for particular cases, as for example the case of cold medium where the temperature is so low that the blackbody intensity is negligible compared to the incident intensity, or the case of a purely scattering medium, where no absorption or emission are considered [177, 236].

6.3.5   The macroscopic radiative source term

For participative media it is important to know the net radiative energy variation of a volume element at every location of space. To do so, a balance of fluxes crossing all the faces of a control volume dV is written.
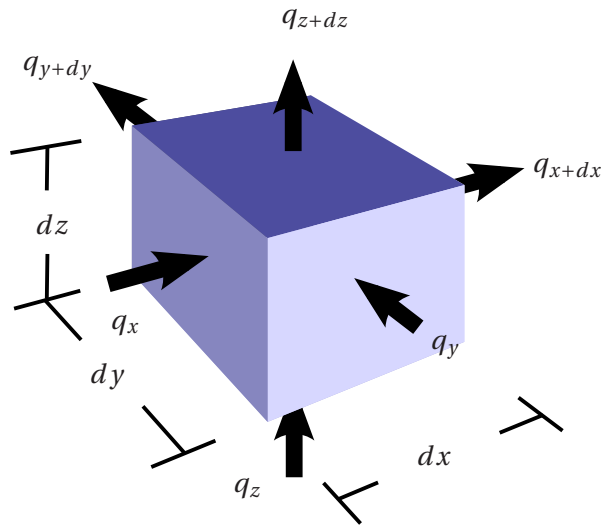
Figure 6.8: Radiative heat flux.

Consider de control volume shown in Fig. 6.8. The total energy variation in dV is the difference between the incoming fluxes at x, y, and z, and the outgoing fluxes at $x + dx$, $y + dy$ and $z + dz$:

$$q^r(x)dydz - q^r(x+dx)dydz + q^r(y)dxdz - q^r(y+dy)dxdz + q^r(z)dxdy - q^r(z+dz)dxdy \quad (6.57)$$

or introducing partial derivatives:

$$-\left(\frac{\partial q^r}{\partial x} + \frac{\partial q^r}{\partial y} + \frac{\partial q^r}{\partial z}\right)dxdydz = -\nabla \cdot \mathbf{q^r}dV \quad (6.58)$$

This equation shows that the variation of radiative energy in a control volume is simply the divergence of the radiative flux. From its definition in eq. (6.24) the divergence of the monochromatic radiative flux is expressed as:

$$\boldsymbol{\nabla} \cdot \mathbf{q}_{\tilde{v}}^{\mathbf{r}} = \boldsymbol{\nabla} \cdot \int_{4\pi} I_{\tilde{v}} \mathbf{s} \, d\Omega \tag{6.59}$$

Integrating eq. (6.49) we get:

$$\int_{4\pi} \mathbf{s} \cdot \boldsymbol{\nabla} I_{\tilde{v}} \, d\Omega = \int_{4\pi} \kappa_{\tilde{v}} I_{b\tilde{v}} \, d\Omega - \int_{4\pi} \beta_{\tilde{v}} I_{\tilde{v}} \, d\Omega + \int_{4\pi} \frac{\sigma_{s\tilde{v}}}{4\pi} \int_{4\pi} I_{\tilde{v}}(\mathbf{s}_i) \Phi_{\tilde{v}}(\mathbf{s}, \mathbf{s}_i) \, d\Omega_i \, d\Omega \tag{6.60}$$

which can be written:

$$\boldsymbol{\nabla} \cdot \int_{4\pi} I_{\tilde{v}} \mathbf{s} \, d\Omega = 4\pi \kappa_{\tilde{v}} I_{b\tilde{v}} - \int_{4\pi} \beta_{\tilde{v}} I_{\tilde{v}} \, d\Omega + \frac{\sigma_{s\tilde{v}}}{4\pi} \int_{4\pi} I_{\tilde{v}}(\mathbf{s}_i) \left(\int_{4\pi} \Phi_{\tilde{v}}(\mathbf{s}, \mathbf{s}_i) \, d\Omega \right) d\Omega_i \tag{6.61}$$

In the case of a non-scattering medium ($\sigma_{\tilde{v}} = 0$), this expression can be written:

$$\boldsymbol{\nabla} \cdot \mathbf{q}_{\tilde{v}}^{\mathbf{r}} = \kappa_{\tilde{v}} \left(4\pi I_{b\tilde{v}} - \int_{4\pi} I_{\tilde{v}}(\mathbf{s}) \, d\Omega \right) = \kappa_{\tilde{v}} (4\pi I_{b\tilde{v}} - G_{\tilde{v}}) \tag{6.62}$$

that simply expresses that the variation of radiative energy inside a control volume is the difference between the emitted energy and the absorbed irradiation. The divergence of the total radiative flux is obtained by integration over the electromagnetic spectrum and is:

$$\boldsymbol{\nabla} \cdot \mathbf{q}^{\mathbf{r}} = \int_0^\infty \kappa_{\tilde{v}} (4\pi I_{b\tilde{v}} - G_{\tilde{v}}) \, d\tilde{v} \tag{6.63}$$

This quantity is also known as the radiative source term:

$$\mathscr{S}_r = \boldsymbol{\nabla} \cdot \mathbf{q}^{\mathbf{r}} \tag{6.64}$$

For the particular case of a medium with a constant absorption coefficient $\kappa_{\tilde{v}} = \overline{\kappa} = cst$, the radiative source term simplifies to:

$$\mathscr{S}_r = \boldsymbol{\nabla} \cdot \mathbf{q}^{\mathbf{r}} = \overline{\kappa} \left(4\sigma T^4 - \int_{4\pi} I \, d\Omega \right) = \overline{\kappa} (4\sigma T^4 - G) \tag{6.65}$$

6.4   Radiative properties of participating media

One of the most difficult parts when describing the radiation of real gases (either for atmospheric radiation [91] or heat transfer in combustion systems) is the representation of their spectral properties. In the last decades many improvements have been achieved in the understanding of gas radiation, and in particular H_2O and CO_2 radiative properties, which are the major greenhouse effect gases and the principal products of hydrocarbon combustion [263, 146].

The theoretical basis of spectroscopy relies on the developments made on quantum mechanics at the beginning of the 20th century [177, 236].

For a gas molecule on thermodynamic equilibrium, the distribution of the emission/absorption lines in the spectrum depends on the allowed energy transitions of the gas. The energy level of a molecule composed on many atoms can be changed mainly by three methods: (a) through a change in the energy levels of the electrons in the atoms of the molecule, (b) by a change in the rotational momentum of the molecule or (c) by a variation of the vibration motion between the atoms composing the molecule.
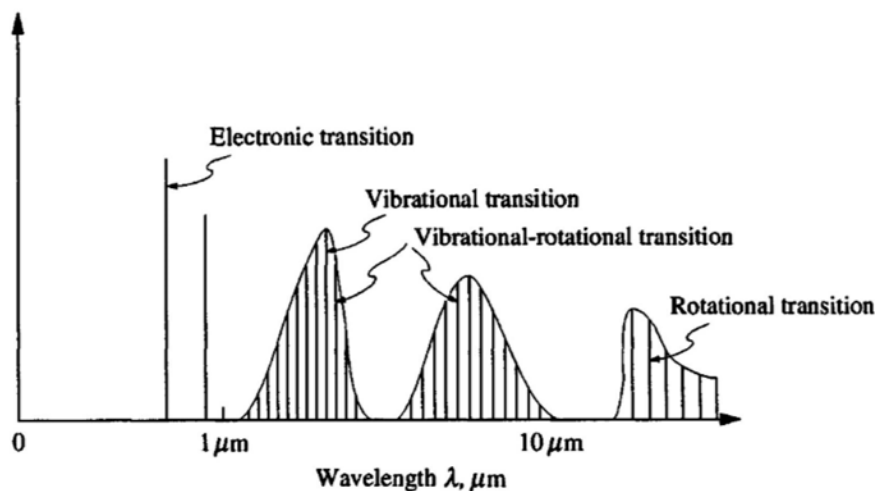

Figure 6.9: Spectral lines due to electronic, vibrational and rotational energy changes in a gas molecule. Extracted from [177].

Figure 6.9 shows an schematic representation of the energy levels (the wavenumbers) at which each one of these energy transitions operates. It can be observed that in the center of the image the vibrational and rotational transitions are superposed.

Electronic transitions in combustion applications constitute a negligible part of the heat transfer. It is useful however to study this method as it gives a good introduction to the three main energy transitions.

6.4.1 Electronic energy transitions in atoms

In the most simple case of interaction between matter and light, i.e. in the interaction between an atom and a photon, it has been demonstrated that only the photons carrying a specific amount of energy (i.e. associated to a specific frequency eq. 6.66) can be absorbed by the atom. Such absorption causes a change in the potential energy of the electron cloud in the atom. From that excited state the

atom can spontaneously go back to a lower quantic energy level, releasing a fixed amount of energy. Intermediate levels of energy are therefore not possible. The energy release produces a photon at a frequency associated to the specific energy. The relation between energy and frequency uses the Planck constant h:

$$\Delta E = h\nu \tag{6.66}$$

Energy absorption and emission are therefore made at discrete values which differ from one element to the other. This kind of energy exchange is called electronic transition, and in general operates at very high energy levels.

The intrinsic energy level of an atom can be calculated as:

$$E_n = -hcR_\infty \frac{Z^2}{n^2} \tag{6.67}$$

where $R_\infty = 1,0973731 \, 10^7$ [m^{-1}] is the Rydberg constant, Z is the atomic number and n is the principal quantum number. For example the energy necessary to jump from the E_2 to the E_1 level in a hydrogen atom (the electronic transition which requires the lowest energy jump) is equal to $\Delta E_{2\rightarrow1} = E_2 - E_1 = 10,2$ [eV], which corresponds to a frequency $\nu = \Delta E_{2\rightarrow1}/h = 2,466 \, 10^{15}$ [Hz]. This frequency is located in the high violet zone of the visible spectrum (see Fig. 6.1), at the limit of the thermal radiation zone of the spectrum. Higher energy transitions occur at lower wavelenghts (higher frequencies), outside the thermal radiation zone, and only at a limited number of specific frequencies, for this reason in most engineering applications electronic transitions are neglected.

6.4.2 Molecular energy transitions

Molecules have additional energy variation processes: the energetic state of a multi-atomic molecule can be also modified by a variation of the rotational and/or the vibrational state of the molecule.

As shown in Fig. 6.10 the relative position of each atom in the molecule is modified by rotation of the whole molecule around the three axes (Fig. 6.10-a) and by relative pseudo-elastic vibration between the atoms in different directions (Fig. 6.10-b). For a molecule with N atoms three degrees of freedom are allowed for rotation, and $3N - 3$ are possible for the vibration [250].

Three transition modes are then observed: rotational transitions, vibrational transitions and combined vibrational-rotational transitions. The associated quantic energy levels are derived from Scrhödinger wave equation [232]: eqs. (6.68), (6.69) and (6.70) represent the energy levels for the rotational, vibrational and rotational-vibrational transitions, where j and ν are the rotational and vibrational quantum numbers (which take only integer values).
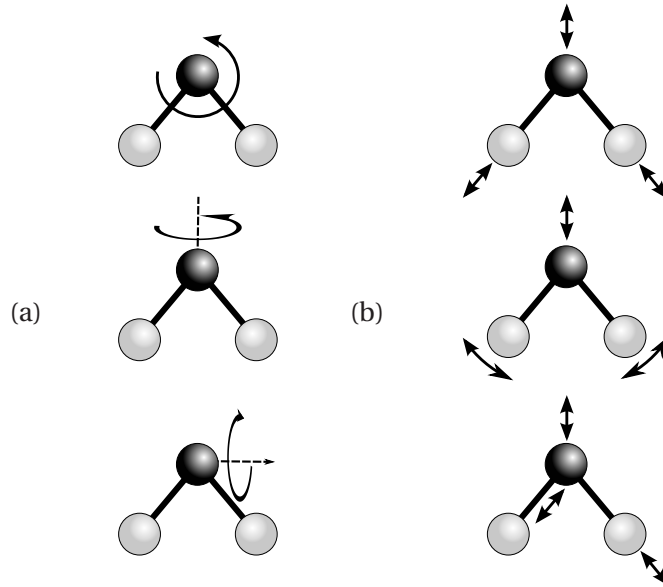
Figure 6.10: Non-linear triatomic molecule: H_2O. (a) Rotational degrees of freedom. (b) Vibrational degrees of freedom.

$$E_j = hc_0 B j(j+1) \quad , \quad j = 0,1,2,... \tag{6.68}$$

$$E_v = h\nu_e(v+1/2) \quad , \quad v = 0,1,2,... \tag{6.69}$$

$$E_{vj} = h\nu_e(v+1/2) + B_v j(j+1) \quad , \quad v,j = 0,1,2,... \tag{6.70}$$

Eq.(6.68) is the solution of the Schödinger wave equation for a rigid rotator model, eq.(6.69) is the solution for an harmonic oscillator and eq.(6.70) is the solution for the combined problem. Here B (B_v) is a rotational constant that depends on the moment of inertia of the molecule, and ν_e is the equilibrium frequency or eigenfrequency of the oscillator.

Eqs. (6.71) and (6.72), obtained using eqs. (6.68), (6.69) and eq. (6.66), show the associated wavenumbers of the rotational an the vibrational transitions between the states $j \to j+1$ and $v \to v+1$:

$$\tilde{\nu} = (E_{j+1} - E_j)/hc_0 \quad = \quad 2B(j+1), \quad j = 0,1,2,... \tag{6.71}$$

$$\tilde{\nu} = (E_{v+1} - E_v)/hc_0 \quad = \quad (\nu_e/c_0)(v+1-v) = \nu_e/c_0 \tag{6.72}$$

Figure 6.11 show the energy jumps by absorption and emission of photons associated to their frequency in the rotational and vibrational transitions [177]. While rotational transitions can be spread

over many different frequencies and constitute a wide range of energy variations, vibrational transitions occur only at one frequency (the eigenfrequency ν_e) with a constant energy interval between quantic levels.
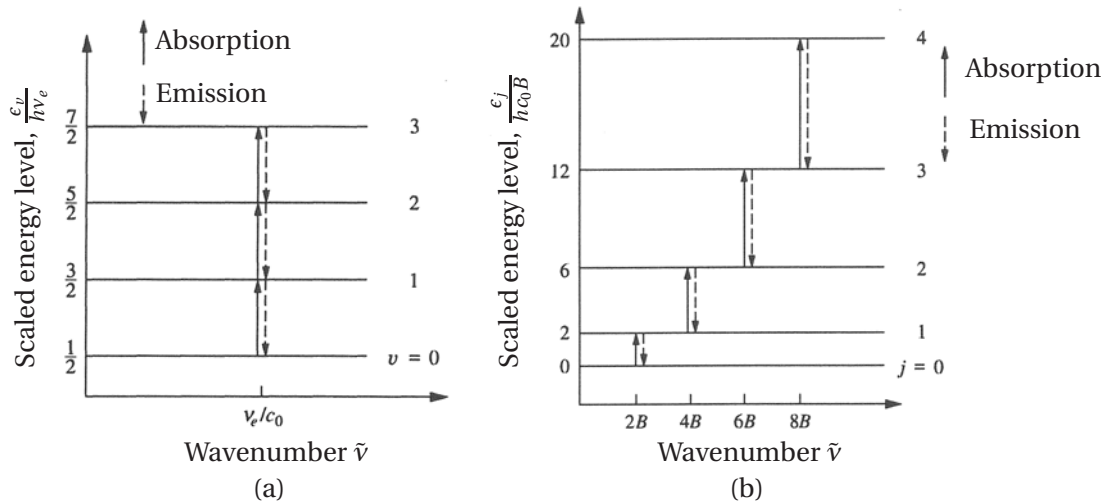

Figure 6.11: Scaled discrete energy levels and spectral positions: (a) vibrational transitions using the hypothesis of an harmonic oscillator, (b) rotational transitions using the hypothesis of a rigid rotator. Extracted from [177]

Analysis of eq. (6.70) is slightly more complex: transitions are allowed between energy levels[2] $\Delta j = +1, -1, 0$ for the rotational transition and $\Delta \nu = +1, -1$ for the vibrational transition. Separating the problem in three branches P ($\Delta j = -1$), Q ($\Delta j = 0$) and R ($\Delta j = +1$), the associated frequencies are given in eqs. (6.73)-(6.75). Fig. 6.12 illustrates the frequencies and energy variations for rotational-vibrational transitions [177].

$$\tilde{\nu}_P = \tilde{\nu}_0 - (B_{\nu+1} + B_\nu)j + (B_{\nu+1} - B_\nu)j^2, \quad j = 1, 2, 3, \dots \tag{6.73}$$

$$\tilde{\nu}_Q = \tilde{\nu}_0 + (B_{\nu+1} - B_\nu)j + (B_{\nu+1} - B_\nu)j^2, \quad j = 1, 2, 3, \dots \tag{6.74}$$

$$\tilde{\nu}_R = \tilde{\nu}_0 - 2B_{\nu+1} + (3B_{\nu+1} - B_\nu)j + (B_{\nu+1} - B_\nu)j^2, \quad j = 0, 1, 2, \dots \tag{6.75}$$

6.4.3 Line radiative intensity and broadening

In the previous section it was shown that molecules emit and absorb photons at discrete frequencies. However in reality spectral lines are never strictly monochromatic: absorption and emission take

---

[2]The transition $\Delta j = 0$ corresponds to emission and instant re-absorption.
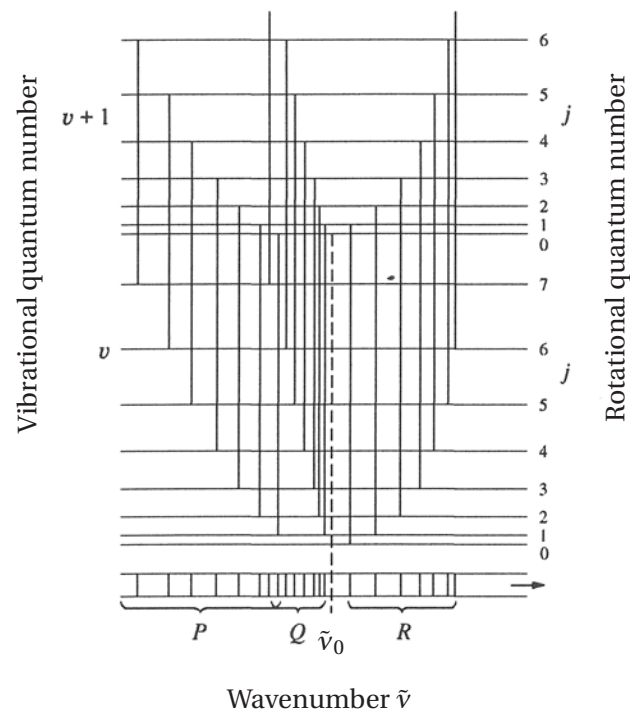
Figure 6.12: Vibration-rotation spectral lines. Extracted from [177]

place in a tiny but finite range of frequencies around the discrete associated value given by quantum mechanics. This range is broadened by different phenomena, the three most important being natural line broadening, collision broadening and Doppler broadening.

- **Natural line broadening**

  The Heisenberg's uncertainty principle says that for a given energy transition, only a probability of emission/absorption around the associated frequency can be constructed, leading to a natural broadening of absorption lines (Fig. 6.13). This broadening is observed in excited molecules that spontaneously release energy.

  The line shape of a naturally broadened absorption wavelenght around $\tilde{v}_0$ is described by:

  $$\kappa_{\tilde{v}} = \frac{S}{\pi} \frac{b_N}{(\tilde{v} - \tilde{v}_0)^2 + b_N^2} \tag{6.76}$$

  where b_N is the half-width of the profile and S is the line strength given by:

  $$S = \int_{\Delta\tilde{v}} \kappa_{\tilde{v}} d\tilde{v} \tag{6.77}$$

The half-width b_N is small compared with other broadening mechanisms, thus in most engineering applications natural broadening is neglected or combined with the collision broadening.

- **Collision broadening**

In combustion applications collisions between molecules occur more often than the natural spontaneous energy release. However the mechanism of collision broadening is also based in the Heisenberg principle: when two molecules collide energy is released in a range around the associated frequency.

The width of the broadened line by molecular collision is derived from the electron theory of Lorentz or from quantum mechanics [26, 91]:

$$\kappa_{\tilde{\nu}} = \frac{S}{\pi} \frac{b_C}{(\tilde{\nu} - \tilde{\nu}_0)^2 + b_C^2} \tag{6.78}$$

where b_C is the line half-width and $\tilde{\nu}_0$ is the wavenumber at the line center.

The value of b_C depends on the probability of collision between two molecules, which can be infered from the thermodynamics [91]:

$$b_C = \frac{2}{\sqrt{\pi}} \frac{D^2 p}{c_0 \sqrt{mkT}} = b_C^0 \frac{p}{p_0} \sqrt{\frac{T_0}{T}} \tag{6.79}$$

where D is the effective diameter of the molecule, m is its mass, T is the gas temperature, p is the pressure and 0-indexed variables designate a reference state. Eq. (6.79) shows that line broadening is important at high pressures and low temperatures.

In general the collision and natural broadening are combined and called Lorentz broadening. When both mechanisms are combined the half-with coefficient is called b_L and is calculated using eq. 6.79.

- **Doppler broadening**

The third kind of broadening is produced by the Doppler effect, caused by the compression or expansion of the traveling wave. In this case the broadened absorption profile is written as [177, 236, 91]:

$$\kappa_{\tilde{\nu}} = \sqrt{\frac{\ln 2}{\pi}} \left(\frac{S}{b_D} \right) \exp \left[-(\ln 2) \left(\frac{\tilde{\nu} - \tilde{\nu}_0}{b_D} \right)^2 \right] \tag{6.80}$$

where b_D is the Doppler half-width (Eq. 6.81):

$$b_D = \frac{\tilde{\nu}_0}{c_0} \sqrt{\frac{2kT}{m} \ln 2} \tag{6.81}$$

The Dopler half-width b_D depends on the frequency $\tilde{\nu}_0$, unlike in collision and natural broadening. Figure 6.13 shows profiles for both Lorentz and Doppler broadening. The combined effect produces a series of broadening shapes called Voigt profiles, represented by the shaded zone in Fig. 6.13.
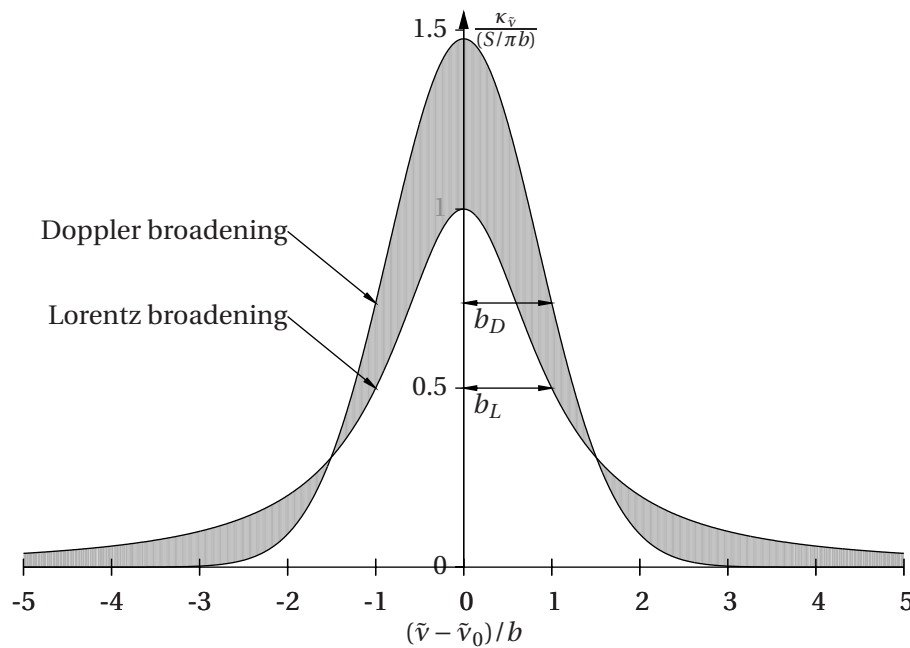
Figure 6.13: Spectral line broadening.

It can be seen from Eqs. (6.68)-(6.70), that in the case where $B_{\nu+1} = B_\nu$, i.e. when the moment of inertia of the molecule is conserved after a rotational transition, the R-branch of the rotational-vibrational transition disappears and equally spaced absoprtion lines apear on both sides of the eigenfrequency $\tilde{\nu}_e$ (where no line can be seen). This leads to absorption arrangements with broadened lines as the one shown in fig. 6.14. In a complex molecule however, vibration-rotation transitions can produce closely spaced profiles that in many cases can overlap.

6.4.4   Radiation in combustion applications

Most combustion applications involve temperatures ranging from 300K to 3000K. While gases emit and absorb at discrete frequencies, solid objects like walls and black particles (soot, coal, etc.) emit as a blackbody. Figure 6.15 shows the blackbody emitted energy for the temperature range $T = [300K; 2900K]$ and the wavelength range $\lambda = [10^{-7}; 10^{-3}]$ [m]. The shaded zone represents the visible spectrum.

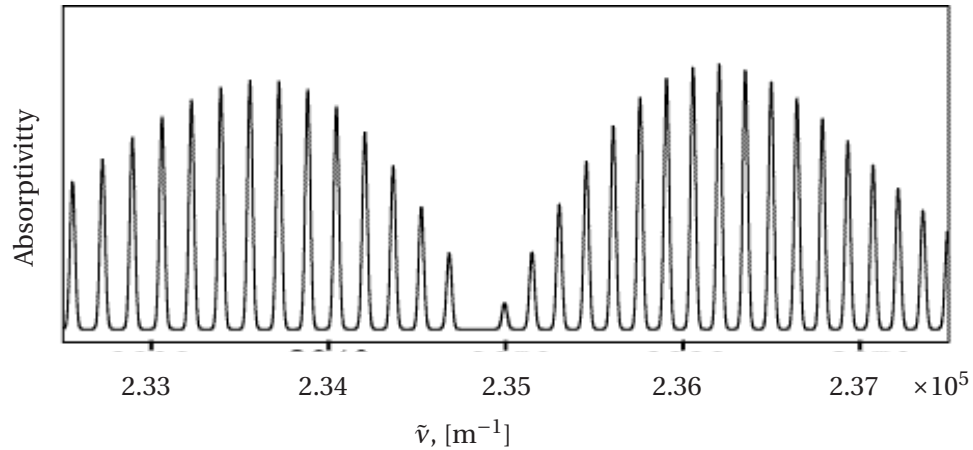Figure 6.14: CO_2 Absorptivity (broadened) lines around $\tilde{\nu}_e \approx 2.35$ [m^{-1}].

Thermal radiation is considered important in the range $\lambda = [10^{-7}; 10^{-4}]$ [m], where most rotational-vibrational transitions take place for greenhouse gases.

The wavelength of maximum emitted energy is given by the Wien law (eq. 6.13), which gives here values located between $\lambda = 10^{-6}$ [m] and $\lambda = 10^{-5}$ [m] (dotted line in Fig. 6.15). In this temperature range the maximum values of energy release lay outside the frequencies of the visible spectrum. This is the reason why thermographic imaging techniques are based on the infrared region of the spectrum. For numerical applications it means as well that the region of major interest is in the near infrared range.

Highly absorbing gases and black particles can emit energies up to $E_b = 4,0112\,10^6$ [W/m^2] when their temperature reaches $T = 2900$K. Even in this case the energy released is about three orders of magnitude smaller than the energy released by the combustion of an hydrocarbon fuel. This means that the main properties of the flame are mainly controlled by the combustion processes, and justifies that radiation is rarely included in combustion calculations.

Still, radiation plays three important roles in a combustion system:

- gas-to-gas radiation interaction may lead to reactant pre-heating and hot gas cooling, which would modify the flame speed and the final combustion temperature.

- gas-to-solid radiation interaction results in increased thermal fluxes to the walls and hot gas cooling. This is important for the control of wall temperatures, which in turn has an influence on the flame attachment to (or extinction near) the walls.

- solid-to-gas radiation interaction, in particular when solid particles as soot are present, also results in important changes of the flame structure.
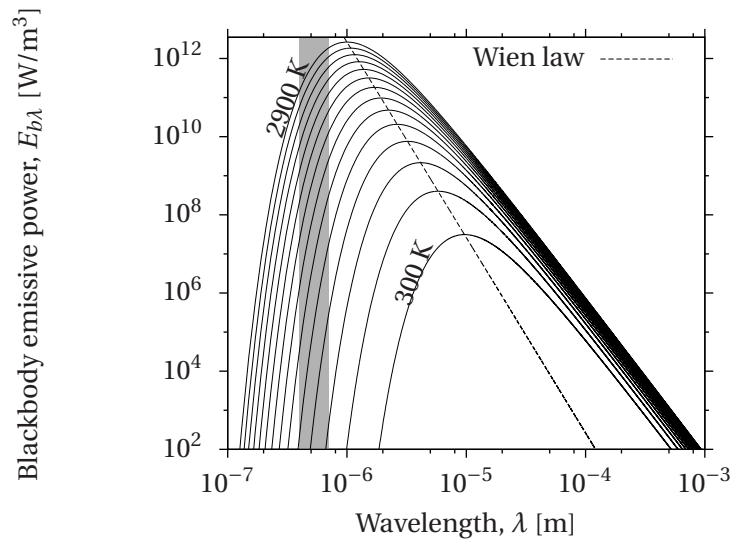
Figure 6.15: Blackbody emission curves for temperatures varying from 300K to 2900K, by 200K. The shaded zone represents the visible zone of the spectrum. The infra-red zone and part of the ultra-violet zones of the spectrum are respectively located to the right and the left of the shaded zone.

For example, in spherical premixed methane+oxygen+CO_2 flames at high pressures (up to 5 atm) Chen et al. have shown that radiation absorption increases the flame speed and the flammability limit [41]. This has an important impact for Exhaust Gases Recirculation (EGR) techniques currently studied in the domain of piston engine combustion, where radiation could play an important role.

Another example is the modification of the composition of the hot gases: Poitou has shown [204] that mass fractions of species like *CO* can be modified by the inclusion of radiation in combustion processes.

Finally, as shown in chapter 4, aerothermal interaction of the fluid with the solid can lead to important heat fluxes at the walls. Radiation can be seen as an accelerator of such exchange, increasing the energy flux from the fluid to the solid. Moreover, in modern aeronautical combustion chambers thermal protection by cool air injection through multiperforations has succeeded to lower the heat transfer associated to convection, giving radiation an even more important role in the energy transfer to the liner.

The calculation of radiation in numerical combustion is usually neglected. The first reason, as already mentioned, is that compared to combustion heat release, radiation has a negligible direct impact on the flame [3]. The second is that the CPU cost of radiation is extremely high for accurate radiative models, and this was not judged necessary to calculate flames. Recently, Poitou [204] made a de-

---

[3]This is true for combustion chamber applications, but radiation effects have a major role in flame extinction in sooting compartment fires [104, 276] and flame propagation in wildfires [269, 35, 30].

tailed study on the optimum CPU/accuracy ratio for different radiation approaches on quasi one-dimensional flames, showing that recent improvements of the code PRISSMA can lower the restitution times without significant accuracy loss.

Now combustion simulations do not focus anymore on the flame structure only, but includes thermal effects, unsteady effects and emissions. In this context, a numerical code developed in order to treat realistic industrial cases in unstructured meshes with restitution times sufficiently small to perform coupled unsteady simulations with a combustion code, without loosing accuracy in the spectral model. The details of this code are presented in section 6.6.

6.5   Numerical simulation of radiation

The numerical resolution of the radiative heat transfer problem depends on the proper numerical representation of the spectral data and the accuracy of the spatial integration of the RTE. The two major ingredients of radiation modeling are then the spectral approximation and the spatial integration.

6.5.1   Spectral models for participating media

Introduction

As described in section 6.4.3, every spectral line can be characterized by its strength S and its line half-width b. To describe the molecular absorption/transmission/emission profiles of gases that accurately represent the interaction of the mixture with the electromagnetic radiation, four kinds of approaches can be found in the literature: the line-by-line method, the narrow-band models, the wide-band models and the global approach.

- **Line-by-line (LBL)**

  The most sophisticated and accurate method for the representation of the absorption spectrum is the line-by-line (LBL) method. As it can be inferred from its name, in this approach each line of the infinite spectrum (or at least over a several hundred thousands spectral lines) is represented by its strength and half-witdh, and line overlapping is reconstructed. These properties are determined by measurements, as for example the HITRAN and the HITEMP databases [220] where the properties of several million lines for specific molecules are given.

  The LBL method remains today (and probably for several years) a reference tool only used for validation in extremely simple cases. The LBL data however is used to build simpler models as the ones presented below.

- **Spectral Narrow-Band (SNB)**

In a narrow spectral range the absorption coefficient of a gas can vary rapidly (see Fig. 6.14). However in the same interval other radiation quantities remain almost unchanged, as for example blackbody intensity. A conscious averaging of the absorption spectrum over such intervals produce a smoothed absorption profile that behaves, in principle, like the LBL model [263, 177, 236].

In the latest generation of SNB models it was observed that in a small spectral range the absorption coefficient could take the same value several times at slightly different frequencies, producing at each time the same intensity $I_{\tilde{\nu}}$ and radiative flux. Given that in the narrow spectral range the precise location of the frequency do not influence the mean band quantities, a reorganization of the absorption coefficients within the band can be done. Such rearrangement is called the correlated k-distribution of the spectral narrow band method (SNBcK). The smoothed monotonic profile obtained can then be easily integrated by numerical methods [138, 10]. Goutière et al. have shown that the level of accuracy of the SNBcK simulations is good and that this method can be used to produce reference simulations [95, 96].

- **Wide band**

  Here, larger spectral ranges (wide-bands) are considered. In this case the quantities that where considered constant in the SNB method, are no longer considered as such. The dependence of the Planck function with the varying absorption coefficient within the wide band must be modeled [108, 44, 71, 70]. The main advantage of this method is the reduction of the number of bands compared to the SNB methods. However this method is not commonly used in the available literature.

- **Global models**

  In a global approach quantities are related to the total (spectrally integrated) properties. The full spectrum is reduced to a limited number of data, in general to a constant value of the absorption coefficient. In the global model the length of the band is the size of the spectrum. One approach proposed by Hottel and Saroufim is to consider the gas mixture as the somation of gray virtual gases weighted by a certain coefficient: it is called the Weighted Sum of Gray-Gases (WSGG) [175]. An updated version was presented by Denison and Webb: the Spectral Line WSGG (SLW) [56, 57], where the spectral properties are directly constructed from a LBL database. Applying the k-distribution method to a global model, André et al. [8] describes a general formulation presented in the global models by Pierrot et al. [196, 195] and Modest [176]. Gray virtual gas properties are generally obtained by comparison with experimental results or against SNB simulations [241].

  The major interest of the global models is the low computational cost of the simulations. This characteristic must be exploited in order to carry out coupled Combustion-Radiation simulations. The main challenge remains to develop a method that remains accurate.

6.5.2 Spatial integration of the RTE

The RTE describes the variation of a monochromatic electromagnetic wave on a particular direction. Integration of the angular and frequency data gives the radiative source term which must be taken into account in the fluid energy equation.

The integral or the differential forms of the RTE can be used (Eqs. 6.49 and 6.55), which can be transformed in two different classes of resolution methods. The spatial, angular and frequency discretization can be performed using different approaches. The most commonly used methods to numerically resolve the RTE are summarized below. They are split into two classes: integral or differential methods.

Integral methods

Integral methods resolve the integral form of the ETR (Eq. 6.55). In this category the most commonly used approaches are Hottel's zonal method and the ray tracing method.

(a) Zonal method   (b) Ray tracing   (c) Monte Carlo method
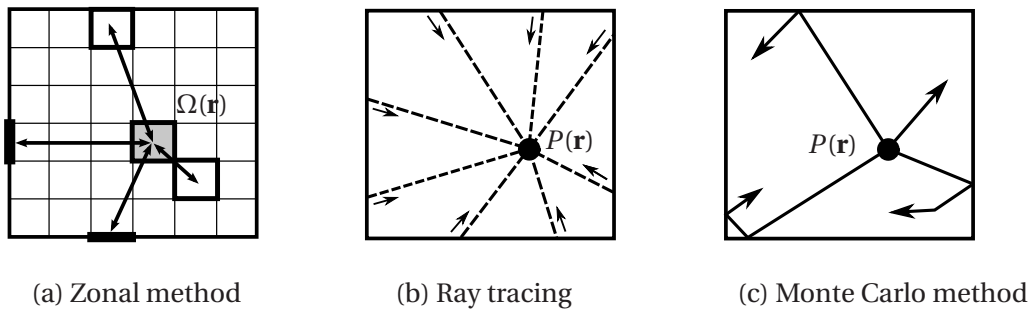
Figure 6.16: Integral approaches for the resolution of the RTE: (a) schematic representation of some volume/volume and volume/surface interactions, (b) examples of ray tracing trajectories and their segmentation, (c) example of photon paths and their interaction with walls and the medium (absorption, scattering).

- **The zonal method**

  This technique was introduced by Hottel, Cohen and Sarofim [105, 106] to solve engineering problems. It consists of a spatial discretization of the domain and its boundary. Radiative properties as intensity and absorption coefficient are considered uniform over the volumes and surface elements.

Three kinds of interaction can take then place: surface/surface interaction, surface/volume interaction and volume/volume interaction (Fig. 6.16-a). Every element can exchange energy with any other element in the domain and this exchange can be modeled using an interaction matrix. Depending on the matrix properties efficient mathematical methods and algorithms can be be implemented to accelerate the computation.

The limitations of such method include: the necessity to rely on the calculation of view factors for the surface/volume and surface/surface interactions that can become extremely difficult in complex geometries, the computational cost of mesh refinement[4] and the difficulty to implement reflection phenomena.

Until very recently however, this was the preferred method for radiation computation on simple combustion chambers, as for example the incinerator calculated by Olsommer et al. [189] in 1997 and more recently by Silva et al. [237].

- **Ray tracing**

  Here the ETR is integrated along radiation beams. At each point of the domain the solid angle is discretized in a number of directions, high enough to consider that radiation is uniformly distributed in space. For each direction (called beam) the optical path is cut in small segments of size l, considered uniform and isothermal (Fig. 6.16-b). A mean transmittance $T_{\tilde{v}}(l)$ can then be calculated for that segment. The ETR is integrated starting from the boundary surfaces to the evaluation point $P(\mathbf{r})$. The intensity at $\mathbf{r}$ along the direction $\mathbf{s}$ and for the wavelength $\tilde{v}$ is expressed by [177, 236]:

  $$I_{\tilde{v}}(\mathbf{r}, \mathbf{s}) = I_{\tilde{v}}(\mathbf{r}_w, \mathbf{s}) T_{\tilde{v}}(\mathbf{r}_w \rightarrow \mathbf{r}) + \sum_{k=1}^{N} (1 - T_{\tilde{v}}(l_k)) I_{b\tilde{v}}(\mathbf{r}_k) \qquad (6.82)$$

  where $\mathbf{r}_w$ is the position of the starting point on the wall and N is the number of segments of the beam.

  The precision of a ray tracing simulation depends on the number of directions and the number of segments per direction. The problem becomes more complex if the reflection of the walls is taken into account. In general, this method has the highest accuracy but also the highest CPU cost. It is often used to create benchmark cases to test other models.

- **The Monte Carlo method (MC)**

  The term "Monte Carlo" describes a large and widely-used class of approaches in the simulation of naturally random processes. The name was coined by John Von Newumann and Stanislaw Ulam at the Los Alamos Scientific Laboratory during the Manhattan Project. It refers to the well known casino in Monaco and was the code-name for the secret project carried out during the development of the nuclear bomb [172].

---

[4]Dividing one cell by two creates a new element, i.e. $2 * N$ new terms in the matrix (one new column and row) where N is the number of original elements.

The general idea behind the Monte Carlo approach is to use statistical analysis to calculate the evolution of a system from its response to a random sampling of possible inputs. This approach avoids to test all possible inputs systematically, and gives the most probable evolution at a reduced cost.

In the present case of the resolution of the RTE, for a given local absorption coefficient, local temperature and boundary temperature, random samples are generated for a random beam direction, frequency and point of emission following a prescribed pdf. The system response, i.e. the beam absorption or scattering, constitutes one realization.

Convergence is obtained when first and second order statistics are not modified by further realizations. Computational time can be saved by an optimal shape of the pdf.

Monte Carlo methods are very accurate but still computationally restrictive. However, recent techniques for parallel computing have shown promising improvements (see for example Zhang et al. [278] and Roger et al. [216]). Monte Carlo methods are particularly appreciated in the study of anisotropic diffusion of radiation.

Differential methods

Here the differential form of the RTE is solved by using an approximation of the incident intensity. Differential methods are the most commonly used techniques in complex industrial applications due to the good ratio between restitution time and accuracy. Some similarities with CFD numerics make them particularly attractive to combustionists.

- **Flux methods**

  As shown before, the radiation intensity $I_{\tilde{v}}(\mathbf{r}, \mathbf{s})$ depends on the location $\mathbf{r}$, the direction of propagation $\mathbf{s}$ and the wavelength $\tilde{v}$. The angular dependence of the intensity the most complex part to evaluate. One idea is to separate the angular and the spatial dependencies in order to simplify the equations to solve. If the intensity is considered invariant over a certain interval of solid angle, the integro-differential RTE can be reduced to a series of coupled linear differential equations.

  Varying the number of intervals leads to different kinds of flux methods, such as two-flux (the pioneering works of Schuster in 1905 and Schwarzchild in 1906 are presented in [37]), four-flux [4] or six-flux methods [192]. As the number of solid angle intervals increase, the accuracy of the method increases as well.

  The simplicity of the final governing equations make it easy to develop numerical methods. A good number of such models were developed for one-dimensional problems (mostly atmospheric radiation problems) but not all of them are suited to combustion problems in complex geometries [263, 91].

One particular method, often classified within the flux methods, is the Discrete Ordinates Method (DOM), which is based on finite volume discretization of the domain and an angular discretization of space. This method is the one chosen in the present work for the integration of the RTE on the complex geometries of industrial combustion systems. A detailed explanation of the DOM is presented in section 6.6.

- **Spherical harmonics approximation P_N.**

This approximation was first introduced by Jeans [115]. The principle of this method is to construct the intensity $I(\mathbf{r}, \mathbf{s})$ as a generalized Fourier series by splitting the angular and the spatial dependencies into two terms:

$$I(\mathbf{r}, \mathbf{s}) = \sum_{l=0}^{\infty} \sum_{m=0}^{l} L_l^m(\mathbf{r}) Y_l^m(\mathbf{s}) \tag{6.83}$$

where $Y_l^m(\mathbf{s})$ are the associated spherical harmonics:

$$Y_l^m(\mathbf{s}) = (-1)^{(m+|m|)/2} \left(\frac{(l-|m|)!}{(l+|m|)!} \right)^{\frac{1}{2}} e^{im\phi} P_l^{|m|} \cos\theta \tag{6.84}$$

where θ and ϕ are the polar and azimuthal coordinates of the vector $\mathbf{s}$ and P_l is a Legendre polynomial. For $l < N$ a set of $N+1$ first order differential equations is obtained, which need $N+1$ boundary conditions to be solved.

Odd values for N are commonly used. The P_1 method is known as the simplest and the fastest method. In such case, RTE is reduced to a local differential form dependent only on the closest nodes (similar to a diffusion operator in a CFD code). This approximation is accurate only when the medium is optically thick where the radiative intensity depends only on the volume directly surrounding the point. For these reasons the method is also known as the diffusion approximation [177].

Increments in the order of the method rapidly rises the restitution time and the complexity of the calculation (an increasingly bigger stencil is required). At higher orders neither the velocity nor the accuracy of the method are attractive [263].

6.6   The code PRISSMA

The acronym PRISSMA stands for Parallel RadIative Solver with Spectral integration on Multicomponent mediA. It is jointly developed by EMAC and CERFACS for the calculation of radiation in complex unsteady combustion applications. It is based on the DOM, and uses different spectral models.

6.6.1 DOM on unstructured meshes

Angular discretization

In differential methods the angular integration of the RTE is performed over a discrete number of directions. In DOM such integration is approximated by a numerical quadrature[5], for any quantity $f(\mathbf{s})$, we write [37]:

$$\int_{4\pi} f(\mathbf{s})d\Omega \simeq \sum_{i=1}^{N_{dir}} \omega_i^d f(\mathbf{s}_i) \tag{6.85}$$

where N_{dir} is the discrete number of directions, and ω_i^d is the directional quadrature weight associated to the direction.

Different angular quadratures exist in the litterature (Carlson [34], Fiveland [81] and Truelove [258]). Known angular quadratures include the S_N approximation (where $N_{dir} = N(N+2)$, see Fig. 6.17), the T_N quadrature ($N_{dir} = N^2$), the LC_{11} quadrature ($N_{dir} = 96$) and the polar/azimuthal quadratures. Different authors have studied the influence of the angular discretization: Koch and Becker [136] made a detailed comparison of the different quadrature methods showing that the more accurate results are obtained with the LC_{11} quadrature. Kayakol et al. studied the influence of the order of the S_N quadrature in gas turbine applications showing that the S_4 quadrature predicts good values of wall heat fluxes [130], Jensen et al. [117] and Joseph et al. [122] showed that the accuracy of the LC_{11} approaches the results obtained with a Monte Carlo code for turbulent flame configurations.

Spatial discretization

In the present work the spatial discretization is based on the finite volume approach using the methodology developped by Joseph [121].

Although particules like ashes, soot and droplets can cause scattering and diffusion of photons, their size is smaller than the wavelengths thus in combustion applications scattering effects are neglected. This allows to write the RTE in the following form:

$$\frac{dI_{\tilde{\nu}}}{ds} = \kappa_{\tilde{\nu}}(I_{b\tilde{\nu}} - I_{\tilde{\nu}}(\mathbf{s})) \tag{6.86}$$

which represents the radiative intensity variation in the direction $\mathbf{s}$. Integrating over a small control volume V (delimited by the surface A) leads to:

$$\int_A I_{\tilde{\nu}}\mathbf{s}\cdot\mathbf{n}dA = \int_V \kappa_{\tilde{\nu}}(I_{b\tilde{\nu}} - I_{\tilde{\nu}}(\mathbf{s}))dV \tag{6.87}$$

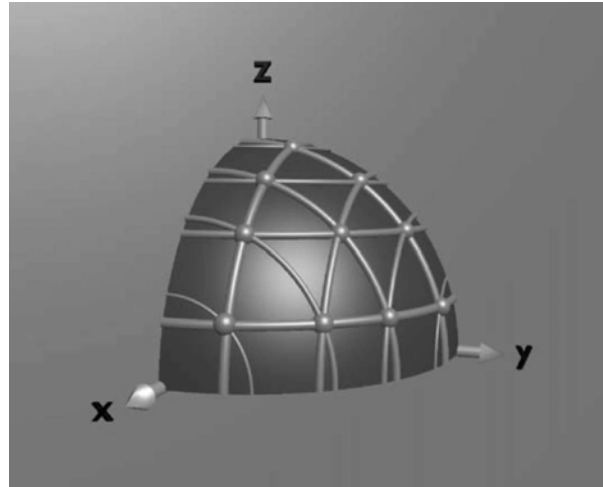[5]Not to be confused with the *spectral* quadrature eq. (6.121)

Figure 6.17: S_8 quadrature, from Koch and Becker [136]: one quadrant is decomposed over 10 directions (i.e. a total of 80 directions), indicated by the small spheres on the surface.

where the Gauss–Ostrogradsky theorem was used in the Left-Hand-Side (LHS). In the finite volume approach, this integral is approximated by a sum over the faces of the structured or unstructured cell. In the case of a tetrahedral discretization , the sum is done over $N_f = 4$ faces.

Consider a cell with N_f faces noted j each one with a surface area A_j, the mean radiation intensity at each face, $I_{\tilde{\nu},j}$, is defined as:

$$I_{\tilde{\nu},j} = \frac{1}{A_j} \int_{A_j} I_{\tilde{\nu}}(\mathbf{s}) dA_j \tag{6.88}$$

Similarly, the average irradiation $I_{\tilde{\nu},P}$ and the emitted intensity $I_{b\tilde{\nu},P}$ can be defined at the center, P, of the control volume V:

$$I_{\tilde{\nu},P} = \frac{1}{V} \int_V I_{\tilde{\nu}}(\mathbf{s}) dV \tag{6.89}$$

$$I_{b\tilde{\nu},P} = \frac{1}{V} \int_V I_{b\tilde{\nu}}(\mathbf{s}) dV \tag{6.90}$$

If the control volume is small enough, the intensities $I_{\tilde{\nu}}$ and $I_{b\tilde{\nu}}$ can be considered constant. Eq. (6.87) can then be written in the discrete form:

$$\sum_{j=1}^{N_f} I_{\tilde{\nu},j}(\mathbf{s})(\mathbf{s}\cdot\mathbf{n}_j)A_j = \kappa_{\tilde{\nu}}(I_{b\tilde{\nu},P} - I_{\tilde{\nu},P}(\mathbf{s}))V \tag{6.91}$$

where $\mathbf{n}_j$ is the unity normal vector of face j pointing outwards. The projection of this normal on the beam direction $D_j = \mathbf{n}_j \cdot \mathbf{s}$ permits to detect if radiation enters ($D_j < 0$) or exits ($D_j > 0$) the cell through face j.

Eq. (6.91) can be solved with the exponential scheme proposed by Sakami [225, 226] or the mean flux scheme proposed by Ströle et al. [247]. This last method has been shown to be well suited for unstructured meshes [121, 204], and is used here.

In the mean flux scheme, the mean value of the irradiance in the volume is written as the weighted budget between the incident and the out-going intensities:

$$I_{\tilde{\nu},P} = \alpha\overline{I_{\tilde{\nu},out}} + (1-\alpha)\overline{I_{\tilde{\nu},in}} \tag{6.92}$$

where α is the weighting factor and $\overline{I_{\tilde{\nu},in}}$ and $\overline{I_{\tilde{\nu},out}}$ are the surface averaged intensities at all the entry and all the exit faces of the control volume:

$$\overline{I_{\tilde{\nu},in}} = \frac{\sum_{j|D_j<0} D_j A_j I_{\tilde{\nu},j}}{\sum_{j|D_j<0} D_j A_j} \tag{6.93}$$

$$\overline{I_{\tilde{\nu},out}} = \frac{\sum_{j|D_j>0} D_j A_j I_{\tilde{\nu},j}}{\sum_{j|D_j>0} D_j A_j} \tag{6.94}$$

In this expressions the product $D_j A_j$ corresponds to the area of the projection of surface j on a plane perpendicular to the evaluation direction $\mathbf{s}$ (Fig. 6.18). By definition:

$$\sum_{j|D_j>0} D_j A_j = -\sum_{j|D_j<0} D_j A_j = A_\Delta \tag{6.95}$$

where A_Δ represents the area of the projection of all the in (or all the out) surfaces on a plane perpendicular to $\mathbf{s}$. With these expressions eq. (6.92) becomes:

$$I_{\tilde{\nu},P} = \frac{\alpha\sum_{j|D_j>0} D_j A_j I_{\tilde{\nu},j} - (1-\alpha)\sum_{j|D_j<0} D_j A_j I_{\tilde{\nu},j}}{A_\Delta} \tag{6.96}$$

factoring by α gives:

$$I_{\tilde{\nu},P} = \frac{\alpha\sum_{j=1}^{N_f} D_j A_j I_{\tilde{\nu},j} - \sum_{j|D_j<0} D_j A_j I_{\tilde{\nu},j}}{A_\Delta} \tag{6.97}$$
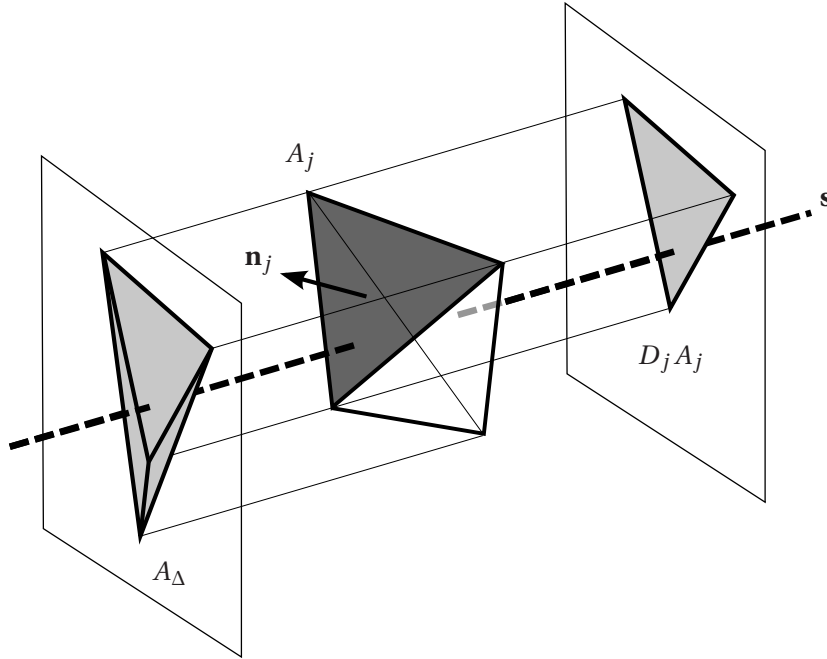
Figure 6.18: Projection of face j, $D_j A_j$, and projection of the whole entry (or exit) faces A_Δ.

where the term $\sum_{j=1}^{N_f} D_j A_j I_{\tilde{v},j}$ can be replaced using eq. (6.91):

$$I_{\tilde{v},P} = \frac{\alpha V \kappa_{\tilde{v}} (I_{b\tilde{v},P} - I_{\tilde{v},P}) - \sum_{j|D_j<0} D_j A_j I_{\tilde{v},j}}{A_\Delta} \tag{6.98}$$

developing this expression:

$$A_\Delta I_{\tilde{v},P} + \alpha V \kappa_{\tilde{v}} I_{\tilde{v},P} = \alpha V \kappa_{\tilde{v}} I_{b\tilde{v},P} - \sum_{j|D_j<0} D_j A_j I_{\tilde{v},j} \tag{6.99}$$

which leads to:

$$I_{\tilde{v},P} = \frac{\alpha V \kappa_{\tilde{v}} I_{b\tilde{v}} - \sum_{j|D_j<0} D_j A_j I_{\tilde{v},j}}{\alpha \kappa_{\tilde{v}} V + A_\Delta} \tag{6.100}$$

In the mean flux scheme approximation the radiative intensity at each one of the exit faces is not explicitly calculated: the mean exit intensity $\overline{I_{\tilde{v},out}}$ is applied to each one of them. Knowing the value of the intensities at each entry face, $I_{\tilde{v},P}$ is calculated using Eq. (6.100). The mean exit intensity is obtained from eq. (6.92):

$$\overline{I_{\tilde{v},out}} = \frac{I_{\tilde{v},P} - (1-\alpha)\overline{I_{\tilde{v},in}}}{\alpha} \tag{6.101}$$

When $\alpha = 1$ the spatial discretization is called the Step Scheme. For the case where $\alpha = 0.5$ the discretization is called the Diamond Mean Flux Scheme (DMFS), and is considered the best choice for applications on unstructured meshes on irregular geometries [121].

6.6.2 Cell sweep procedure

As shown in the previous section, the mean radiative intensity of a control volume (mesh cell) and its exit faces is calculated from the intensities at the entry faces. Therefore the resolution algorithm must start with an initial guess for the entry intensities, followed by the propagation of information from the entry to the exit faces and finally an iterative procedure in order to converge to a solution. This procedure however is computationally very expensive. Recognizing that entry intensities are known at boundaries, for a given direction $\mathbf{s}_i$, the first treated cells are those located at this limit (see Fig. 6.19). Then, the calculated the outgoing intensities are transmitted to the adjacent cells which in turn can be solved and allow the calculation of another cell row. The algorithm continues until it reaches the opposite boundary [121]. This approach represents an efficient sequential algorithm.
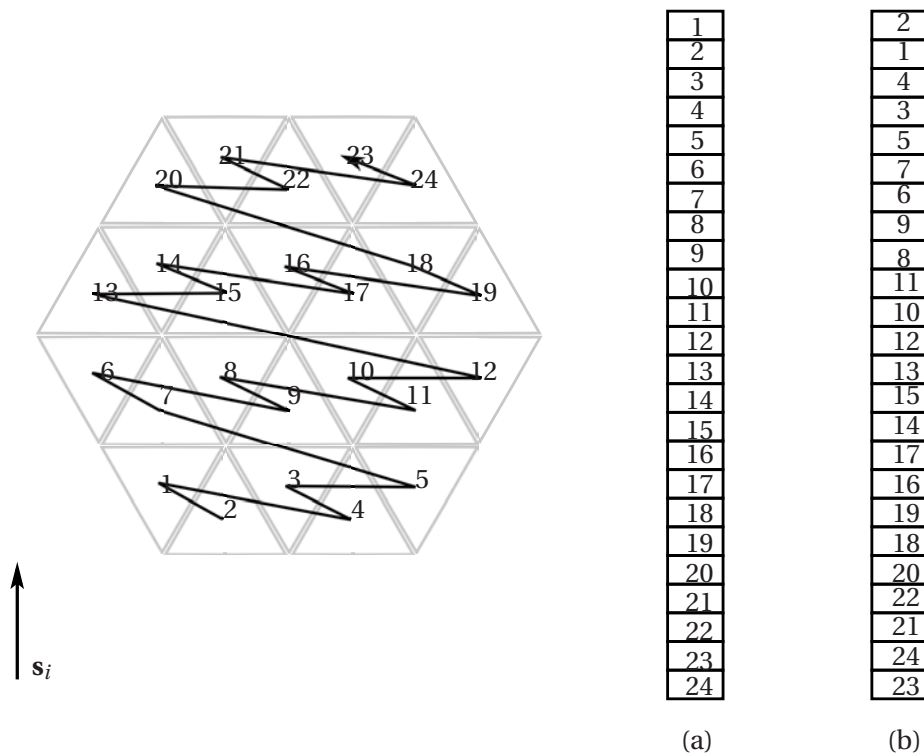

Figure 6.19: Cell sweeping in the direction $\mathbf{s}_i$: (a) original mesh order, (b) *pathway* along the direction $\mathbf{s}_i$: mesh order after the sweeping procedure.

For each direction a *pathway* is written, which needs to be calculated only once for a given mesh and a given quadrature. A software that calculates these pathways has been developed. It is based on a linked-list data structure, and has been included in the PRISSMA project as a pre-processing tool that can be used on a variety of mesh formats.

Figure 6.20 shows the calculation time of the pathways for meshes with different number of cells obtained in one Power5+ processor at a clock-rate of 1.5GHz. As expected, the preprocessing of hexahedral meshes takes longer than tetrahedral meshes. The time difference is estimated to a factor $t_{\text{tetra}}/t_{\text{hexa}} \approx 1.25$.

Figure 6.21 shows the influence of the angular quadrature on the construction time of the pathways in a tetrahedral mesh with one million cells. The almost linear evolution is only broken at the passage between the S_8 (80 directions) and the LC_{11} (90 directions) quadratures.
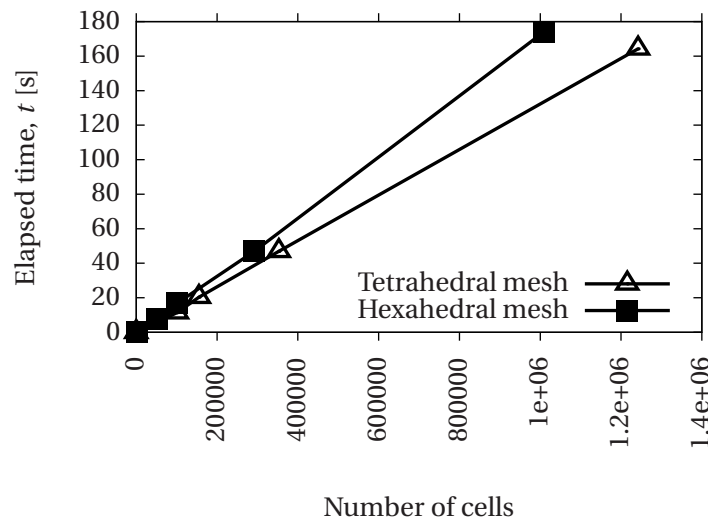

Figure 6.20: Total computational time for the sweeping algorithm. Tetrahedral elements are composed of only 4 faces which produces a slight improvement in the algorithm performance.

6.6.3 Spectral models

In the present section a closer examination of the spectral models implemented in the code PRISSMA is presented. The models are exposed in a descending order of complexity and accuracy.
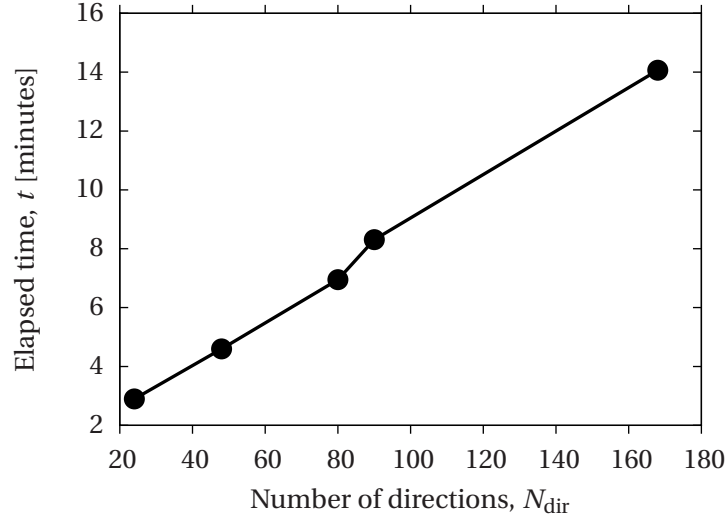
Figure 6.21: Sweeping algorithm. Computational time on a tetrahedral mesh with 1M cells for different angular quadratures: S_4 (24 directions), S_6 (48 directions), S_8 (80 directions), LC_{11} (96 directions) and S_{12} (168 directions).

Spectral Narrow Band Correlated-k model

The Spectral Narrow Band correlated-k (SNBcK) model is the most complex method implemented in PRISSMA, and is the second most accurate method available after the LBL method. This model is built around the SNB hypothesis and the correlated-k approach. In the SNB hypothesis the evolution of the Planck function in the spectral interval or band $\Delta\tilde{v} = \tilde{v}_b - \tilde{v}_b$ is considered linear:

$$\Delta\tilde{v}\frac{I_{b\tilde{v}_a} + I_{b\tilde{v}_b}}{2} = I_{b\tilde{v}} = \text{constant} \tag{6.102}$$

The model is then constructed in three steps: firstly the line distribution and their intensities in the narrow band are defined, secondly a mathematic representation of the line intensity distribution in the band is introduced (k-distribution), and finally a reorganization of the obtained profiles is carried out using the correlated k method:

1. **Line distribution in the narrow band**

   The monochromatic absorption for a homogeneous path of length l is given by $\alpha_{\tilde{v}}(l) = 1 - e^{\kappa_{\tilde{v}}l}$. However, in section 6.4.3 it was shown that absorption takes place in a finite region around $\tilde{v}$ (line broadening). The integral of the absorption over the broadened line is called the equivalent width and is given by:

$$W(l) = \int_{-\infty}^{\infty} \left(1 - e^{-\kappa_{\tilde{\nu}} l}\right) d\tilde{\nu} \tag{6.103}$$

The dimensionless average absoption of the shape is defined as:

$$A(l) = \frac{W(l)}{\delta} \tag{6.104}$$

where δ is the spacing between two spectral lines.

Fig. 6.14 shows that many different Lorentz shapes are present in a narrow band, which in the SNB approach are treated as a group. In a band containing N lines with a mean spacing of $\overline{\delta}$, the band width is $\Delta\tilde{\nu} = N\overline{\delta}$, the total absorption of all the lines is $\sum_{i=1}^{N} W_i(l)$ and the mean absorption is [90]:

$$\overline{A}(l) = \frac{1}{\overline{\delta}} \underbrace{\frac{1}{N} \sum_{i=1}^{N} W_i(l)}_{\overline{W}} = \frac{\overline{W}}{\overline{\delta}} \tag{6.105}$$

If the number of lines in the band tend to infinity $N \to \infty$ the mean equivalent width of the band can be written as an integral. However, the values of $W_{i|[i=1;\infty]}$ are unknown, and a statistical approach is preferred. Considering $p(S)dS$ as the fraction of lines having intensities between S and $S + dS$ (Fig. 6.22), the mean equivalent width of the narrow band can be expressed in terms of the distribution function:

$$\overline{W}(l) = \int_{0}^{\infty} \underbrace{\left[\int_{-\infty}^{\infty} \alpha_{\tilde{\nu}} d\tilde{\nu}\right]}_{W(l)} p(S)dS = \int_{0}^{\infty} \underbrace{\left[\int_{-\infty}^{\infty} 1 - e^{-\kappa_{\tilde{\nu}} l} d\tilde{\nu}\right]}_{W(l)} p(S)dS \tag{6.106}$$

The form of $p(S)$ depends on the line distribution over the narrow band. Figure 6.22 shows the two most used models: (a) in the Elsasser approach [72] lines are equally spaced and have the same intensities, (b) whereas in the statistical model the spectral lines have random strengths and are randomly distributed across the narrow band. The best known of the statistical approaches is the Malkmus model:

$$p(S) = \frac{1}{S} \exp\left(-\frac{S}{\overline{S}}\right) \tag{6.107}$$

where the mean line intensity is given by:

$$\overline{S} = \int_{0}^{\infty} S p(S) dS \tag{6.108}$$

The transmitivity of the narrow band $\overline{\tau_{\Delta\tilde{\nu}}}(l)$ is given by [90, 89]:
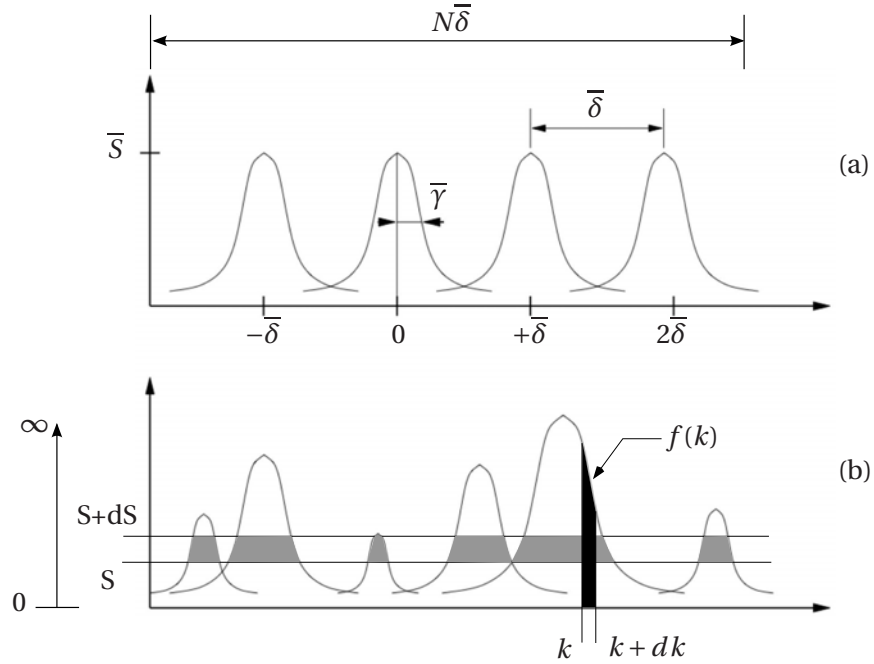
Figure 6.22: Band line distribution models: (a) Elsasser model using equally spaced Lorentz lines of equal mean intensity, (b) statistical model.

$$\overline{\tau_{\Delta\tilde{\nu}}}(l) = \exp\left(-\frac{\overline{W}}{\overline{\delta}}\right) \tag{6.109}$$

Introducing the Lorentz profile eq. (6.78) into eq. (6.106) the value of $\overline{W}$ is obtained [183], and the transmitivity of the gas is:

$$\overline{\tau_{\Delta\tilde{\nu}}}(l) = \exp\left[\phi_{\Delta\tilde{\nu}}\left(1 - \left(1 + \frac{2\overline{\kappa}_{\Delta\tilde{\nu}}l}{\phi_{\Delta\tilde{\nu}}}\right)^{1/2}\right)\right] \tag{6.110}$$

where $\phi_{\Delta\tilde{\nu}} = 2\overline{\gamma}/\overline{\delta}$ is the line shape parameter, $\overline{\gamma}$ is the average of the Lorentz lines half-width b_L given by Eq. (6.79) [243, 236, 90] and $\overline{\kappa_{\Delta\nu}}$ is the mean absorption coefficient in the narrow band, defined as:

$$\frac{1}{\Delta\tilde{\nu}}\int_{\Delta\tilde{\nu}}\kappa_{\tilde{\nu}}d\tilde{\nu} = \overline{\kappa_{\Delta\tilde{\nu}}} \equiv \frac{\overline{S}}{\overline{\delta}} \tag{6.111}$$

This gives the mean values of the spectral properties of the whole band $\Delta\tilde{\nu}$ without having to keep a record of each one of the lines in the band.

2. **Band representation (k-distribution)**

In a narrow band $\Delta\tilde{\nu}$, transmission is a quantity that can be calculated independently from the position of the absorption absorption lines. It is sufficient to know what fraction of the spectrum, $f(k)dk$ (Fig. 6.22-b), is occupied by the absorption coefficients between k and $k+dk$ [90, 62] in order to construct the mean transmitivity of the band $\overline{\tau_{\Delta\tilde{\nu}}}(l)$ along a path of length l:

$$\overline{\tau_{\Delta\tilde{\nu}}}(l) = \frac{1}{\Delta\tilde{\nu}} \int_{\Delta\tilde{\nu}} e^{-\kappa_{\tilde{\nu}}l} d\tilde{\nu} \tag{6.112}$$

which can be alternatively written[6]:

$$\overline{\tau_{\Delta\tilde{\nu}}}(l) = \int_0^\infty e^{-kl} f(k)dk \tag{6.113}$$

which is called the k-distribution approach. The function $f(k)$ is a probability density function (pdf) that gives the probability of finding the wavelength k in the spectrum of a given gas. The form of this function is unknown, however eq. (6.113) shows that by definition:

$$\overline{\tau_{\Delta\tilde{\nu}}}(l) = \mathscr{L}\{f(k)\} \tag{6.114}$$

thus the pdf can be expressed as the inverse Laplace transform of the transmitivity:

$$f(k) = \mathscr{L}^{-1}\{\overline{\tau}_{\Delta\tilde{\nu}}(l)\} \tag{6.115}$$

From this observation, and using the Malkmus model eq. (6.110), Domoto [62] proposed an analytical expression of the distribution of the absorption coefficients in a band, or k-distribution:

$$f(k) = \sqrt{\frac{\phi_{\Delta\tilde{\nu}}\overline{\kappa}_{\Delta\tilde{\nu}}}{2\pi k^3}} \exp\left[-\frac{\phi_{\Delta\tilde{\nu}}}{2} \frac{(k-\overline{\kappa}_{\Delta\tilde{\nu}})^2}{k\overline{\kappa}_{\Delta\tilde{\nu}}}\right] \tag{6.116}$$

which is a pdf of a Gaussian distribution (or Wald distribution).

3. **Band reordering (correlated k)**

Expression (6.116) is difficult to integrate as it rapidly fluctuates between consecutive values of k. It is then convenient to make use of the cumulative distribution function (cdf) of $f(k)$, called $g(k)$:

$$g(k) = \int_0^k f(k')dk' \tag{6.117}$$

where $g(k)$ is a smooth and monotonic function that can be easily integrated and can only take values in the range [0;1]. The cdf of the Gaussian distribution $f(k)$ is written:

---

[6]This pdf approach is similar to the pdf models in combustion (cf. section 5.2.2), where the mean of the reduced temperature can be written: $\overline{\Theta} = \int_0^1 \Theta' P(\Theta')d\Theta'$, with $P(\Theta')d\Theta' = \text{Probability}(\Theta' \leq \Theta < \Theta' + d\Theta')$ (For details see [203]).

$$g(k) = \frac{1}{2}\text{erfc}\left[\sqrt{\frac{\phi_{\Delta\tilde{v}}\overline{\kappa}_{\Delta\tilde{v}}}{2k}}\left(1 - \frac{k}{\overline{\kappa}_{\Delta\tilde{v}}}\right)\right] + \frac{1}{2}\exp(2\phi_{\Delta\tilde{v}})\text{erfc}\left[\sqrt{\frac{\phi_{\Delta\tilde{v}}\overline{\kappa}_{\Delta\tilde{v}}}{2k}}\left(1 + \frac{k}{\overline{\kappa}_{\Delta\tilde{v}}}\right)\right] \quad (6.118)$$

Figure 6.23 shows the profiles of $g(k)$ for four different values of the band shape factor $\phi_{\Delta\tilde{v}}$. For $\phi_{\Delta\tilde{v}} = 100$ the broadening of the different spectral lines cause an overlapping of lines (either the mean line half-width $\overline{\gamma}$ is big or the mean line spacing $\overline{\delta}$ is low) inducing an almost constant value of k in the narrow band. For low values of $\phi_{\Delta\tilde{v}}$ line broadening is weak and the value of k can vary in the $g(k)$ space.
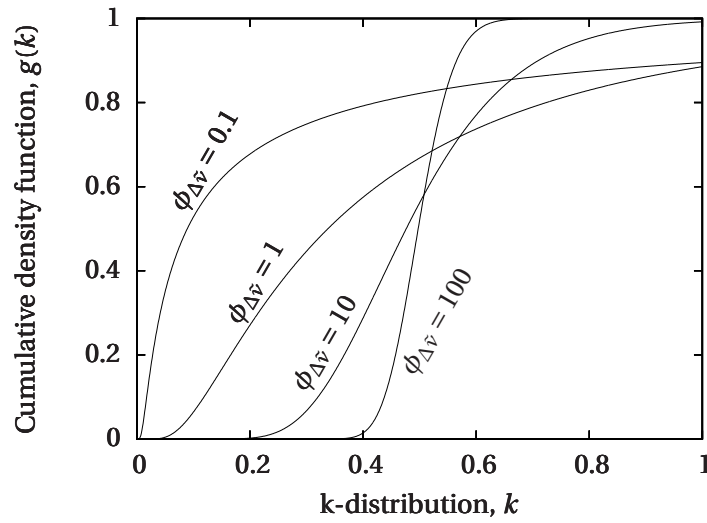

Figure 6.23: Form of the cumulative density function $g(k)$ for different values of the band shape factor $\phi_{\Delta\tilde{v}}$.

The value of the band mean transmitivity $\overline{\tau}_{\Delta\tilde{v}}(l)$ depends on the value of k. In order to obtain the spectral properties of the narrow band from the $g(k)$, the cdf must be numerically inverted into the function $k(g)$. The mean transmissivity is expressed as:

$$\overline{\tau}_{\Delta\tilde{v}}(l) = \frac{1}{\Delta\tilde{v}}\int_{\Delta\tilde{v}}e^{-\kappa_{\tilde{v}}l}d\tilde{v} = \int_0^1 e^{-k(g)l}f(k(g))dg \quad (6.119)$$

For any other quantity $F(\tilde{v})$, expression (6.119) can be generalized to obtain the average narrow band value $\overline{F}_{\Delta\tilde{v}}$:

$$\overline{F}_{\Delta\tilde{v}} = \frac{1}{\Delta\tilde{v}}\int_{\Delta\tilde{v}}F(\tilde{v})d\tilde{v} = \int_0^1 F(f(k(g)))dg \quad (6.120)$$

The main interest of using the inverted function $k(g)$ is to perform a straightforward numerical integration of (6.120) using the Gauss-Legendre method that can then be written:

$$\overline{F}_{\Delta\tilde{v}} = \int_0^1 F(f(k(g)))dg \approx \sum_{n=1}^{N_q} \omega_n F(k(g_n)) \tag{6.121}$$

where g_n and ω_n are respectively the quadrature points of the discrete integration and the associated weights.

- **The SNB database**

  In order to use the Malkmus model the SNB database elaborated by the EM2C laboratory [243] is used. The values of $\overline{\kappa}_{\Delta\tilde{v}}$ and the shape factor $\overline{\delta} = 2\overline{\gamma}/\phi_{\Delta\tilde{v}}$ are given for temperatures between 300K and 2900K (every 200K). The data incorporates information for three major species: H_2O, CO_2 and CO. Recently the SNB properties of CH_4 have been published [253] and can be easily incorporated in the calculation. Spectral properties for any other hydrocarbon fuels are inexistent. Such gases are considered as transparent[7]. The spectral data decomposition for each species is shown in Table 6.3.

Table 6.3: Spectral data for different species. Each narrow band length is $\Delta\tilde{v} = 25[\text{cm}^{-1}]$.

Species	Total number of narrow bands	Wavenumber range [cm^{-1}]
H_2O	367	150 - 2900
CO_2	96	450 - 1200
		1950 - 2450
		3300 - 3800
		4700 - 5225
CO	48	1750 - 2335
		3775 - 4350

The line broadening parameter $\overline{\gamma}$ (given in [cm^{-1}] in the database) is supposed identical for all bands. The authors of the SNB database propose a series of correlations to take into account the temperature (T), pressure (p) and composition (in molar fractions X_k) dependency:

$$\overline{\gamma}_{H_2O} = 0.066p\left(\frac{T}{296}\right)\left(7\left(\frac{T}{296}\right)X_{H_2O} + 1.2(X_{H_2O} + X_{N_2}) + 1.5X_{CO_2}\right) \tag{6.122}$$

$$\overline{\gamma}_{CO_2}|_{T<900} = T\left(\frac{T}{296}\right)^{0.7}\left(0.07X_{CO_2} + 0.058X_{N_2} + 0.015X_{H_2O}\right) \tag{6.123}$$

$$\overline{\gamma}_{CO_2}|_{T\geq900} = 0.45913T\sqrt{\frac{T}{900}}\left(0.07X_{CO_2} + 0.058X_{N_2} + 0.015X_{H_2O}\right) \tag{6.124}$$

$$\overline{\gamma}_{CO} = p\sqrt{\frac{T}{296}}\left(0.07X_{CO_2} + 0.06(X_{CO} + X_{H_2O} + X_{N_2})\right) \tag{6.125}$$

---

[7]This however is not precisely the case of hydrocarbons composed of long carbonated chains.

- **Spectral domain**

  In fig. 6.24 the spectral domain covered by the radiation data is presented. The light gray zone represents the computational domain of PRISSMA that covers all the wavelengths from 150 [cm^{-1}] to 9300 [cm^{-1}]. Note that the visible zone of the spectrum is not covered.
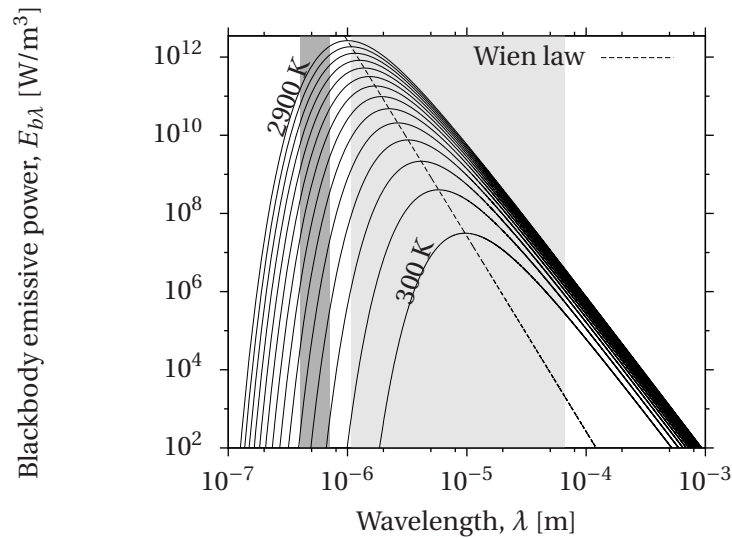

Figure 6.24: Logarithmic plot of the blackbody emissive power for temperatures ranging from 300K to 2900K. The dark gray area corresponds to the visible spectrum. The light gray area correspond to the infrared spectrum solved by the code PRISSMA.

  It can be seen as well that the maximum emitted energy is well captured for a wide range of temperatures between 300K and 2900K. High frequencies (low wavelengths) do not bring a considerable amount of energy (note the logarithmic scale of Fig. 6.24). In Fig. 6.25, the same profiles are plotted using a linear scale in the abscissa. Notice that most of the energy neglected in the present radiative calculation comes from the lower frequencies. This however does not affect the radiative behavior of the modeled gases, as their absorption coefficients are almost null outside the considered spectral domain. The impact will concern mainly walls and soot which radiate at such low frequencies.

  The total energy reconstructed from the considered spectral interval covers 98,55% of the total black-body radiation at $T = 300$K, but only 96,93% for $T = 1600$K and 70% for $T = 2900$K. For this reason additional bands have been added to the code in order to cover blackbody radiation up to $\tilde{\nu} = 20000$ [cm^{-1}], unnecessary for gas emission and absorption but useful for soot and solid walls radiation.

- **Spectral properties of a mixture**

  To take into account multispecies mixtures different models have been proposed by Liu [156]. In PRISSMA the mean absorption coefficient and the shape parameters for a mixture of N species is given by [121, 243]:
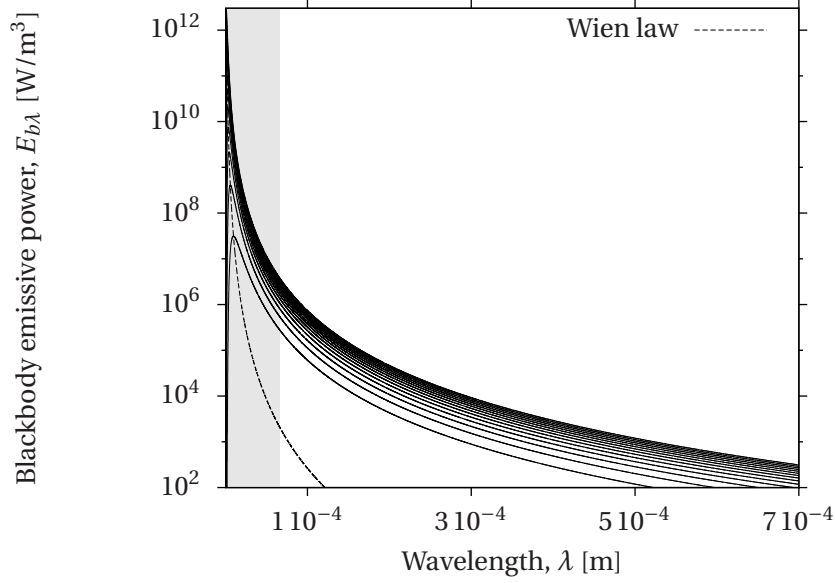
Figure 6.25: Linear plot of the blackbody emissive power shown in fig6.24.

$$\overline{\kappa}_{mix,\Delta\tilde{v}} \quad = \quad \sum_{k=1}^{N} \overline{\kappa}_{k,\Delta\tilde{v}} \tag{6.126}$$

$$\frac{\overline{\kappa}^2_{mix,\Delta\tilde{v}}}{\phi_{mix,\Delta\tilde{v}}} \quad = \quad \sum_{k=1}^{N} \frac{\overline{\kappa}^2_{k,\Delta\tilde{v}}}{\phi_{k,\Delta\tilde{v}}} \tag{6.127}$$

- **SNBcK algorithm**

  The resolution procedure can be resumed as follows:

  1. From the SNB database, the values of $\overline{\delta}$ and $\overline{\kappa}_{\Delta\tilde{v}}$ are read for each narrow band.

  2. Depending on the gas composition, pressure and temperature, the narrow band averaged values of the absorption intensity and the line shape parameters are calculated.

  3. From the knowledge of $\overline{\kappa}_{mix,\Delta\tilde{v}}$ and $\phi_{mix,\Delta\tilde{v}}$, the function $g(k)$ is calculated. Using a dichotomy or a Newton method $g(k)$ is transformed in $k(g)$.

  4. A Gauss-Legendre quadrature is applied to obtain the integrals of the radiative quantities on the narrow band. An infinite number of quatrature points gives an exact description of the function ($k(g)$ would be properly described in such case). It has been observed that convergence is obtained for $N_q \approx 10$ points.

Full Spectrum - Spectral Narrow Band Correlated-k model

In order to accelerate the restitution time of a radiative solver, and to simplify the complexities due to the spectral distribution of the absorption coefficient, new techniques of spectral integration have been developed. In particular, they take advantage of the fact that in combustion applications only total quantities (integrated over the spectrum) are relevant. An example of such approach is the FS-SNBcK model, originally proposed by Liu et al. [155, 157] and further developed by Poitou et al. [205].

Given the property $F(\kappa_{\tilde{v}})$, a function of the absorption coefficient $\kappa_{\tilde{v}}$, $\widehat{F}_{\Delta\tilde{v}}$ is defined as the blackbody-weighted narrow band integral value of F over a spectral band $\Delta\tilde{v}$:

$$\widehat{F}_{\Delta\tilde{v}} = \int_{\Delta\tilde{v}} I_{b,\tilde{v}} F(\kappa_{\tilde{v}}) d\tilde{v} \tag{6.128}$$

If the interval $\Delta\tilde{v}$ is not too large the Planck function is equal to $I_{b,\Delta\tilde{v}}$:

$$\widehat{F}_{\Delta\tilde{v}} = I_{b,\Delta\tilde{v}} \int_{\Delta\tilde{v}} F(\kappa_{\tilde{v}}) d\tilde{v} = I_{b,\Delta\tilde{v}} \Delta\tilde{v} \overline{F_{\Delta\tilde{v}}} \tag{6.129}$$

where $\overline{F_{\Delta\tilde{v}}}$ represents the mean band value of F:

$$\overline{F_{\Delta\tilde{v}}} = \frac{1}{\Delta\tilde{v}} \int_{\Delta\tilde{v}} F(\kappa_{\tilde{v}}) d\tilde{v} \tag{6.130}$$

As seen in the previous section, the average value of a function F that only depends on the absorption coefficient, can be reordered using a k-distribution:

$$\overline{F_{\Delta\tilde{v}}} = \frac{1}{\Delta\tilde{v}} \int_{\Delta\tilde{v}} F(\kappa_{\tilde{v}}) d\tilde{v} = \int_0^\infty F(k) f(k) dk \tag{6.131}$$

Using a finite number of narrow bands N_B, an expression for the total (integrated over all the spectrum) value $\widehat{F}$ can be written:

$$\widehat{F} = \sum_{i=1}^{N_B} I_{\Delta\tilde{v}_i} \Delta\tilde{v}_i \overline{F_{\Delta\tilde{v}_i}} = \sum_{i=1}^{N_B} \Delta\tilde{v}_i I_{b,\Delta\tilde{v}_i} \int_0^\infty F(k) f_i(k) dk \tag{6.132}$$

where subscript i denotes the band number and $f_i(k)$ is the pdf on the i-th band. Variables $\tilde{v}_i$ and k are independent so the discrete integration on i and the integration on $\tilde{v}$ can be switched, leading to:

$$\widehat{F} = \int_0^\infty \left(\sum_{i=1}^{N_B} \Delta\tilde{v}_i I_{b,\Delta\tilde{v}_i} F(k) f_i(k) \right) dk \tag{6.133}$$

This expression may be rewritten as the *expectancy* of the function $F(k)$, if the corresponding probability density function is correctly defined. By definition the pdf must be normalized such as:

$$\int_0^\infty \sum_{i=1}^{N_B} \Delta\tilde{\nu}_i I_{b,\Delta\tilde{\nu}_i} f_i(k) dk = \sum_{i=1}^{N_B} \Delta\tilde{\nu}_i I_{b,\Delta\tilde{\nu}_i} \underbrace{\int_0^\infty f_i(k) dk}_{=\, 1,\, \text{by definition}} = \frac{\sigma T^4}{\pi} \tag{6.134}$$

So the integration over the spectrum may be expressed:

$$\widehat{F} = \frac{\sigma T^4}{\pi} \int_0^\infty \underbrace{\sum_{i=1}^{N_B} \frac{\Delta\tilde{\nu}_i I_{b,\Delta\tilde{\nu}_i} f_i(k)}{\sigma T^4/\pi}}_{f_{FS}(k)} F(k) dk \tag{6.135}$$

Where $f_{FS}(k)$ represents the *full spectrum normalized probability density function*, with a cdf:

$$\begin{aligned} g_{FS}(k) &= \int_0^k f_{FS}(k') dk' = \int_0^k \sum_{i=1}^{N_B} \frac{\Delta\tilde{\nu}_i I_{b,\Delta\tilde{\nu}_i} f_i(k')}{\sigma T^4/\pi} dk' \\ &= \sum_{i=1}^{N_B} \frac{\Delta\tilde{\nu}_i I_{b,\Delta\tilde{\nu}_i}}{\sigma T^4/\pi} \underbrace{\int_0^k f_i(k') dk'}_{g_i(k)} \end{aligned} \tag{6.136}$$

As each one of the cdf functions $g_i(k)$, g_{FS} is monotone and can be inverted in order to obtain $k(g_{FS})$. Eq.(6.135) becomes:

$$\widehat{F} = \frac{\sigma T^4}{\pi} \int_0^1 F(k(g_{FS})) dg_{FS} \tag{6.137}$$

where, as in the case of the narrow band model, a numerical integration can be carried out. Using a discrete quadrature with N_q points, eq.(6.137) can be written:

$$\widehat{F} \approx \frac{\sigma T^4}{\pi} \sum_{j=1}^{N_q} \omega_j F(k(g_{FS,j})) \tag{6.138}$$

It is only at this last step that the calculation of $\widehat{F}$ (over the entire spectrum) is approximated numerically, using a pseudo-spectral quadrature.

Tabualted FS-SNBcK model

A faster alternative to the FS-SNBcK model is to tabulate the model data before using the RTE solver. The computational power is then concentrated in the spatial integration of the RTE instead of the inversion of the function $g(k)$. An interpolator is however necessary to adjust the data to the specific simulation.

The development of a tabulated version of the FS-SNBcK model is done in two steps: first a table carrying the values of the absorption coefficient is constructed taking into account the dependency on each property of the flow (mainly temperature and molar fractions). Secondly, the tabulated values are loaded in the solver and an interpolation procedure is carried out.

In PRISSMA, the absoprtion coefficients are tabulated using four variables, namely: temperature and molar mass of H_2O, CO_2 and CO. In absence of shocks, the variations of pressure in a combustion process provokes a minimal variation of the absorption coefficient, so for the radiative problem the pressure can be considered constant.

For one set of parameters $(T(i), X_k(j)|k = 1..3)$, N_q quadrature values of the FS-SNBcK model are stored in a four-dimensional matrix. The temperature and molar fraction ranges are considered constant in steps of ΔT and $\Delta X_k|k = 1..3$. The total number of stored values in the matrix can be expressed as:

$$N_{\text{val}} = N_q \times \frac{T_{\max} - T_{\min}}{\Delta T} \times \prod_{k=1}^{3} \frac{X_{k,\max} - X_{k,\min}}{\Delta X_k} \tag{6.139}$$

A good selection of the maximum and minimum values and the discretization step would ensure a good quality in the resolution of the ETR by the solver. Compared with the FS-SNBcK model, the restitution time is improved in more than one order of magnitude, with a minimal loss in the quality of the results.

The linear interpolator used in PRISSMA to reconstruct the absorption coefficient uses the 16 closest vertex of the four-dimensional matrix to the point (T,X_k) of the simulation. This is expressed using:

$$\kappa(T, X_k) = \left(\sum_{i=1}^{16} \frac{d_i}{16} \right) \sum_{j=1}^{16} \frac{1}{d_j} \kappa_j \tag{6.140}$$

where d_j is the distance between (T,X_k) and the evaluation point j, and is given by:

$$d_j = \omega_T \sqrt{(T - T_j)^2} + \sum_{k=1}^{3} \omega_{X_k} \sqrt{(X_k - X_j)^2} \tag{6.141}$$

where ω_T and ω_{X_k} are the relative interpolation weights for each parameter. In the most general case the values taken for these weights are $\omega_T = 1$ and $\omega_{X_k} = \Delta T/\Delta X_k$.

A comprehensive analysis of this method has been performed and presented by Poitou [204].

Weighted Sum of Gray Gases

A simpler spectral model included in PRISSMA is the Weighted Sum of Gray Gases (WSGG) presented by Hottel and Sarofim in the 60's. In such model the spectral behavior of a mixture is derived from a weighted addition of a representative set of gray virtual gases. Hottel and Sarofim introduced the WSGG model [106]. Modest in turn presented a similar version of WSGG [175] and Soufiani performed a comprehensive analysis of the model [241].

In the WSGG method it is assumed that in a gray medium of length l the mean emissivity of the gas can be approximated by a weighted sum of the absorption coefficients of K "virtual" gray gases [236]:

$$\epsilon(T,l) \approx \sum_{k=0}^{K} a_k(T)(1 - e^{-\kappa_k l p_a}) \tag{6.142}$$

where the coefficients κ_k and a_k are the fitting parameters of the model and p_a is the partial pressure of the predominant absorbing species (usually H_2O). The dependence of the coefficient a_k versus the temperature is adjusted by using a fifth-order polynomial:

$$a_k(T) = \sum_{j=0}^{5} \alpha_{kj} T^j \tag{6.143}$$

Values for κ_k and a_k are given by Soufiani and Djavdan [241] and reproduced in Table 6.4.

Table 6.4: WSGG parameters κ_k [m^{-1} atm^{-1}] and α_k

k	κ_k	α_{k0}	α_{k1}	α_{k2}	α_{k3}	α_{k4}	α_{k5}
1	1.2531	1.6879d-1	2.5682d-4	9.5161d-8	-3.166d-10	1.4834d-13	-2.156d-17
2	8.4258	4.9577d-2	9.3954d-4	-1.6416d-6	1.1478d-9	-3.76d-13	4.7503d-17
3	87.064	2.789d-1	-5.1265d-4	6.732d-7	-5.1488d-10	1.8887d-13	-2.5856d-17

The main limitation of such a model comes from the fact that the fitting parameters strongly depend on the mixture, and in particular on the H_2O concentration. WSGG models usually under-predicts the radiative intensity in combustion.

Note that the FS-SNBcK model presented in the previous section is very similar to the WSGG model. The difference comes from the construction of the "gray gases": in the first case spectral data is constructed from the gas properties and the SNB database, whereas in the second case radiative gas properties are obtained by curve fitting against known experimental data.

Gray gas models: mean absorption coefficients

As shown in eq. (6.65), when the gas absorption coefficient is constant the ETR can be reduced to a simple expression, where only the irradiance term must be integrated over all the directions. This is the case in the gray gas model, with the absorption coefficient κ is considered constant over all the spectrum. This however leads to inaccurate predictions of the radiative heat fluxes, and is particularly inaccurate in combustion applications.

Gray gas computations are still useful to make fast predictions of orders of magnitudes involved in the system. Two methods are commonly employed: the first one uses a constant value which is equally applied to all points of the domain, and the second uses a polynomial correlation to acknowledge variations with respect to the local temperature, pressure and gas mixture. Eq. (6.144) shows the polynomial expression used to calculate the absorption coefficient of species k. Table 6.5 summarizes the polynomial coefficients.

$$\overline{\kappa}_k = C_0 + C_1 \left(\frac{1000}{T}\right) + C_2 \left(\frac{1000}{T}\right)^2 + C_3 \left(\frac{1000}{T}\right)^3 + C_4 \left(\frac{1000}{T}\right)^4 \tag{6.144}$$

Table 6.5: Polynomial coefficients of $\overline{\kappa}_k$ for different gases.

Species	C_0	C_1	C_2	C_3	C_4	C_5
H_2O	$-2.3093\,10^{-1}$	-1.1239	9.4153	-2.9988	$5.1382\,10^{-1}$	$-1.8684\,10^{-5}$
CO_2	18.741	-121.31	273.5	-194.05	56.31	$-5,8169$
$CO\,(T < 750)$	4.7869	$-6.953\,10^{-2}$	$2.95775\,10^{-4}$	$-4.25732\,10^{-7}$	$2.02894\,10^{-10}$	
$CO\,(T > 750)$	10.09	$-1.183\,10^{-2}$	$4.7753\,10^{-6}$	$-5.87209\,10^{-10}$	$-2.5334\,10^{-14}$	
CH_4	6.6334	3568.6	$1.6682\,10^{-8}$	$2.5611\,10^{-10}$	$2.6558\,10^{-14}$	

Alternatively, Gore et al. [92] presented a different curve-fitting polynomial eq. (6.145) using the coefficients shown in Table 6.6.

$$\overline{\kappa}_{G,k} = \exp\left(C_0 + C_1 \ln T + C_2 \ln^2 T + C_3 \ln^3 T + C_4 \ln^4 T\right) \tag{6.145}$$

Table 6.6: Coefficients used to calculate the eq.(6.145) for different gases.

Species	C_0	C_1	C_2	C_3	C_4
H_2O	278.713	-153.24	32.1971	-3.0087	0.104055
CO_2	969.86	-588.38	132.89	-13.182	0.48396

The total absorption coefficient of a mixture can be calculated from this correlations using expression (6.146), where both the pressure p and mixture dependencies are included:

$$\overline{\kappa}_{\text{mix}} = p \sum_{k=1}^{N} X_k \overline{\kappa}_k \qquad (6.146)$$

Using a gray gas model, the radiative source term is simply calculated using as:

$$\mathscr{S}_r = 4\sigma (T^4 - T_{\text{ref}}^4)\overline{\kappa} \qquad (6.147)$$

where T_{ref} is a reference temperature (usually the wall temperature is taken as reference).

This is the simplest method to include radiation effects in a CFD code [229]. It is called the thin gas approximation, because it only depends on the local properties and the temperature of the distant walls T_{ref} (as if there was no gas in between). Reabsorption is neglected in this approximation, as well as radiative heat flux to the solid walls. Energy losses obtained with the thin gas approximation can over or under-predict the real radiative heat losses, sometimes by several orders of magnitude.

The gray gas correlations can be checked using the spectral properties of the RTE solver. There are different ways to calculate a mean coefficient from the knowledge of the spectral properties [255]. Alternatives include the Rosseland mean coefficient $\overline{\kappa}_R$, the Planck internal mean coefficient $\overline{\kappa}_i$ [263], the Patch mean coefficient $\overline{\kappa}_e$ [193], the Ludwing mean absorption coefficient based on the narrow band model $\kappa_{t,n}$ and Planck's mean absorption coefficient. A detailed presentation of all these coefficients is given in Viskanta and Mengüç [263].

In the present work, only Planck's mean absorption coefficient is tested. This coefficient may be written as:

$$\overline{\kappa}_P = \frac{\int_0^\infty \kappa_{\tilde{\nu}} I_{b\tilde{\nu}} d\tilde{\nu}}{\int_0^\infty I_{b\tilde{\nu}} d\tilde{\nu}} = \frac{1}{\sigma T^4} \int_0^\infty \kappa_{\tilde{\nu}} I_{b\tilde{\nu}} d\tilde{\nu} \qquad (6.148)$$

Using the SNB database and the spectral integration presented in section 6.6.3, the mean Planck coefficient is compared to the polynomial approximation (eq. 6.144 and 6.145), to point out the differences between the polynomial approximations.

Figure 6.26 and 6.27 where obtained using a simple 1D solver of the integral RTE equation (6.56). The developed code allows to evaluate the spectral models against the accurate transitivity model of Malkmus (Eq. 6.110). In the figures mean Planck absorption coefficient and the polynomial approximations, for one species and for a multicomponent mixture, are compared. At low temperatures the polynomial approximations over-predict the gas mean absorption up to an error of 30% of the mean Planck coefficient. Figure 6.27 shows that the profile is not the same in both approximations at low temperatures, however, at high temperatures the polynomial approximation gets closer to the mean Planck absorption coefficient.
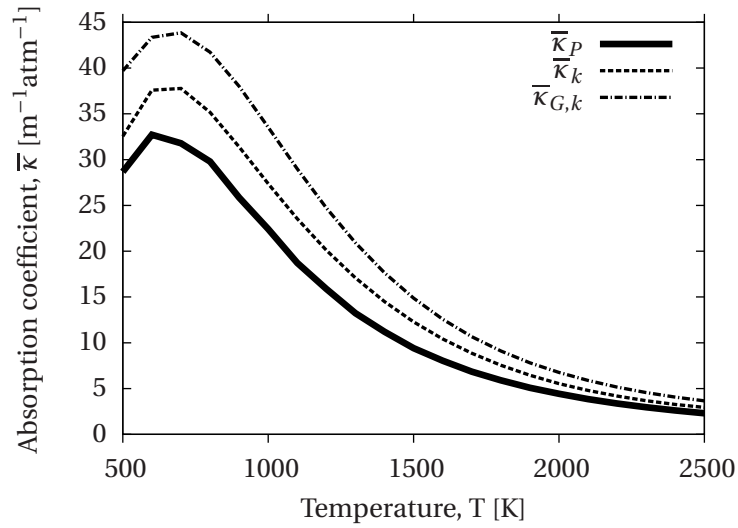
Figure 6.26: Evolution of the mean Planck absorption coefficient of CO_2 with the temperature, calculated from eq. 6.144, 6.145 and 6.148.

Radiative properties of soot particle clouds

Although soot might not be emitted in large amounts, it plays a key role in the flame structure in the zone where the particles are not yet re-oxidized. The most important impact of soot on a flame is to lower its temperature due to radiation emission.

Radiative properties of solid spherical particles can be derived both from empirical correlations and from the electromagnetic theory. However the complexity and heterogeneity of soot clouds in combustion systems makes it difficult to construct a general expression for soot radiative properties.

Soot radiation can be many times more important than gas radiation for two main reasons: firstly, at some frequencies emission levels are higher for the soot than for the gas and secondly emission takes place over the whole spectrum for soot particles, even in the frequencies where the gas does not emit any energy.

Experiments have shown that along an optical path incident radiation in a soot cloud attenuates following Bouguer's law [23]:

$$I_\lambda = I_\lambda(0) \exp\left(\int_0^L -\kappa_{\lambda,s}(x)dx\right) \tag{6.149}$$

It has also been shown from the Rayleigh limit of the Mie theory that for particles with a small size parameter ($x_p = \pi d_p/\lambda$), scattering is negligible compared to absorption, so that the extinction co-
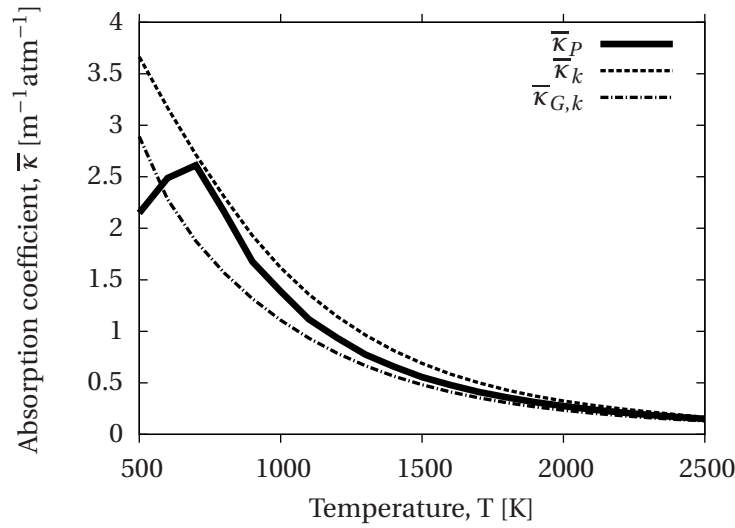
Figure 6.27: Evolution of the mean absorption coefficient with the temperature for the mixture: $X_{H_2O} = 0.1258587$, $X_{CO_2} = 0.01200788$, $X_{CO} = 0.242343442$, calculated from eq. 6.144, 6.145 and 6.148.
.

efficient can be assumed to be equal to the absorption coefficient [236].

The absorption coefficient, is described by empirical approximations such as in eq. (6.150), where k_s is a model constant and α an exponential factor. Some authors like Siegel and Howell [236] propose a generalization of the exponential factor with a dependence on the wavelength by using a polynomial expression for $\alpha = \alpha(\lambda)$, or a simple expression like $\alpha = c_1 + c_2 \ln \lambda$.

$$\kappa_{\lambda,s} = \frac{f_v k_s}{\lambda^\alpha} \tag{6.150}$$

Mean values of α have been proposed by Köylü and Faeth [140] for different hydrocarbon fuels. The values obtained by exponential measurements were around $\alpha = 0.83 \pm 0.08$ [140]. Figure 6.28 shows the evolution of the absorption coefficient against the wavenumber of a soot cloud suspended in a non radiating gas using the value of $\alpha = 0.83$. Table 6.7 shows the values of α for different fuels, valid only for the infrared region of the spectrum comprised between $\lambda \approx 0.514 \mu m$ and $\lambda \approx 5.2 \mu m$. In the visible region, for wavelengths comprised between $\lambda \approx 0.3 \mu m$ and $\lambda \approx 0.8 \mu m$, $\alpha = 1.39$.

Values for k_s in the visible and the infrared spectrum take values from 3.7 to 7.5 depending on the flame characteristics [235].

Outside the Rayleigh limit of the Mie theory, when the size parameter ($x_p = \pi d_p / \lambda$) is big enough, the electromagnetic expression of the absorption coefficient of soot can be used (Eq. 6.151), which depends on the particle's index of refraction n and extinction coefficient k:
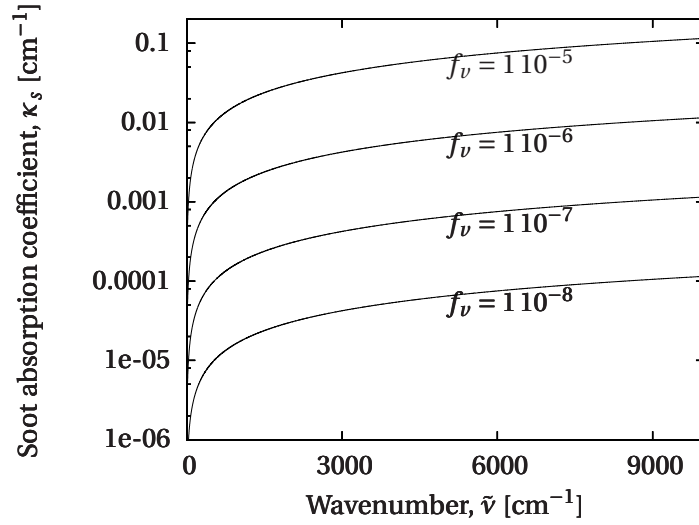
Figure 6.28: Soot absoprtion coefficient for different soot concentrations.

Table 6.7: Values of α (eq.(6.150) for different fuels [234]

Source of soot	Mean α
Benzene	0.94, 0.95
Candle	0.93
Furnace samples	0.96, 1.14, 1.25
Propane	1.0

$$\kappa_{\lambda,s} = \frac{f_v 36\pi}{\lambda} F(\lambda) = \frac{f_v 36\pi}{\lambda} \frac{nk}{(n^2 - k^2 + 2)^2 + (4n^2 k^2)} \qquad (6.151)$$

The total absorption coefficient of a participating gas containing particles is generally considered equal to the addition of the gas phase and the soot particles absorption coefficients: $\kappa_{tot} = \kappa + \kappa_s$. Figure 6.29 shows how the total absorption coefficient of a gas column can change with the inclusion of soot: the effect is particularly important in high temperature gases, but even at low temperatures the inclusion of soot can change the absorption coefficient up to one order of magnitude.
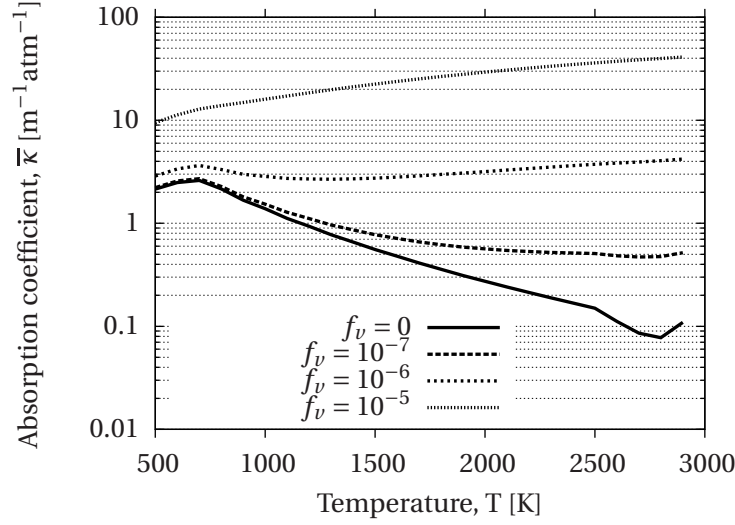
Figure 6.29: Evolution of the mean absorption coefficient with the temperature for the mixture: $X_{H_2O} = 0.1258587$, $X_{CO_2} = 0.01200788$, $X_{CO} = 0.242343442$, with different soot volume fractions.
.

6.6.4 The discretized Radiative Transfer Equation

Using an angular quadrature (eq. 6.85), a spectral quadrature (eq. 6.121) and a SNBcK model, (eq. 6.63) the radiative source term is discretized as:

$$\mathscr{S}_r \simeq \sum_{i=1}^{N_B} \Delta\tilde{\nu}_i \left[\sum_{j=1}^{N_q} \omega_j k_{ij} \left(4\pi I_{b,\Delta\tilde{\nu}_i} - \sum_{k=1}^{N_{dir}} \omega_k^d I_{ij}(\mathbf{s}_k) \right) \right] \tag{6.152}$$

where N_B narrow bands of length $\Delta\tilde{\nu}_i$ are used for the SNBcK model. The correlated k rearrangement allows the computation of the i-th band using the N_q absorption coefficients k_{ij} and the weight ω_j.

It is useful to split expression (6.152) in two parts: one emission part (first term of the RHS), and a second irradiance part containing the term which needs to be integrated over all directions.

All radiative quantities can be written with the same numerical approximation. Table 6.8 summarizes the numerical approximations used to integrate the RTE in the code PRISSMA.

6.6.5 Parallelism techniques

Interestingly enough, Table 6.8 shows that the discrete approximation of the RTE is very modular. Many of the terms are independent from each other, and thus they can be computed independently.

Table 6.8: RTE terms and their discrete approximations

Term	Definition	Discrete approximation
Total emission	$4\pi\sigma T^4 \int_0^\infty \kappa_{\tilde{v}} d\tilde{v}$	$\sum_{i=1}^{N_B} \Delta\tilde{v}_i \sum_{j=1}^{N_q} \omega_j k_{ij} 4\pi I_{b,\Delta\tilde{v}_i}$
Total irradiation	$\int_0^\infty \kappa_{\tilde{v}} \int_{4\pi} I_{\tilde{v}}(\mathbf{s}) d\Omega d\tilde{v}$	$\sum_{i=1}^{N_B} \Delta\tilde{v}_i \sum_{j=1}^{N_q} \omega_j k_{ij} \sum_{k=1}^{N_{dir}} \omega_k^d I_{ij}(\mathbf{s}_k)$
Incident spectral intensity	$G_{\tilde{v}} = \int_{4\pi} I_{\tilde{v}}(\mathbf{s}) d\Omega$	$\sum_{k=1}^{N_{dir}} \omega_k^d I_{ij}(\mathbf{s}_k)$
Spectral radiative flux	$\mathbf{q}_{\tilde{v}} = \int_{4\pi} I_{\tilde{v}}(\mathbf{s})\mathbf{s}\, d\Omega$	$\sum_{k=1}^{N_{dir}} \omega_k^d I_{ij}(\mathbf{s}_k) \cdot \mathbf{s}_k$
Spectral wall irradiance	$H_{\tilde{v}}(\mathbf{r}_w) = \int_{\mathbf{n}\cdot\mathbf{s}'<0} I_{\tilde{v}}(\mathbf{r}_w,\mathbf{s}')\lvert\mathbf{n}\cdot\mathbf{s}'\rvert d\Omega'$	$\sum_{\mathbf{n}\cdot\mathbf{s}'<0} \omega_k^d I_{ij}(\mathbf{s}_k)\lvert\mathbf{n}\cdot\mathbf{s}_k\rvert$
Diffuse wall intensity (B.C.)	$I_{\tilde{v}}(\mathbf{r}_w,s) = \epsilon(\mathbf{r}_w) I_{b\tilde{v}}(\mathbf{r}_w)$ $+\rho^d(\mathbf{r}_w)\frac{H_{\tilde{v}}(\mathbf{r}_w)}{\pi}$	$\epsilon(\mathbf{r}_w) I_{b,\Delta\tilde{v}_i}(\mathbf{r}_w)$ $+\frac{(1-\epsilon(\mathbf{r}_w))}{\pi}\sum_{\mathbf{n}\cdot\mathbf{s}'<0} \omega_k^d I_{ij}(\mathbf{s}_k)\lvert\mathbf{n}\cdot\mathbf{s}_k\rvert$
Spectral heat flux at the wall	$q_w = \mathbf{q}_{\tilde{v}}(\mathbf{r}_w)\cdot\mathbf{n}(\mathbf{r}_w)$	$\epsilon(\mathbf{r}_w)\pi I_{b,\Delta\tilde{v}_i}(\mathbf{r}_w) - H_{\tilde{v}}(\mathbf{r}_w)$

Better yet, angular integration is independent of the spectral integration, and can be realized in any order. It is then natural to take advantage of this modularity to parallelize the radiative solver. Parallel algorithms are presented below, taking into account the limitations of massively parallel architectures (resources distribution, and particularly memory allocation).

Spatial decomposition

The first thing to notice is that the absorption coefficient k_{ij} and the Planck function $I_{b\tilde{v}}$, are quantities that depend only on local properties. Each cell on the domain can thus calculate this value independently.

A first level of parallelism can be then accomplished by distributing the fluid cells over different processors. In the present work, this distribution of the computation of the emission term of the RTE is called spatial decomposition.

As in CFD, local properties can be evaluated at the center or at the nodes of the cells. Depending on the type of unstructured mesh one method can be more efficient than the other: for tetrahedral meshes, the number of nodes is far smaller than the number of cells. In that case the emission term is computed faster from nodal values. For hexahedral meshes it is more interesting to use the local values at the center of the cells.
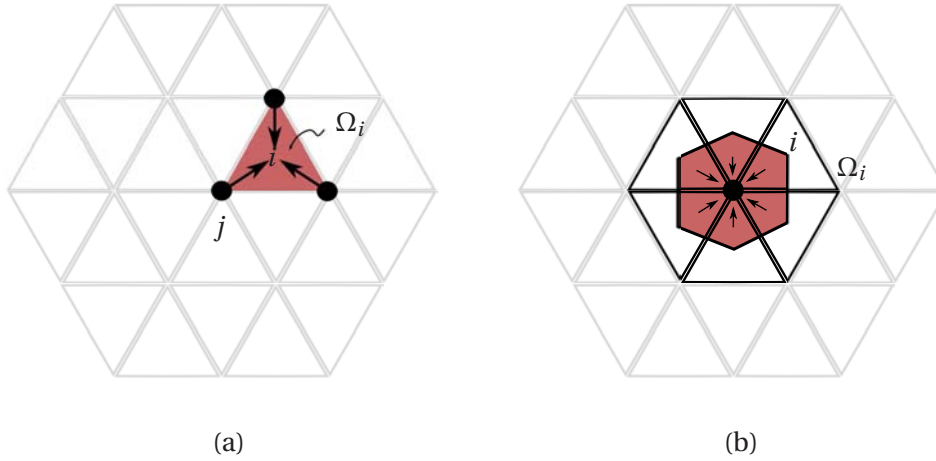
Figure 6.30: (a) Gathering information from the nodes to the cell. (b) Scattering information from the cells to the nodes.

A so-called gather/scatter method allows to distribute the data from the nodes to the cells and vice-versa. This procedure must however be conservative, avoiding the loss of information. The most common technique used in CFD codes is the volume weighted communication, as shown in Fig. 6.30. Data at the center of the cell is obtained by applying the following operator (gathering information at the center of the cell):

$$f_i = \frac{1}{N_i} \sum_{j|j\in\Omega_i} f_j \tag{6.153}$$

where f_i is the value of the quantity f at the center of the cell Ω_i, delimited by N_i vertices and f_j is the value of the quantity f at the nodes of the cell.

The inverse operation (scattering data of the cell into the nodes) can be accomplished using:

$$f_j = \frac{1}{V_j} \sum_{i|j\in\Omega_i} \frac{f_i V_i}{N_i} \tag{6.154}$$

where V_j is the volume associated to the node j, V_i is the volume of the cell i and N_i is the number of

vertices of cell i.

Spatial decomposition and gather/scatter processes are straightforward techniques that can easily reach important speed-up factors, and for the emission term a satisfactory load-balancing can be rapidly achieved.

Angular decomposition

One of the main problems of the numerical integration of the RTE is the difficulty to establish a correct parallelization of the irradiation term. In the case of a non-scattering medium, each direction is independent of the other: each processor can then calculate a fraction of the total number of directions (angular decomposition).

There are some obvious limitations to this technique: the best result can only be obtained when the number of processors and directions are the same. If the ratio of the number of processors over the number of directions N_P/N_{dir} is not an integer value, the parallel integration suffers from a bottleneck: some processor will be doing double work, pulling down the efficiency of the code.

To avoid this problem, the parallel code should be able to compute a fraction of a direction. One way of doing it is to combine the angular and the spatial decomposition: when the number of processors is bigger than the number of directions, each processor only calculates a subset of the cells in that direction. The major problem with this method is that, as explained in section 6.6.2, the order in which cells are treated in a given direction is important. The control and optimal distribution of the subset of cells over the processors is discussed further in this section.

Spectral decomposition

It is also possible to parallelize over the frequencies: one processor calculates a fraction of the total frequencies in a given direction. The independence of frequency and direction allows to add the contribution of each independent processor.

Spectral decomposition is only possible in models where a high number of frequencies are resolved. In PRISSMA only the SNBcK model can make use of this parallelism. A combined spatial-angular-spectral decomposition permits to perform RTE integrations with a high number of processors. The higher number of processors that can be used are: $N_P^{\mathrm{max}} = N_B N_{\mathrm{dir}}$, e.g. for an S_4 quadrature and with a spectral model using 370 bands: $N_P^{\mathrm{max}} = 8880$ processors.

Another option is to perform a parallel spectral decomposition dividing also the spectral quadrature of each band. This would permit to rise the maximum number of processors up to $N_p^{\mathrm{max}} = N_B N_{\mathrm{dir}} N_q$. In addition, for global spectral models where only one "band" (the full spectrum) is used, the maximum number of processors can be: $N_p^{\mathrm{max}} = N_{\mathrm{dir}} N_q$.

Mesh partitioning

When the number of processors is different from the number of directions in the computation of the irradiance term, an unbalanced computation occurs: for example, if the total number of directions is 24 and the number of processors is 32, there are 8 free processors and 24 processors calculating only one direction.

In the previous section we have seen that for the SNBcK model, one direction can be decomposed in frequency. In the global methods however the only way to decompose a direction is to partition the mesh. There are two possible methods of mesh partitioning:

- **Pathway partitioning**

  As seen in Fig. 6.31, one way to partition the mesh is to subdivide a pathway (previously calculated using the sweeping process of section 6.6.2) in different subdomains. In this case, the information about the incident irradiation at the interface between the subdomains is unknown (except for the subdomain limiting with the boundary), and a guess is made. Once the data is propagated from cell to cell in the subdomain, a communication between the processors is made to correct the initial guess. If necessary an iterative procedure is engaged until convergence to a certain level of error is obtained.

  The advantage of this process is that it is easy to implement. However a major drawback is that it must still keep in memory the hole mesh, which can be a limiting condition in applications where the geometrical complexity is high.

- **Geometrical partitioning**

  Here, the mesh is partitioned using a classical partitionning method as in CFD [83]. Figure 6.32 shows how the domain could be partitioned. In this case each subdomain calculates the RTE independently of the others, using independent pathway tables. Communications at the frontiers between the processors are then allowed to update the calculated values of the incident radiation at the border faces. An iterative converging process must be set up to account for the updating of information at the interfaces.

  Contrary to the pathway partitioning method, each processor only keeps the information of the subdomain, thus heavily reducing the memory requirements and consequently improving the computational speed.

Mesh partitioning for the calculation of the irradiance term suffers a major drawback: information from one boundary must cross each sub-domain before reaching the opposite surface. One iterations is needed for each sub-domain crossed by the light beam. The computational time expended in this method becomes similar to the time use without domain decomposition, even worse the addition of communication between processors can slow down the computation. However, this decomposition permits to carry out simulations in massively parallel computers using the global spectral models. In
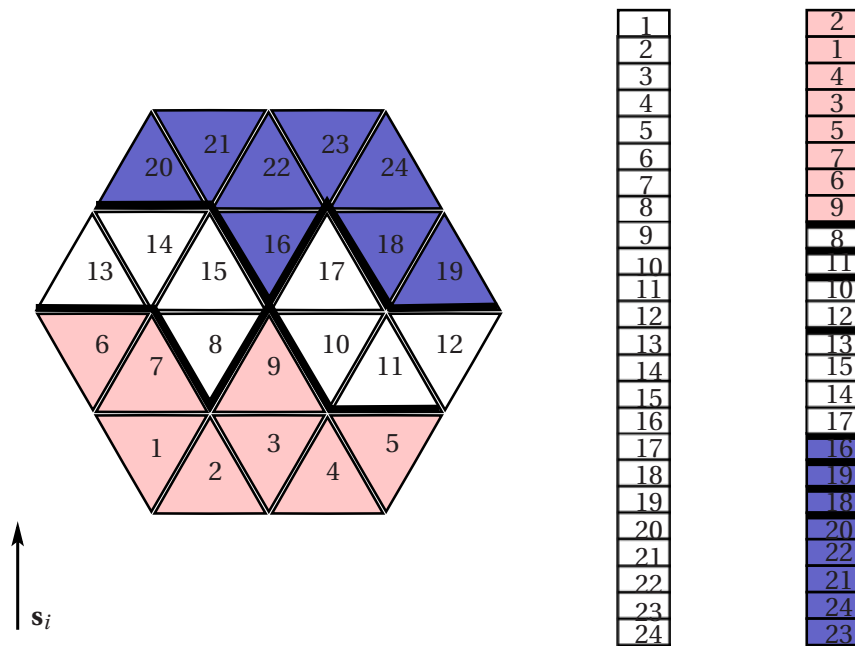
Figure 6.31: Mesh partitioning by pathway parallelism. Bold lines: the faces and cells where an initial guess of the incident radiation is needed at first iteration.

addition, memory usage is of great concern in radiation, domain partitioning can allow a reduction in memory use.

6.6.6   Test cases

Validation of the RTE solver is obtained by comparison with Monte Carlo and ray tracing simulations and with examples obtained from the literature. Test cases were also performed to evaluate the accuracy of the spectral models.

Finally, speed-up have been measured on different computers. The analysis os the results indicate the need for future developments.

Test cases

Two cases proposed by Coelho et al. [47] are evaluated in the present section to verify the validity of the spectral models and the accuracy of the parallel code.

(a)   (b)
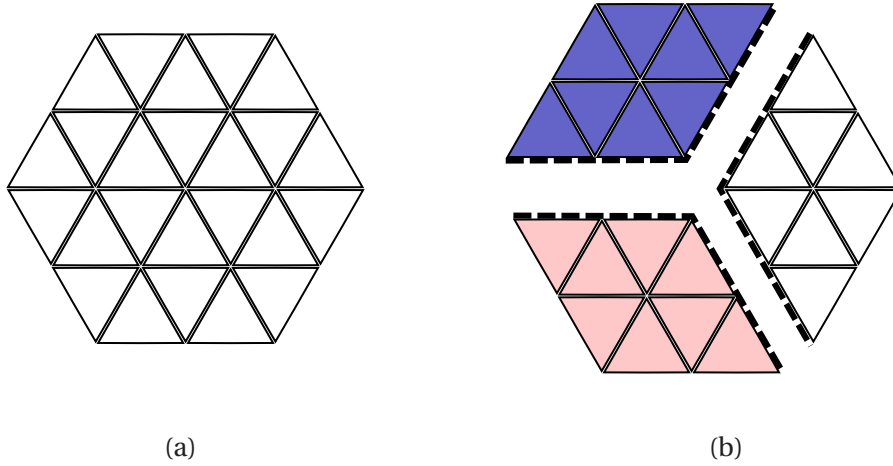
Figure 6.32: Mesh partitioning by geometrical decomposition.

The first case is a cylindrical enclosure of length $L = 3.0m$ and radius $R = 0.5m$. The temperature of the walls is $300K$. Species molar fractions of the gas are 20% H_2O, 10% CO_2 and 70% N_2. There is no soot and the temperature of the medium is $1800K$. It was resolved on a mesh with $19\,343$ tetrahedron cells. Three spectral models are tested: SNBcK, FS-SNBcK and WSGG.

In Fig. 6.33 the Monte Carlo result (although not fully converged), gives good approximation of the result (as evidenced by the error bars), subsequently confirmed by the accurate SNBcK method. This particular case, without any soot concentration, highlights the fact that even in a simple homogeneous gray case the WSGG model strongly underestimates the radiative source term. In the other hand, the FS-SNBcK model shows a very good agreement with the reference simulations.

The second case is a cylinder of length $L = 1.2m$ and radius $R = 0.3m$. The walls are black at $800K$, except the right wall ($x = L$), which is maintained at $300K$. The temperature and the molar fractions of H_2O and CO_2 are given by analytical profiles:

$$T(x,r) = 800 + 1200 * (1 - r/R)(x/L)$$
$$X_{H_2O} = 0.05\left[1 - 2(x/L - 0.5)^2\right](2 - r/R) \tag{6.155}$$
$$X_{CO_2} = 0.04\left[1 - 3(x/L - 0.5)^2\right](2.5 - r/R)$$

with the soot volumetric fraction is $f_v = 10^{-7}$. This case was resolved using a mesh with $27\,749$ tetra-
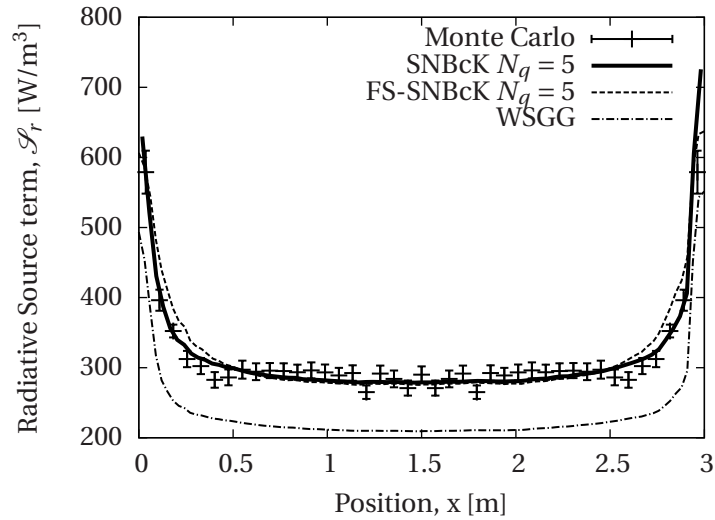
Figure 6.33: Test case 1: homogeneous cylinder. Radiative source term along the axis of the cylinder.

hedron cells and four spectral models were tested: SNBcK, FS-SNBcK, TFS-SNBcK and WSGG.

In this second case it can be seen (Fig. 6.34) that for a non homogeneous media the FS-SNBcK and the TFS-SNBcK spectral models follow closely the evolution of the radiative source term given by the ray tracing simulation. Again, the WSGG model shows a divergent trend where the media shows inhomogeneity.

It is important to note that the best advantage of the WSGG model is to be fast. However, the TFS-SNBcK introduced in the present work (section 6.6.3) and presented in detail by Poitou [204] has similar performance with a very accurate result.

Speedup

In PRISSMA, two options of parallelism are implemented: a spatial-angular decomposition for global spectral models, and a spatial-angular-spectral decomposition for the SNBcK model.

Fig. 6.35 shows the speedup factor for for the FS-SNBcK model. This factor is the ratio between the computational time at a given reference number of processors N_{ref} (in the present case eight processors) and the computational at N_p processors: Speedup = N_{ref}/N_p. The test case consist of a cubic enclosure with 1M cells, representing an anisothermal non-homogeneous mixture of combustion gases. Diffuse reflection at the solid walls was included. In this case, it is shown that simulations from 8 to 32 processors present an almost perfect scalability with a small decrease at 48 processors.

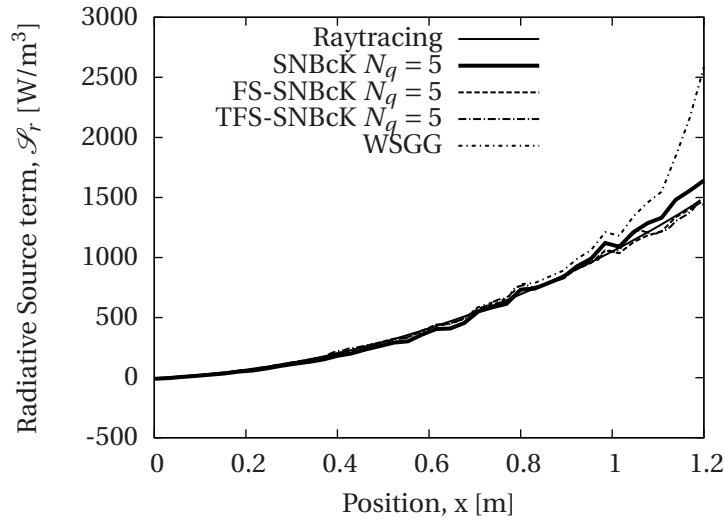Simulations up to 32 processors where carried out at in-house CERFACS computing facilities (featur-

Figure 6.34: Test case 2: inhomogeneous cylinder. Radiative source term along the axis of the cylinder.

ing PowerPC970MP processors at a clock-rate of 2.5 Ghz). However, when the code ran on a massively parallel architecture (featuring Intel Quad-Core E5472 processors at a clock-rate of 3GHz[8]) its performance decreased after $N_p \approx 50$ processors (Fig. 6.36).

Different tests where performed to detect the reason for such performance loss. While memory management could be improved, it was found that the limiting part was the computation of the irradiance term of eq. (6.152). Figure 6.37 shows the distribution of the computational times among the different parts of the code, namely: the total simulation time, the time spent on the resolution of the spectral model and the time used to integrate the irradiance term.

For simulations up to 32 processors, the spectral model dictates the total time of the simulation. Spatial-angular decomposition permits to reduce the computational time in this zone. However, parallelization of the irradiance term is limited: a bottleneck point is achieved at 48 processors: while some processors others remain on stand-by.

Therefore for massively parallel computations it will be essential to implement a mesh partitioning method (pathway or geometrical) that permits to distribute the computation of the irradiance term on all the processors.

---

[8]The tests where carried out on the SGI Altix ICE server of the CINES center in Montpelier, France.
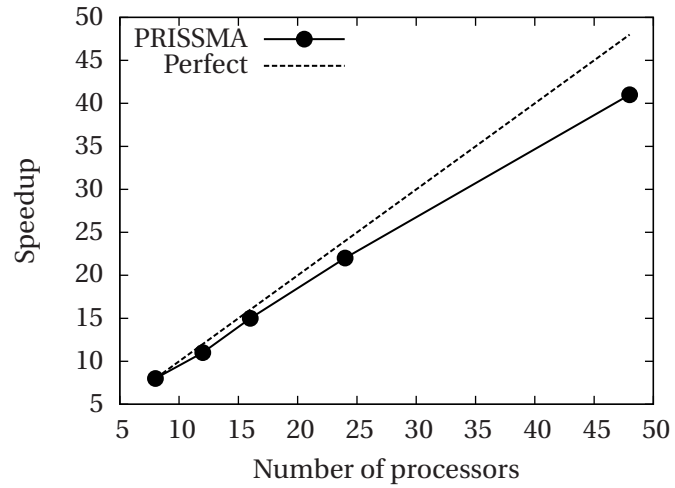
Figure 6.35: Speedup factor for the FS-SNBcK model from 8 to 48 processors.
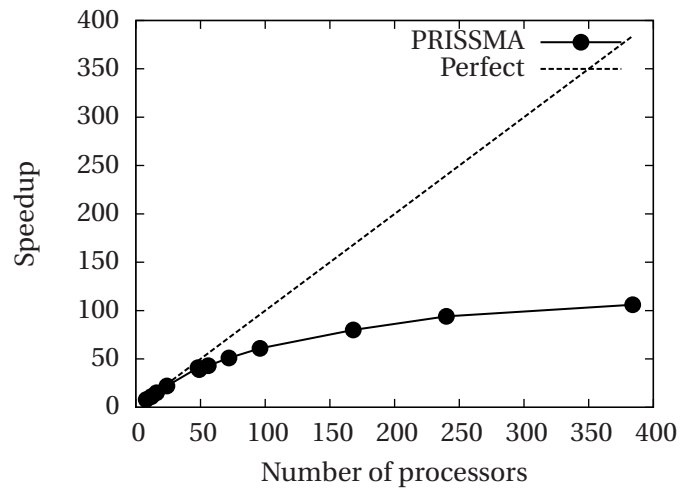

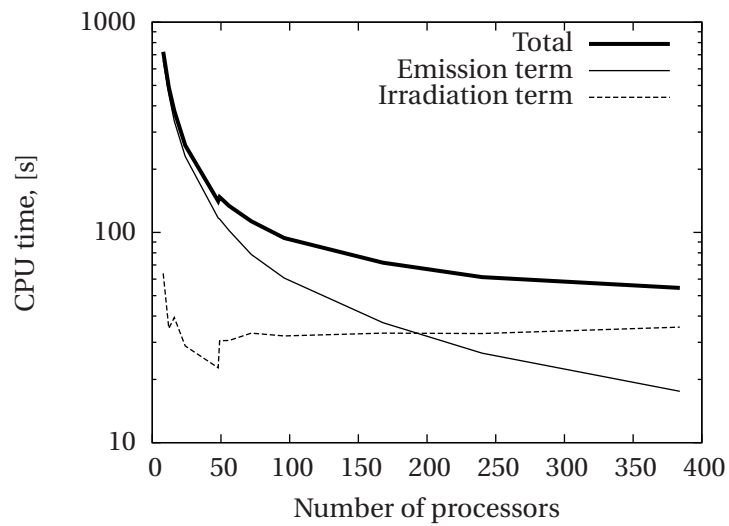Figure 6.36: Speedup factor for the FS-SNBcK model from 8 to 384 processors.

Figure 6.37: Computational time repartition. The spatial-angular parallel technique shows a good acceleration in the first 48 processors, then a bottleneck is reached: the irradiance computation becomes predominant and provokes a stagnation in the scalability of the code. A mesh partitioning is thus required.

Part II

Multi-physics simulations on parallel architectures

7

Combined conduction, convection and radiation

Contents

7.1   Introduction

Multi-physics is the development and study of systems involving the simultaneous resolution of multiple physical phenomena.

All the processes observed in nature (the flight of a bird, the movement of the planets, the lightnings in a storm) result from the complex interaction of many different phenomena. The wide range of observed patterns and the great number of different experiences was in the past confusing and made difficult to understand the origins and the causes of nature's behavior.

Nature seemed impossible to be explained by our very terrestrial experience. However, by close inspection, under certain specific circumstances it was shown that some phenomena followed recurrent patterns. By observation, testing and prediction some parts of nature showed a scientific explanation. Chemistry, physics, biology and all other sciences constitute today the accumulated body of knowledge that explains such recurrent patterns. Science is fragmented in different disciplines, and from the beginning it was conceived as a method where simplifications, hypothesis and suppositions where introduced in order to deal with simpler problems.

In the study of a specific phenomenon the simplifying hypothesis constitute the limits of the problem. The phenomenon is then studied as an isolated element of the rest of the universe. In physics, the behavior of these subsystems is expressed using mathematical models and, in most cases, they involve the inclusion of partial differential equations.

The isolation of subsystems implies the inclusion of a limiting interface with the other subsystems. Through this interface the external conditions of the universe are communicated into the subsystem, bounding the mathematical model, they are a model of the external properties. The response of the subsystem is the result of the interactions between the internal equations and the interface conditions. A small variation of the interface conditions can give rise to variations in the behavior of the subsystem (the study of this effect is known as the sensitivity analysis).

An interaction process involving different physical subsystems is called a coupling. Coupled physical processes containing three or more subsystems are called a multi-physics couplings.

7.1.1   Principles of coupling

The interface conditions in a physical subsystem do not change randomly, their variation is caused by the interactions with the rest of the universe (or complementary subsystems). The assessment of accurate boundary conditions is obtained from the modelization of such interactions. When the interaction between two subsystems is handled by the exchange of information at their interface, the joint problem is called a coupling, and the exchanged information is called the *interface variables*.

In a coupling, the elimination of the boundary model and the use of interface variables between the

subsystems adds one degree of freedom to the joint problem. To close the system the exchange of interface variables must be subject to closing rules, called the *interface equations* which are commonly based on conservation laws [28].
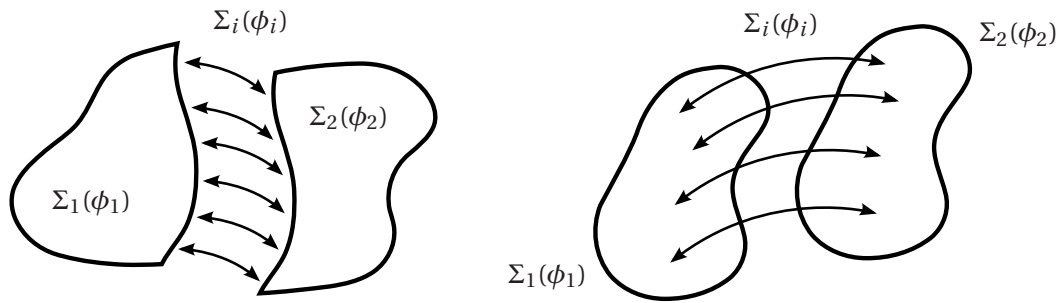

Figure 7.1: Coupling subsystems: each part is governed by a set of equations, Σ, and a set of variables, ϕ. (left) two-dimensional interface, (right) three-dimensional interface.

Figure 7.1 shows two examples of interfacing between subsystems. In the left image, a coupled system representing the joint resolution of a physical problem where the subsystem 1, governed by the equations $\Sigma_1(\phi_1)$ and described by the variables ϕ_1 interacts with the subsystem 2 by means of a common surface, using the interface variables ϕ_i and the interface equations $\Sigma(\phi_i)$; this is typical of ocean-atmosphere problems and Fluid-Structure Interaction (FSI) simulations. In the second image (right), both subsystems act on the same domain but each one resolves a different set of equations and variables, where the variables ϕ_i are communicated using the equations $\Sigma(\phi_i)$ using a three-dimensional interface. Examples of this coupling method include two-phase flows and Radiation-Fluid Thermal Interaction (RFTI).

7.1.2   Numerical aspects of coupling

In addition to the mathematical modeling of the interface variables and equations, the numerical aspect of coupled systems must be carefully managed. In the first part of this work it was shown that a discretization of space and time is used to integrate the equations of each subsystem. A coupled application must account for the differences in the discretization of every involved subsystem.

Interface variables and equations must deal with multiple time and length scales (from where the name multi-physics wad derived). Data interpolation and time synchronization are essential elements of coupled systems.
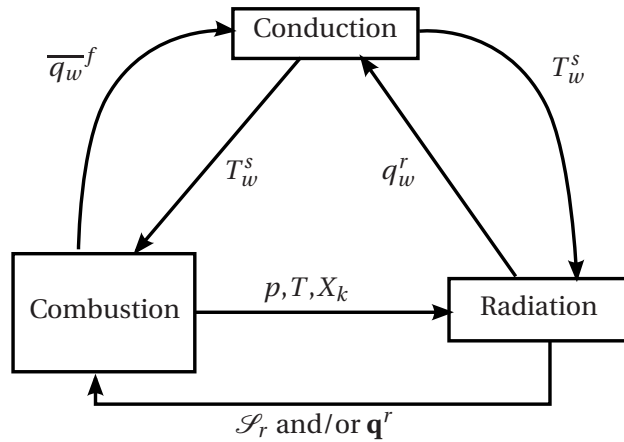
Figure 7.2: Flux of interface variables ϕ_i for a fully coupled thermal system.

In addition, information exchange between coupled subsystems form a closed iterative loop. Control theory shows that under certain circumstances such kind of system can become unstable [190]. Stability limits depend on the choice of the interface variables and equations and the treatment of the space-time synchronization.

7.1.3 Combined heat transfer

In the first part of the present work three physical subsystems were presented. They correspond to the three heat transfer modes observed in nature: conduction, convection and radiation. In this work Multi-Physics Coupled (MPC) simulations make reference to the coupled simulation using these three subsystems.

Note that heat transfer in combustion applications without heat conduction or radiation represents in itself a complex phenomenon constructed from smaller subsystems including chemistry, combustion modeling, turbulence, among others.

In combustion applications conduction, convection and radiation act simultaneously. The unsteady interaction between these three transfer modes redistributes energy in the system. It forms a closed loop where one mode bounds the evolution of the two others. In Fig. 7.2 a schematic representation of the energy flux is presented. The surface temperature of the solid, T_w^s, limits the quantity of energy radiated by the walls inside the domain. A variation of radiation acts as an energy source, $\mathscr{S}_r$, and provokes a variation in temperature in the fluid. At the interface with the solid, heat flux by convection, q_w^f, and radiation from the fluid to the solid, q_w^r, modifies the wall temperature.

Other phenomena may increase or decrease the energy content of the system. In combustion applications heat sources include chemical reactions, soot, laser or electric ignitors and cooling systems.

A good knowledge of the heat transfer loop is essential for an accurate thermal representation of the system.

In the final chapter of this work one implementation of a coupled multi-physics system is presented. The final objective is the application of the multi-physics system to an industrial aeronautical case, in order to show the feasibility of unsteady couplings, in particular with the use of LES and realistic radiation solvers. The numerical methods implemented are mostly based on the work done by Duchaine et al. [67], Gonçalves dos Santos et al. [64] and Poitou [204].

7.1.4   Technical approach in multi-physics

The resolution of the coupled system can be approached using many different technical methods. In this section a brief description of these methods is exposed and a detailed look at the selected method is presented.

Close-ended simulation code

A close-ended (c-e) code refers to an autonomous self-containing simulation code that resolves the full thermal problem using only internal resources and databases. A stand alone code that can carry up a full thermal simulation would be extremely consistent but extremely complex.

The development of such a code is in principle possible, as all the thermal phenomena can be properly modeled using the Boltzmann equation as shown by Mishra et al. [174], Cheng et al. [42] and Succi [249]. However the numerical implementation and resolution of one specific heat transfer phenomenon may vary from one problem to the other.

While this approach may seem hazardous, in some specific applications this can be considered as a viable possibility:

- Fluid-Solid interaction: in applications where the heat flux at the interface can be considered steady, the solid can be modeled as a *static fluid* with its own physical properties. This approach however can be inappropriate in unsteady flows where the rapid variation of the fluxes in the fluid domain can provoke discontinuities at the interface of the solid, thus generating numerical stiffness.

- Solid-Radiation simulations: if radiative heat transfer is done in the vacuum (no participating media, e.g. in space applications), the solid heat transfer code can be used to calculate the view factors for the radiation problem, and perform simulations using a simultaneous resolution of radiation and conduction.

- Radiation-Fluid code: as shown in section 6.5.2 simple models for the RTE can be developed and implemented in CFD codes, e.g. using the thin gas approximation or the spherical har-

monics approximation [177]. These are very simplified models which do not take into account the directional dependence of radiation and are only accurate in very specific cases (optically thin or thick gases).

In all these cases, the strong interconnection between the different physical models can produce a very efficient code, but this can also be a weakness: the development of the numerical methods for each subsystem can become complex. Maintaining the code requires a team of trained managers in the different physical subparts, and the simulation of only one heat transfer mode can imply a loss in efficiency and difficulty to operate (e.g. performing a radiation only simulation in a radiation-fluid code).

Open-ended distributed toolbox

In the open-ended (o-e) coupling strategy, every single subsystem is independently resolved using specialized simulation codes. Each code can be developed by a different research team. The numerical methods for each code acknowledge the specificities of each physical phenomena. The time and length scales are independently resolved.

In this approach an additional tool is necessary: in order to extract data from one code and inject it into another, a specialized communication and management software is required. The software that controls the resource administration and the data exchange is called a *coupler*. In addition, using different independent codes demand a careful study of the data to be exchanged and the communications frequency.

One of the main objectives of the present work is to develop, implement and study tools and techniques for an open-ended (o-e) coupling strategy.

Data exchange

In the o-e strategy data must be collected from one subsystem and inserted to another. Data exchange can be done through a file or directly inside the memory, which requires access to the source files of the codes. If the source code is available, direct communications by memory read/write functions can be handled by the coupler. On the other hand, if source files are not accessible, the easiest way of data communication is through disk access. If the first method is more efficient, it is also more intrusive in the codes. In the present work all source codes are available and direct data exchange is implemented.
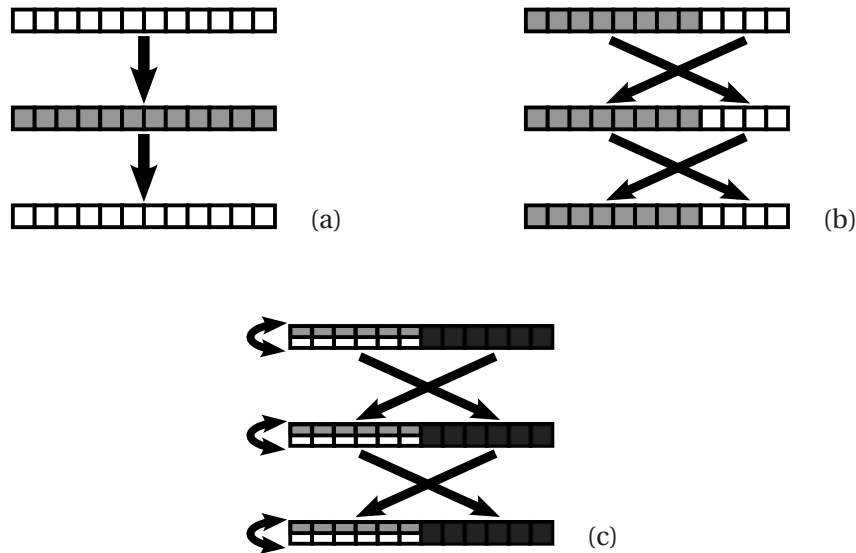
Figure 7.3: Coupling strategies: each square represents one processor, each color represents a code and each arrow represents data exchanges. (a) SCS, (b) PCS and (c) MCS.

Computational resource distribution

Coupled simulations on massively parallel architectures must be distributed over all processors in an optimal way. This depends on the computational speed of each code and the coupling frequency.

Duchaine et al. [67] present two methods for resource distribution: the Sequential Coupling Strategy (SCS) and the Parallel Coupling Strategy (PCS). In the first method (Fig. 7.3-a), each code performs a simulation sequence one after the other, using all the processors at once. The result is a chained simulation where each code has access to the full computational resources when running. The main advantage of this method is the simple CPU synchronization (one code begins when the other ends), but there are two major drawbacks: memory can become a limiting factor as both codes are loaded at the same time on the same processors[1], and the total restitution time can be high. In the Parallel Coupling Strategy (PCS) all codes run simultaneously in different processors, and must be synchronized in physical time[2] and CPU time[3] (Fig. 7.3-b).

---

[1]This is true if data exchange is done by memory access. One alternative is to load and unload each code and perform communications via file exchange. In such case the major inconvenient is the large amount of time used in system communications to load the software and the data.

[2]The physical time synchronization refers to the frequency at which data exchange is performed.

[3]Synchronization in CPU time refers to the speed at which each code reaches the point of data exchange.

In a multi-physics simulation with more than two codes, it is possible to use a Mixed Coupling Strategy (MCS) where two codes use the same number of processors in SCS, while other codes run on different processors using PCS (Fig. 7.3-c).

Conclusion

In the present work the selected coupling strategy consists of o-e codes which communicate by memory access (using a coupler) in a PCS or MCS strategy. In order to use a coupler it is necessary to follow some development steps:

- **Data input/output:** Detect which information (physical fields or interface variables ϕ_i) is required by each code to perform the coupled simulation.

- **Interfacing:** Determine the procedure for data exchange (interface equations Σ_i). Develop a tool to specify the exact memory location of the target code where information from the source will be placed. This can be particularly critical in massively parallel machines where the memory is spread over many different computational nodes.

- **Interpolation:** As the meshes of the different codes are not necessarily coincident, an interpolation method must be acknowledged. Interpolation methods include (among others): nearest point, linear interpolation and conservative flux interpolation, as presented by Boer et al. [54].

- **Data processing:** Update the original source code to integrate the information received from the other codes.

- **Synchronization in physical time:** Establish the coupling frequency.

- **Synchronization in CPU time:** Distribute the coupled simulation to reach optimal CPU times.

First, two-code couplings are performed (Radiation-Fluid and Fluid-Solid) before developing couplings that include the three heat transfer modes.

7.2 Fluid-Solid Thermal Interactions (FSTI)

In literature the name Fluid-Structure Interaction (FSI) is commonly used to designate the coupled system where fluid surface pressure produces an elastic deformation of the solid structure [79, 113]. In the present work the term Fluid-Solid Thermal Interactions (FSTI) designate the coupled system where energy is exchanged between the fluid and the solid by natural or forced convection. Some authors refer to this interaction as Conjugate Heat Transfer (CHT) [16, 68, 129, 167, 212], but in such cases radiation is not involved, so here the term FSTI is preferred.
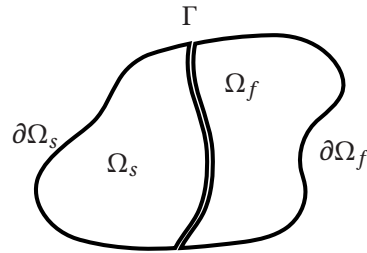
Figure 7.4: Elements of the FSTI: fluid and solid volumes Ω_f and Ω_s, non-coincident surfaces $\partial\Omega_f$ and $\partial\Omega_s$ and fluid-solid interface Γ.

A coupled FSTI system involves the interaction between two non coincident volumes (Ω_s and Ω_f in Fig. 7.4) delimited by a surface ($\partial\Omega_s$ and $\partial\Omega_s$ in Fig. 7.4) and a shared limiting surface (Γ in Fig. 7.4). The equations that govern the evolution of the solid and the fluid subsystems have been presented in chapters 4 and 5.

The temperature of the solid at the interface T_w^s can be used to bound the fluid using an iso-thermal boundary condition. However, this wall temperature is a priori unknown. T_w^s can be obtained by using the boundary conditions imposed on the surfaces $\partial\Omega_s$ and a mean heat flux $\overline{q_w}^f$ imposed on the surface Γ, where $\overline{q_w}^f$ is the mean value of the heat flux in the fluid at the interface Γ.

Once the temperature of the solid is obtained, T_w^s is imposed in the fluid solver. This step leads to a new mean heat flux $\overline{q_w}^f$ at the surface Γ, different from the one used in the first place to deduce T_w^s. The interface variables T_w^s and $\overline{q_w}^f$ must be exchanged many times between the two subsystems until the coupling reaches a stable state.

A good determination of the fluid heat flux at the interface q_w^f is thus essential for the proper calculation of the coupled system. In LES applications the computation of this quantity requires an special treatment. Before studying the coupled FSTI system a closer look at the way q_w^f is calculated in LES is presented in the next section.

7.2.1   The near-wall flow

Introduction

Heat exchange at the fluid interface between the solid and the flow is mainly ruled by the shape of the thermal boundary layer in the near-wall zone of the fluid.

The boundary layer is the zone that lays in the immediate vicinity of a solid surface. From the con-

servation principle, properties like momentum, temperature and pressure have the same value for all the molecules of fluid and solid in contact at the interface between the two domains. From this point velocity and the temperature evolve, changing in shape before reaching the conditions of the free stream flow. This transition zone is known as the boundary layer [227, 213].

For low Reynolds numbers a laminar boundary layer is formed. In combustion applications Reynolds numbers are high and the boundary layer shows a turbulent structure. The homogenization due to turbulence causes an augmentation in the heat and mass transfers between the flow and the solid structure [38].

The shear stress and the heat flux at the wall can be calculated from the knowledge of the structure of the Turbulent Boundary Layer (TBL). In the following sections an introduction to TBL theory is presented and the impact of the chemistry is exposed.

Wall models

The fluxes in the boundary layer change proportionally to the velocity and temperature gradients, and when Reynolds numbers are high, those gradients are stiff.

To numerically detect such gradients one option consist to discretize the boundary zone using fine layers of cells. This approach is commonly called the Wall-Resolved (WR) method. Gradients are accurately calculated using the numerical scheme of the Navier-Stokes solver. The major drawback of this method is that cell sizes can become so small that the total number of cells of the mesh becomes extremely high (the CPU cost rises) and the size of the smallest cell rapidly drops (the time step is lowered thus the CPU cost is risen).

A second approach is the Wall-Modeled (WM) method, where instead of explicitly building the boundary layer, a model is included in the first cell of the mesh. Using an analytical development, the approximated heat flux and shear stress can be imposed at the boundary. This approach leads to a considerable gain in grid resolution [198, 197], while maintaining a satisfactory precision even in complex flows [178].

Figure 7.5 shows how both the WM and the WR methods act in the near wall region in a coupling context: fluid space discetization is represented by void circles (∘) and solid numerical domain by solid circles (•). In the classical WR method (Fig. 7.5-left) the nodes at the interface between the two domains are considered in contact. The boundary node in the fluid domain is called a "non-slip" node as the fluid velocity is zero. Continuity of temperature and heat flux must be guaranteed in a non-slip boundary node for a FSTI coupling.

In the second case (Fig. 7.5-right) the WM approach is carried out using a "slip" boundary node (a) that is not in direct contact with the solid wall (b). Velocity and temperature in this node adapt in order to satisfy the wall model (c), given the conditions at the solid wall (b and d) and the mean flow parameters at the first off-wall node (e). A WM approach can be useful in the stability of coupled
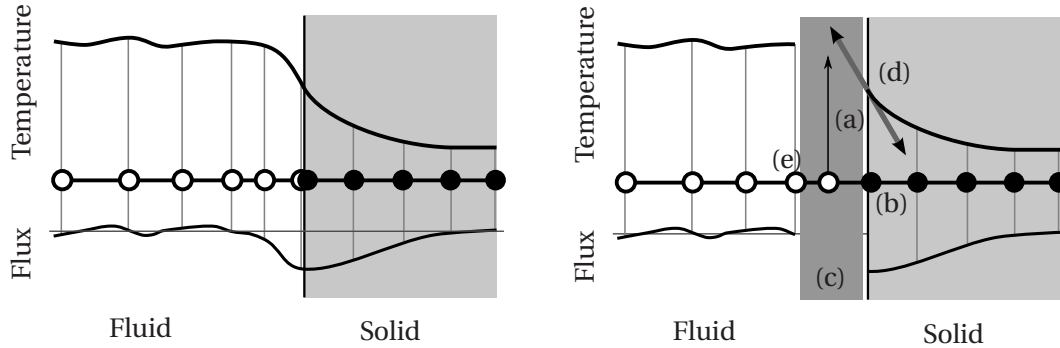
Figure 7.5: Near wall flow resolution: (left) Low-Reynolds number, Wall-Resolved approach, (right) High-Reynolds number, Wall-Modeled method.

systems as it adds one additional equation to the interface (the law of the wall model). Continuity of the temperature is not required between the nodes (a) and (b).

The idea of the near-wall models is to build an expression of the form:

$$\frac{df}{dy} = F$$
$$\frac{dg}{dy} = G \tag{7.1}$$

where f and g are the total flux of momentum and energy in the wall-normal direction y, that depend on the available variables at the wall (temperature T_w^f and gas composition $Y_{k,w}$) and the free-stream flow (main flow velocity u, temperature T^f and gas composition Y_k).

If F and G are simple functions eqs. (7.1) can be integrated and the wall heat flux $q_w^f = g$ and the wall shear stress $\tau_w = f$ can be obtained. The simplest case is obtained for $F = G = 0$, but another possibility is to use constant values for $F = F_0$ and $G = G_0$ (Fig. 7.6). On the other hand, if F and G are unknown functions of y no model can be constructed.

The study and development of wall-functions was initially proposed by Deardorff [55] and Schumann [233]. Subsequent developments focused on the inclusion of more physical elements such as heat fluxes [97], streamwise pressure gradients [103] or chemical reactions [32], and their implementation on numerical solvers [112].
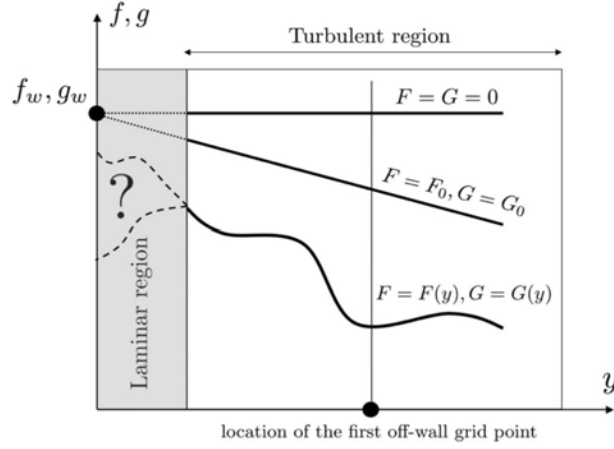
Figure 7.6: In this image the fluid is located at $y > 0$. The estimation of the wall flux is obtained from data at the first off-wall grid point located in the turbulent region, as presented by Cabrit and Nicoud [32]: f represents the total shear stress and g the total heat flux.

The turbulent compressible boundary layer

Lets consider the fully developed TBL over an infinite flat plate. This corresponds to an statistically steady ($\frac{\partial}{\partial t}$=0) flow where temperature and velocity profiles only vary on the wall-normal direction y ($\frac{\partial}{\partial x}$=0 and $\frac{\partial}{\partial z}$=0). It is considered that the mean streamwise velocity $\overline{u}$ is the only non-zero component of the velocity field ($\overline{v}=\overline{w}$=0). In addition the streamwise pressure gradient that drives the flow is considered small, $\frac{\partial \overline{p}}{\partial x} \approx 0$.

Under this assumptions the mean momentum and the energy equations become:

$$\frac{d\overline{\tau}_{\text{tot}}}{dy} = \frac{d}{dy}\left(\overline{\mu\frac{du}{dy}} - \overline{\rho\widetilde{u''v''}}\right) = 0 \tag{7.2}$$

$$\frac{d\overline{q}_{\text{tot}}}{dy} = \frac{d}{dy}\left(\overline{\rho\widetilde{v''h_s''}} + \overline{\rho}\sum_{k=1}^{N}\widetilde{v''Y_k''}\Delta h_{f,k}^0 - \overline{\lambda\frac{dT}{dy}} + \overline{\rho}\sum_{k=1}^{N}\overline{h_kY_kV_{k,y}} + \overline{q_y^r}\right) = 0 \tag{7.3}$$

where the viscous effect term $\overline{\tau_{iy}(du_i/dy)}$ has been neglected in Eq. (7.3) because in applications at low Mach numbers ($M < 0.2$) it shows a neglible contribution compared with other terms [32]. Table 7.1 identifies each one of the terms in these equations.

These equations accurately describe the TBL. To build the functions f and g from the available variables in an LES it is necessary to model certain of the terms given in Table 7.1. Lets examine each one of the TBL equations independently:

Table 7.1: Terms of the momentum and energy equations in the TBL.

Term	Description
$\overline{\mu \dfrac{du}{dy}}$	Laminar shear stress
$\overline{\rho}\,\widetilde{u''v''}$	Turbulent shear stress
$\overline{\rho}\,\widetilde{v''h_s''}$	Turbulent flux of sensible enthalpy
$\overline{\rho}\sum_{k=1}^{N}\widetilde{v''Y_k''}\Delta h_{f,k}^0$	Turbulent flux of chemical enthalpy
$\overline{\lambda \dfrac{dT}{dy}}$	Fourier heat flux
$\overline{\rho}\sum_{k=1}^{N}\overline{h_k Y_k V_{k,y}}$	Species diffusion flux
$\overline{q_y^r}$	Radiative heat flux

- **The dynamic boundary layer**

  Prandtl showed using experimental data [214] that, with an appropriate adimensionalization, the momentum equation of the TBL can be divided in two zones: a linear sub-layer and a logarithmic sub-layer (Fig. 7.7).

  Scaling of the variables is performed using the procedure presented in section 5.2.3. Table 7.2 summarizes this procedure and shows the friction variables and the wall unit scaled variables employed (w subscripted variables correspond to parietal quantities).

  The first approximation in the analysis of the momentum equation of the TBL, is to use the Boussinesq assumption to approximate the turbulent shear stress [24, 228]:

  $$\overline{\rho}\,\widetilde{u''v''} \approx \mu_t \frac{d\overline{u}}{dy} \tag{7.4}$$

  where μ_t is the turbulent dynamic viscosity.

  With this approximation the total shear stress $\overline{\tau_{\text{tot}}}$ is written:

  $$\overline{\tau_{\text{tot}}} \approx \frac{d\overline{u}}{dy}(\overline{\mu}+\mu_t) \tag{7.5}$$

Table 7.2: Friction and dimensionless variables used in TBL analysis.

Variable	Description
$u_\tau = \sqrt{\frac{\tau_w}{\rho_w}}$	Friction velocity
$y_\tau = \frac{\nu_w}{u_\tau}$	Characteristic friction length
$T_\tau = \frac{q_w^f}{\rho_w C_{p,w} u_\tau}$	Friction temperature
$Re_\tau = \frac{h u_\tau}{\nu_w}$	Friction Reynolds number
$y^+ = \frac{y}{y_\tau}$	Dimensionless wall distance
$u^+ = \frac{u}{u_\tau}$	Dimensionless velocity
$T^+ = \frac{T_w^f - T}{T_\tau}$	Dimensionless temperature
$\mu^+ = \frac{\mu}{\mu_w}$	Dimensionless dynamic viscosity
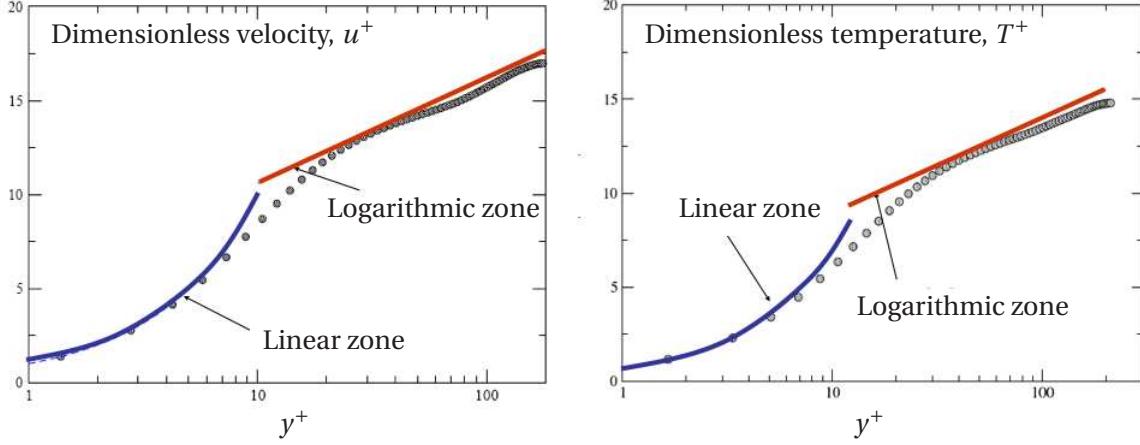
Figure 7.7: Velocity and temperature profiles of the TBL in wall units.

which in non-dimensional units gives:

$$\frac{du^+}{dy^+}(\mu^+ + \mu_t^+) = 1 \tag{7.6}$$

From Eq. (7.2) the total shear stress is considered constant all along the TBL. The total wall heat flux can be expressed: $\overline{\tau_w} = \overline{\tau_{\text{tot}}}$. The two zones of the TBL are described as follows:

1. *The linear sub-layer*

   In the first zone, in the immediate vicinity of the wall, it has been shown that the turbulent structures are almost inexistent [38]. The basic assumption is thus to consider that $\mu^+ \gg \mu_t^+$. The total shear stress in the TBL reduces to:

   $$\frac{du^+}{dy^+}\mu^+ = 1 \tag{7.7}$$

   Considering that the variation of viscosity within this small fluid layer is negligeable: $\mu_t^+ = \overline{\mu}/\overline{\mu_w} \approx 1$, integration of Eq. (7.7) gives the velocity profile:

   $$u^+ = y^+ \tag{7.8}$$

   which is an expression valid on the region $0 < y^+ < 10$. This zone is not often used for the WM approach, as the first off-wall node must be very close to the wall in order for this expression to be valid.

2. *The logarithmic sub-layer*

In the region above the linear sub-layer the opposite situation is encountered: the laminar term in the total shear stress equation is negligible compared with the turbulent term, which leads to:

$$\overline{\tau_{\text{tot}}} \approx \frac{d\overline{u}}{dy}\mu_t \tag{7.9}$$

where the turbulent dynamic viscosity μ_t is defined by the Prandtl mixing-lenght model [214]:

$$\mu_t = \overline{\rho}\,l^2\frac{d\overline{u}}{dy}$$

For near wall flows the mixing length is defined as $l = \kappa y$, where κ is the von Kármán constant which commonly takes the value $\kappa = 0.41$ [107, 7, 191, 132]. The turbulent dynamic viscosity is then expressed:

$$\mu_t = \overline{\rho}(\kappa y)^2\frac{d\overline{u}}{dy} \tag{7.10}$$

In non-diemnsional units the total shear stress reduces to:

$$\left(\frac{\overline{\rho}}{\overline{\rho_w}}\right)^{1/2} du^+ = \frac{dy^+}{\kappa y^+} \tag{7.11}$$

which can be integrated using the Van Driest transformation [66]:

$$u_{VD}^+ = \int_0^{u^+}\left(\frac{\overline{\rho}}{\overline{\rho_w}}\right)^{1/2} du^+ = \frac{1}{\kappa}\ln y^+ + C_u \tag{7.12}$$

where the classical values proposed by Österlund et al. [191] of $\kappa = 0.41$ and $C_u = 5.5$ are used.

The transition zone between the laminar linear sub-layer and the turbulent logarithmic zone is called the buffer sub-layer.

- **The thermal boundary layer**

  In a similar way, the total heat flux in the TBL is given by Eq. (7.3):

$$\overline{q_{\text{tot}}} = \overline{\rho}\,\widetilde{v''h_s''} + \overline{\rho}\sum_{k=1}^{N}\widetilde{v''Y_k''}\Delta h_{f,k}^0 - \lambda\frac{\overline{dT}}{dy} + \overline{\rho}\sum_{k=1}^{N}\widehat{h_k Y_k V_{k,y}} + \overline{q_y^r} \tag{7.13}$$

where the total heat flux is constant along all the TBL leading to $\overline{q_{\text{tot}}} \approx \overline{q_w}^f$. Again two zones can be identified:

1. *The linear sub-layer*

   In the immediate vicinity of the solid wall, the turbulent terms of the total heat flux can be neglected. If radiation effects are avoided, the total heat flux reduces to the laminar Fourier heat flux.

The total heat flux is approximated using a Reynolds analogy:

$$\overline{q}_{\text{tot}} = \overline{q_w}^f = \lambda \overline{\frac{dT}{dy}} \approx \frac{\overline{\mu C_p}}{Pr} \frac{d\overline{T}}{dy} \tag{7.14}$$

which leads to the nondimensional profile of the temperature in the linear sub-layer:

$$T^+ = Pr\, y^+ \tag{7.15}$$

2. *The logarithmic sub-layer*

   Neglecting the laminar contribution and the effects of chemistry, the total heat flux reads:

$$\overline{q}_{\text{tot}} = \frac{\mu_t \overline{C_p}}{Pr_t} \frac{d\overline{T}}{dy} \tag{7.16}$$

where the turbulent flux of sensible enthalpy $\overline{\rho} \widetilde{v'' h_s''}$ has been approximated using:

$$\overline{\rho} \widetilde{v'' h_s''} \approx -\lambda_t \frac{d\overline{T}}{dy} \tag{7.17}$$

and the turbulent heat diffusion λ_t is expressed assuming a Reynolds analogy:

$$\lambda_t = \frac{\mu_t \overline{C_p}}{Pr_t} \tag{7.18}$$

where Pr_t is the turbulent Prandtl number generally taken equal to $Pr_t = 0.7$ [131]. Introducing the nondimensional units this expression and using similarity arguments, Kader shows that the temperature distribution obeys a logarithmic law [126]:

$$T^+ = \alpha \ln(F_\kappa y^+) \tag{7.19}$$

where $\alpha = \kappa^{-1} Pr_t$ and $F_\kappa = 2.96$ are integration constants [132].

3. *Effects of chemistry*

   When the chemical terms are not neglected, the total heat flux in the boundary layer is:

$$\overline{q}_{\text{tot}} = \overline{\rho} \widetilde{v'' h_s''} + \overline{\rho} \sum_{k=1}^{N} \widetilde{v'' Y_k''} \Delta h_{f,k}^0 - \lambda \overline{\frac{dT}{dy}} + \overline{\rho} \sum_{k=1}^{N} \widehat{h_k Y_k V_{k,y}} \tag{7.20}$$

Cabrit and Nicoud [32] show that the wall heat flux can be modeled using expression:

$$\overline{q_w}^f \approx -\mu_t \left(\underbrace{\frac{\overline{C_p}}{Pr_t}}_{\text{Sensible enthalpy}} + \underbrace{\frac{1}{Sc_{t,k}} \sum_{k=1}^{N} \frac{W_k}{\overline{W}} \frac{d\overline{X_k}}{d\overline{T}} \bigg|_{\text{eq}} \Delta h_{f,k}^0}_{\text{Chemical enthalpy}} \right) \frac{d\overline{T}}{dy} \tag{7.21}$$

where the laminar contribution of the Fourier flux is neglected in the turbulent zone, the turbulent Schmidt number $Sc_{t,k}$ of species k is used to model the chemical term, and the chemical equilibrium factor $\left.\frac{d\overline{X_k}}{dT}\right|_{eq}$ is used to model the gradient of species in the TBL.

The integration of this expression in conjunction with the model for the wall shear stress $\overline{\tau_w}$, leads to a coupled expression for the velocity and temperature profiles:

$$\frac{2}{\alpha}\left(\sqrt{D}-\sqrt{D-\alpha u^+}\right) = \frac{1}{\kappa}\ln y^+ + C \tag{7.22}$$

$$T^+ = \frac{1-D}{B_q} + \frac{\alpha}{B_q}u^+ \tag{7.23}$$

where

$$\alpha = \frac{C_p B_q}{\frac{C_p}{Pr_t} + \frac{1}{Sc_{t,k}}\sum_{k=1}^{N}\left.\frac{d\overline{X_k}}{dT}\right|_{eq}\Delta h^0_{f,k}} \tag{7.24}$$

$$B_q = \frac{T_\tau}{T_w} = \frac{\overline{q_w}}{\overline{\rho_w}C_p u_\tau T_w} \tag{7.25}$$

with integration constants taking the values:

$$C = 5.5 \tag{7.26}$$

$$\frac{1-D}{B_q} = K(Pr) = \beta(Pr) - Pr_t C + \left(\frac{Pr_t}{\kappa} + 2.12(1-2\ln(20))\right) \tag{7.27}$$

$$\beta(Pr) = (3.85Pr^{1/3} - 1.3)^2 + 2.12\ln Pr \tag{7.28}$$

Numerical study of the TBL

In recent years the development of wall models has gained an impulse with the use of Direct Numerical Simulations (DNS) which permit to access information not available using experimental methods.

To study the turbulent boundary layer, DNS of turbulent channel flows are carried out. They consist on rectangular enclosures (Fig. 7.8), where the top and bottom surfaces represent solid walls, while the remaining boundaries are periodic. This configuration simulates the flow between two infinite long walls, giving access to information about the induced boundary layers between them. For such kinds of simulations Jiménez and Moin [118] show that the turbulent structures of the TBL require a minimum value for the box dimensions and the cell sizes. The literature on turbulent channel flows is recent but extensible, and include the studies made by Moin [179, 180], Kim et al. [134] Jimenez and Moser [184] among others.

In channel flow simulations, the flow is impulsed by the inclusion of a source term $\overline{\mathcal{S}_x}$, in the streamwise direction, which is constant in space and time. The value of such artificial term is given equal to
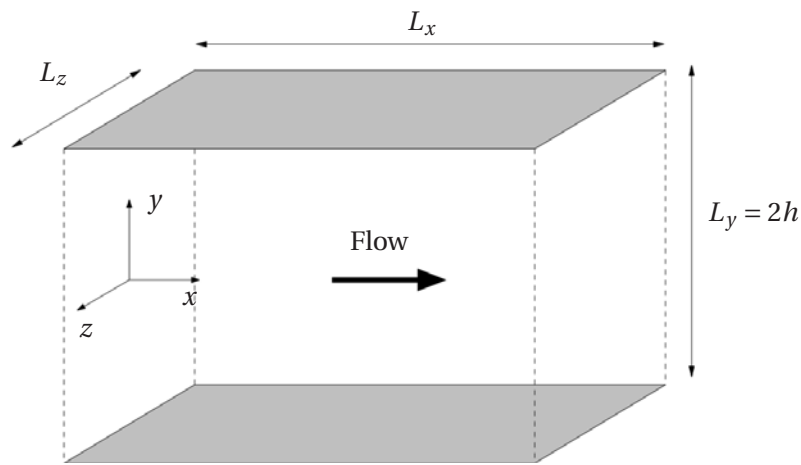
Figure 7.8: Box dimensions of the computational domain for the turbulent channel flow simulations.

the pressure gradient needed to drive the flow up to a target Reynolds number. A non-slip boundary condition in the upper and lower boundaries force the creation of a dynamic boundary layer in the flow.

In a similar way, the inclusion of a source term $\overline{\mathscr{Q}}$, constant in space and time, in the energy equation heats up the flow to a target mean volume temperature. Using an isothermal boundary condition in the upper and lower walls of the box induces the creation of a thermal boundary layer.

The wall-normal variation of every variable is obtained by statistical analysis of the DNS. Figure 7.9 shows the three steps involved in the statistical procedure: (a) firstly, a temporal averaging of the simulation is carried out and the mean and RMS values of each quantity is saved, (b) secondly a spatial averaging is carried out in one homogeneous direction, (c) and finally the same spatial averaging is performed in the second homogeneous direction.

One example of the results obtained for an anisothermal turbulent channel flow, including the effects of the chemical terms, is shown in Fig. 7.10. In these results the effects of radiation have been neglected. In order to verify if this is a valid hypothesis the inclusion of radiation in the simulations is necessary, and will be analyzed in section 7.3.3.

Once the heat flux from the fluid $\overline{q_w}^f$ has been well established, communications between the solid and the fluid solver are performed.

7.2.2 FSTI coupling

Research on the effects of FSTI in aeronautical applications is recent and not very extensive. Most of the work done in this field is related to the effects of hot gases on the structure of the guiding vanes
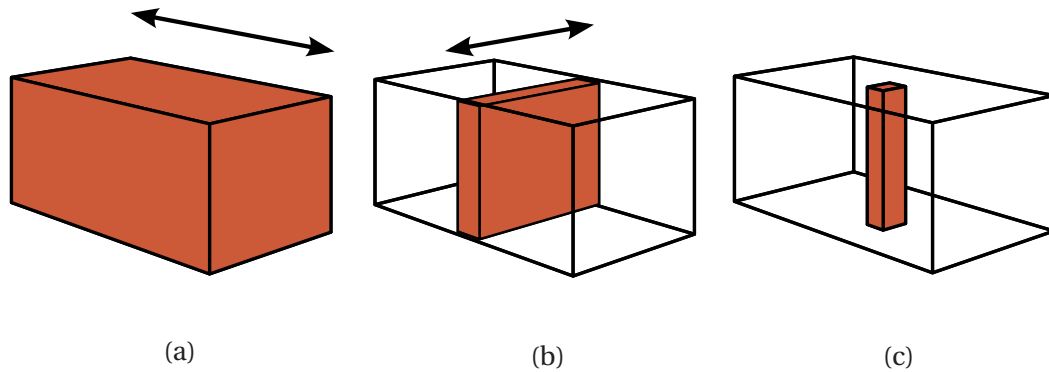
Figure 7.9: Statistical procedure for the analysis of turbulent channels: (a) temporal averaging, (b) spatial averaging in the homogeneous direction x, (c) spatial averaging in the homogeneous direction z.

at the exit of the combustion chamber [67, 266, 129, 167]. A good review of some of the work done in this area at NASA is presented by Grag [84].

In the domain of climatology coupled methods for the study of Ocean-Atmosphere-Ice and Land-Atmosphere interactions have been developed over the years [256], where asynchronous coupling of the different subsystems is widely used [267]. The stability limits of the iterative numerical procedure have been studied by different authors, including Dufresne et al. [69], Breton et al. [28], Chemin [40] and Giles [86] among others.

Introduction

Without chemistry effects due to ablation or pyrolysis, the thermal exchanges between the solid and the fluid at the interface are limited to the Fourier heat flux, which is proportional to the temperature gradient and follows Newton's heat flux law:

$$q_w^f = h^f (\overline{T}^f - T_w^f) \tag{7.29}$$

where, h^f is the heat transfer coefficient of the fluid and $\overline{T}^f$ is the mean temperature in the fluid flow. At the interface between the solid and the fluid the wall heat flux must be also equal to Eq. (7.14).

In the same way the heat flux inside the solid can be expressed using Newton's heat flux law:

$$q_w^s = h^s (T_w^s - \overline{T}^s) \tag{7.30}$$

where $\overline{T}^s$ is the mean temperature inside the solid. By convention heat flux is positive when energy is transported from the fluid to the solid.
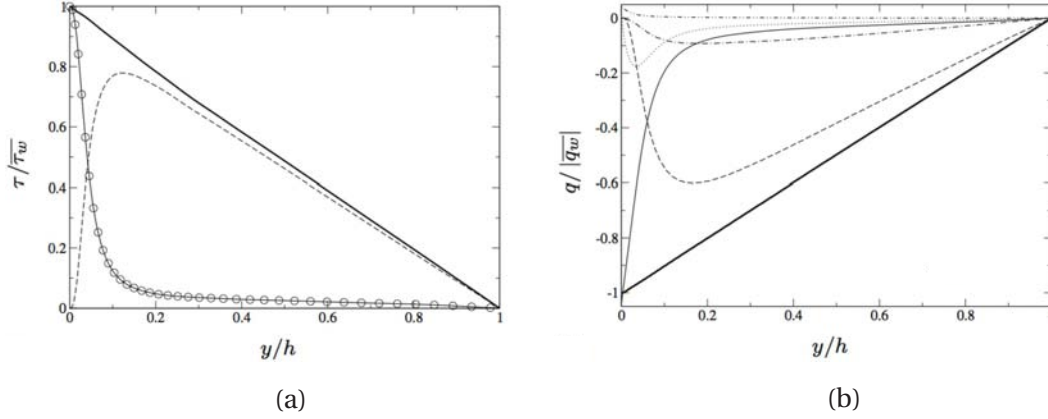
(a)   (b)

Figure 7.10: Profiles of the boundary layer on the half-height h of the channel extracted from [32]. (a) Total shear stress $\overline{\tau}_{\text{tot}}$ normalized by the wall shear stress $\overline{\tau}_w$ and its components: laminar shear stress $\overline{\mu(dy/dy)}$ (——— thin), turbulent shear stress $-\overline{\rho}\widetilde{u''v''}$ (– – – –), total shear stress $\overline{\mu(dy/dy)} - \overline{\rho}\widetilde{u''v''}$ (——— thick), approximation $\overline{\mu}\overline{du/dy}$ (∘). (b) Total heat flux $\overline{q}_{\text{tot}}$ normalized by the total heat flux at the wall $|\overline{q_w}^f|$ (——— thick) and its components: turbulent flux of sensible enthalpy $\overline{\rho}\widetilde{v''h''_s}$ (– – – –), turbulent flux of chemical enthalpy $\overline{\rho}\sum_{k=1}^{N}\widetilde{v''Y''_k}\Delta h^0_{f,k}$ (— · —), Fourier heat flux $-\overline{\lambda(dT/dy)}$ (········), viscous effect $-\int \overline{\tau_{iy}(du_i/dy)}dy$ (— ·· —).

The energy conservation imposes $q_w^f = q_w^s$ if the efficacy of the heat exchange is equal to one (no losses due to irregularities at the interface). For the same reasons the temperature of the molecules of fluid and solid in contact at the interface is the same, thus $T_w^f = T_w^s$. Shown in Fig. 7.11, the heat flux and the temperature correspond to the interface variables of the coupled FSTI system.

The numerical approach

The interface equations that close the coupled system can be written using different mathematical constructions, among which the simpler correspond to the five algebraic approaches shown bellow:

1. **Dirichlet problem:** the temperature continuity is imposed at the interface:

$$\left\{ \begin{array}{ccc} T_w^f & = & T_w^s \\ T_w^s & = & T_w^f \end{array} \right.$$

2. **Neumann problem:** at the interface the heat flux is imposed:

$$\left\{ \begin{array}{ccc} q_w^f & = & q_w^s \\ q_w^s & = & q_w^f \end{array} \right.$$
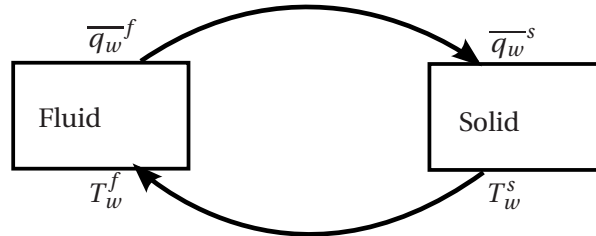
Figure 7.11: The two subsystems of the FSTI, along with the interface variables on each side of the communications loop.

3. **Mixed Neumann-Dirichlet problem:** the temperature is imposed in one side of the interface, while the heat flux is imposed in the other:

$$\left\{ \begin{array}{rcl} q_w^f & = & q_w^s \\ T_w^s & = & T_w^f \end{array} \right.$$

or,

$$\left\{ \begin{array}{rcl} T_w^f & = & T_w^s \\ q_w^s & = & q_w^f \end{array} \right.$$

This last system is generally used on FSTI configurations of experimental [75], aeronautical [84] and climatology applications [256]. Indeed, Giles [86] concludes that the key point to achieving numerical stability is the use of Neumann boundary conditions for the structural calculation and Dirichlet boundary conditions for the fluid calculation, as stability is guaranteed for $r = (\rho^f C_p^f)/(\rho^s C_p^s) \ll 1$.

4. **Mixed Neumann-Fourier problem:** in some cases stability and convergence can be enforced by changing the Neumann condition for a Fourier condition:

$$\left\{ \begin{array}{rcl} T_w^f & = & T_w^s \\ q_w^s + k T_w^s & = & q_w^f + k T_w^f \end{array} \right.$$

where k is a proportionality coefficient, similar to a heat transfer coefficient, that enhances the stability of the coupling [40, 74, 75, 67].

5. **Mixed Fourier-Fourier problem:** the enhancement of the stability of the coupling can also be forced on both sides of the interface:

$$\begin{cases} q_w^f + kT_w^f &= q_w^s + kT_w^s \\ q_w^s + kT_w^s &= q_w^f + kT_w^f \end{cases}$$

Chemin [40] gives a detailed presentation of the stability limits of the Neumann-Fourier and the Fourier-Fourier problems in the case of steady coupled applications.

In order to study the FSTI in the present work the mixed Neumann-Direchlet approximation was employed. The coupled simulations performed showed no instabilities. However the low stability range of this kind of system demands the development of a more elegant set of interface equations in the future.

Figure 7.11 shows a classical loop where the Mixed Neumann-Dirichlet problem is solved. In the present work this is the method employed to solve the FSTI. The interface equations read:

$$\begin{cases} T_w^f &= G(q_w^s) = \frac{q_w^s}{h^s} + \overline{T}^s \\ q_w^s &= F(T_w^f) = h^f(\overline{T}^f - T_w^f) \end{cases}$$

where the second relation can be written:

$$q_w^s = F(T_w^f) = F(G(q_w^s)) = H(q_w^s) \tag{7.31}$$

In this expression the function H shows a fixed point, i.e. a point for which $H(x) = x$. This fixed point problem is equivalent to the search for the zeros in expression:

$$x - H(x) = 0 \tag{7.32}$$

A fixed point problem for the thermal interaction between the fluid and the solid can be viewed as the local variation of heat flux (or temperature), at a given position in the interface Γ. The variable x can, e.g., be considered as a vector containing the values of heat flux at a one or many points in this surface. Lets consider in this case that x correspond to the value of heat flux at only one given point on the interface between the fluid and the solid. Using an iterative procedure, the fixed point problem can be solved using a relaxation process:

$$x^{n+1} = H(x^n) \quad , \quad n = 0, 1, 2, 3, \dots \tag{7.33}$$

where n is the evaluation iteration. The point x^0 is the initial value of the sequence, which in the case of the FSTI corresponds to the initial heat flux (or the initial temperature field) at one point of the interface. The iterative procedure is performed until the convergence criterion is reached:

$$||x^{n+1} - x^n|| < \epsilon \tag{7.34}$$

where ϵ is an arbitrary level of error. In the case of the FSTI, this guarantees that: $q_w^{s\,n+1} = H(q_w^{s\,n})$.
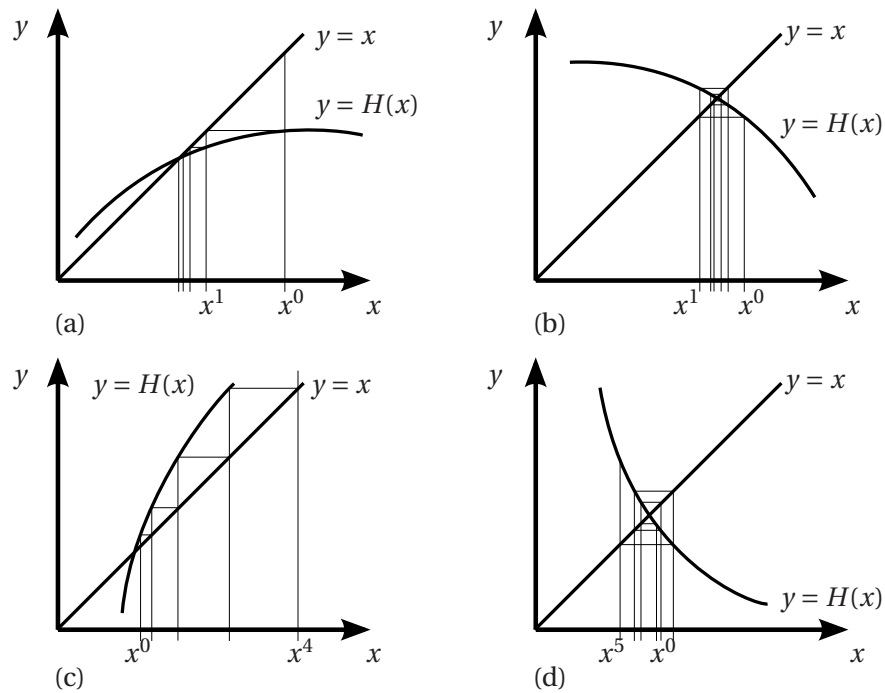
Figure 7.12: Iterative process for the system of Eq. 7.35. Four scenarios are possible: (a) monotone convergent, (b) oscillatory convergent, (c) monotone divergent or (d) oscillatory divergent process.

The iterative procedure seeks to solve the problem:

$$\begin{cases} x^{n+1} & = & y \\ H(x^n) & = & y \end{cases} \tag{7.35}$$

where y is the ordinate of the functions presented in Fig. 7.12. Finding a solution of the iterative process corresponds to finding the intersection of the two functions of Eq. (7.35). The convergence of the sequence depends on the shape of the function $H(x)$. Four scenarios are possible: (Fig. 7.12-a) if the slope of the function H is positive and lower than 1, the sequence $\{x^0, x^1, x^2, ...\}$ is monotone and converges to the solution of the system; (Fig. 7.12-b) the sequence is also convergent but oscillates around the solution of the system if the slope of the function H is negative and grater than -1; (Fig. 7.12-c) the sequence is monotone and divergent if the slope of the function H is greater than 1 and (Fig. 7.12-d) oscillatory and divergent if the slope is lower than -1.

For the divergent sequences the iterative process derives, even if the initial guess x^0 is close to the solution. The convergence of the sequence depends on the condition: $|H'(x)| < 1$. In the case of the FSTI this condition is given by:

$$|H'(q_w^s)| = \left| \frac{dF}{dT_w^f} \frac{dG}{dq_w^s} \right| < 1 \qquad (7.36)$$

where the derivatives of F and G are:

$$\frac{dF}{dT_w^f} = -h^f \qquad (7.37)$$

$$\frac{dG}{dq_w^s} = \frac{1}{h^s} \qquad (7.38)$$

leading to the convergence condition:

$$|H'(q_w^s)| = \frac{h^f}{h^s} < 1 \qquad (7.39)$$

For several years the Neumann-Dirichlet problem has been used in climatology to solve the Land-Atmosphere and the Ocean-Atmosphere coupled systems [162]. Convergence to a unique solution (a fixed point) was always assured as the ratio of the heat transfer coefficients was of the order $h^f/h^s \approx$ 0.1. With the inclusion of ice in the ocean, the value of h^s dramatically lowered, increasing the value of the ratio up to $h^f/h^s \approx 100$ rendering the coupled system unstable [28, 69].

For combustion applications it can be shown that the ratio of the convective heat coefficients at the interface is proportional to:

$$\frac{h^f}{h^s} \approx \frac{\lambda^f}{\lambda^s} \frac{(T_w^s - \overline{T}^s)}{(\overline{T}^f - T_w^f)} \qquad (7.40)$$

if we consider that the variation of temperature between the interface and the solid is the same order of magnitude that the variation between the interface and the fluid, this ratio becomes: $h^f/h^s \approx \lambda^f/\lambda^s$. Typical values of the heat conduction coefficient are:

$$\lambda_{\text{air}} = 0.025$$
$$\lambda_{\text{water}} = 0.6$$
$$\lambda_{\text{iron}} = [15; 40]$$
$$\lambda_{\text{combustion gas}} \approx 0.13$$

For combustion applications the iterative coupled systems, based on the Neumann-Dirichlet problem, the solution of the system converge to a fixed point. The iterative process can however present an oscillatory behavior as shown in Fig. 7.12-b.

Sometimes even if convergence is assured, the convergence speed of the relaxation algorithm of Eq. (7.33) is low. In order to accelerate the process one alternative consists in using the over-relaxation method, described by the sequence:

$$x^{n+1} = (1 - \omega)x^n + \omega H(x^n) \qquad (7.41)$$

where values of $\omega > 1$ are used to speedup a slow-convergent process, and values of $0 < \omega < 1$ are used to establish convergence of a diverging iterative process. Using $\omega = 0$ the iterative process ignores the evolution of x and simply imposes $x^{n+1} = x^n = x^0$. If $\omega = 1$ the method degrades back to the classical relaxation process [78].

Interface data exchanges can be optimized using more sophisticated interface operators as shown by Roux et al. [221]. Recently Roe et al. [215] introduced a much more detailed formulation of the interface equations for the FSTI. Instead of only imposing a variable exchange at the interface using the Neumann-Dirichlet problem, the interface equations are explicitly influenced by the neighboring subdomains. In the Combined Interface Boundary Condition (CIBC) method the Dirichlet condition is replaced by: $T_w^{f\,n+1} = T_w^{s\,n} + \delta T_w^{s\,n}$, where $\delta T_w^{s\,n}$ is a partial differential equation (PDE) that leads to expression:

$$T_w^{f\,n+1} = T_w^{s\,n} + \frac{\Delta t}{\rho_w^f C_{p,w}^f} \left[-\frac{\partial q_w^{f\,n}}{\partial x} + \omega \left(\frac{\partial q_w^{s\,n}}{\partial t} - \frac{\partial q_w^{f\,n}}{\partial t} \right) \right] \qquad (7.42)$$

where Δt is the time step. This method permits to broaden the stability limits of the classical staggered methods, but demands the resolution of one additional PDE at the interface [215].

In the present work all the simulations use the Neumann-Dirichlet approximation; no instabilities were observed in any of the applications.

Coupling methodology

In order to carry out coupled simulations on massively parallel computers, the data exchange frequency and the processor repartition must be optimized. These two parameters depend on the characteristic time of the solid, τ_s, the fluid, τ_f, and the velocity of each code. Coupled simulations must attain the good "physical" coupling time in the simulation at the same "CPU" time in the computer.

- **Synchronization in physical time**

  The characteristic time of the solid τ_s is many orders of magnitude higher than the characteristic time of the fluid τ_f. In the typical times simulated in an LES the temperature of the solid does not change. Using the time step of the fluid in both codes is a waste of computational resources. This problem is also present in other domains as in climate system modeling. In such case the solution consists in the asynchronous resolution of the coupled system [169, 161, 267].

  In the Asynchronous Coupled Simulations (ACS) the computed times are not the same in each code. At the interface the transfered heat flux corresponds to the mean value $\overline{q_w}^f$ over a given
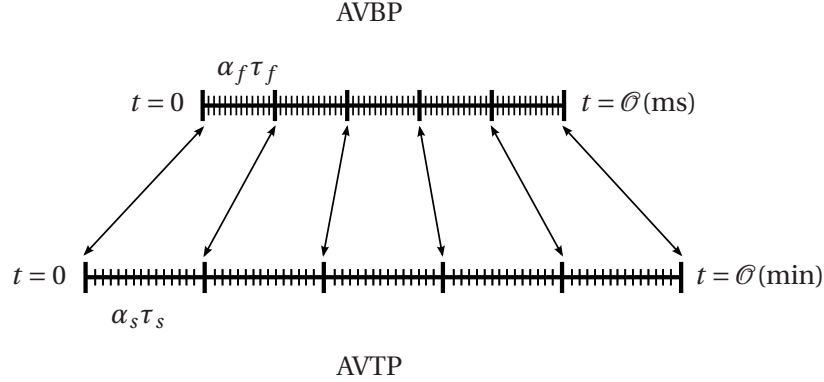
Figure 7.13: Coupling sequence of the FSTI. Both codes start at $t = 0$ but the computed physical times are different.

characteristic time $\alpha_f \tau_f$, where α_f is a nondimensional coupling factor that indicates how many characteristic times are computed between two coupling iterations. Then the solid code uses this information to carry out one simulation for $\alpha_s \tau_s$ seconds, that leads to a new value of T_w^s. This value is introduced as a boundary condition in the fluid and the cycle loops until the heat flux and the interface temperatures converge to a stable value (Fig. 7.13).

Between two consecutive coupling iterations the solid code computes a time equal to $\alpha_s \tau_s$ while the Navier-Stokes solver computes the time $\alpha_f \tau_f$. ACS are a shortcut to avoid expensive calculations by engaging in a rapid evolution of the solid to a state where the interaction between both subsystems is balanced.

A synchronization in physical time is obtained when both $\alpha_s \tau_s$ and $\alpha_f \tau_f$ are computed in each code, i.e. when the corresponding number of iterations have been calculated. The number of iterations between two coupling iterations in the ACS is obtained from expression:

$$n_f \quad = \quad \alpha_f \frac{\tau_f}{\Delta t_{\text{LES}}} \tag{7.43}$$

$$n_s \quad = \quad \alpha_s \frac{\tau_s}{\Delta t_{\text{sol}}} \tag{7.44}$$

where Δt_{LES} and Δt_{sol} correspond to the time steps of the LES and the solid codes. This values are needed in order to synchronize the data exchange and to distribute the processors between the codes.

- **Synchronization in CPU time**

  To guarantee that both codes arrive at the same time to the coupling iteration they must obey:

$$n_f t_{\text{LES}}(P_{\text{LES}}) = n_s t_{\text{sol}}(P_{\text{sol}}) \tag{7.45}$$

where t_{sol} and t_{LES} are the execution times of one iteration in the solid and fluid solvers, which depend on the number of processors allowed to each code P_{sol} and P_{LES}. This execution time can be written in other terms:

$$
\begin{aligned}
t_{LES} &= \gamma_f(P_{LES})\frac{t^1_{LES}}{P_{LES}} \\
t_{rad} &= \gamma_r(P_{rad})\frac{t^1_{rad}}{P_{rad}}
\end{aligned}
\tag{7.46}
$$

where t^1_* is the computational time on 1 processor for each solver, P_* is the number of processors available for each code and $\gamma_*(P_*)$ is the speed-up function for the LES and the conduction solvers. As shown by Gourdain et al. [94] this function may be characterized in different ways: for efficient codes the speed-up is linear, with a slope $\gamma(P) = 1$ in a perfectly scaling code. Assuming this is the case for both codes and knowing the total number of processors $P_{s\text{-}f} = P_{sol} + P_{LES}$, a balanced distribution of the processors can be obtained:

$$
\frac{P_{LES}}{P_{s\text{-}f}} = \frac{1}{1 + (n_s t^1_{sol}/n_f t^1_{LES})}
\tag{7.47}
$$

Expression (7.47) can also be written to directly show the total number of processors allocated to the solid solver:

$$
P_{sol} = P_{s\text{-}f}(1 - C_{s\text{-}f})
\tag{7.48}
$$

where,

$$
C_{s\text{-}f} = \frac{1}{1 + (n_s t^1_{sol}/n_f t^1_{LES})}
\tag{7.49}
$$

is the Solid-to-Fluid CPU coupling coefficient.

FSTI simulations are carried out using $P_{s\text{-}f}$ processors, distributed among the codes using Eq. (7.47) and (7.48). The heat conduction code performs n_s iterations and the LES code computes n_f iterations before exchanging data. Communications are handled by a coupling software, and the interface equations are applied to the exchanged data before performing again n_f and n_s iterations until the next coupling point.

In the construction of a full multi-physics system, the next step is to study the coupling between the fluid properties and the heat transfer by radiation.

7.3   Radiation-Fluid Thermal Interactions (RFTI)

7.3.1   Background

Radiation plays a central role in the heat transfer from the flame to the walls in a combustion chamber [146]. In aeronautics the current tendency is to develop lean combustion systems that can operate at high pressures [164]. This implies a rise in the energy emission by radiation, but most importantly a reduction in the available air used to cool down the solid structure. Therefore the increased radiation can eventually pose serious problems to liner durability [61].

In combustion two kinds of radiation are considered: non-luminous radiation emitted by combustion gases like CO_2, H_2O and CO (cf. section 6.4) and luminous radiation generated by soot particles (cf. section 6.6.3). Early methods that acknowledge the contribution due to radiation (both luminous and non-luminous) in aeronautical combustion chambers were summarized by Lefebvre [147]. They were based on empirical global correlations, but they can lead to inaccurate results, as local effects of radiation are not out of reach of these methods.

First reported results of gas turbine three-dimensional Radiative Heat Transfer (RHT) simulations include the work of by Mengüç et al. [171], using a P_3-approximation (cf. section 6.5.2). The authors showed a strong dependence of the radiative heat flux on the axial an radial variations of the flow properties of the calculation, thus suggesting the need for fully three-dimensional radiation simulations to capture local fluctuating radiative heat fluxes.

Radiation can also trigger local variations of the fluid flow. Interactions between the medium, the flame, the local soot concentration and radiation have been studied by different authors [87, 48, 150, 154, 268]. In particular Radiation Turbulence Interaction (RTI) is an active research area that can be traced back to the analytical studies made by Cox [50] and recently to the work of Poitou et al. [206], Coelho [46], Deshmukh et al. [58] and Gupta et al. [99].

The interaction between radiation and the fluid flow is more evident in sooting flames. Blackbody radiation by soot particles tend to emit more energy than the gas alone. Many different teams around the world are currently developing methods to correctly predict the formation and transport of soot particles and to evaluate its interaction with radiation and flames. Wang et al. [264] studied radiation in a sooting non-premixed jet flame using the P_1-approximation, detailed chemistry and the method of moments for soot prediction, and showed the importance of non-gray gas modeling. He concluded that the P_1-approximation yields to large errors in the spatial distribution of the heat flux in such flames. Narayanan and Trouvé [185] studied local flame extinction caused by soot radiation using a Discrete Transfer Method (DTM) approach. Watanabe et al. [268] used the Discrete Ordinates Method (DOM) to show the influence of radiation on soot formation in non-premixed flames.

Direct Numerical Simulations coupled with Monte Carlo or DOM methods have also been used to study the interaction between radiation and a flame front. Such studies include the work of Deshmukh et al. [58], Wu et al. [272], Roger et al. [217] and Wang [265]. With the aim of studying Radiation-

Fluid interaction using LES and DOM solvers, Poitou [204] showed that flame thickening in LES (cf. section 5.2.2) and sub-gridscale fluctuations of temperature and gas composition (cf. section 5.2.1) do not affect the radiative field at the scale of the LES mesh. However at the scale of the large turbulent structures, RFTI is not negligible and modifies the final temperature of the combustion gases, the distribution of the minor species (like CO) and the flame dynamics. The results where obtained using the same code coupling method as in the present work, and are consistent with the results previously reported by Gonçalves dos Santos et al. [64]. Other attempts to compute LES simulations with a 3D RHT solver include the work of Jones and Paul [120] and Gonçalves dos Santos [65].

7.3.2   RFTI coupling

The properties of the fluid give the value of the absorption coefficient needed for the RTE calculation. In exchange radiation induces a modification of the energy content in the fluid. The way in which this interaction is performed is presented bellow:

- **Interface variables**

  Radiation is coupled with the fluid flow via the radiative heat flux q_i^r defined in Eq. (5.56). This particular term can be separated from the other components of the heat flux vector in the energy equation. As shown in Eq. (6.64) the divergence of the radiative heat flux can be calculated using the approximation of Eq. (6.152). This term, called the radiative source term $\mathscr{S}_r$, works as a source (or sink) term in the energy equation of the fluid flow.

  Eq. (6.122) to (6.125) show that in a non-gray gas the absorption coefficient κ is a function of the temperature T, the pressure p and the gas composition (mole fractions of species X_k). The radiative code needs these fields to compute the radiative source term.

  In a coupled thermal system, $\mathscr{S}_r$, T, p and X_k are the so called interface variables ϕ_i of the RFTI. Figure 7.14 shows how data flows from the LES solver to the DOM code and vice-versa. It is important to note that even if the radiative heat flux $\mathbf{q}^r$ can be calculated from the radiative source term, the fields $\mathbf{q}^r$ and G can be useful in the analysis of the results.

- **Interface equations**

  Interface conditions for the RFTI on each side of the "interface" read:

$$\begin{cases} \kappa_v & = & f(T^f, p^f, X_k^f) \\ I_{bv} & = & g(T^f, \kappa_v) \\ \mathscr{S}_r^f & = & \mathscr{S}_r^r(I_{bv}, \kappa_v) \end{cases}$$

  where f-indexed variables correspond to the values on the fluid side of the interface and r-indexed values correspond to the values on the radiation side. The internal energy of the fluid $e = e(T^f, P^f, X_k^f)$ changes with a variation of the radiative source term $\mathscr{S}_r^f$ imposed and vise-versa. The interface equation is weakly imposed in the radiation code through the functions
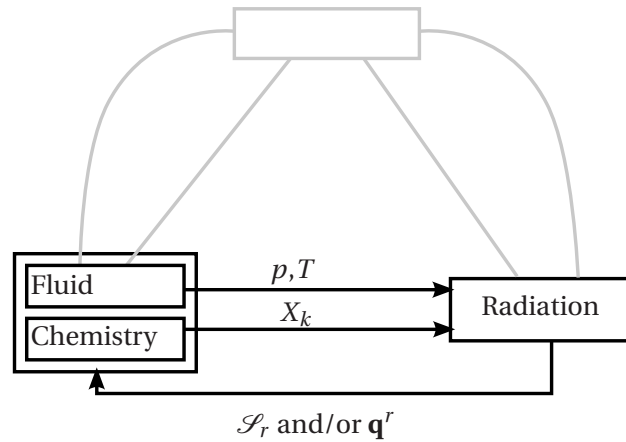
Figure 7.14: Radiation-Fluid interaction in combustion applications.

$f(T^f, p^f, X_k^f)$ and $g(T^f, \kappa_\nu)$, used to calculate the absorption coefficient of the gas and the local blackbody radiation. On the other side of the interface the radiative source term is imposed in the energy equation using a Dirichlet condition.

Interpolation at the interface between the subsystems is often used as the meshes are not necessarily coincident. In such case the interpolation process acts as a spatial filter, $\langle . \rangle$, on the interface variables exchanged, and in particular on the Dirichlet condition which becomes: $\mathscr{S}_r^f = \langle \mathscr{S}_r^r \rangle$. Poitou [204] shows that spatial filtering of the radiative source term can actually help when the interpolation method is not very accurate.

RFTI coupling methodology

- **Data exchange**

  As described in section 5.3 the LES/DNS code AVBP decomposes the computational domain in geometrical subdivisions to compute the reactive Navier-Stokes equations, over many processors of parallel computers.

  On the other side, in the RHT solver PRISSMA, parallelism is mainly done by spatial-angular-spectral decomposition (cf. section 6.6.5). This implies that each processor keeps in memory the full mesh. At the end of one radiation calculation , data is gathered in the master processor which keeps the full radiative source term field (Fig. 7.15).

  Therefore, the distributed fluid fields must be collected from the different AVBP processors and sent to all processors allocated to PRISSMA. In turn the radiation fields stocked in the master processor for PRISSMA must be correctly distributed over the AVBP processors. This data distribution process is performed by an intermediate code or interface.

The first task that the interface must accomplish is to detect and build a data exchange system between the codes, in the form of a connectivity matrix $\mathscr{X}$:

$$
\begin{aligned}
\mathscr{X}[i,p] &= [j] \\
\mathscr{X}^{-1}[j] &= [i,p]
\end{aligned}
\tag{7.50}
$$

where j is the cell in the radiation code closer to the cell i of the processor p in the LES code (Fig. 7.15).
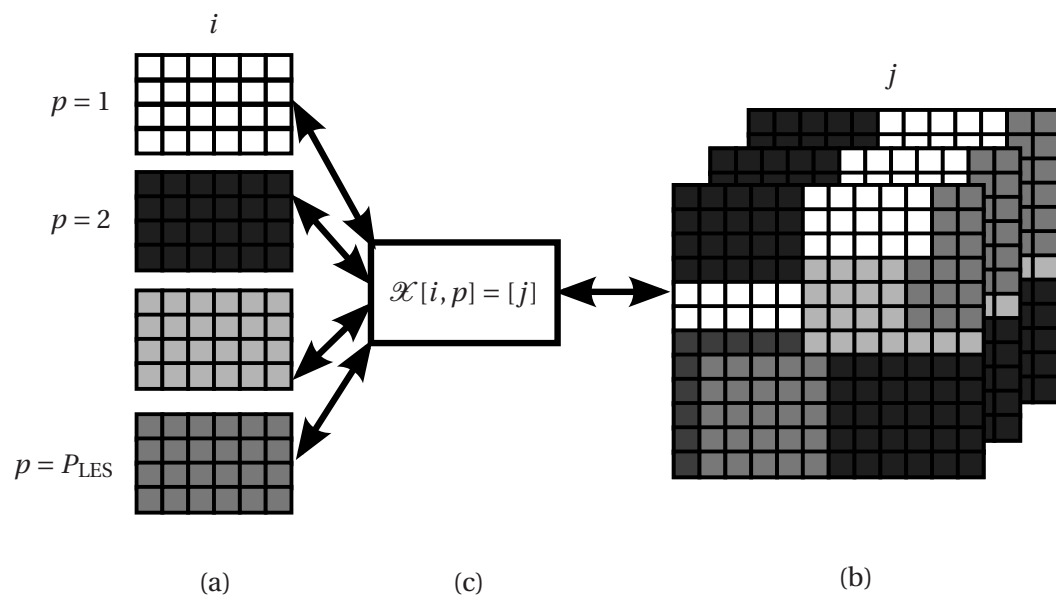
Figure 7.15: Connectivity: (a) domain partitioning in the LES code, (b) corresponding cells in the DOM code, (c) connectivity matrix $\mathscr{X}$ in the interfacing code.

The first task in coupled simulations is to communicate the coordinates of each point of the domain and their corresponding processor to the interface. The interface then builds the connectivity matrix $\mathscr{X}$ using a brute force or a search algorithm (e.g. BSP-trees).

When the two meshs are non-coincident, it is necessary to interpolate the data at the interface. The most common interpolation methods consist of: proximal interpolation (also known as nearest-neighbor interpolation), linear interpolation and conservative interpolation. In the present work only coincident meshes have been used and the interpolation aspect is not addressed.

- **Synchronization in physical time**

Compared to the scales of an industrial combustion system, light travels infinitely fast: a solution of the RTE represents an instantaneous snapshot of radiation associated to the CFD fields. The time between two consecutive snapshots, Δt_{rad}, must be big enough to see differences. This occurs when the hot and cold zones of the fluid have moved enough to change the heat fluxes, i.e. when the fluid molecules are transported from one cell to the next. One criterion for the value of the coupling time step is then given by the fluid's characteristic convective time step:

$$\tau_{conv} = \frac{l}{\overline{u}} \tag{7.51}$$

where l is a characteristic length and $\overline{u}$ is the mean velocity of the fluid. In the case of a LES mesh with minimum size Δx_{min}, Leacanu [145] and Wang [265] propose to use for the coupling time step:

$$\Delta t_{rad} \approx \tau_{conv}(l = \Delta x_{min}) = \frac{\Delta x_{min}}{\overline{u}} \tag{7.52}$$

On the other hand, LES time step for a compressible CFD solver is based on the propagation velocity of acoustics, i.e. the speed of sound. For an explicit time-marching scheme (as the one used in AVBP), a necessary condition for stability is the Courant–Friedrichs–Lewy condition (CFL), which takes the form:

$$\Delta t_{CFL} = CFL \frac{\Delta x_{min}}{\overline{u} + c_s} \tag{7.53}$$

where CFL depends on the numerical scheme and c_s is the sound speed. For the schemes used in AVBP, CFL≈ 0.7. We have the relation:

$$\Delta t_{CFL} \approx \frac{\Delta x_{min}}{c_s} = \frac{\overline{u}}{c_s} \frac{\Delta x_{min}}{\overline{u}} = M \Delta t_{rad} \tag{7.54}$$

In low Mach flows (which is the case in aeronautical combustors) the LES time step is much smaller than the radiation time step. The ratio gives the number of LES iterations that can be calculated between two DOM calculations:

$$N_{it} = \frac{\Delta t_{rad}}{\Delta t_{CFL}} \propto \frac{1}{M} \tag{7.55}$$

- **Synchronization in CPU time**

To avoid waiting processors, the CPU time required for one radiation calculation, t_{rad}, must correspond to the time needed for: $N_{it} \cdot t_{LES} = t_{rad}$, where t_{LES} is the computational time for 1 iteration of AVBP. These values depend on the number of processors allocated to each code:

$$
\begin{aligned}
t_{\mathrm{LES}} &= \gamma_{\mathrm{f}}(P_{\mathrm{LES}})\frac{t^1_{\mathrm{LES}}}{P_{\mathrm{LES}}} \\
t_{\mathrm{rad}} &= \gamma_{\mathrm{r}}(P_{\mathrm{rad}})\frac{t^1_{\mathrm{rad}}}{P_{\mathrm{rad}}}
\end{aligned}
\tag{7.56}
$$

where t^1_* is the computational time on 1 processor, P_* is the number of processors available and $\gamma_*(P_*)$ is the speed-up function. Given the total number of processors available for the coupling $P_{\mathrm{r\text{-}f}} = P_{\mathrm{rad}} + P_{\mathrm{LES}}$, and proceeding in the same way as done in section 7.2.2 for the FSTI, a balanced distribution of the processors can be obtained:

$$
P_{\mathrm{LES}} = \frac{P_{\mathrm{r\text{-}f}} \cdot t^1_{\mathrm{LES}}}{t^1_{\mathrm{rad}}/N_{\mathrm{it}} + t^1_{\mathrm{LES}}}
\tag{7.57}
$$

This resource distribution was first proposed in [6]. To directly obtain the number of processors allowed to the radiation code:

$$
P_{\mathrm{rad}} = P_{\mathrm{r\text{-}f}}(1 - C_{\mathrm{r\text{-}f}})
\tag{7.58}
$$

where,

$$
C_{\mathrm{r\text{-}f}} = \frac{t^1_{\mathrm{LES}}}{t^1_{\mathrm{rad}}/N_{\mathrm{it}} + t^1_{\mathrm{LES}}}
\tag{7.59}
$$

is the Radiation-to-Fluid CPU coupling coefficient.

Other expressions can be derived when the speedup is not perfect. In the case where the speed-up shape function is linear but non perfect ($\gamma_*(P_*) = \text{constant} = \gamma_*$), expression (7.57) can be written:

$$
P_{\mathrm{LES}} = \frac{P_{\mathrm{r\text{-}f}} \cdot \gamma_{\mathrm{f}} t^1_{\mathrm{LES}}}{\gamma_{\mathrm{r}} t^1_{\mathrm{rad}}/N_{\mathrm{it}} + \gamma_{\mathrm{f}} t^1_{\mathrm{LES}}}
\tag{7.60}
$$

Finally, for a non linear speed-up function ($\gamma_*(P_*) \neq \text{constant}$), Eq. (7.60) must be resolved implicitly using an iterative method in order to obtain the optimum processor repartition.

7.3.3 Effects of radiation on the thermal boundary layer

In section 7.2.1 it was shown that the heat transfer between the solid and the fluid is driven by the thermal boundary layer in the near-wall flow. A wall model (WM) was presented for non-reacting (Eq. 7.19) and reacting flows (Eq. 7.23). In both cases the effects due to radiation where neglected.

The effects of the radiative heat flux in channel flows was investigated by Soufiani et al. [242], but it was only recently that the term q^r_y of the total heat flux (Eq. 7.13) was studied using the DNS approach coupled with a realistic RTE solver [5].

Following the statistical approach presented in section 7.2.1, DNS of two turbulent anisothermal and reacting channel flows where performed: in the first case a *Weak Gradient* (WG) simulation is carried out in a channel with a half-height $h = 22$ [mm] where the difference between the solid wall temperature and the mean volume temperature of the gas is $\Delta T = 250$K. In the second case a *Strong Gradient* (SG) simulation is performed in a channel with half-height $h = 30$ [mm] and with a temperature difference of $\Delta T = 1250$K.

Simulations including radiation have been performed on the same cases. Comparisons between WG and the *Weak Gradient with Radiation* (WG+R) case and between SG and the *Strong Gradient with Radiation* (SG+R) permit to identify the role of radiation in the structure of the TBL.

Details on the friction Reynolds number, Re_τ, the flow Reynolds number, Re, the bulk temperature, T_b, the wall temperature, T_w and the mesh are presented in Table 7.3 for each simulation. Both simulations used hexahedral elements with a wall-normal refinement that guarantee a position of the first off-wall point at $y^+ < 1$.

Table 7.3: Anisothermal turbulent channel: simulation parameters.

Case	Re_τ	Re	T_b	T_w	h[mm]	Nodes	Δx^+	Δy^+	L_x	L_y	L_z
WG	400	7530	2000	1750	22	$44 \times 159 \times 44 = 307\,824$	32	12	$3.5h$	$2h$	$1.3h$
SG	670	5000	2350	1150	30	$77 \times 169 \times 80 = 1\,041\,040$	34	12	$3.9h$	$2h$	$1.5h$

In both cases the gas is a mixture of seven reacting species describing the products of combustion of hydrocarbons: CO, CO_2, H, H_2, H_2O, OH and N_2. The chemical kinetic scheme employed was developed by Artal et al. [12], and is composed of the seven reactions presented in Table 7.4.

Table 7.4: Chemical kinetic scheme used in the simulations (Artal et al. [12]).

Reactions:		
$2\,H + M$	$\rightleftharpoons$	$H_2 + M$
$2\,H + H_2$	$\rightleftharpoons$	$2\,H_2$
$2\,H + H_2O$	$\rightleftharpoons$	$H_2 + H_2O$
$2\,H + CO_2$	$\rightleftharpoons$	$H_2 + CO_2$
$H + OH + M$	$\rightleftharpoons$	$H_2O + M$
$OH + H_2$	$\rightleftharpoons$	$H + H_2O$
$OH + CO$	$\rightleftharpoons$	$H + CO_2$

Figure 7.16 shows the instantaneous temperature and CO_2 mass fraction fields of the SG case on planes located near the solid walls and the periodic boundary conditions. The turbulent structures
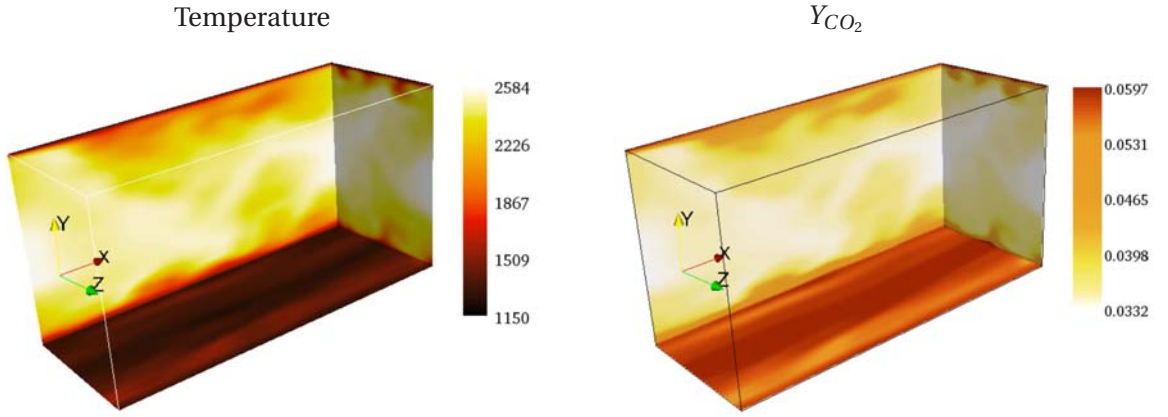
Temperature Y_{CO_2}

Figure 7.16: Instantaneous temperature and CO_2 mass fraction fields for the SG case.

are evident in both fields. Ligament structures can also be observed near the solid wall. Eddy detachment from the solid walls can also be observed. These figures clearly show that the simulations are turbulent and inhomogeneous.

In a multicomponent reacting turbulent flow, the energy conservation can be expressed in terms of the specific enthalpy[4]:

$$\rho \frac{Dh}{Dt} = \frac{Dp}{Dt} + \tau_{ij} \frac{\partial u_i}{\partial x_j} - \frac{\partial q_i}{\partial x_i} + \mathcal{Q} \tag{7.61}$$

where $\mathcal{Q}$ is a constant source term in space and time used to maintain the mean temperature of the fluid at the target value.

Applying the statistical averaging procedure presented in section 7.2.1 to Eq. (7.61) the following is obtained:

$$\overline{\frac{d}{dy}\rho v h} = \overline{v \frac{dp}{dy}} + \overline{\tau_{iy} \frac{du_i}{dy}} - \overline{\frac{dq_y}{dy}} + \overline{\mathcal{Q}} \tag{7.62}$$

From the continuity equation it can be shown that $\widetilde{v} = $ constant $= 0$, as the normal velocity at the wall is equal to zero. Hence the term $\widetilde{vh}$ can be considered equal to: $\widetilde{vh} = \widetilde{v}\widetilde{h} + \widetilde{v''h''} = \widetilde{v''h''}$. Eq. (7.62) can then be written:

$$\frac{d\overline{\rho}\widetilde{v''h''}}{dy} = \overline{v \frac{dp}{dy}} + \overline{\tau_{iy} \frac{du_i}{dy}} - \overline{\frac{dq_y}{dy}} + \overline{\mathcal{Q}} \tag{7.63}$$

---

[4]Reference [203] gives details on the different forms of the energy transport equation.

Neglecting the pressure forces $\overline{vdp/dy}$ and viscous effects[5] in the wall normal direction $\overline{\tau_{iy}du_i/dy}$, and decomposing the heat flux q_y in its different terms, equation (7.63) can be rearranged as:

$$\frac{d\overline{q_{tot}}}{dy} \approx \frac{d}{dy}\left(\underbrace{\overline{\rho}\widetilde{v''h_s''} + \overline{\rho}\sum_k \widetilde{v''Y_k''}\Delta h_{f,k}^0}_{\overline{q_y^{turb}}} + \underbrace{\overline{\rho h_k Y_k V_{k,y}}}_{\overline{q_y^{multi}}} \underbrace{-\lambda\frac{dT}{dy}}_{\overline{q_y^{Fourier}}} - \overline{q_y^r}\right) = \overline{\mathscr{Q}} \qquad (7.64)$$

where $\overline{q_{tot}}$ is the total heat flux, $\overline{q_y^{turb}}$ is the turbulent flux of specific enthalpy[6], $\overline{q_y^{multi}}$ is the multi-component laminar flux and $\overline{q_y^{Fourier}}$ is the Fourier flux. These three terms are compared against the radiative flux term $\overline{q_y^r}$ in the WG+R and the SG+R cases. The mean value of the energy source term $\overline{\mathscr{Q}}$ is constant in the wall-normal direction, and that the total heat flux $\overline{q_{tot}} = \overline{q_y^{turb}} + \overline{q_y^{multi}} + \overline{q_y^{Fourier}} + \overline{q_y^r}$ has a linear profile of slope $\overline{\mathscr{Q}}$.
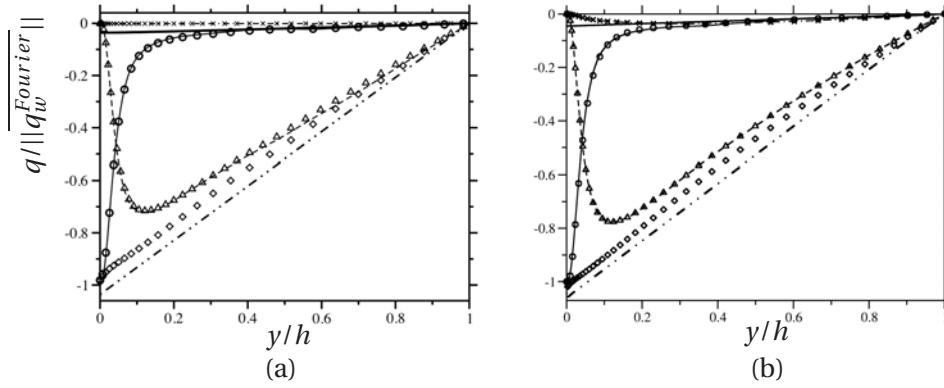
Figure 7.17: Heat flux balance scaled by the modulus of the Fourier flux at the wall $||\overline{q_w^{Fourier}}||$. (a) WG case (b) SG case. Symbols correspond to simulations without radiation, and lines to coupled multicomponent simulations with radiation.   — ·· — and ◊: total heat flux q_{tot};   —— and ○: Fourier heat flux $\overline{q_y^{Fourier}}$;   — · — and ×: multicomponent laminar flux $\overline{q_y^{multi}}$;   - - - - and △: turbulent flux of specific enthalpy $\overline{q_y^{turb}}$;   —— : radiative heat flux.

Each term of Eq. (7.64) is plotted in Fig. 7.17 using symbols for the WG and the SG cases and lines for the WG+R and the SG+R cases. In every case the Fourier heat flux is maximum at the wall, but rapidly vanishes in the turbulent zone. In this area of the TBL, the contributions of the turbulent fluxes is dominant over the other terms. All the terms show the same profiles in the coupled and the

---

[5]In the present simulation the mach number is low.

[6]This term can be written in three different ways: $\overline{q_y^{turb}} = \overline{\rho}\widetilde{v''h_s''} + \overline{\rho}\sum_k \widetilde{v''Y_k''}\Delta h_{f,k}^0 = \overline{\rho\widetilde{vh_s}} + \overline{\rho}\sum_k \widetilde{vY_k}\Delta h_{f,k}^0 = \overline{\rho\widetilde{vh}} = \overline{\rho v''h''}$

non coupled simulations, except for the total heat flux $\overline{q_{tot}}$. This quantity is affected by the inclusion of the radiative heat flux. The difference in the slope on both cases is compensated by the inclusion of $\overline{q_y^r}$.

For the cases WG and WG+R, the optical thickness of the boundary layer can be calculated from the mean Planck absorption coefficient $\overline{\kappa}_P$ (Eq. 6.148) and the channel half-height: $\tau = \overline{\kappa}_P h \approx 0.0066 \ll 1$. This value indicates that less than 1% of the energy emitted at the center of the channel is absorbed by the TBL. Most the radiated energy impact the solid walls before getting absorbed by the medium. This is the reason why, while the total heat flux $\overline{q_{tot}}$ is incremented, no component seems affected by the inclusion of radiation.

The total heat flux at the wall $\overline{q_w}$ is equal to the total heat Fourier flux at the wall, incremented by the radiative heat flux $\overline{q_w^r}$. In the case of the WG+R case the total parietal heat flux shows an increment of 7% compared with the WG case. For the SG+R case, where the temperature difference is higher, the inclusion of radiation increments wall heat flux by only 4%. Figure 7.17 shows that the differences in the SG case are less important that the differences in the WG case: heat diffusion is more increased by temperature than radiation.

The present conclusion may not be valid for sooty cases where optical thicknesses may increase significantly. It was shown in Fig. 6.29 that even a low concentration of soot can strongly influence the absorption coefficient of the media, in particular at high temperatures. Such applications include ablating components of (e.g. in rocket nozzles) and pyrolyzing surfaces.

Law of the wall including the radiative heat flux

The effects of radiation in the TBL are only observed at the wall. Absorption is minimum and all the energy emitted by the hot spots is directly transfered to the solid. The total heat flux imposed at the wall can be calculated using a classical wall model, q_w^{WM}, corrected with the value of the radiative heat flux obtained from a RTE solver $q_w^{r,f}$:

$$q_w^f = q_w^{\text{WM}} + q_w^{r,f} \tag{7.65}$$

In aeronautical applications one of the zones where the thermal stress is stronger is in the liner that isolates the hot combustion chamber. Figure 7.18 gives an idea of the temperature evolution through a liner, where the inferior zone represents the inside of the combustion chamber and the superior zone the annulus that feeds with air the system. In such configurations, where the external flow is at low temperature, the combustion chamber losses heat through the walls by convection, conduction and radiation.

Continuity of energy imposes a continuity in the heat flux at the internal wall $w2$, inside the solid and at the external wall $w2$:

$$q_{w1}^f = q_{w1}^{\text{WM}} + q_{w1}^{r,f} = q^s = q_{w2}^s \tag{7.66}$$
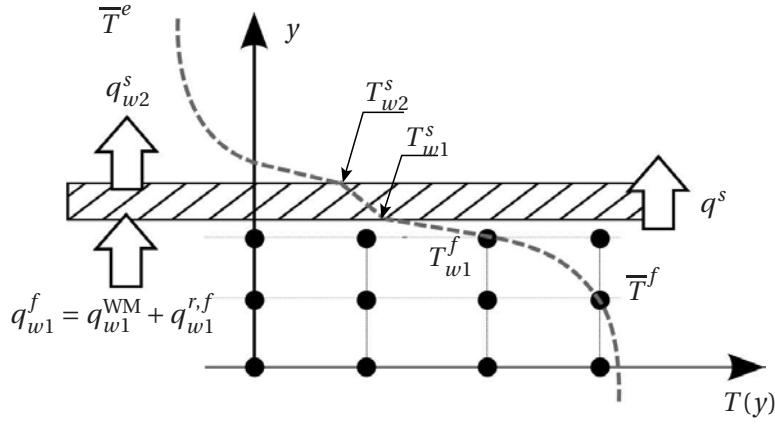
Figure 7.18: Schematic representation of heat fluxes through a solid liner of a combustion chamber. At the lower side of the wall the LES mesh is represented by the dots. The evolution of the temperature between the hot interior of the chamber and the external flow is represented by a dashed line.

The key point is to express the total heat losses using the known values: the mean external temperature in the annulus $\overline{T}^e$, the mean temperature at the first off-wall node $\overline{T}^f$, the thermal conductivity of the solid λ^s, the wall thickness e, the exchange coefficient at the external wall h_{w2} and the radiative heat flux of the fluid at the wall $q_{w1}^{r,f}$.

Eq. (7.66) can be expressed using Newton's heat flux law:

$$h_{w1}(T_{w1}^f - \overline{T}^f) + q_w^{r,f} = h^s(T_{w2}^s - T_{w1}^s) = h_{w2}(\overline{T}^e - T_{w2}^s) \tag{7.67}$$

where the heat transfer coefficients h correspond to the inverse of the thermal resistance: $r = 1/h$. The same expression can then be written:

$$\frac{(T_{w1}^f - \overline{T}^f) + r_{w1}q_w^{r,f}}{r_{w1}} = \frac{(T_{w2}^s - T_{w1}^s)}{r^s} = \frac{(\overline{T}^e - T_{w2}^s)}{r_{w2}} \tag{7.68}$$

where the thermal resistance of the solid wall can be written: $r^s = \lambda^s/e$.

Denoting $r_t = r^s + r_{w2}$ the equivalent resistance between the interior of the solid wall and the external flow in the annulus, the total heat flux at the internal interface of between the fluid and the solid can be written:

$$q_{w1}^f = \frac{(\overline{T}^e - \overline{T}^f + r_{w1}q_w^{r,f})}{r_t + r_{w1}} \tag{7.69}$$

if r_t is given as an input, the only unknown value in this expression is the resistance r_{w1}. This quantity can be obtained from the classic thermal law of the wall: $r_{w1} = (T_{w1}^f - \overline{T}^f)/q_{w1}^{\text{WM}}$.

The total heat flux imposed in the LES code is q_{w1}^f, where the contributions of the convective heat

flux and the radiative heat flux can be clearly identified:

$$q_{w1}^f = \frac{\overline{T}^e - \overline{T}^f}{r_t + r_{w1}} + \frac{q_w^{r,f}}{r_t/r_{w1} + 1} \tag{7.70}$$

Note that neglecting the radiative heat flux reduces expression (7.70) to the classical law of the wall.

7.4 Solid-Radiation Thermal Interactions (SRTI)

The remaining interaction in the thermal system corresponds to the Solid-Radiation Thermal Inter-action (SRTI). Radiative heat transfer involving non-transparent solids is performed in two ways:

- **by direct solid-to-solid interaction:** if the gas between surfaces 1 and solid 2 is considered transparent, radiative heat transfer can be directly calculated from the geometrical properties of the surfaces and their temperatures T_1 and T_2 by:

$$q_{1 \to 2}^r = h_r F_{12}(T_1 - T_2) \tag{7.71}$$

  where the radiative exchange coefficient $h_r = 4\epsilon\sigma T_m^3$ with the mean temperature $T_m = (T_1 + T_2)/2$. The view factor F_{12} corresponds to the fraction of the energy emitted by surface 1 and received by surface 2. This factor is purely geometrical and can be calculated using a double surface integral, or for simple geometries can be consulted in a database [177, 236].

  If surface 1 exchanges heat with N other surfaces, the net heat flux is given by:

$$q_1^r = h_r(T_1 - T_r) \tag{7.72}$$

  where T_r is the radiant temperature of the system, which is a mean weighted temperature:

$$T_r = \sum_{k=1}^{N} F_{1 \to k} T_k \tag{7.73}$$

  Computer programs that solve large problems using this method include TRASYS [116] and Thermal Simulation System [43] developed by NASA. Their main goal is to calculate the view factors (using numerical integration or Monte Carlo methods) and to solve the surface-to-surface interaction matrix.

- **by direct solid-fluid-solid interaction:** if the gas between the solid walls of the system is not transparent, the computation of the radiative heat fluxes must be carried out using the tools presented in this work. The heat flux imposed to the solid is the addition of the convective and the radiative heat fluxes, that in the case of a wall-modeled LES simulation takes the form of Eq. (7.70).

In the present work the SRTI has not been studied independently, but it is one subsystem of the fully Multi-Physics Coupling (MPC). A SRTI coupled system works using almost the same principles as a FSTI system:

- **Interface variables**:

  At the interface between the radiation and the conduction subsystems, on the wall surface, the exchanged quantities are the radiative heat flux q_w^r and the wall temperature T_w^s (Fig. 7.19).
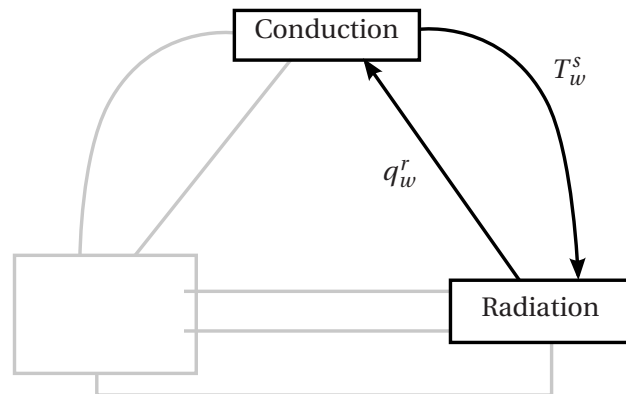
Figure 7.19: Data exchange between the radiation and the conduction subsystems.

- **Interface equations**

  The system is closed using a Neumann-Dirichlet iterative process:

$$\begin{cases} T_w^r & = & T_w^s \\ q_w^s & = & q_w^r \end{cases}$$

In its present state, the developed software do not permit to directly interconnect the radiation and the conduction solvers. Data exchange is mainly performed through the LES solver, which centralizes the problem. This method is efficient in three aspects:

- with this approach no interfacing, interpolation or connectivity is needed between the radiative and the conduction solvers. They are independent from each other.

- secondly it allows to easily unplug the units to study the FSTI and the RFTI independently.

- an finally it reduces communications and simplifies the technical set-up.

Other possible uses of the SRTI involve the heating and cooling of semi-transparent solids where radiation can penetrate, as for example in glass, plexiglas or semi-transparent plastic in photovoltaic captors, glass fabrication and thermal isolation of buildings. In such case a radiative source term might be calculated inside the solid using a similar procedure than the one presented in the RFTI.

Applications where only radiation and conduction are involved are not in the scope of this work. However the implementation of a SRTI coupled system using the available units is easy to develop if needed.

7.5 Multi-physics coupling

7.5.1 The time scales of heat transfer

There is an inverse relashionship between the characteristic time of each transfer mode and the restitution time of the simulations performed with each code. As shown in Fig. 7.20, conduction, which in industrial applications has a large characteristic time, has a computational restitution time[7] ten times smaller than the combustion code. On the other hand, radiation, where the characteristic time of the phenomena is driven by the speed of light, has a CPU restitution time $100\,000$ times bigger[8] than conduction.
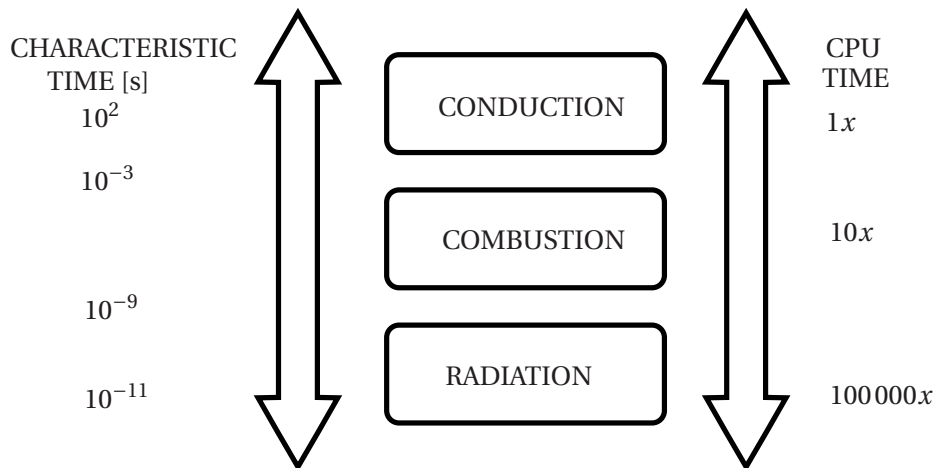
Figure 7.20: Characteristic time and computational restitution time scales for each heat transfer mode.

---

[7]The computational restitution time is the total computational time per processor per node of the mesh.
[8]Comparisons made using the SNBcK model for the radiation code.

This is one of the reasons why MPC are difficult to treat: short term variations take much more time to integrate than long term variations in heat transfer numerical methods. Another characteristic of multi-physics is that it has to deal with different physical time scales. In the FSTI and RFTI, synchronization in time deals with the problems caused by the characteristic times (left arrow in Fig. 7.20), while CPU synchronization deals with the computational speed (right arrow in Fig. 7.20).

The techniques used to perform MPC simulations require two additional steps: first the communications scheme of the MPC should be addressed, and second a new processor repartition must be added in order to balance the CPU time distribution between the three codes.

7.5.2 Multi-physics coupling (MPC)

The three simulation codes AVBP, AVTP and PRISSMA are coupled by the superposition of the FSTI and the RFTI coupled systems. The interface equations and variables in the MPC are those presented in the previous couplings.

Fig 7.21 shows how the coupling loop is performed. Note that all data passes through the combustion code, i.e. no direct communications are needed between the Radiation and the conduction code as no radiation effects are computed at the interior of the solid.
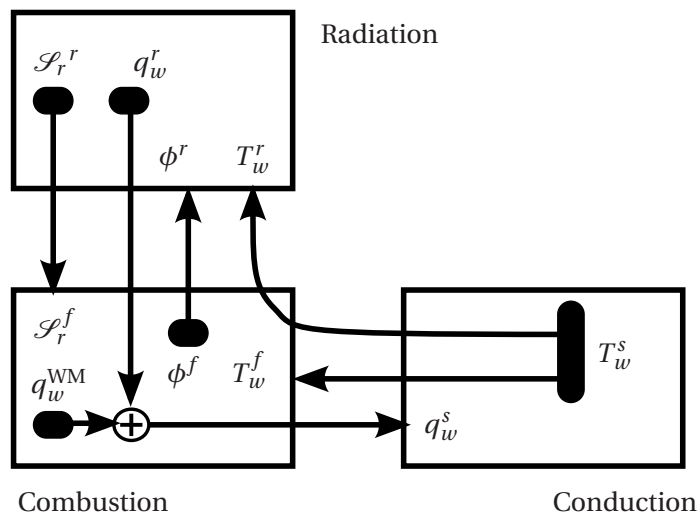
Figure 7.21: Data exchange between the three subsystems in the MPC.

The temperature of the solid at the interface with the fluid T_w^s is communicated to the combustion code, which in turn send the information to the radiation code. The fluid properties $\phi^f = \{p^f, T^f, Y_k^f\}$ are also transmitted to the radiation solver, which uses these two informations to calculate the radia-

tive source term $\mathscr{S}_r{}^r$ and the radiative heat flux at the solid walls q_w^r. In the combustion solver the knowledge of the interface conditions $\mathscr{S}_r{}^f$ and T_w^f permits to calculate the new fluid properties ϕ^f and the heat losses at the interface with the wall q_w^{WM} (when using a wall model approach). The total heat flux imposed at the solid boundary q_w^s is equal to the addition of the radiative and the convective heat fluxes.

7.5.3 Synchronization of the solvers

Given a total number of available processors P_{tot}, one part will be used to load the three solvers and the remaining processors are used to pilot the coupling and run the interfacing codes. Assuming that the execution speed is only influenced by the computational speed of the simulation codes the total P_{tot} processors are divided in a control group, P_c (used by the coupler and the interfacing codes that handle the communications between the solvers), and a simulation group of P cores: $P_{\mathrm{tot}} = P + P_c$.

In general the radiation code requires more memory and CPU resources than the solid and LES codes. It is then preferred that this code performs the RHT integration on independent cores of the computer. On the other hand AVBP and AVTP can run on independent cores or sharing all the processors in a SCS or PCS coupling strategy (see section 7.1.4).

Processor sharing

In the case where solid and fluid solvers share all the processors, synchronization in CPU time can be achieved only if the next expression is verified:

$$t_{\mathrm{rad}} = N_{\mathrm{it}}\, t_{\text{s-f}} \tag{7.74}$$

with,

$$t_{\text{s-f}} = \frac{t_{\mathrm{LES}}^1}{P_{\mathrm{LES}}} + \frac{t_{\mathrm{sol}}^1}{P_{\mathrm{sol}}} = \frac{t_{\mathrm{LES}}^1 + t_{\mathrm{sol}}^1}{P_{\text{s-f}}} \tag{7.75}$$

where $P_{\text{s-f}} = P_{\mathrm{LES}} = P_{\mathrm{sol}}$ is the number of processors shared by the fluid and solid codes, and t_*^1 is the time for one iteration of the respective code on one processor.

As shown in Eq. (7.74) the resources distribution must guarantee that the Radiation-Fluid coupling is performed in a synchronized way. FSTI coupling is not explicitly developed because the overall shared computational time $t_{\text{s-f}}$ takes into account the speed limitations caused by the shared processors.

The ratio between the processors needed by AVBP and AVTP against the number of processors needed by PRISSMA can be expressed using Eq. (7.76):

$$\frac{P_{\text{s-f}}}{P_{\text{rad}}} = \frac{c_s}{\text{CFL}\overline{u}} \frac{t_{\text{LES}}^1 + t_{\text{sol}}^1}{t_{\text{rad}}^1} \tag{7.76}$$

Independent run

In order to know the processor distribution in a coupled simulation where no core is shared, the three unknowns P_{rad}, P_{sol} and P_{LES} can be obtained by resolving the system composed of Eq. (7.57), Eq. (7.47) and Eq. (7.77).

$$P = P_{\text{rad}} + P_{\text{LES}} + P_{\text{sol}} \tag{7.77}$$

The LES code is shared by the two elementary couplings (Fluid-Solid and Radiation-Fluid). This implies that the number of processors for the LES code must be the same in both couplings and must verify:

$$P_{\text{r-f}}C_{\text{r-f}} = P_{\text{s-f}}C_{\text{s-f}} = P_{\text{LES}} \tag{7.78}$$

$$P_{\text{r-f}} = C \cdot P_{\text{s-f}} \tag{7.79}$$

where $P_{\text{r-f}}$ and $P_{\text{s-f}}$ are the total allowed processors for the RFTI coupling and the FSTI coupling respectively, and the constant C is the simulation CPU coupling coefficient, obtained from the properties of each code and the coupling frequencies:

$$C = \frac{C_{\text{s-f}}}{C_{\text{r-f}}} = \frac{t_{\text{LES}}^1 + \frac{t_{\text{DOM}}^1}{N_{\text{it}}}}{t_{\text{LES}}^1 + \frac{n_s}{n_f} t_{\text{sol}}^1} \tag{7.80}$$

The total number of processors available for the full coupling is given by Eq. (7.77).

The first and second terms on the RHS of eq.(7.77) represent $P_{\text{r-f}}$ whereas the second and third terms represent $P_{\text{s-f}}$. Combining these expressions, it can be shown that for a given total number of processors P, the optimum number of processors used by the LES code is obtained by:

$$P_{\text{LES}} = \frac{P}{\frac{1}{C_{\text{r-f}}} + \frac{1}{C_{\text{s-f}}} - 1} \tag{7.81}$$

Once the value of P_{LES} is calculated, Eq. (7.57) and (7.47) can be used to obtain $P_{\text{r-f}}$ and $P_{\text{s-f}}$. The optimum number of processors allowed to the radiation and the solid solvers is given by:

$$P_{\text{rad}} = P_{\text{r-f}} - P_{\text{LES}} \tag{7.82}$$

$$P_{\text{sol}} = P_{\text{s-f}} - P_{\text{LES}} \tag{7.83}$$

Using the data given in Table 7.5 a simulation carried out on $P = 256$ processors will be distributed[9]: $P_{\text{LES}} = 176$ for the combustion code, $P_{\text{rad}} = 79$ processor for the radiation code and $P_{\text{sol}} = 1$ for the solid conduction code.

Table 7.5: Data obtained from a coupling sequence in which a small solid is plunged inside a large fluid domain. Because of the differences on mesh sizes the solid simulation runs comparatively faster.

Quantity	Value
t_{sol}^1	0.08
t_{LES}^1	13.44
t_{DOM}^1	480
N_{it}	80
n_s	648
n_f	615
$C_{\text{r-f}}$	0.6893
$C_{\text{s-f}}$	0.9937
C	1.4416

[9]Ultimately integer values of the obtained processor distribution are used. Values smaller than one must be rounded up to 1.

Part III

Multi-physics simulation of an helicopter combustion chamber

<div style="text-align: right; font-size: 3em;">8</div>

LES simulation of an helicopter combustion chamber

In this part, the the simulation codes (AVBP, AVTP and PRISSMA) and the coupling tools presented along the previous chapters are used to study the influence of heat transfer in an industrial application: the combustion chamber of an helicopter. The main objective is to show the feasibility of such kind of simulations and the differences encountered between the coupled and the uncoupled simulations.

First an uncoupled LES simulation is performed and presented in this chapter as a reference. Details on the simulated case, the numerical approach and an analysis of the mean and the instantaneous solutions are presented. In chapter 9 a RFTI coupling is performed and the effects of radiation in aeronautical combustion chambers is studied. Then, a FSTI coupled simulation is performed in order to evaluate the effects caused by the inclusion of heat conduction on the injector of the combustion chamber, and the results are presented in chapter 10. Finally, in chapter 11, a MPC simulation including conduction, combustion and radiation is performed. It will be shown that taking into account the coupled thermal effects can lead to variations in the energy distribution in the combustion chamber.

Contents

A reference uncoupled LES was performed using the standard tools of AVBP. Results are presented in the present section. A comprehensive presentation of the case studied here can also be found in the thesis of G. Boudier [19], who presented his main results in [20] and [21].

8.1   The study case

The application consists on the simulation of the combustion chamber of a gas turbine that powers an helicopter (Fig. 8.1). The engine generates approximatley 400 kW of power at take off, and is composed of a centrifuge compressor, a combustion chamber and two turbine stages (high and low pressure). The energy generated is delivered to the helicopter's rotor via a transmission box. The combustion chamber is designed as a reverse-flow annular combustor. Such geometry is specially well adapted to the small space available in an helicopter engine, but its volume to area ratio demands a complex wall cooling system [146]. Figure 8.1 (b) shows the toroidal shape of the chamber and, and a schematic representation of one sector of the chamber is shown in Fig. 8.2. The fuel is injected into the chamber through a vaporizer: the T-shaped injector is immersed in the flame tube and allows the vaporization of the liquid fuel before it reaches the combustion zone. In the primary zone of the combustion chamber no liquid phase is present. The injected mixture is only composed of gaseous fuel and air.

Figure 8.3 (left) shows the main zones of the combustion chamber: the primary zone (A), the intermediate zone (B), the dilution zone (C) and the chamber exit (D). The relative position of any component of the chamber with respect to the motor axis is used to differentiate the relative location of each element (Fig. 8.3-right): structures located below the injector belong to the "internal side" of the chamber (E) and structures located above the injector belong to the "external side" (F).

In the internal side of the flame tube a series of holes, called primary holes, are carved in the wall in order to inject air to help the combustion process (Fig. 8.2). On the external wall, dilution holes permit to confine the combustion to the primary zone and guarantee a good mixing with the combustion products. The cooling films scattered along the tube walls generate a thermal protective layer that isolates the structure from the hot combustion gases. All the air passing through the openings is drawn from the annulus around the chamber (Fig. 8.4).

An additional thermal protection of the flame tube is obtained by using metallic plates containing a multitude of perforations of a small diameter (< 5 [mm]). This multi-perforated plates generate a thermal boundary layer inside the chamber that protects the structure from direct impingement of the combustion gases [170]. They also help in the combustion process and the hydrodynamics of the chamber by injecting air in a given direction as shown in Fig. 8.4.
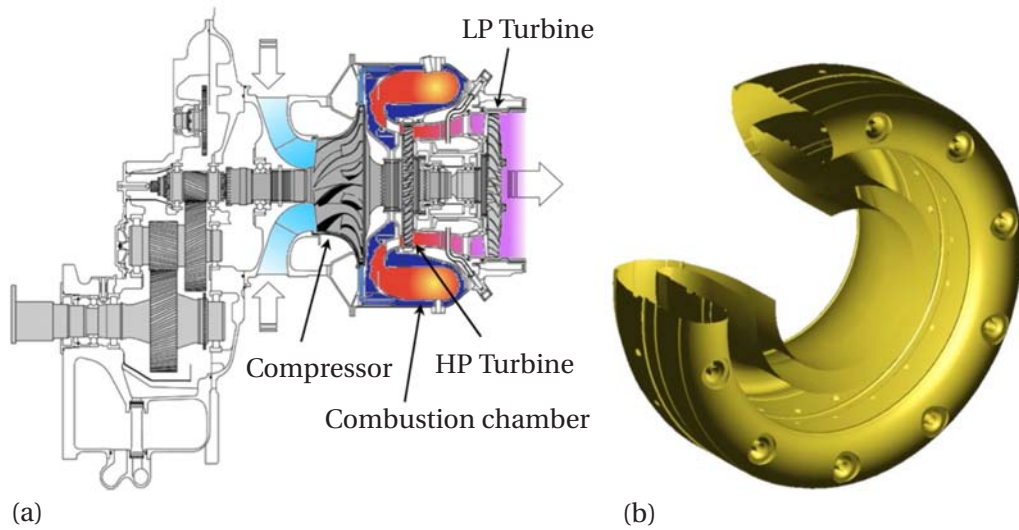
Figure 8.1: (a) Schematic representation of the helicopter engine: the flow evolves from the left to the right passing through the compressor, entering the annular combustion chamber ending up in the turbines where the thermal energy is transformed into mechanical energy and is transfered to the different mechanisms of the helicopter via the gear box. (b) 3/4th view of the annular combustion chamber.

In a typical operation of the chamber a fuel-rhich gas is delivered using the vaporization injection cane. Reaction takes place in the primary zone of the chamber and is confined by the primary holes. The cooling films and the multi-perforated plates act as a protective coat against the hot combustion gases and help the mixing and the homogenization of the exhaust gases.

A total mass flow rate of air equal to $\dot{m}_{\text{air}} = 0.14627$ [kg/s] and a fuel mass flow rate of $\dot{m}_{\text{F}} = 0.0028$ [kg/s] are injected in one sector of the system. From the chemical properties of JP10 (Table 8.1) a global equivalence ratio of $\phi_g \approx 0.3$ can be deduced using Eq. (5.36). The chemical formula for the jet fuel used corresponds to the longest carbonated chain of the mixture: $C_{10}H_{16}$. The combustion process generates a total power of $P = 120$ [kW] per sector.

8.2 Numerical parameters

The computational domain is limited to a 36° sector (one tenth of the chamber) containing one vaporizer. In the dilution and primary holes, in order to capture the good penetration angle of the jets, the computational domain has been slightly extended outside the chamber. Characteristic boundary conditions [202] are applied on all inlets and outlets, except for the multi-perforated plates and the cooling films. The solid and multi-perforated walls are treated using an adiabatic boundary condition and perfectly reflecting acoustic properties. On the lateral boundaries an axi-periodic condition
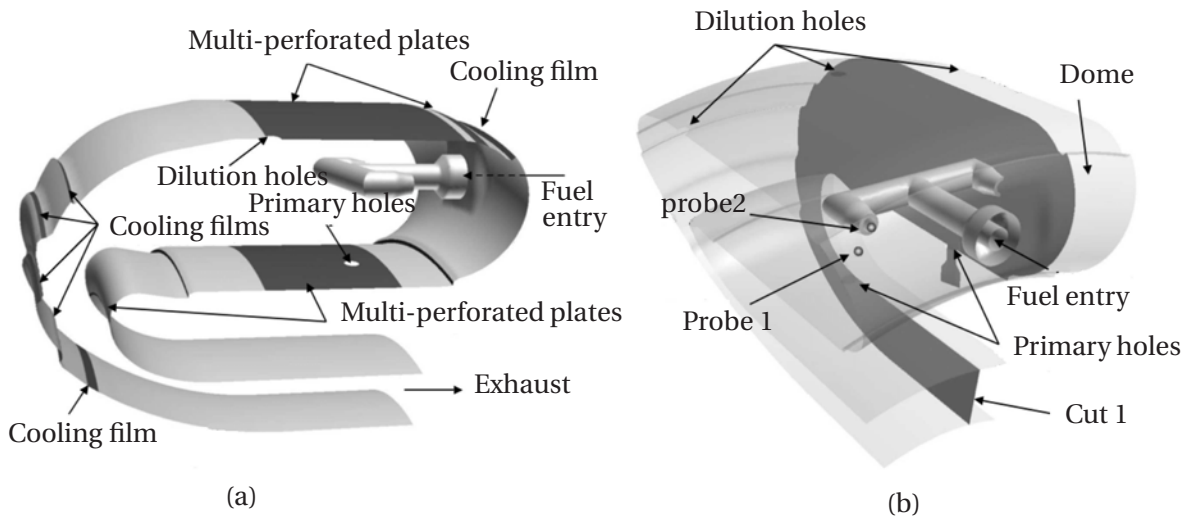
Figure 8.2: Schematic representation of one sector of the combustion chamber representing 1/10th of the total volume.

was imposed. The mesh shown in Fig. 8.5 consists of 1 242 086 tetrahedral cells composed of 230 118 nodes. The maximum and minimum cell volumes are 3.12671 10^{-8} [m^3] and 1.81795 10^{-11} [m^3] respectively.

The numerical method employed in the integration is the Lax-Wendroff scheme [101, 144]. The mean time step imposed by the CFL condition (Eq. 7.53) is 1.4 10^{-7} [s]. The Dynamic Thickened Flame (DTF) model is used to resolve the flame front, with the approach presented in section 5.2.2, using at least three cells. Thickening provokes a smooth (non-physical) flame front, which is compensated by the activation of the efficiency factor by imposing a flame wrinkling in the flame front that improves the prediction of the good turbulent flame speed.

The chemical approach consists of a four species and one reaction kinetic scheme presented in Eq. (8.1). The fuel corresponds to the species JP10 which is a combustible commonly used in aeronautical applications (JP stands for Jet Propellant). The reduced chemical scheme was derived from a complex scheme containing 43 species and 174 reactions [151, 29], and was fitted to guarantee correct flame speeds, ignition delay times and final combustion temperatures [19].

$$JP10 + 14O_2 \rightarrow 10CO_2 + 8H_2O \tag{8.1}$$

JP10 is a mixture of many different hydrocarbons, but for most properties it can be reduced to the longest carbonated chain in the mixture: $C_{10}H_{16}$. As shown in Fig. 8.6 this one-step scheme can predict the correct temperature and flame speed for equivalence ratios inferior to $\phi = 1.2$. The global equivalence ratio of the chamber being situated around $\phi_g = 0.3$, the final combustion temperature
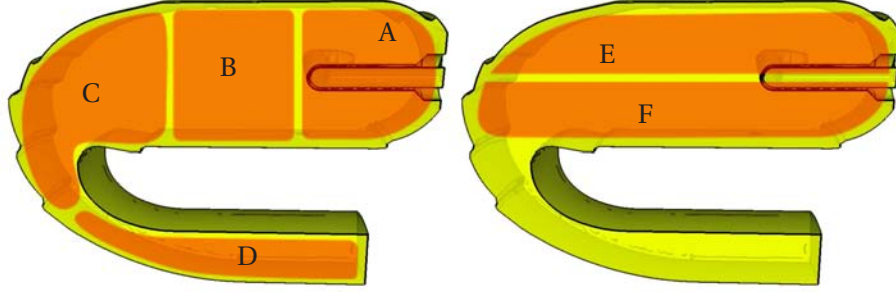
Figure 8.3: 1/20th sector where the zones of the chamber are shown: (A) primary zone, (B) intermediate zone, (C) dilution zone, (D) chamber exit, (E) external side of the chamber and (F) internal side of the chamber.

Table 8.1: Chemical properties of JP10 [19].

Property	JP10	unit
Chemical formula	$C_{10}H_{16}$	
Mean molar mass (eq. 5.5)	0.136	kg/mol
Stoichiometric ratio (eq. 5.32)	3.28836	-
Formation enthalpy, $\Delta h_{f,F}^0$	-31.574	kJ/mol
Heat released per mole, Q^m	5.809	MJ/mol
Heat released per kg, Q	42.7	MJ/kg

will be well predicted. However, at the exit of the vaporizer, combustion zones with equivalence ratios reaching $\phi = 3$ may locally exist. The resulting over-prediction of the flame speed can lead to flame instability.

To avoid this problem, a corrective function $f(\phi)$ is applied to the pre-exponential factor of the reaction rate. This approach was introduced by Légier [148] and is commonly known as the Pre-Exponential Adjustment (PEA) method [80, 20, 82]. Using this approach the expression of the reaction rate becomes:

$$\mathcal{Q} = f(\phi) A_f [X_{C_{10}H_{16}}]^{n'_1} [X_{O_2}]^{n'_2} \exp\left(\frac{-T_a}{T}\right) \tag{8.2}$$

where the corrective function is defined as:

$$f(\phi) = \frac{1}{2}\left(1 + \tanh\left(\frac{1.39 - \phi}{0.26}\right)\right) + \frac{0.33}{4}\left(1 + \tanh\left(\frac{\phi - 1.6}{0.8}\right)\right)\left(1 + \tanh\left(\frac{1.85 - \phi}{0.8}\right)\right) \tag{8.3}$$
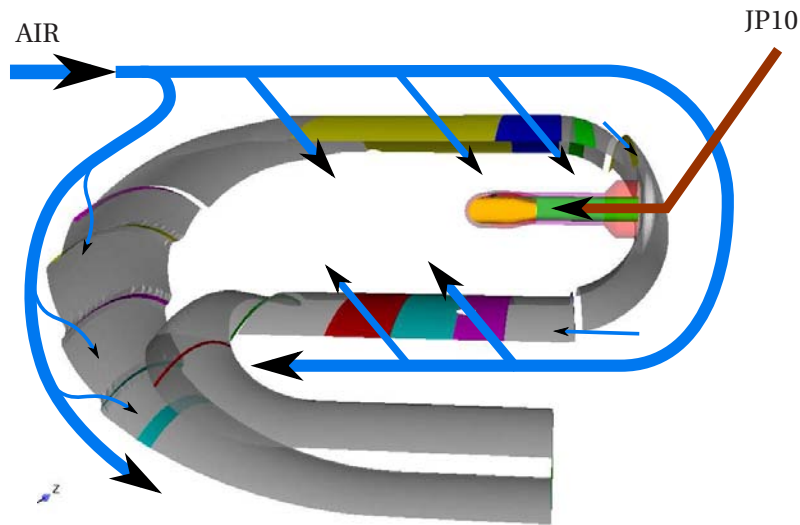
Figure 8.4: General flow in the annulus and injection zones of air and fuel through the flame tube. Multi-perforations, cooling films and the vaporizer are shown with colors in the surface of the chamber.

with the constants of the function taking the values shown on Table 8.2.

Table 8.2: Values of the constants used in the PEA function Eq. (8.2).

Constant	Value
Pre-exponential factor, A_f	$7.8\,10^{14}$ (csg units)
First partial order, n_1'	1.5
Second partial order, n_2'	0.55
Activation energy, E_a	30000 [cal/mol]

Fig.8.6 shows the evolution of the temperature T and the flame speed s_L of JP10 using a one-step kinetic mechanism with and without the PEA, compared against a complex chemistry [151, 29]. The corrective function $f(\phi)$ is adjusted in order to artificially establish the good flame speed. However only the thermodynamic properties of the mixture control the combustion temperature as shown in Eq. (5.31). For this reason the predicted temperatures remain over-predicted for equivalence ratios above $\phi = 1.2$.

The three visualization cuts presented in Fig. 8.7 (left) will be used to illustrate the general behavior
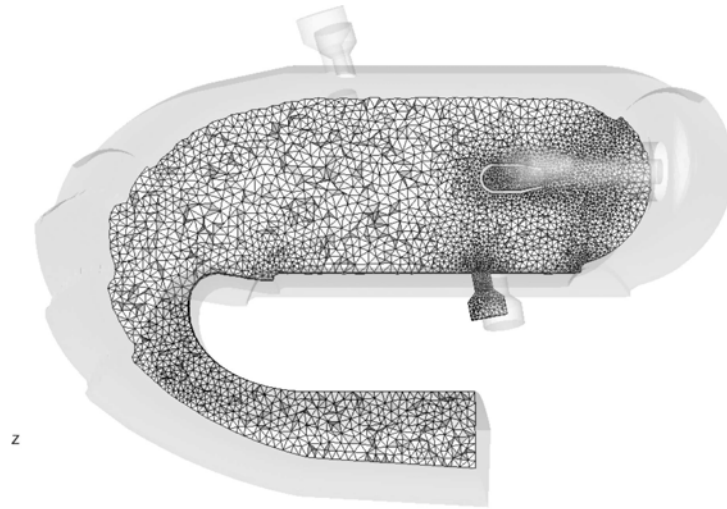
Figure 8.5: Mesh used for the LES computation.

of the combustion chamber: the first and second are vertical surfaces crossing the injection area and the middle of the sector, and the third is an horizontal plane crossing the T-injector in its middle. In Fig. 8.7 (right) the domain partitioning for the parallel computation is presented. Some computations were carried up on 32 processors on an IBM iDataPlex computer featuring Intel Xeon "Nehalem" processors at clock rate of 2.66 Ghz, and others were performed on an IBM JS21 architecture featuring PowerPC970MP processors at 2.5 Ghz. In the fastest simulation (including data input/output and statistical recordings) the reduced computational time of one simulation is about $3.2\,10^{-5}$ [s/(iteration×node×processor)]. The restitution time for a 30 [ms] simulation on 1 processor is in this case equal to $T_{\mathrm{CPU}} = 438.32$ [hours].

8.3 Quality of the LES simulation

In order to evaluate the quality of the LES, the M factor (commonly called the Pope criterion) was calculated. Pope [209, 210] introduced this criterion in order to compare the resolved kinetic energy k_{res} with the sub-grid scale kinetic energy k_{SGS}:

$$M = \frac{\langle k_{\mathrm{SGS}} \rangle}{\langle k_{\mathrm{SGS}} \rangle + \langle k_{\mathrm{res}} \rangle} \tag{8.4}$$

In a good-quality LES the sub-grid models should only account for a small percentage of the total kinetic energy, while most of the flow should be explicitly resolved. The coefficient M varies from 0 to 1, where $M = 0$ corresponds to a DNS (all the turbulence scales are explicitly resolved) and $M = 1$
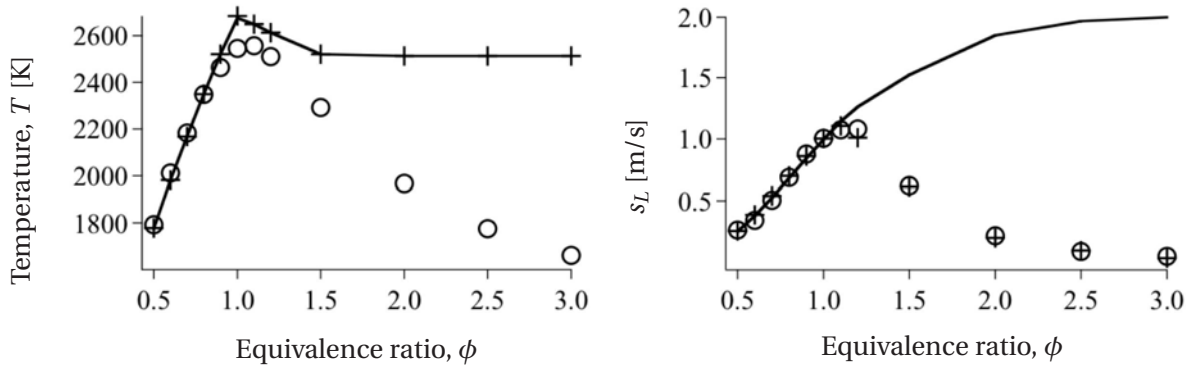
Figure 8.6: Temperature and flame speed for JP10 as a function of the equivalence ratio ϕ, obtained with a complex chemistry ($\circ$), a one-step kinetic scheme (———) and a one-step chemistry with PEA (+).
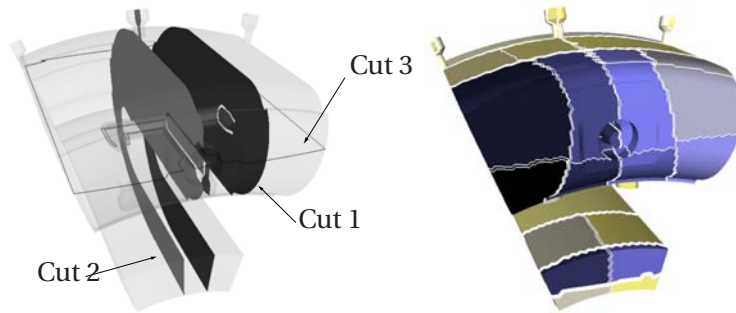
Figure 8.7: (left) Location of the visualization cuts. (right) Mesh partitioning for 32 processors.

corresponds to a RANS simulation (all the turbulence spectrum is modeled). In a good LES the numerical discretization must assure that $M \leq 0.2$. The value of the SGS kinetic energy is not commonly available, but it can be estimated from the SGS viscosity model [224]:

$$\nu_{\text{SGS}} = C_M \overline{\Delta} \sqrt{k_{\text{SGS}}} \tag{8.5}$$

where C_M is a constant value obtained from homogeneous isotropic turbulence simulations, and $\overline{\Delta}$ is a characteristic length of the LES filter. In Fig. 8.8 the Pope criterion is presented in cut 1, with an iso-contour line at $M = 0.8$. In the high-velocity and low-temperature zones of the domain, where $M > 0.8$, the strong turbulence is not well resolved. Boudier has shown [22, 20] that, even with very refined meshes, these zones remain difficult to resolve using the LES approach. In all the rest of the domain, where $M \leq 0.2$, the flow is well resolved by the LES.
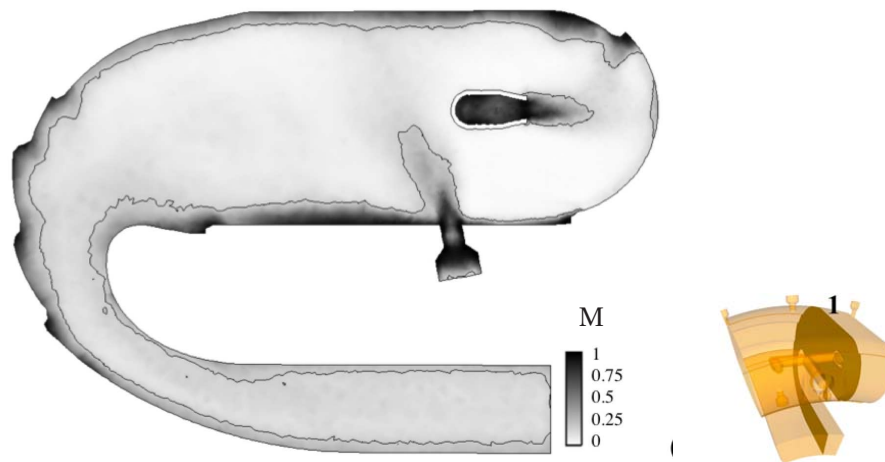
Figure 8.8: M criterion field in cut 1 and iso-line at $M = 0.8$.

8.4   Instantaneous fields

A stable LES simulation of 110 [ms] has been performed on the combustion chamber. The temporal evolution of the mean volume pressure and the mean volume temperature of the chamber are presented in Fig. 8.9. No periodic phenomenon is visible, and a spectral analysis of the the signals revealed no special excitation frequency of the mean flow. The fluctuations observed are very small and are mainly related to the turbulent combustion process.

An instantaneous snapshot of the magnitude of the velocity field $||V||$ normalized by the axial magnitude of the injection velocity u_{inj} is presented in Fig. 8.10. A high velocity zone is formed at the exit of the vaporizer. At the core of the injection jet the Mach number reaches values up to $M = 0.75$, and the jet impacts the dome at a high velocity (around 300 [m/s]). At the same time the strong injection of air in the film on top of the dome interacts with the jet and creates a circulation of gases towards the internal side of the chamber. This clockwise movement is enhanced by the film injection of air in the at the bottom of the dome. Turbulent structures can be seen inside the vaporizer suggesting a strong interaction with the injector walls.

The high velocity air injected through the primary holes penetrates almost to the external wall of the chamber. This movement enhances the recirculation of gases in the primary zone of the chamber. The clockwise recirculation of gases leads to a strong mixture and a complete combustion of the fuel.

In Fig. 8.11 a 3D view of the computed domain and the instantaneous flame shape can be observed. In this snapshot the traced iso-surface of heat release features an empty cone-shaped structure that reaches the dome, suggesting a strong interaction between the flame and the wall at the dome. The flame is anchored to the injector lips, but is also visible around the fixation of the vaporizer. The dome and the vaporizer suffer a strong thermal charge.
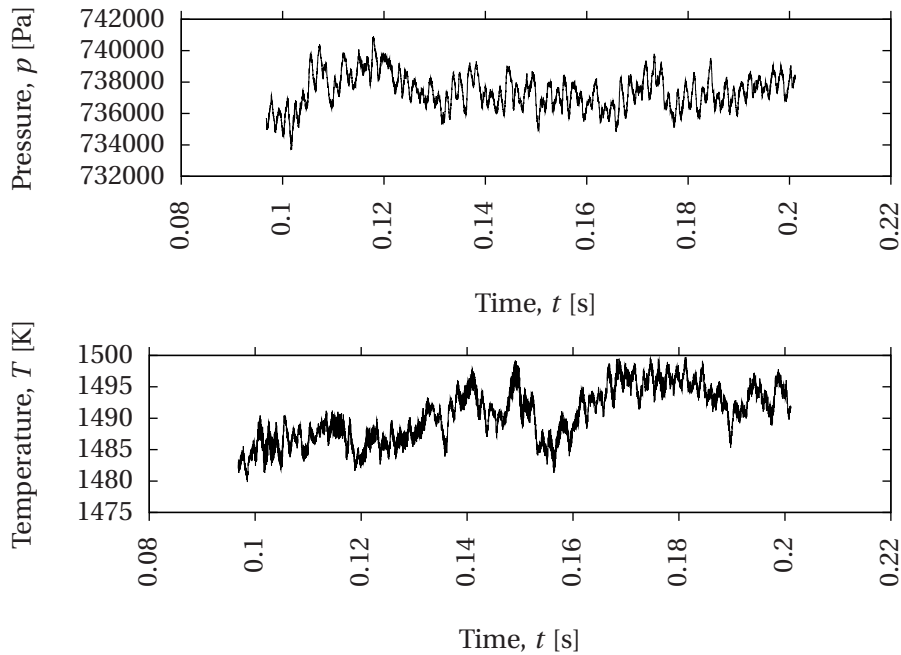
Figure 8.9: Temporal evolution of the mean pressure and temperature for the reference LES simulation.

A detailed view of the normalized temperature field in cut 1 is presented in Fig. 8.12. This image shows the non-homogeneity of the temperature inside the combustion chamber: the hot products of combustion are mainly located in the internal section of the primary zone (A), convected by the circular motion of the flow. A strong temperature gradient between the core of the injection jet and its surroundings (B) indicate the presence of the flame. The dome is in contact with extremely hot gases, except for a narrow zone just in front of the injector (C).

Downstream the primary zone, the dilution jets create a thermal barrier that homogenizes the temperature and the mixture of the combustion products. From the dilution zone to the exit of the chamber, the gas temperature only changes near the film cooling zones (D). It can be also noted that near the multi-perforated zones, the injected air creates a protective thermal layer of low temperature gases (E).

8.5   The combustion model and the flame structure

The instantaneous view of the primary zone presented in Fig. 8.13 shows the values for the thickening $\mathscr{F}$ and the efficiency factor $\mathscr{E}$. The DTF model shows a good performance in this simulation, applying the thickening procedure only in the reacting zones. As the mesh resolution is relatively coarse, the
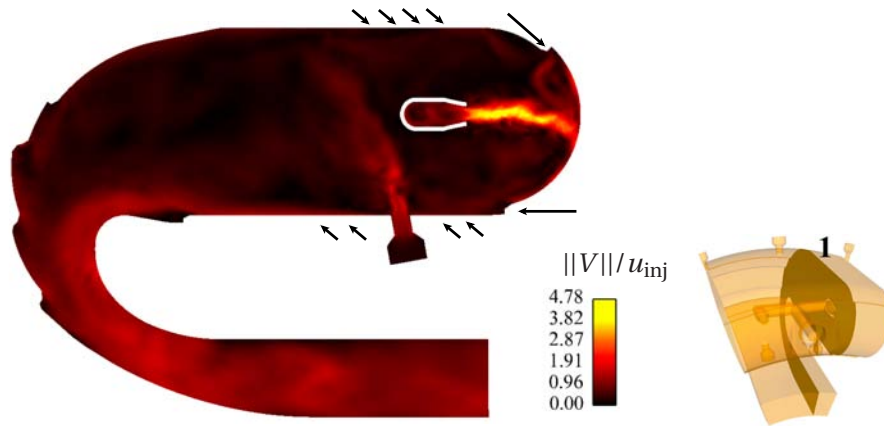
Figure 8.10: Fields of instantaneous velocity magnitude scaled by the axial injection velocity. Arrows show the direction of air injection contributing to the recirculation motion in the primary zone.

efficiency factor is activated around the fuel jet but quickly vanishes in the rest of the reacting zone.

The simulation predicts a flame structure observed in Fig. 8.14, where the data presented includes an instantaneous field of mixture fraction (Eq. 5.38) with the stoechiometric mixture fraction $z = z_{st}$ isoline (Eq. 5.39), and iso-contours of reaction rate $\widetilde{\omega}_F$ colored with the Takeno index [275]. Using the notation introduced by Vervisch [260], the Takeno index $N_{F,O}$ can be written:

$$N_{F,O} = \frac{\nabla Y_F . \nabla Y_O}{||\nabla Y_F||.||\nabla Y_O||} \tag{8.6}$$

This expression indicates the relative direction of the fuel and oxidant gradients. Reacting zones where both gradients point in the same direction are premixed, while regions where the vectors point in opposite directions are non-premixed. Figure 8.14, where black iso-contour lines represent the premixed combustion regime and white lines represent the non-premixed combustion regime, shows the fuel-rich mixture injected in the chamber, burning in a premixed regime at the exit of injector. The premixed flame is anchored at tip of the vaporizer and almost reaches the dome of the chamber.

This rich premixed flame produces pockets of hot fuel and combustion gases that are convected further away in the primary zone. The fuel pockets interact with the air injected at the external wall of the chamber (through the multi-perforated plate, the top cooling film and the primary holes) and at the interior side of the flame tube (mainly through the lower cooling film, but also through the multi-perforated plate). They lead to two additional reacting zones, where fuel is burned in non-premixed (diffusion) flames anchored near the cooling films at the external and internal sides of the dome. The presence of non-premixed flames explains the maximum temperature observed in the chamber, corresponding to the temperature obtained at stoichiometry.

The flame structure in the primary zone is summarized in fig.8.14 (right). Premixed combustion oc-
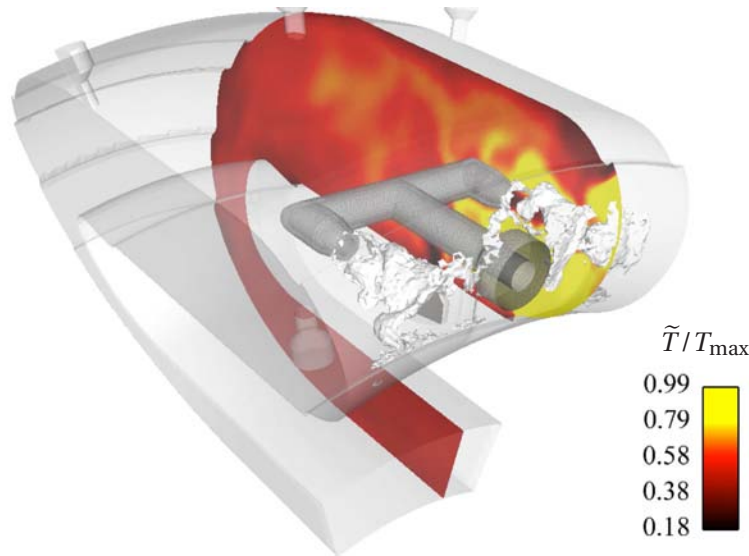
Figure 8.11: Instantaneous view of the reference LES simulation featuring the temperature field on cut 1 and an iso-surface of heat release at $\widetilde{\dot\omega}_T = 2.32$ [MW/m^3].

curs at the exit of the vaporizer, with the flame anchored at the injector tip. Two additional flames are anchored near the cooling films, reacting with the unburned fuel produced by the premixed flame. Air injected through the multi-perforations and the cooling films induce a clockwise motion of the flow which causes the convection of hot gases to the internal side of the primary zone. The hot products interact with the primary and secondary jets which homogenize the mixture and the exhaust gas temperature.

8.6   Averaged and standard deviation fields

The mean behavior of the flow is obtained with temporal averaging applied every 50 iterations which corresponds to a sampling frequency of around $f_e = 143$ [KHz]. This means that in a 30 [ms] simulation 4286 snapshots are used to calculate the time-averaged variables and their standard deviation.

Figure 8.15 shows the time averaged mass fractions of fuel (top), oxygen (middle) and combustion gas products ($\langle \widetilde{Y_P} \rangle = \langle \widetilde{Y_{H_2O}} \rangle + \langle \widetilde{Y_{CO_2}} \rangle$), in cuts 3 (left) and 1 (right). Although the global equivalence ratio of the chamber is $\phi_g = 0.3$, air is mainly injected through the flame tube, and the mixture inside the T-injector has an equivalence of $\phi \gg 1$. The fuel is not completely consumed in the premixed flame and the excess is transported inside the primary zone (A), where it is finally consumed in the top and bottom diffusion flames. The air injected through the primary and the dilution holes (B) finalizes the oxidation process of the combustion products generated by the premixed (E) and the diffusion flames. The air injected through the multi-perforations (C) and the cooling films (D) also help the
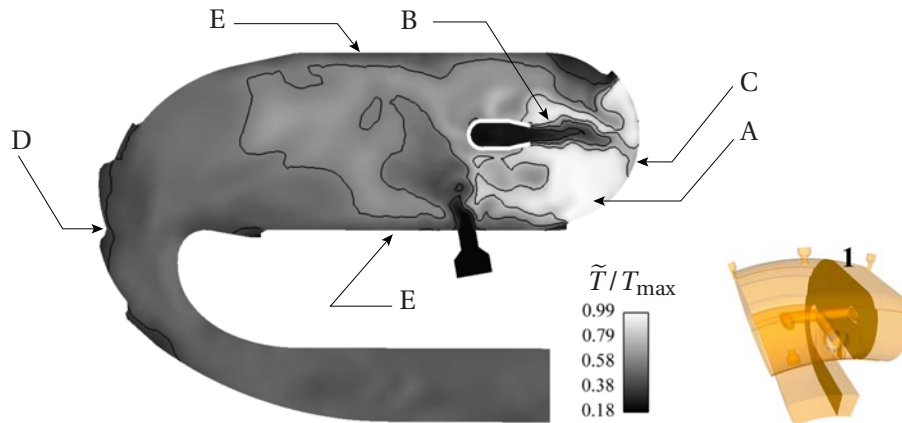
Figure 8.12: Instantaneous temperature field scaled by the maximum temperature. Black lines represent six equally spaced iso-contour levels of temperature at 0.18, 0.342, 0.504, 0.666, 0.828 and 0.99.
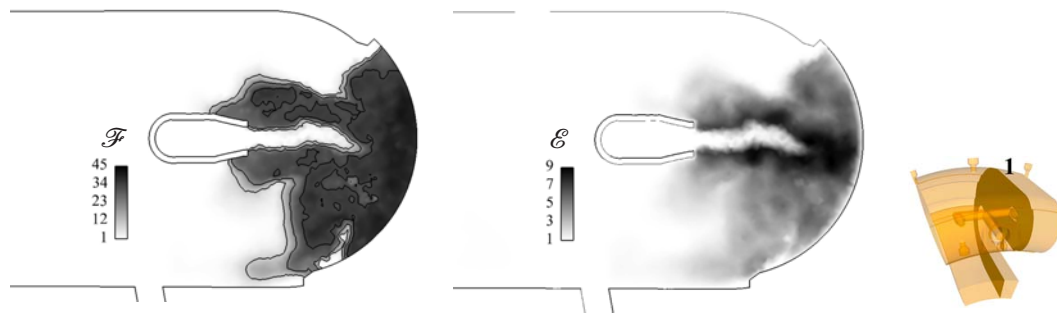
Figure 8.13: Instantaneous thickening (left) and efficiency factor (right) on cut 1. On the left, four iso-contour levels were added at $\mathscr{F} = 10$, $\mathscr{F} = 21.666$, $\mathscr{F} = 33.333$ and $\mathscr{F} = 45$.

oxidation in the dilution zone (F), producing an homogeneous mixture at the exit of the chamber (G).

The mean velocity and temperature fields in cut 1 are presented in Fig. 8.16. In the left image the normalized magnitude of the velocity vector is shown, with a zero axial velocity contour to identify backflow. The main flow features two recirculation zones: one is formed just behind the primary holes but is limited by the multi-perforated plates injecting air in the direction of the main flow (A). This very localized recirculation bubble can be the source of large eddy detachment that enhances the mixture of air and combustion products in the dilution zone. The second inverted flow is observed near the external multi-perforated wall (B). This rather large zone is mainly caused by the inclination of the holes in the multi-perforated plate. Between this zone and the injection zone a small corridor allows the evacuation of the combustion products emitted by the top non-premixed flame (C).

The right image of Fig. 8.16 shows that hot gases are mainly localized around the injector tip, in the internal side of the dome and near the anchored diffusion flames (D). As seen in instantaneous im-
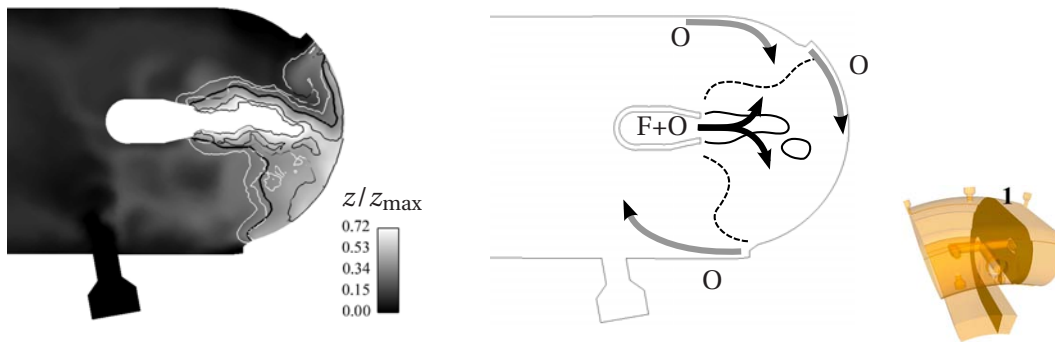
Figure 8.14: (Left) Instantaneous field of mixture fraction. The thick black line represents the stoichiometric mixture fraction z_{st}. Iso-contour lines of reaction rate $\widetilde{\omega}_F$ are also presented, colored with the Takeno index (black represents premixed combustion and white represents non-premixed combustion). (Right) General flow behavior in the primary zone and flame structure: black arrows represent the fuel injection, grey arrows represent the air flow, the black solid line represents a premixed flame and the dashed lines represent non-premixed flames.

ages, gases at very high temperature are constantly in contact with the dome and there is only a small zone in front of the injector where the gas temperature is lower. The hot combustion products are mainly evacuated below the injector. Their interaction with the primary jet produces two effects: first the temperature of the flow is homogenized and second some hot gases are entrained by the jet to the top inverted flow zone and recirculate around the injector, heating up the air injected through the multi-perforations (zone E).

Most of these processes can also be observed in cut 2 (Fig. 8.17). In this plane the top inverted flow zone exends from the dilution holes all the way back to the dome (A). Here the hot gases recirculation cycle is clearer: combustion gases escape below the injector (B), then the multi-perforations and the nearby primary holes cool them down and provoke a circulation flow. The hot gases that reach the top inverted flow are reinjected in the primary zone (C). The dilution holes act as a thermal barrier, mixing the gases an homogenizing the exhaust gases temperature. The cooling films situated at the elbow of the chamber provide a thermal protection of the walls and redirect the flow to the exit of the combustion chamber.

The standard deviation fields (RMS) indicate the variability of each quantity around its average value. The temperature RMS field presented in Fig. 8.18 (left) shows that temperature fluctuations are strong around the premixed flame at the exit of the injector and near the non-premixed flame anchored at the top of the dome (A). The other non-premixed flame at the bottom of the dome seems more stable, producing less temperature fluctuations. Near the primary holes temperature fluctuations are caused by the rapid mixture of cold and hot gases (B). In Fig. 8.18 (right) the RMS field of temperature plotted in cut 2 shows stronger fluctuations at the top non-premixed flame near the cane fixation (C). A fluctuation zone can be observed below the injection cane which suggests a stronger turbulent
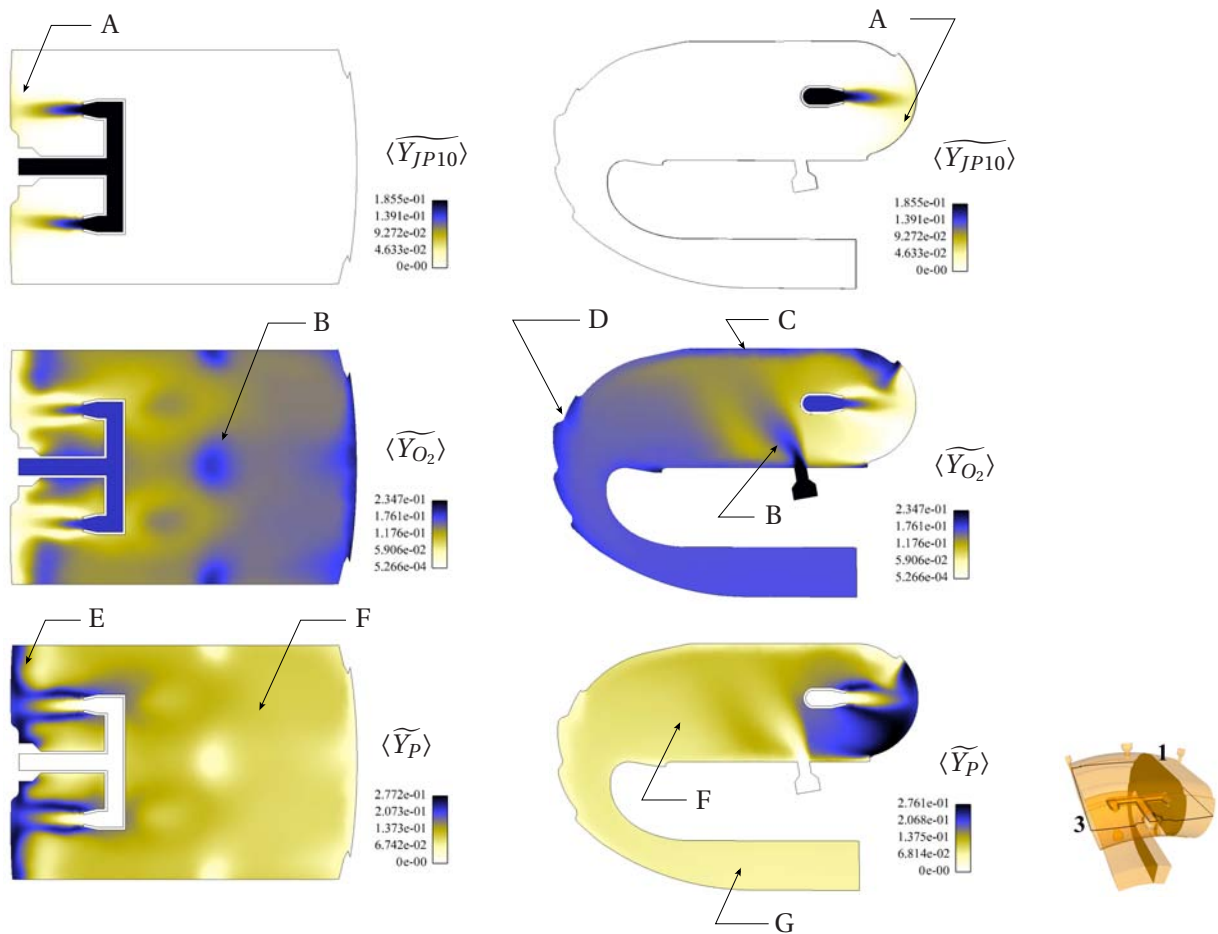
Figure 8.15: Time averaged fields of species mass fractions for fuel, oxygen and combustion products ($\langle \widetilde{Y_P} \rangle = \langle \widetilde{Y_{H_2O}} \rangle + \langle \widetilde{Y_{CO_2}} \rangle$), traced in cuts 3 (left) and 1 (right).

behavior in the middle plane. The maximum temperature fluctuations reaches 22% of the maximum temperature in this area.

One zone of particular interest for industrial design is the exit plane of the combustion chamber. The hot gases ejected by the chamber are guided into the engine turbine using nozzle guided vanes that accelerate and redirect the flow in a rotary motion. The blades that compose the solid walls of the nozzle vanes are subjected to strong thermal stress and must withstand the maximum temperature found in the efflux gases. Figure 8.19 shows the average temperature field in this zone and the RMS temperature field normalized by the maximum temperature of the chamber. The mean temperature is stronger in the external side of the exit plane. This is mainly due to the use of protective cooling films in the elbow of the chamber that lower the gas temperature near the internal wall of the exit zone. It is shown that the efflux gases temperature is not completely homogeneous in the azimuthal
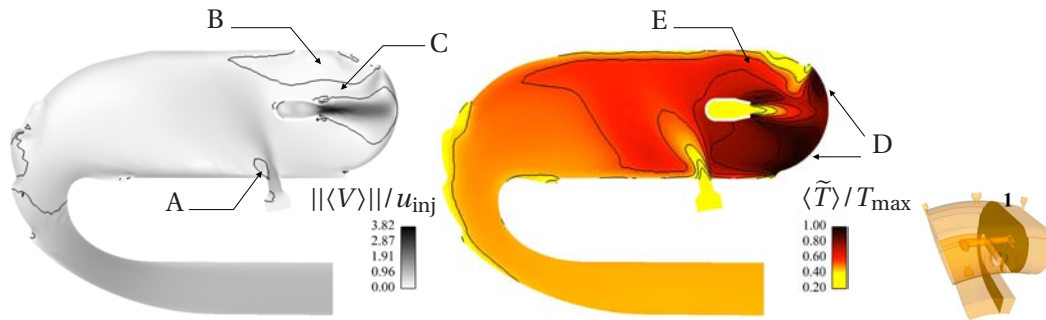
Figure 8.16: Cut 1. (left) Magnitude of the mean velocity normalized by the injection axial velocity. An iso-contour line delimits the zones where the axial velocity is zero. (right) Normalized mean temperature and iso-temperature lines delimiting six equally spaced temperature levels.
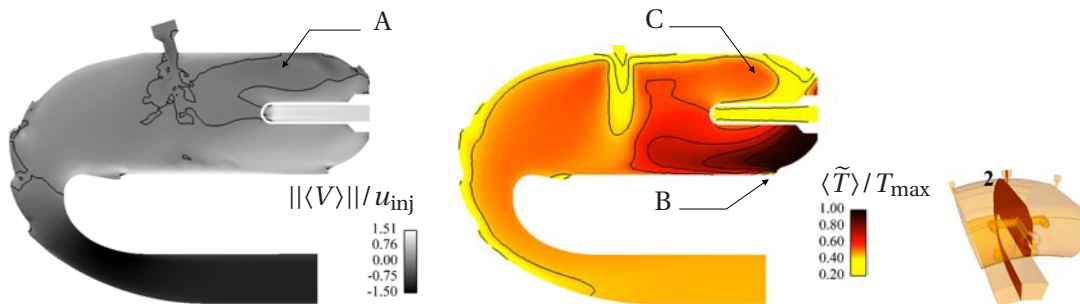
Figure 8.17: Cut 2. (left) Magnitude of the mean velocity normalized by the axial injection velocity. An iso-contour line delimits the zones where the axial velocity is zero. (right) Normalized mean temperature and iso-temperature lines delimiting six equally spaced temperature levels: { 0.2, 0.36, 0.52, 0.68, 0.84, 1} .

nor in the radial directions, and that stronger fluctuations occur in the internal side of the chamber exit.

The time averaged velocity field was used to trace pathlines inside the domain to observe the general behavior of the mean flow. In Fig. 8.20 (left) the lines were created by placing particles in the base of the injector. Each particle evolves in the domain following the averaged velocity vector field. In this case the pathlines were colored by the local temperature, showing that most of the mass injected in the vaporizer is heated up in the interior zone of the dome (A) and then convected to the back of the chamber (B) where it cools down to finally get ejected through the exit nozzle.

In Fig. 8.20 (right) pathlines are plotted for particles injected at the primary and dilution holes. Pathlines injected in the dilution holes are black, while those injected in the primary holes are colored with the local mean temperature. It can be observed how both jets act like thermal barriers blocking the hot gases and mixing the combustion products with air. The penetration of the jets is strong, reaching in each case the opposite side of the chamber. It can also be observed that the air injected in
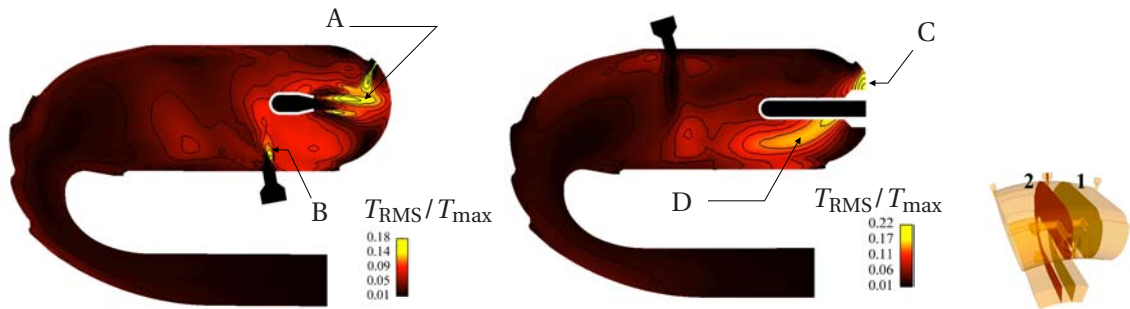
Figure 8.18: Temperature RMS fields with six iso-contour lines at T_{RMS}/T_{max} = $\{0.045, 0.08, 0.115, 0.15, 0.185, 0.22\}$. (left) Cut 1. (right) Cut 2.
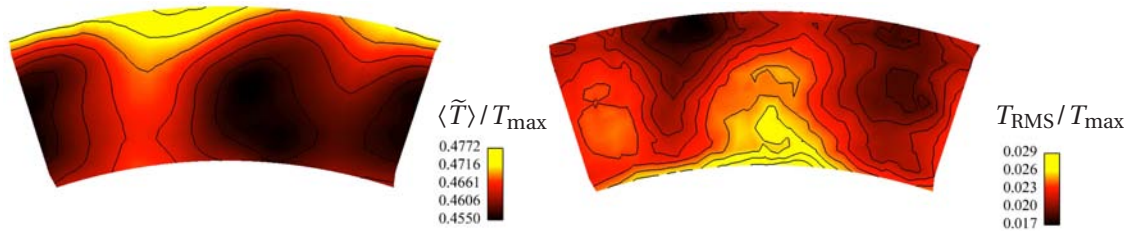
Figure 8.19: Normalized mean (left) and RMS (right) temperature fields in the chamber exit plane.

the primary holes can also be convected through the recirculation zone on the top of the cane injector (C).

Figure 8.21 is used to show how the injected flow impacts the dome of the chamber. In the left image the pathlines are colored with the magnitude of the mean velocity, showing the high velocity of the jet impacting the dome. In the right image the pathlines are colored with the mean gas temperature: in front of the injectors a radial flow is formed due to the impact of the jets. As already said, this shows that a strong thermal and dynamic interaction takes place between the combustion gases and the solid structure of the dome.
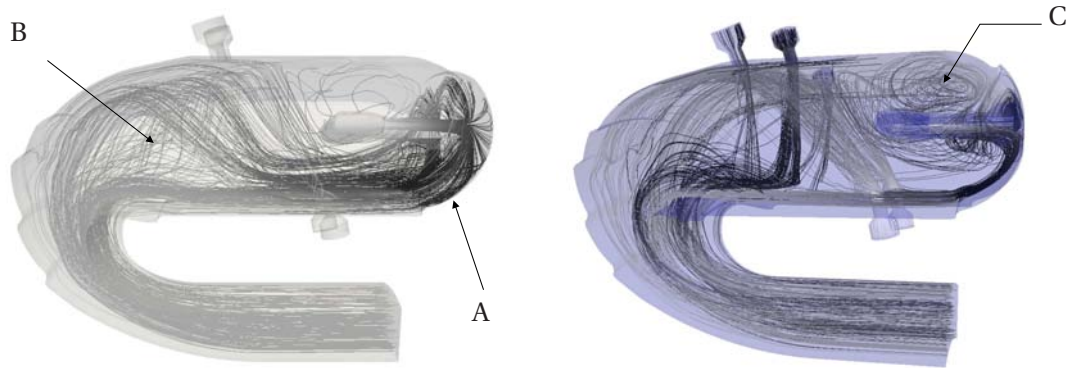
Figure 8.20: Pathlines showing the general flow structure of the chamber. (left) Particles injected in the vaporizer and colored by the temperature. (right) Particles injected in the dilution holes (black) and the primary holes, colored with the temperature.

(a)   (b)
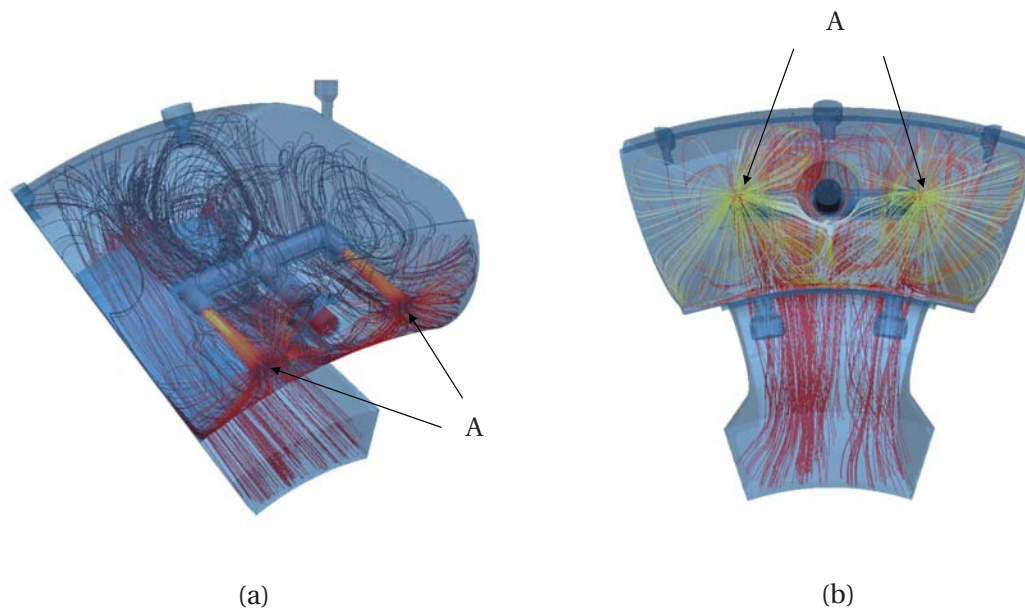
Figure 8.21: Pathlines generated by injection of particles in the vaporizer. (a) colored using the velocity magnitude. (b) colored using the temperature.

9

Coupled RFTI simulations of an helicopter combustion chamber

Contents

Coupled combustion-radiation calculations of the industrial combustion chamber of chapter 8 have been performed in order to evaluate the effects of radiation on the flow. The objectives of this study are summarized in four points:

- to determine the feasibility of coupled combustion-radiation calculations in different parallel computers using the codes AVBP and PRISSMA and the coupler PALM,

- to evaluate the accuracy of the radiation models in an industrial application,

- to study the impact of radiation on the flow in a combustion chamber,

- to determine if radiation computed with time-averaged temperature and species fields are accurate.

9.1   Radiation: numerical parameters

The mesh used in the radiation code is the same as the one used in the LES of the previous chapter. This allows to avoid difficulties related to the interpolation of data between meshes. Spatial integration of the Radiative Heat Transfer solver is done using the S_4 angular quadrature, corresponding to a spatial discretization of 24 directions. The sweeping algorithm presented in section 6.6.2 completed the 1.2 million cell-long process in three minutes on one processor. Other angular quadratures were tested, including S_6 (48 directions), S_8 (80 directions), S_{12} (168 directions) and LC_{11} (96 directions), showing no differences for the present application.

The solid walls of the combustion chamber are considered almost black, with an emissivity equal to $\epsilon = 0.95$. The temperature of the walls depends on the mean local temperature of the gases: wall temperatures evolve from 1200K at the base of the vaporizer down to 600K at the multi-perforated walls. The cooling films, the inlet and outlet surfaces are considered completely absorbent (black walls with $\epsilon = 1$) and at the mean surface temperature of the gas.

The lateral axi-periodic boundary conditions require that all luminance crossing one of these planes must be injected back in the second plane. In addition the 36° inclination between the planes require an azimuthal rotation of the beam direction on the entry plane. The axi-periodic imposes that no radiative energy is lost through these planes. However the implementation of such condition is very complex in a DOM solver. A much less elegant solution has been proposed to account for the axi-periodic condition: knowing that the energy balance through the surfaces is zero and supposing that two adjacent sectors show a very similar radiative field, we consider in this work that the axi-periodic boundaries can be initially approximated by a perfectly reflecting boundary condition, i.e. using an emissivity of $\epsilon = 0$. The planes act as mirrors reflecting all incident radiation back into the domain, avoiding energy losses and taking into account the inhomogeneity of the radiative field in the adjacent sector.

9.2   Evaluation of the radiation fields

As a first step, one instantaneous LES solution has been extracted from the simulation of chapter 8 and used in the radiation code PRISSMA. The radiative source term $\mathscr{S}_r$ (Eq. 6.64), the radiative heat flux vector $\mathbf{q}^r$ (Eq. 6.24), the irradiation field G (see Table 6.8), and the wall radiative heat flux field q_w^r (Eq. 6.32) were calculated.

9.2.1   The mean absorption coefficient

The importance of energy absorption inside the combustion chamber may be estimated via the mean Planck absorption coefficient introduced in Eq. (6.148), and approximated using the radiative fields given by PRISSMA:

$$\overline{\kappa}_P = \frac{\mathscr{S}_r + G}{4\sigma T^4} \tag{9.1}$$

The instantaneous field of the mean Planck absorption coefficient is presented in Fig. 9.1. In this case in the cold injected mixture is well protected against the radiation of the hot gases. Moreover the injected mixture is composed of gases that are considered transparent (JP10, O_2 and N_2), as the spectral properties of JP10 are completely unknown. Another limitation is the use of a one-step kinetic scheme for the combustion of the fuel: the species CO is not taken into account, although it is radiatively active. Finally the size of the combustion chamber is very small: the characteristic length l of the chamber lays around 10 centimeter, which strongly limits the optical thickness of the chamber.

The mean value of the mean Planck absorption coefficient is $\langle \overline{\kappa_P} \rangle_{\text{vol}} = 4.4$, which gives an optical thickness of $\tau = \overline{\kappa}_P l \approx 0.44$. This means that the absorption rate is equal to $A = 1 - e^{-\tau l} = 0.35$, i.e. almost 35% of the radiated energy is reabsorbed by the gas, while the remaining energy is transfered to the walls.

This global value does not reflect the local behavior of radiation. Behind the premixed flame the absorption coefficient is very strong reaching a value of $\overline{\kappa_P} = 7.7$, however the characteristic length is here only some centimeters (distance between the flame and the wall) leading to an absorption rate of $A \approx 0.074$. Energy absorption is then weaker in the primary zone and stronger in the dilution zone.

9.2.2   Instantaneous radiative fields

In Fig. 9.2 the radiative source term $\mathscr{S}_r$ is presented in cut 1. An iso-contour line at $\mathscr{S}_r = 0$ is added. A positive value of the source term indicates a zone where energy is emitted while a negative source term indicates energy absorption. The order of magnitude of absorption and emission is the same (around 10^6 [W/m^3]). Energy is mainly emitted in the high temperature gases of the primary zone of
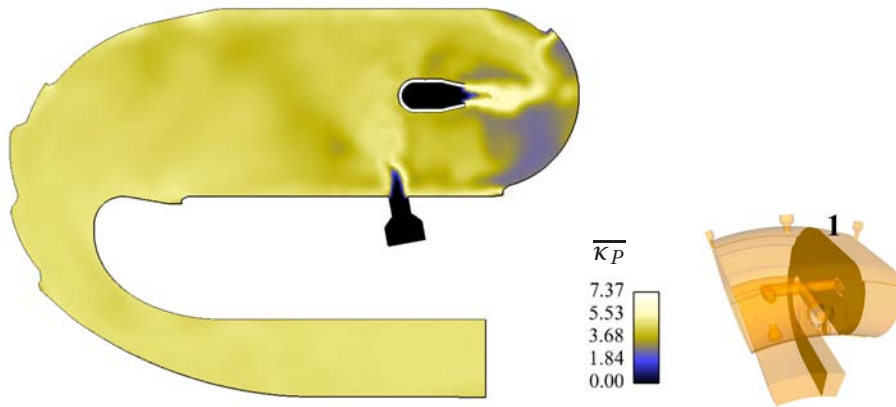
Figure 9.1: Instantaneous field of the mean Planck absorption coefficient $\overline{\kappa_P}$ in cut 1.

the combustion chamber around the three flames. Emission is also important on top of the vaporizer in the recirculation zone. The radiative source term is weaker in the dilution zone but remains at a level close to 10^5 [W/m^3].
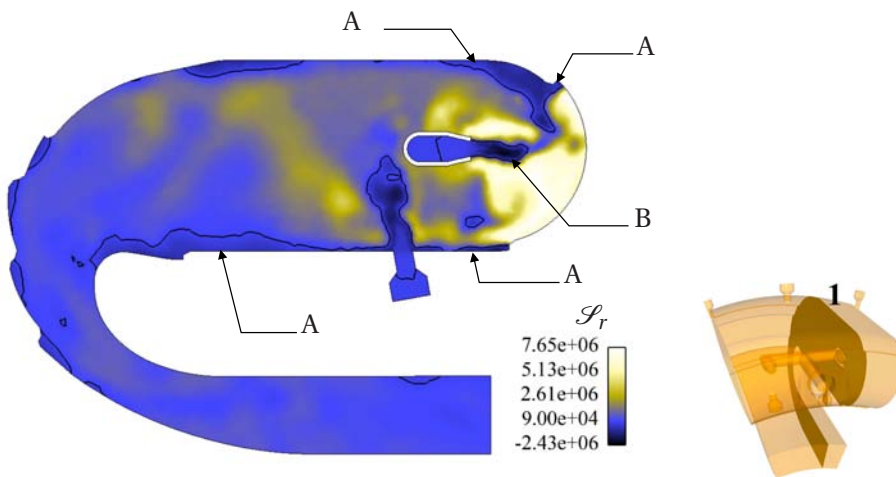

Figure 9.2: Instantaneous field of radiative source term $\mathscr{S}_r$ with an iso-contour line at $\mathscr{S}_r = 0$ in cut 1.

Absorption occurs mainly in the cold zones of the flow: near the multi-perforated plates and in front of cooling films (A). Absorption is particularly strong in the cold gas around the premixed flame anchored in the tip of the injector (B). A closer look at this zone is presented in Fig. 9.3: it can be observed that inside the premixed flame (A) the temperature is low but no products are present. In this zone the gases are considered transparent. There is a narrow zone between the injection and the dome (B) where the products of the premixed combustion are present. In this zone the gas is composed of combustion products at the temperature of the premixed flame which is lower than the temperature reached in the diffusion flames (C). The combustion products act as an absorber and could enhance

the flame dynamics.
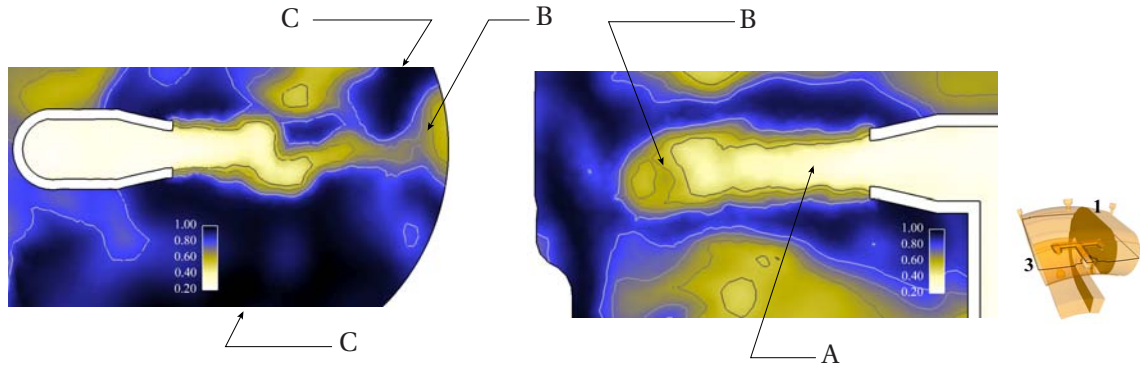
Figure 9.3: Instantaneous field of normalized temperature around the tip of the injector and iso-contour lines of mass fraction of $\widetilde{Y_P}$. (left) cut 1, (right) cut 3.

The chemical activity is many orders of magnitude stronger than the radiative source term. In Fig. 9.4 the instantaneous field of heat release $\widetilde{\omega}_T$ is presented using a gray saturated palette. In the white zones the heat released by the combustion process is higher than $\widetilde{\omega}_T = 10^7$, this term is the most important in the energy equation Eq. (5.46): here the chemistry controls the thermal behavior of the flow. Black zones where the heat release is lower than $\widetilde{\omega}_T = 10^6$ represent the domain where radiation may be predominant over chemistry in the energy equation.
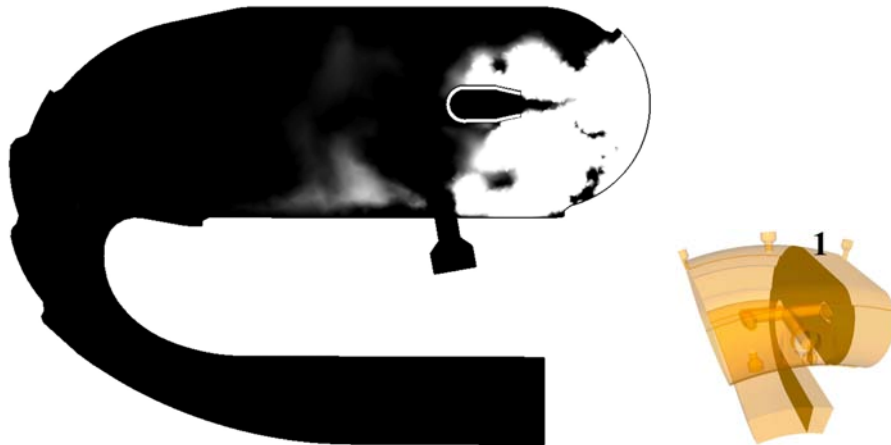
Figure 9.4: Instantaneous field of heat release using a saturated palette to show areas where $\widetilde{\omega}_T < 10^6$ (black) and $\widetilde{\omega}_T > 10^7$ (white).

Comparing figures 9.2 and 9.4 it can be inferred that radiation may modify the temperature field in the dilution zone and the external wall of the chamber (top cooling film). The region just behind the vaporizer could also suffer a temperature variation, but the primary zone is mainly governed by chemistry, so that no strong variations are expected here.
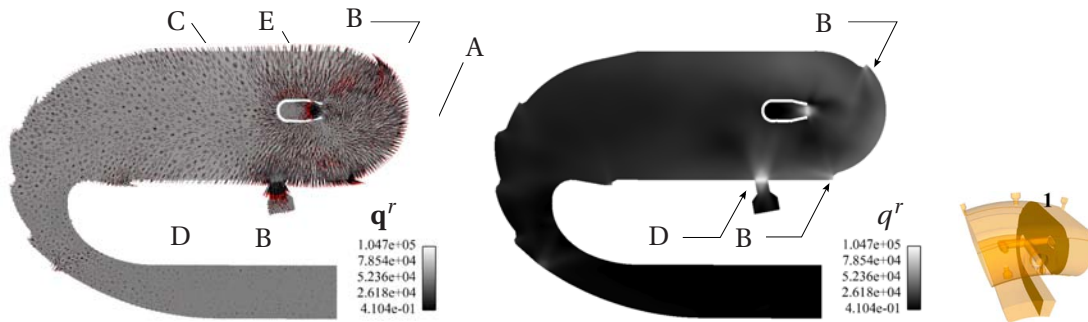
Figure 9.5: Instantaneous view of the heat flux vector field (left) and its magnitude (right) in cut 1

In Fig. 9.5 the radiative heat flux vector field $\mathbf{q}^r$ is presented in cut 1. The primary zone of the chamber is the location where most of the energy is emitted (A). Here the vectors point in the direction of energy emission. In the internal side of the primary zone radiation is emitted in all directions, and particularly towards the dome. Strong heat fluxes can be observed around the top and bottom diffusion flames (B), while energy is mostly incident in the premixed flame (C). High levels of energy flux are also observed near air injections (D) and the radiative heat flux entering the vaporizer is high. As presented before, the injected gases do not absorb energy, but they could potentially be affected by the heating of the interior solid wall of the vaporizer.
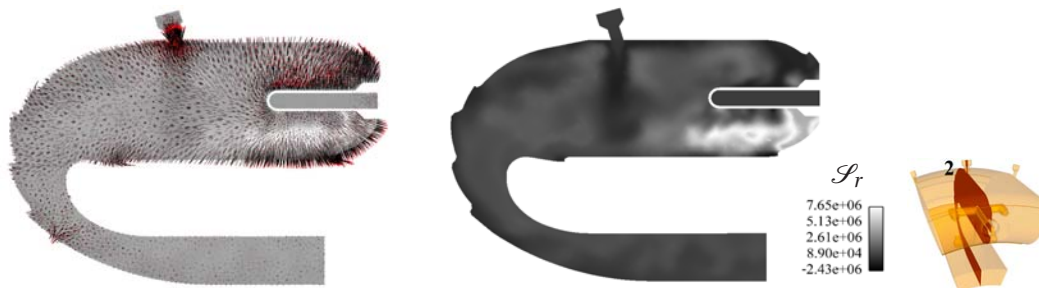
Figure 9.6: Instantaneous view of the heat flux vector field (left) and radiative source term (right) in cut 2

Behind the injector and on the top of the external walls of the vaporizer energy emission is strong (E). This is a consequence of the isothermal boundary condition on these walls. In Fig. 9.6 the heat flux vector field and the radiative source term are presented in cut 2. Radiation from the solid vaporizer is more evident in this view. The gas is hotter in the internal side of the primary zone than the external side, which in the real life modifies the temperature of the injector walls. This is not taken into account in the present simulation: using a mean temperature in the isothermal condition for all the injector induces an error in the computation of the radiative heat fluxes (over-prediction in the external side and under-prediction on the internal side). A good estimation of the boundary temperature is very important for radiation.
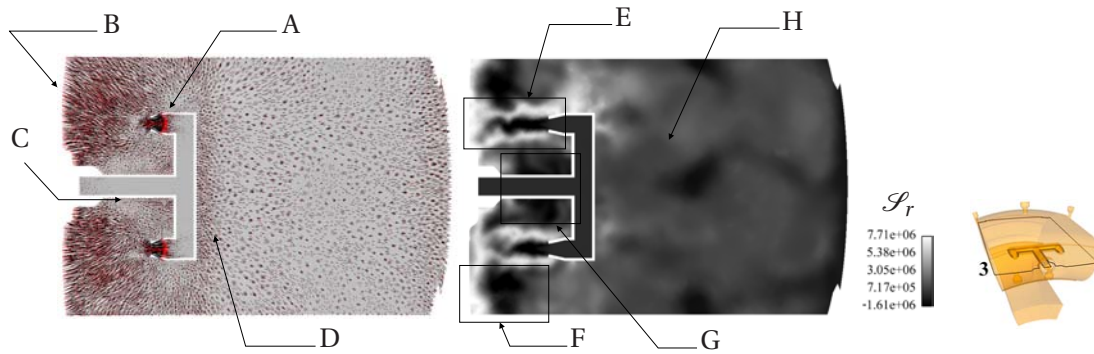
Figure 9.7: Instantaneous view of the heat flux vector field (left) and radiative source term (right) on cut 3

In Fig. 9.7 the radiative heat flux vectors and the radiative source term in cut 3 are shown. Energy flux towards the interior of the injector can be observed (A). In this view it is also evident how most of the energy emitted by the flames is directed towards the dome (B). Heat flux vectors also point out from the vaporizer suggesting that the solid walls emit more energy than they receive (C). Behind the cane an almost constant heat flux is directed towards the dilution zone (D).

In the $\mathscr{S}_r$ field of cut 3 (Fig. 9.7-right), four different zones show a particular behabvior:

- **The jet:** surrounding the premixed flame a high emission cylindrical zone can be observed (E). This corresponds to hot products at high temperatures. Note however that this emission zones are not the main source of radiative energy: most radiation is generated in the lower part of the primary zone as shown in the preceding figures.

- **The corner:** outside the jets, near the intersection between the dome and the side plane, an absorbing zone is formed (F). The mixing of combustion gases with the cooling air in this zone produce an area of low temperature with an important absorption coefficient. This absorptive zone extends for a few centimeters in the axial direction. Here radiation will change the temperature.

- **The vaporizer:** around the central cylindrical structure of the vaporizer the gas absorbs more energy than it releases (G). A modification of the temperature in this zone can also be expected.

- **The dilution zone:** it corresponds to the zone where the volume of hot products is most important (H). In this zone the local emission of energy is not strong compared to the primary zone, but the volume is more important. Moreover in the dilution zone no chemical reaction takes place, so the energy transfer induced by radiation becomes significant in the energy equation.

All the fields presented in this section were obtained using the FS-SNBcK model. In the next section the accuracy of such model is verified and compared to other models.

9.2.3 Impact of the spectral model for the coupled application

The most accurate computations of radiation are obtained using the Monte Carlo method coupled with a Line-by-Line (LBL) spectral model. These methods are mostly used in simple benchmark geometries as the restitution time is very long. In section 6.6.6 results obtained with PRISSMA and a Monte Carlo code where compared on benchmark cases. Although the comparisons showed a very good agreement, real life cases present additional difficulties that can alter the accuracy of the results.

Figure 9.8: Three-dimensional views showing the line along which the profiles of Fig. 9.9 are plotted.

The reference calculation in the present case uses the SNBcK model with 5 spectral quadrature points and a S_4 angular discretization. Six different spectral models were tested: the SNBcK with 15 spectral quadrature points (reference), the FS-SNBcK model with fifteen and five quadrature points, the TFS-SNBcK with fifteen and five quadrature points[1] and the WSGG model (see section 6.6.3). The $\mathscr{S}_r$ profiles obtained in the dilution zone, where absorption is most important, along the line shown in Fig. 9.8 are presented in Fig. 9.9.

The reference simulation (SNBcK) shows a maximum value of $\mathscr{S}_r \approx 2.2\,10^6$ [W/m^3] and negative values reaching $\mathscr{S}_r \approx -5\,10^{-5}$ [W/m^3] near the walls. The differences observed between the FS-SNBcK and its tabulated version are due to the resolution of the temperature and species table, and the linear interpolation used to reconstruct the absorption coefficient. The profiles show that the models based on fifteen quadrature points over-predict the extremum value of the radiative source term, both in the positive and the negative sides. On the contrary, the models based on five quadrature points show a slight under-prediction of the maximum, and over-predict the radiation field in the intermediate zones where fluctuations are stronger. They show however a good agreement in the absorption region near the walls. The WSGG model heavily under predicts the radiative source term everywhere in the domain.

To better understand the strengths and weaknesses of the spectral models, a normalized absolute error field was calculated using:

---

[1]An optimum distcretization method of the table has been proposed by Poitou et al. [204] and is employed here.
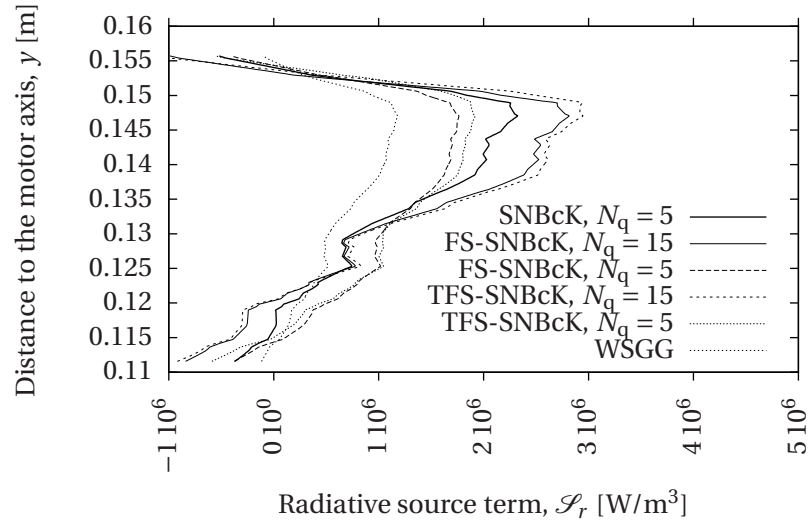
Figure 9.9: Radiative source term plotted on the line shown in Fig. 9.8 for different spectral models on an instantaneous field.

$$\epsilon(\mathscr{S}_r) = \frac{|\mathscr{S}_r^{\text{ref}} - \mathscr{S}_r|}{|\mathscr{S}_r^{\text{ref}}|_{\max}} * 100 \tag{9.2}$$

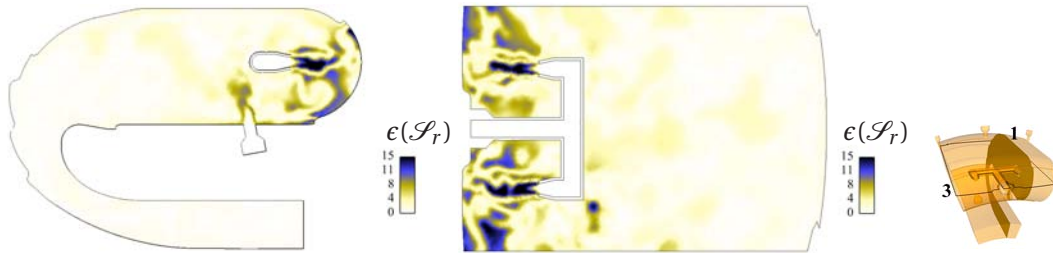where $\mathscr{S}_r^{\text{ref}}$ is the radiative source term reference field (of the SNBcK model).
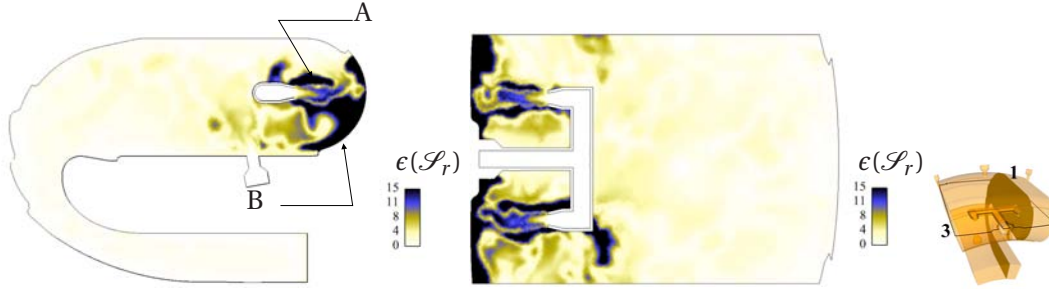

Figure 9.10: Normalized absolute error field $\epsilon(\mathscr{S}_r)$ (Eq. 9.2) between the reference simulation and the FS-SNBcK $N_q = 15$ simulation. (left) cut 1. (right) cut 3.

Figure 9.10 shows $\epsilon(\mathscr{S}_r)$ for the FS-SNBcK model with fifteen spectral quadrature points. In this global model the spectral data corresponds to a statistical repartition of the absorption coefficient along the whole spectrum. This representation can be problematic when applied to gases with non-absorbing spectral bands. The FS-SNBcK model does not distinguish between transparent and absorbent frequencies, and can diverge from the reference for gases mainly composed of CO (this element emits in

a limited number of bands in the near infrared spectrum), gases without soot and transparent gases.

Figure 9.10 shows that the error is maximum in the inner zone of the premixed flame, a region mainly composed by JP10 and air. In this case the maximum error obtained is around $\epsilon(\mathscr{S}_r) \approx 15\%$. The same error is observed in the FS-SNBcK case with $N_q = 5$ shown in Fig. 9.11. In this case however, in addition to the cold transparent zones, the error also reaches a high value in the zones of hot gases, around the diffusion flames (A) and in the internal side of the primary zone (B). In Fig. 9.11, the colors are saturated for comparison with Fig. 9.10 but the maximum error is around 43% in the primary zone.

Figure 9.11: Normalized absolute error field $\epsilon(\mathscr{S}_r)$ (Eq. 9.2) between the reference simulation and the FS-SNBcK $N_q = 5$ simulation. (left) cut 1. (right) cut 3.

In order to identify the reason why the FS-SNBcK ($N_q = 5$) model fails to correctly predict the radiation fields in the hot zones of the flow, a one-dimensional tool included in the PRISSMA suite is used.

Using the narrow band approximation, for a given gas column of length L composed of non-scattering elements that only emit and absorb in one optical path, the mean intensity at the exit of the column on the band can be written:

$$\langle I(L)\rangle_{\Delta v} = \int_{\Delta v} T_v(L)I_{bv}dv = \langle I_b\rangle_{\Delta v}\int_{\Delta v} T_v(L)dv \tag{9.3}$$

which can also be written as:

$$\langle I(L)\rangle_{\Delta v} = \langle I_b\rangle_{\Delta v}\Delta v\langle T(h)\rangle_{\Delta v} \tag{9.4}$$

where quantities integrated over a narrow band are denoted by the operator $\langle . \rangle_{\Delta v}$

An accurate resolution of Eq. (9.4) is obtained with the Malkmus transmissivity model presented in Eq. (6.110). In order to evaluate expression (9.3) the transmissivity of the gas is calculated using Eq. (9.5), where κ_v is obtained from the spectral model.

$$T_v(L) = e^{-\kappa_v L} \tag{9.5}$$

The total exit intensity of the gas column can be calculated by integration of expressions (9.3) or (9.4) over the full spectrum. Figure 9.12 shows the evolution of this intensity for a temperature ranging

from 300K to 2900K. The mixture used in this test case corresponds to the composition found in the high error zones at the bottom of the dome, shown in Fig. 9.11. The length of the gas column corresponds to the previously defined characteristic optical length of the chamber $L = 0.1$ [m].
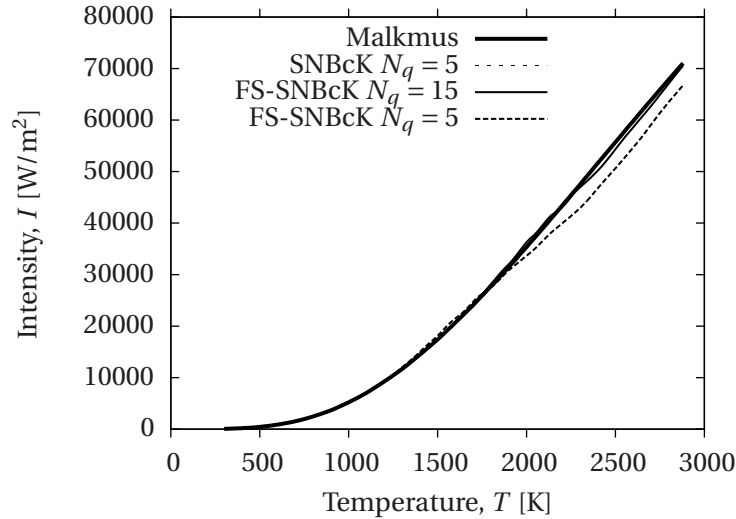

Figure 9.12: Radiative intensity at the exit of a gas column of length $L = 0.1$ [m], composed of combustion gases as a function of their temperature, for different spectral models.

Figure 9.12 shows that the SNBcK model is indeed extremely accurate for all temperatures. The FS-SNBcK models show a very good agreement up to 2000K. For temperatures above this value, the FS-SNBcK model slightly diverges from the reference. In particular the FS-SNBcK $N_q = 5$ case shows a significant under-prediction of the radiative intensity, of about 10% of the reference intensity at $T = 2500$K. Divergence from the reference value is also a consequence of the optical thickness of the medium: in the primary zone the interaction between the gas and the emitted photons occurs in a small volume. Figure 9.13 shows the effect of a smaller optical thickness for the 1D test case with a gas column of length $L = 0.05$ [m].

In this case the error in the prediction of the intensity at $T = 2500$K increases up to 23% for the FS-SNBcK $N_q = 5$ model. This explains the error observed in Fig. 9.11.

Figure 9.14 and 9.15 shows the values of $\epsilon(\mathcal{S}_r)$ for the TFS-SNBcK model with fifteen and five quadrature points respectively. The behavior is globally the same as for the corresponding non-tabulated model. The interpolation procedure used in the tabulated model can potentially add errors to the solution. In the $N_q = 15$ case some differences are evident in the dilution zone behind the vaporizer, and the overall error is slightly higher.

Finally the WSGG model was also tested and results are plotted on Fig. 9.16 (color scales are kept similar to the precedent figures for comparison between the spectral methods). Almost all the inter-
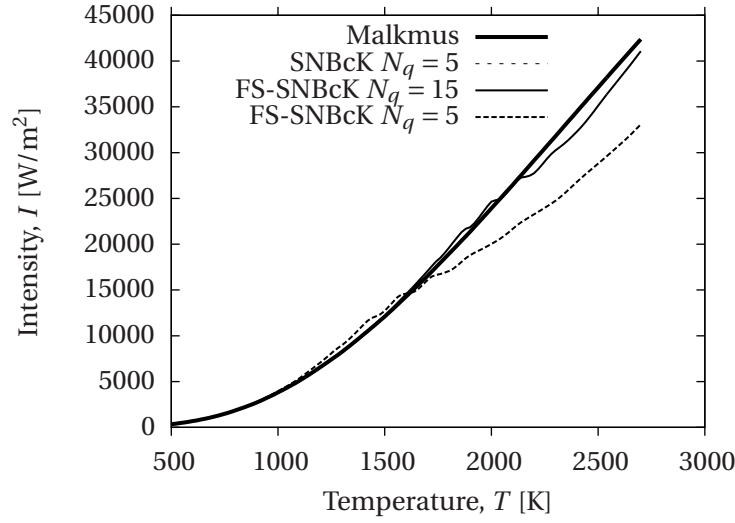
Figure 9.13: Radiative intensity at the exit of a gas column of length $L = 0.05$ [m], composed of combustion gases as a function of their temperature, for different spectral models.

nal side of the primary zone shows a significant error, up to 73%, particularly in the zones of energy emission.

Table 9.1 shows the value of the mean error $\langle \epsilon(\mathscr{S}_r) \rangle_{\text{vol}}$ calculated using Eq. (9.6) as well as the wall clock time needed by PRISSMA to perform the computation on 24 processors of an IBM JS21 architecture. The reference simulation requires more than one day to be completed. Simulations using the FS-SNBcK are two to three orders of magnitude faster than the reference simulation, but still require several minutes to be completed. For unsteady coupled simulations such restitution time is still too long. The TFS-SNBcK simulations resolve the problem very fast (around two minutes of restitution time), with a good accuracy compared to the reference simulation. The WSGG model needs less than one minute, but the accuracy of the solution is not satisfactory.

$$\langle \epsilon(\mathscr{S}_r) \rangle_{\text{vol}} = \frac{1}{N_{\text{nodes}}} \sum_{i=1}^{N_{\text{nodes}}} \epsilon_i(\mathscr{S}_r) \tag{9.6}$$

The tabulation technique accelerates the computation of the radiative fields by three orders of magnitude compared to the SBNcK spectral model: it allows to include detailed spectral properties of gases in an unsteady coupled simulation with LES. This is the model used in the coupled simulations in the present work.
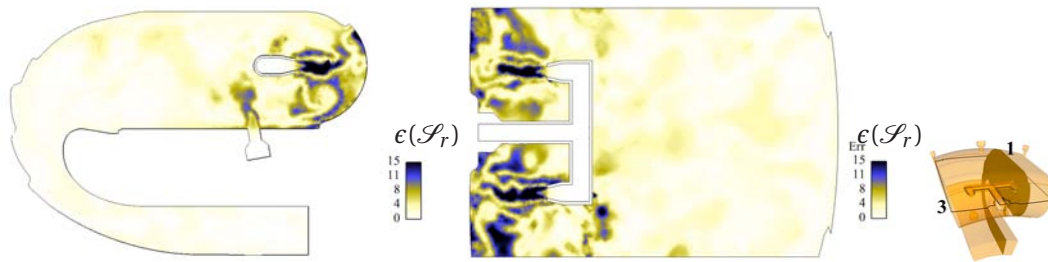
Figure 9.14: Normalized absolute error field between the reference simulation and the TFS-SNBcK $N_q = 15$ simulation. (left) cut 1. (right) cut 3.
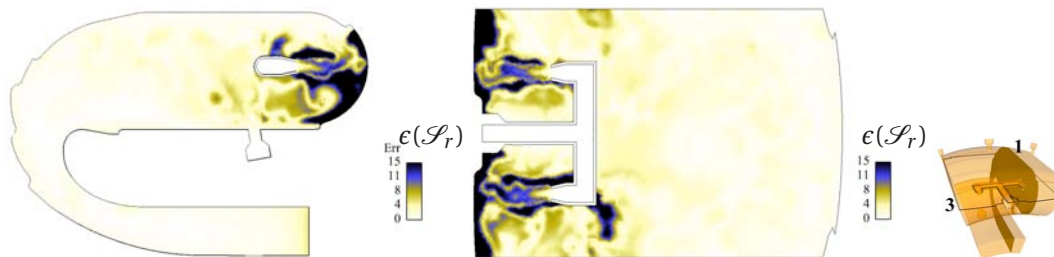

Figure 9.15: Normalized absolute error field between the reference simulation and the TFS-SNBcK $N_q = 5$ simulation. (left) cut 1. (right) cut 3.

9.2.4 Conclusions

The SNBcK model is used as a reference against which the other models are compared. The FS-SNBcK model gives accurate results but the restitution times are too long for its use on coupled simulations. The WSGG model computes the radiation fields very fast, but the results are inaccurate, in particular in the emission zones of the chamber. The TFS-SNBcK shows a good compromise between speed and accuracy. This is the model chosen for the coupled applications.

Note that the WSGG is not very accurate in certain zones of the chamber sometimes predicting energy absorption while the reference predicts energy emission. This model is still more accurate than the gray gas models presented in section 6.6.3. However until very recently many authors have used the gray gas model to characterize the spectral properties of gases [99] [194], using Monte Carlo of Raytracing solvers [59] [240] [273]. In this section it was shown that the spectral model can not be neglected and that a bad selection can lead to the wrong prediction of the radiative fields.
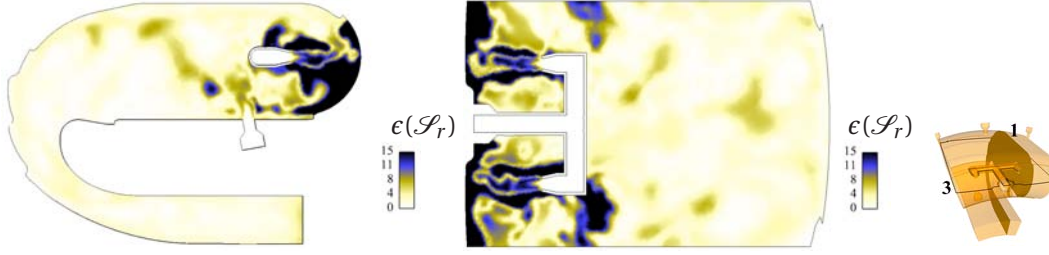
Figure 9.16: Normalized absolute error field between the reference simulation and the WSGG simulation. (left) field on cut 1. (right) field on cut 3.

Table 9.1: Evaluation of the different spectral models.

Model	Mean error, $\langle \epsilon(\mathscr{S}_r) \rangle_{\text{vol}}$	Restitution time, t [s]
SNBcK $N_q = 5$	-	129 286.38
FS-SNBcK $N_q = 15$	2.88	2240.66
FS-SNBcK $N_q = 5$	5.34	676.53
TFS-SNBcK $N_q = 15$	3.7	154.42
TFS-SNBcK $N_q = 5$	5.12	136.13
WSGG	7.68	41.87

9.3 The coupled RFTI

The coupled simulations were performed on both an IBM iDataPlex and an IBM JS21 architectures. The coupler PALM was used in conjunction with the "palmerized" units for AVBP and PRISSMA (and the interfacing unit) as shown in Fig. A.6.

Following the developments presented in section 7.3.2 the processor distribution has been calculated. The values used for the determination of the processor distribution are presented in Table 9.2, and lead to 23.4 processors for radiation and 6.6 processors for LES. These values are "ideal", as they correspond to optimal conditions, where the speed-up of each code is perfect and no in/out data processing is performed (as for example mesh reading, parallel partitioning, etc.). In real conditions, additional tuning may be necessary, depending on each particular case. For the present application the "ideal" processor distribution turned to be optimum in the real case and the coupled simulation was performed using $P_{\text{rad}} = 24$ and $P_{\text{LES}} = 6$. One additional processor was used for the coupling software and a second additional processor was dedicated to the interfacing software. A total of $P_{tot} = P + P_c = 30 + 2 = 32$ processors were finally used. This processor distribution was implemented using the PCS approach presented in section 7.1.4.

The restitution time of the coupled RFTI simulation is larger than the restitution time of the reference

Table 9.2: Coupling parameters for the combustion chamber case.

Quantity	Value
$\Delta t_{\rm rad}$	$9.3\ 10^{-6}$ [s]
$\Delta t_{\rm CFL}$	$1.4\ 10^{-7}$ [s]
$N_{\rm it}$	66.42 [-]
$t_{\rm rad}^{1}$	2808 [s]
$t_{\rm LES}^{1}$	13.3 [s]
$t_{\rm rad}^{24}$	117 [s]
$t_{\rm LES}^{6}$	2.21 [s]
$P_{\rm r\text{-}f}$	30
$C_{\rm r\text{-}f}$	0.22 [–]
$P_{\rm DOM}$	23.4 processors
$P_{\rm LES}$	6.6 processors

LES alone simulation of chapter 8 for two main reasons: first, only 1/5th of the total available processors are used in the LES code (6 instead of 32 in the present case) as most of the resources are used in the radiation code, and second each code carries out processes that can create a slight desynchronization[2] in the data exchange, as e.g. file i/o, initialization and memory managment processes. RFTI coupled simulations showed a restitution time seven times larger than LES alone when computing the same physical time on the same number of processors.

Coupled RFTI simulations have been performed using the radiative approach presented in the previous section. The studied case is exactly the configuration presented in section 8.1. The coupled simulation of the combustion chamber was computed for a period of 10 [ms] before recording statistical quantities for a period of 50 [ms] of physical time.

9.3.1 Probe signals

In order to examine the effect of radiation on the flow dynamics, the temporal evolution of different fluid variables have been recorded at different locations of the domain, including the two shown in Fig. 8.2. Figure 9.17 and 9.18 show the temporal evolution of temperature and pressure at probe 1 and 2 for the uncoupled simulation.

Fast Fourier Transforms (FFT) of the temporal signals were performed to study the spectral signature of the coupled and uncoupled simulations.

---

[2]Two codes are said to be desynchronized if they do not arrive at their respective coupling iteration at the exact same moment. A non-synchronized coupling causes idle processors.
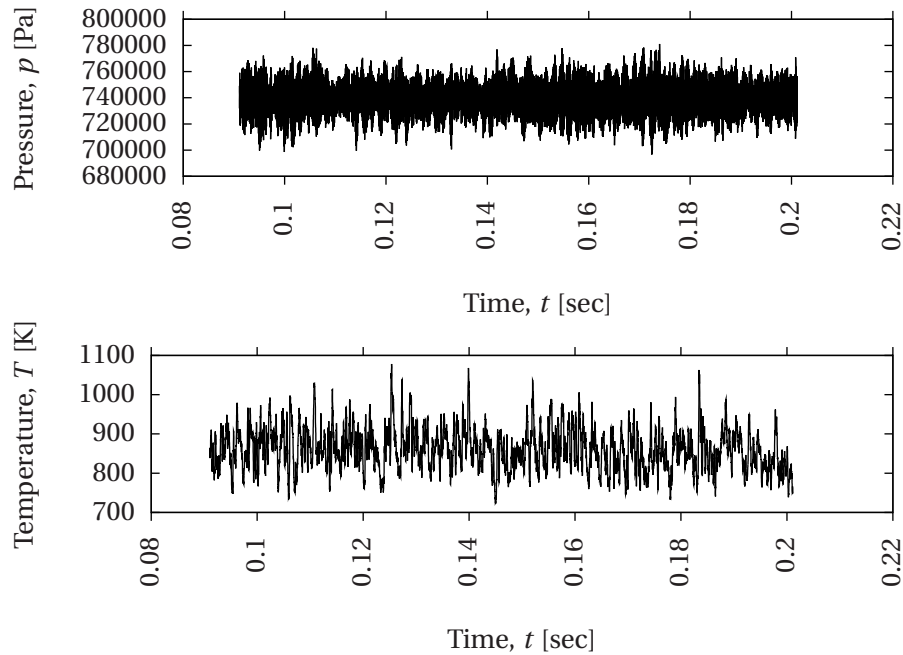
Figure 9.17: Temporal evolution of the pressure and temperature signals at probe 1 for the uncoupled simulation.

In addition to the reference and the RFTI coupled simulations, another simulation was performed using the thin gas approximation presented in Eq. (6.147) and Eq. (6.146). This method is known to be the simplest way to include radiation effects in a fluid calculation. The radiative fields (not presented here) are very different, but the most important effect of the simple radiative model can be observed in the dynamics of the flow.

In Fig. 9.19 the spectrum of the pressure signal obtained using probe 1 is shown. Outside the range shown all frequencies have low amplitudes. Three peak frequencies can be observed around $f = 8000$ [Hz], $f = 8950$ [Hz] and $f = 9200$ [Hz]. The origin of such peaks is not clear. The most probable source of periodic fluctuations is related to the eddy detachment inside the injection cane (no acoustic mode can be associated to these particular frequencies [19]).

In both images the solid line corresponds to the uncoupled (reference) simulation. The dashed line corresponds to the coupled AVBP-PRISSMA simulation in the left image and to the thin gas radiation model on the right image. In both cases the inclusion of radiation rises the amplitude of the signals. In the coupled simulation (left image) a frequency variation can be perceived but is very weak. In the thin gas case the frequency displacement is much more drastic. The peak frequencies are displaced around 50 to 100 [Hz] towards lower frequencies.

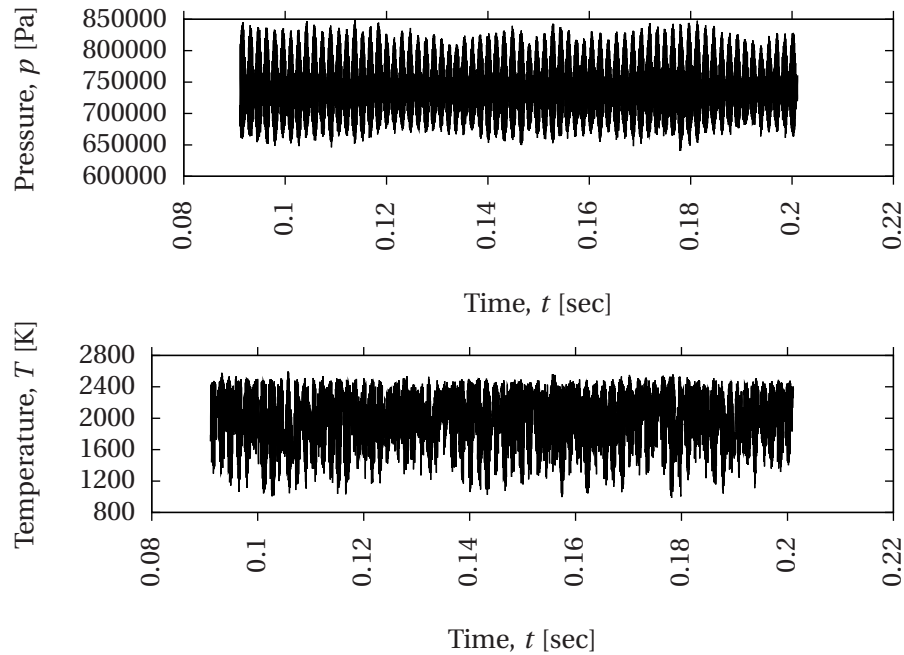The same behavior can be observed on the spectrum of the pressure signal of probe 2 shown in

Figure 9.18: Temporal evolution of the pressure and temperature signals at probe 2 for the uncoupled simulation.

Fig. 9.20. Here the amplitudes are almost the same, but the frequency displacement observed in the thin gas case becomes more clear. An analysis of the temporal signals in different places of the chamber showed only weak differences between the coupled and the uncoupled simulations. The flow dynamics seem in this case unchanged by radiation using a detailed spectral model. It is clear that the simple thin gas radiation model modifies the flow dynamics in a non physical way, and it should be used with caution.

9.3.2 Time-averaged fields

Time averaging is applied to the coupled RFTI solutions, using the same procedure as in section 8.6: a sampling was performed every 50 iterations. First and second order statistics where computed over a simulation time of 45 [ms].

In section 9.2.2 it was shown that the chemical heat release dominates the energy equation in the primary zone of the combustion chamber. The only way radiation can modify the heat release is by preheating the injected mixture. In the present case however the injected gases are considered transparent. Figure 9.21 shows iso-contour lines of the time-averaged heat release for the coupled (black) and the uncoupled (white) simulations in cuts 1 and 3. Only a very slight reduction of the
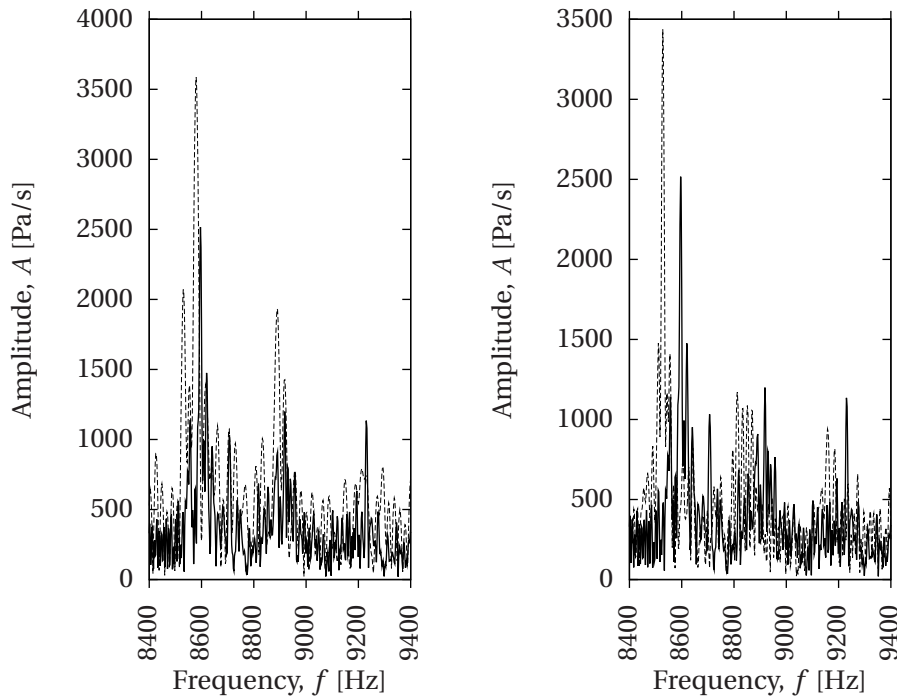
Figure 9.19: Spectral signal of pressure at probe 1. Solid line on both images: uncoupled. (left) dashed line: coupled AVBP-PRISSMA simulation. (right) dashed line: LES with thin gas radiation model.

reaction zone is observed when radiation is included, at the bottom injector in the right image of Fig. 9.21. The same tendency can be perceived at the top injector, but the simulations do not show a clear indication that radiation modifies the mean heat release in this configuration.

The same conclusion is drawn from Fig. 9.22 showing mean and RMS iso-contours of temperature. In the primary zone radiation does not strongly modify the energy content of the flow. In the previous section the zones of the chamber where radiation is expected to have an effect were identified:

- **The jet:** the mean temperature fields shows a perfect concordance between the coupled and the uncoupled simulation in the injection jet zone. However the RMS field shows a slight reduction of the T_{RMS} value in the zone between the bottom injector and the central cylinder of the vaporizer.

- **The corner:** in the zone close to the intersection between the dome and the side boundaries, the temperature distribution is modified (A). In the coupled simulation (black) the mean temperature iso-contours are more dispersed. Absorption of energy coming from the highly emitting combustion gases nearby and from the periodic boundary produce an elevation in the local temperature in this zone. The RMS field shows also that temperature variation can be stronger in this zone.
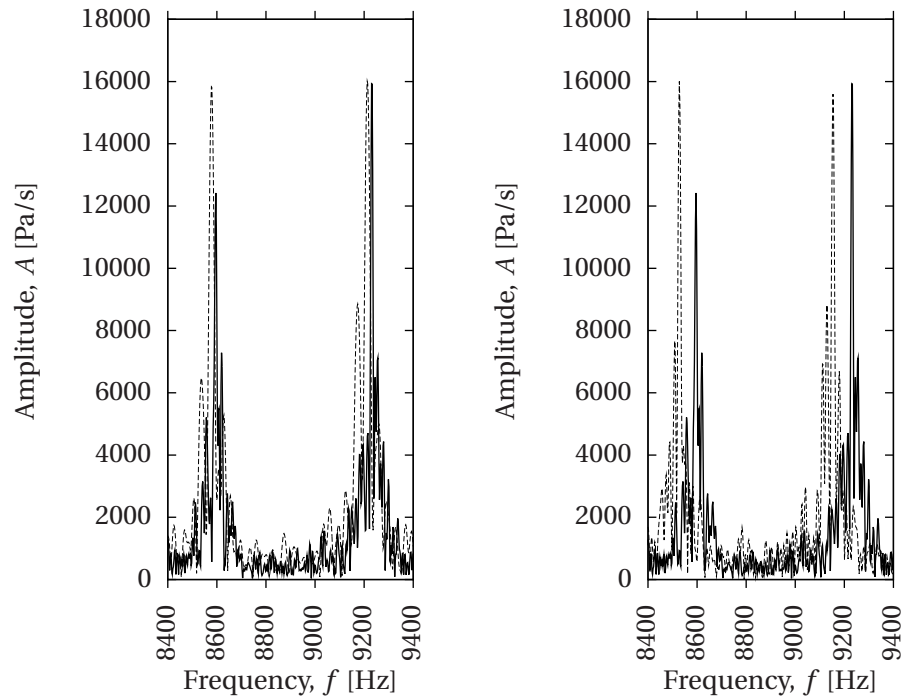
Figure 9.20: Spectral signal of pressure at probe 2. Solid line on both images: uncoupled. (left) dashed line: coupled AVBP-PRISSMA simulation. (right) dashed line: LES with thin gas radiation model.

- **The vaporizer:** Iso-contour lines of mean temperature show a variation near the walls of the vaporizer, in particular near the top and bottom injector exits (B). Temperature variations of lower amplitude are also observed behind the injector and near the central cylinder of the cane. The RMS iso-contours also show different behaviors in the coupled (black line) and the non coupled (white lines) simulations near the external injector walls.

- **The dilution zone:** contrary to the initial expectations the time averaged field shows a weaker difference between the two simulations in the dilution zone. The only marked difference is observed in the bottom of the mean temperature image (C) where a possible interaction between the hot gases and the cold jet from the dilution holes occurs. In the RMS field the differences between both simulations are more evident in the top of the image where a high iso-contour T_{RMS} level appears in the coupled simulation (black line). Towards the center of the image the RMS levels are stronger in the uncoupled simulation (white lines) than in the coupled case.

Figure 9.23 shows the iso-contour lines of mean and RMS temperatures for the coupled (black lines) and the uncoupled (white lines) simulations in cut 2. It can be observed that radiation cools down the fluid in the internal side of the primary zone. The RMS fields on the other hand show little differences.

Finally, in cut 1 (Fig. 9.24), a broadening of the high temperature zone is observed on the internal side
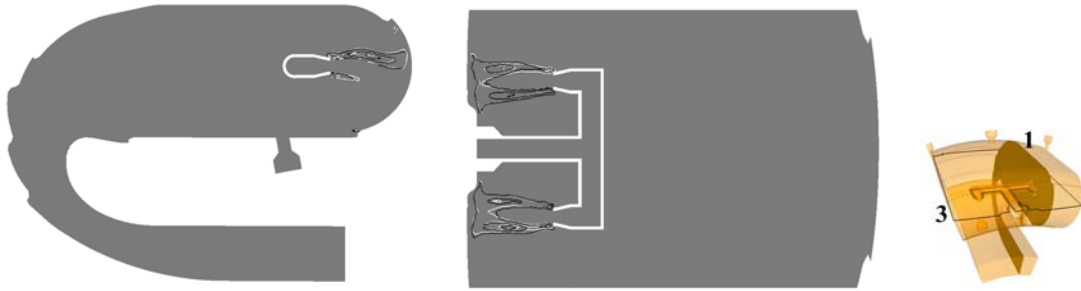
Figure 9.21: Iso-contour lines of the time-averaged heat release. White lines: uncoupled simulation. Black lines: coupled simulation. (left) cut 1. (right) cut 3.
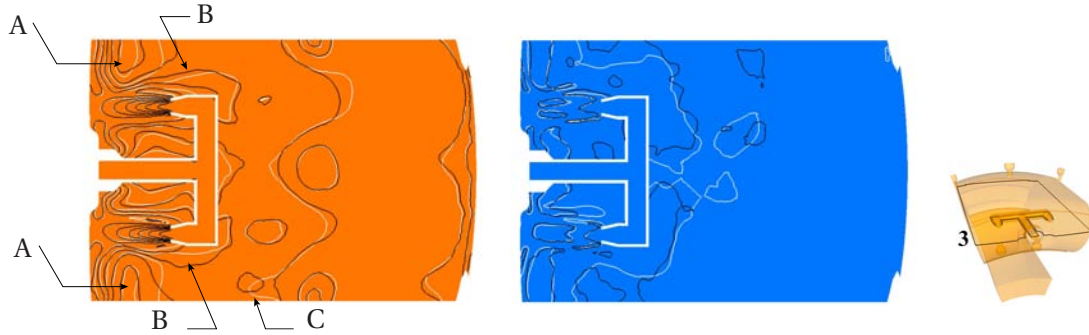

Figure 9.22: Iso-contour lines of the time-averaged temperature (left) RMS temperature (right). White lines: uncoupled simulation. Black lines: coupled simulation.

of the primary zone. The effect in this cut is the opposite to the one observed in Fig. 9.23: RMS values of temperature show differences near the non-premixed flames and the top of the injection cane.

Another way to detect differences in the mean temperature fields is presented in the left image of Fig. 9.25, where the relative temperature difference between the mean fields of both simulations has been traced using expression:

$$\delta(T) = \frac{|\langle \widetilde{T} \rangle - \langle \widetilde{T} \rangle_{\text{r-f}}|}{|\langle \widetilde{T} \rangle|} \tag{9.7}$$

where $\langle \widetilde{T} \rangle_{\text{r-f}}$ is the time averaged temperature field of the coupled (radiation-fluid) simulation. In the same figure, the right image corresponds to the absolute difference between both simulations expressed as:

$$\Delta(T) = \langle \widetilde{T} \rangle_{\text{r-f}} - \langle \widetilde{T} \rangle \tag{9.8}$$

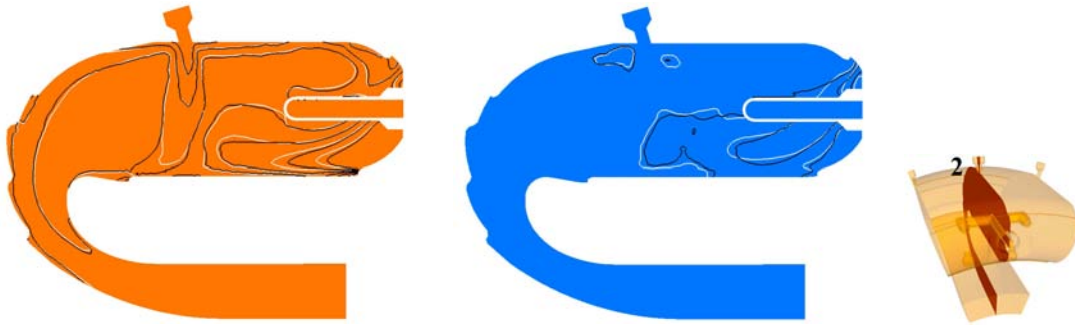The color palette in the left image of Fig. 9.25 was saturated in order to compare the fields obtained in

Figure 9.23: Iso-contour lines of the time-averaged temperature (left) and RMS values of the temperature (right) on cut 2 for the uncoupled simulation (white lines) and the coupled simulation (black lines).
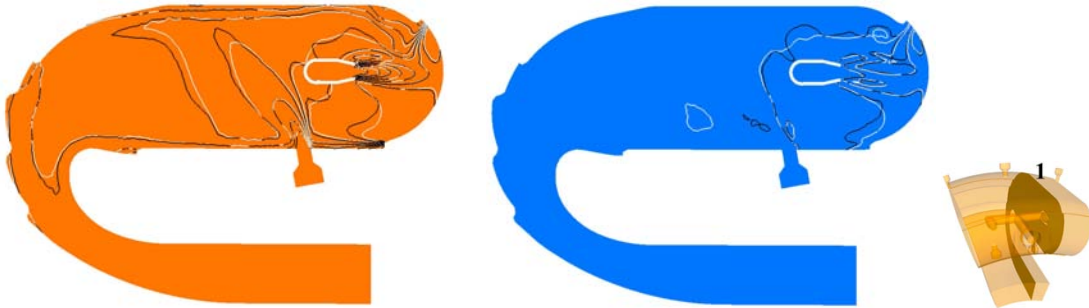

Figure 9.24: Iso-contour lines of the time-averaged temperature (left) and RMS values of the temperature (right) on cut 1 for the uncoupled simulation (white lines) and the coupled simulation (black lines).

this cut with the relative difference fields on other cuts (shown later). The maximum value of the absolute difference in this plane reaches $\delta(T) = 0.22$ at the center of the dark zones between the injector and the periodic boundary condition (A), corresponding to a temperature difference of $\Delta\langle\widetilde{T}\rangle \approx 250\text{K}$. This zone around the external wall of the vaporizer has already shown, in Fig. 9.24, a strong variation when radiation is taken into account. The proximity of this temperature difference to the injector can change the heat transfer between the fluid and the solid an by consequence the thermal behavior of the fluid just before the injector exit.

An initial analysis showed that the primary zone is mainly governed by the chemical reactions in the flame zone and near the dome. However, a broadening of the temperature field in the azimuthal direction (i.e. perpendicularly to the main flow direction) is observed in these zones (C). This is mainly caused by the use of a reflective boundary condition at the sides that emulate the periodicity of the computational domain.

In cut 3 two other zones show an important difference between the simulations: the zone near the
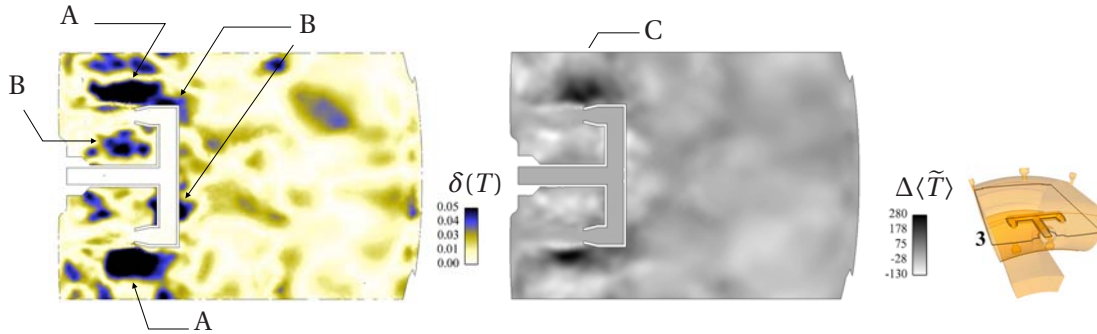
Figure 9.25: (left) relative temperature difference field $\delta(T)$ and (right) temperature difference field $\Delta(T)$ between the coupled and the uncoupled LES-DOM simulations on cut 3.

vaporizer wall and the between the central cylinder and the tips of the injector (B). In both cases the gas is heated up by radiation. This effect is most probably caused by the use of opaque surfaces at high temperatures as boundary conditions for radiation at the vaporizer walls.

In the dilution zone the variation of the mean temperature is weaker. In this zone radiation enhances the homogenization of gas temperature, cooling the hot spots and heating the cold ones.

The relative temperature difference $\delta(T)$ and the total temperature difference $\Delta(T)$ fields in cuts 2 and 1 are shown in Fig. 9.26. Most of the differences are observed in the primary zone, in particular where the non-premixed flames are anchored (A) and in the mixture zone of combustion gases and cold air (B). The total temperature difference fields $\Delta(T)$ clearly shows that in the internal side of the primary zone gases are hotter in the coupled simulation on cut 1 while they are cooled down on cut 2. The opposite effect is observed in the external side of the primary zone, above the injector. The relative differences observed do not exceed in general 5%, which corresponds to approximately 100K.

Figure 9.27 shows the temperature difference at the exit of the combustion chamber. While some spots show a temperature gain in the middle of the geometry, most of the exit plane shows a temperature reduction. An integration on the surface shows a mean temperature reduction of 7.3K. This energy loss is mainly due to radiative heat transfer to the solid walls in the chamber, as shown in Fig. 9.28. The main zones of radiative heat transfer to the solid flame tube are the internal side of the dome (A), the internal side of the injector (B) and above the cane in the external multi-perforated plates (C).

The radial non-homogenity of the temperature profiles at the exit of the combustion chamber is generally studied using the Radial Temperature Function (RTF in english or FRT in french) which describes the ratio between the mean azimutal temperature fluctuation on the exit plane and the variation of temperature between the entry and the exit of the chamber. This quantity is defined by:

$$\text{RTF}(r) = \frac{\overline{\langle T(r) \rangle_\theta} - \overline{\langle T \rangle_{\text{exit}}}}{\overline{\langle T \rangle_{\text{exit}}} - \overline{\langle T \rangle_{\text{inj}}}} \qquad (9.9)$$
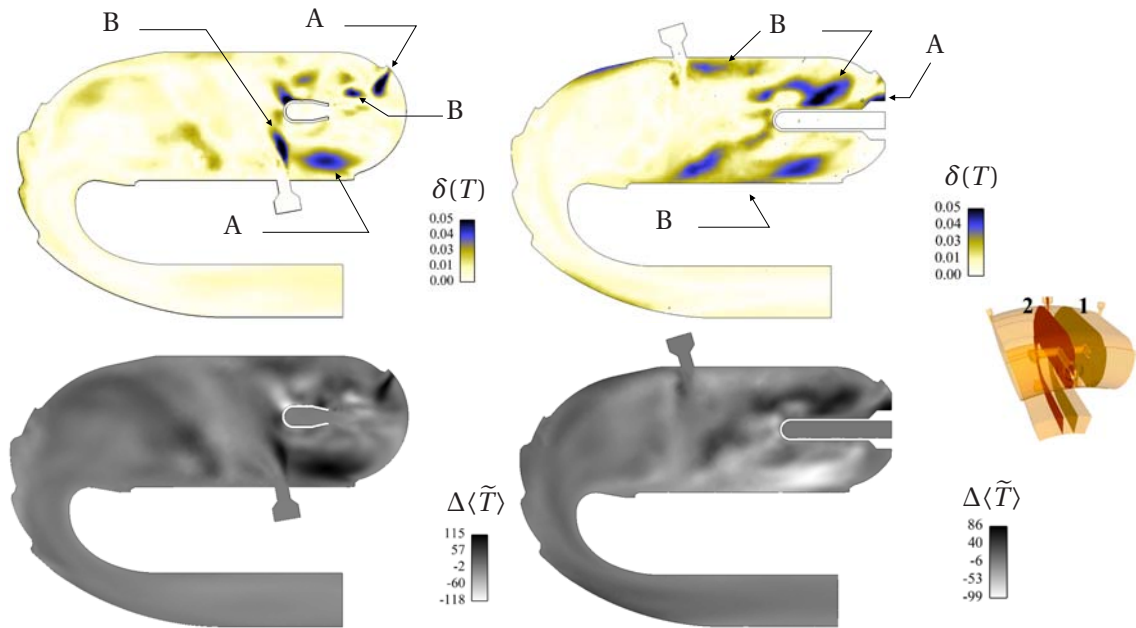
Figure 9.26: (top) relative temperature difference field $\delta(T)$ and (bottom) temperature difference field $\Delta(T)$ between the coupled RFTI and the uncoupled simulations on cut 1 (left) and cut 2 (right).

where $\overline{\langle T(r)\rangle_\theta}$ is the mean azimuthal temperature at the exit plane, that depends on the radial position, $\overline{\langle T\rangle}_{\text{exit}}$ is the mean temperature of the exit plane and $\overline{\langle T\rangle}_{\text{inj}}$ is the mean temperature at the injection. Figure 9.29 shows a comparison between the RTF obtained with and without radiation. The simulation where radiation was included shows a redistribution of the radial temperature, where the peak is attenuated and the cold extremes on the top and the bottom of the exit conduct are heated up. Radiation homogenizes of the temperature profiles at the exit of the combustion chamber.

Even if the RTF shows a different profile in each simulation, the mean temperature at the exit plane of the chamber $\overline{\langle T\rangle}_{\text{exit}}$ is reduced only by a 0.4% with the inclusion of radiation.

9.3.3 Averaged radiation vs. radiation of the averaged fields

One common approach in industry is to calculate radiation in a combustion chamber using a time-averaged or a RANS solution. In such case the radiation code can use the most expensive methods (Monte Carlo or raytracing) as the computation is made for only one field.

A strong hypothesis lays behind this approach, assuming that the temperature and species fluctuations do not contribute to the radiation fields. In other words, it is supposed that radiation of the mean field is equivalent to the time-averaged radiation field: $\mathscr{S}_r(\langle\widetilde{T}\rangle, \langle\widetilde{X_k}\rangle) = \langle\mathscr{S}_r(\widetilde{T}, \widetilde{X_k})\rangle$.
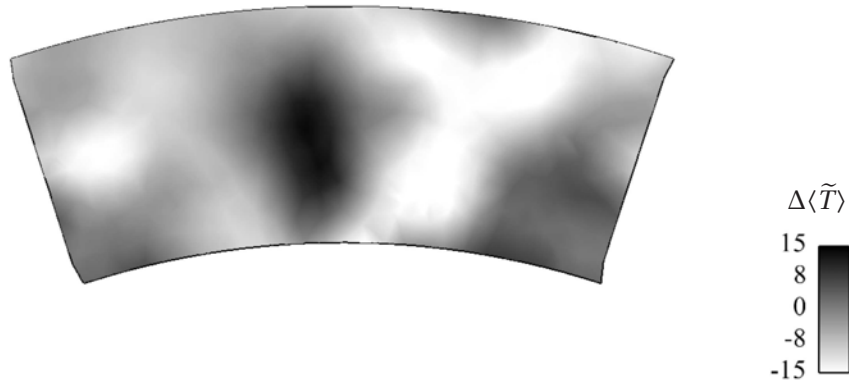
Figure 9.27: Temperature difference between the coupled and the uncoupled simulation in the exit plane of the chamber.
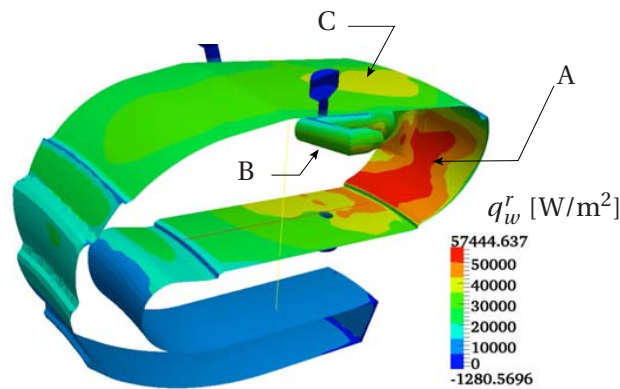

Figure 9.28: Wall radiative heat flux on the flame tube and the injector.

The effects of turbulent mixing on radiation are studied in the context of Turbulence Radiation Interactions (TRI). A good review of TRI can be found in [45]. The major aspect of TRI research is the study of the non-linear relationship between the fluctuations of the gas temperature T and composition X_k and the radiative source term $\mathscr{S}_r$.

Until very recently most of the work in the field of the TRI was performed in the context of RANS where turbulence is itself modeled. Only in the last couple of years LES have been used to study TRI [206] [46], where the large turbulent structures explicitly resolved give access to the correlations involved in TRI.

Poitou et al. [206], Coelho [46] and Roger et al. [218] have shown that sub-grid fluctuations of the fluid do not affect the radiation fields. Moreover, it was shown that the integral values of the radiation fields across a thickened flame remain the same as in a non thickened flame. Coelho [46] and Poitou
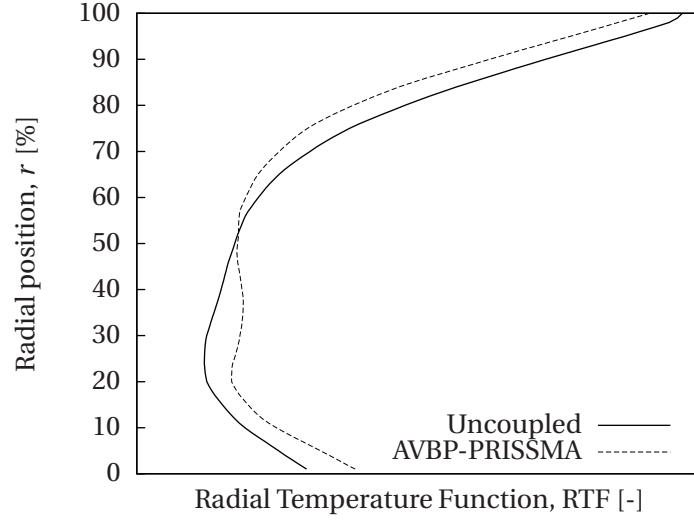
Figure 9.29: RTF profiles for the simulations with and without radiation.

[204] show that the mean radiative source term can be written using expression (9.10):

$$\overline{\mathscr{S}_r(T,X_k)} = 4\pi\sigma\overline{\kappa_P}\overline{T}^4 R_{\kappa_P}(R_T + R_{I_b}) - \int_0^\infty (\overline{\kappa_\nu}\overline{G_\nu} + \overline{\kappa_\nu' G_\nu'})d\nu \qquad (9.10)$$

where $\overline{\kappa_P} = \kappa_P(\overline{T}, \overline{X_k})$ and R_{κ_P}, R_T and R_{I_b} are the emission autocorrelations, namely the absorption coefficient autocorrelation Eq. (9.11), the temperature autocorrelation Eq. (9.12) and the cross temperature-absorption correlation Eq. (9.13). $\overline{\kappa_\nu' G_\nu'}$ is known as the absorption term correlation.

$$R_{\kappa_P} = \frac{\overline{\kappa_P(T,X_k)}}{\kappa_P(\overline{T},\overline{X_k})} \qquad (9.11)$$

$$R_T = 1 + 6\frac{\overline{T'^2}}{\overline{T}^2} + 4\frac{\overline{T'^3}}{\overline{T}^3} + \frac{\overline{T'^4}}{\overline{T}^4} \approx 1 + 6\frac{\overline{T'^2}}{\overline{T}^2} \qquad (9.12)$$

$$R_{I_b} = 4\frac{\overline{\kappa_P' T'}}{\overline{\kappa_P}\overline{T}} + 6\frac{\overline{\kappa_P' T'^2}}{\overline{\kappa_P}\overline{T}^2} + 4\frac{\overline{\kappa_P' T'^3}}{\overline{\kappa_P}\overline{T}^3} + \frac{\overline{\kappa_P' T'^4}}{\overline{\kappa_P}\overline{T}^4} \approx 4\frac{\overline{\kappa_P' T'}}{\overline{\kappa_P}\overline{T}} \approx 4\frac{\overline{T'^2}}{\overline{\kappa_P}\overline{T}}\left(\frac{\partial^2 \kappa_P}{\partial T^2}\right)_{\overline{T}} \qquad (9.13)$$

Kabashnikov et al. [123, 124] introduced the Optically Thin Fluctuations Approximation (OTFA) where the irradiation term is simplified using:

$$\overline{\kappa_\nu G_\nu} = \overline{\kappa_\nu}\overline{G_\nu} + \overline{\kappa_\nu' G_\nu'} \approx \overline{\kappa_\nu}\overline{G_\nu} \qquad (9.14)$$

The absorption coefficient κ_ν can rapidly change over the electromagnetic spectrum and the OTFA hypothesis can be wrong in different zones of the spectrum. It is however a very commonly used approximation as the irradiance term $\overline{\kappa_\nu G_\nu}$ is very difficult to model.

The temperature autocorrelation R_T is always positive as well as the absorption coefficient autocorrelation R_{κ_P}, but the cross temperature-absorption R_{I_b} can be negative. Indeed figures 6.26, 6.27 and 6.29 show that the variation of κ_P with the temperature depend on the mixture and the optical thickness of the media.

A short TRI analysis is presented here by comparing the time averaged radiative fields against the radiation fields obtained from the mean flow fields (Eq. 9.15). Using the OTFA and using the correlation factor $R = R_{\kappa_P}(R_T + R_{I_b})$ the radiative source term difference field is:

$$\Delta \mathcal{S}_r = \overline{\mathcal{S}_r(T, X_k)} - \mathcal{S}_r(\overline{T}, \overline{X_k}) \approx 4\pi\sigma\overline{\kappa_P}\overline{T}^4(R-1) \tag{9.15}$$

It can be observed that the difference $\Delta\mathcal{S}_r$ takes negative values when $R < 1$, and positive values when $R > 1$. When no fluctuations are present the absorption and the temperature autocorrelations are equal to 1 and the cross temperature-absorption is equal to 0. In such case the correlation factor is equal to $R = 1$ and as expected the difference field is equal to $\Delta\mathcal{S}_r = 0$.

Figure 9.30 shows the difference field $\Delta\mathcal{S}_r$ obtained in the case of the combustion chamber application. The differences are almost negligible downstream the elbow of the chamber but are negative in the dilution zone. They are important in the primary zone, near the anchored non-premixed flames and in the internal side (A). As shown in 8.18 in this region the temperature fluctuations are not particularly strong. The cross temperature-absorption correlation R_{I_b} is negative here The R_T autocorrelation is also weak as it depends on the temperature fluctuations. Another term that can generate a negative difference is the absorption autocorrelation $\overline{\kappa_\nu' G_\nu'}$ neglected by the OTFA. This term needs to be studied with more detail in the future.

In the internal side of the primary zone, between the bottom non-premixed flame and the jet from the primary holes, the difference field becomes positive. Looking again at Fig. 8.18 it can be observed that in this zone the temperature fluctuations are strong. In this part of the chamber the temperature autocorrelation R_T clearly prevails over the absorption coefficient autocorrelation R_{κ_P}.

In the right image of Fig. 9.30 a difference field of the magnitude of the radiative heat flux is also presented. In this image it can be observed that the heat flux near the solid walls (C) may change between both simulations. In particular the radiative heat flux near the dome shows a difference of the order of one kW.
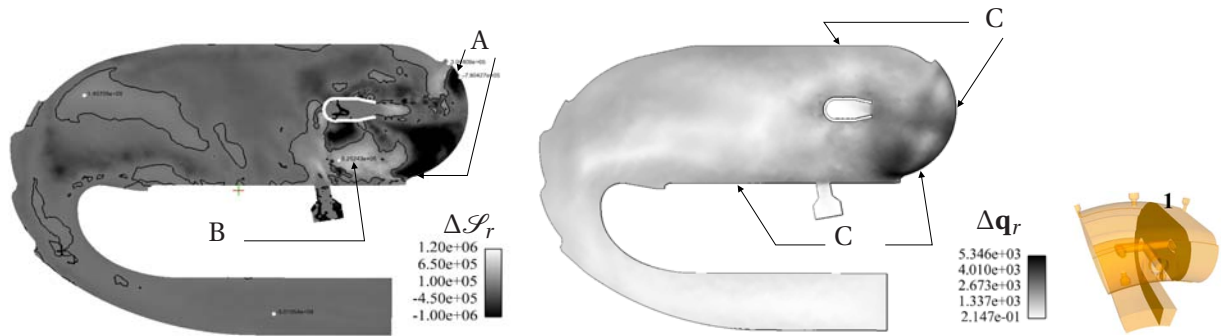
Figure 9.30: Difference field of radiative source term with an iso-contour line at $\Delta \mathscr{S}_r = 0$ (left) and difference fields for the magnitude of the radiative heat flux vector (right).

9.3.4 Wall radiative heat flux

Figure 9.31 shows the wall radiative heat flux on a half sector of the combustion chamber. The left image corresponds to a computation performed by Turbomeca [111], using one instantaneous fluid field of a RANS and a Monte Carlo code. The central image corresponds to the time-averaged radiative heat flux at the wall extracted from the coupled RFTI simulation. The right image was obtained using one time-averaged LES solution. The color palette and the scale are the same in the three cases. It is observed that the RANS based computation under-predicts the radiative heat fluxes compared with the coupled RFTI simulation. The same tendency is observed in the time-averaged LES simulation. As presented in the previous section, neglecting the effects of turbulence can lean to inaccurate results.

The major differences observed between the coupled RFTI simulation and the time-averaged LES simulation are observed in the external wall of the dilution zone (A), in the walls in the elbow of the chamber between the cooling films (B) and in the internal walls of the dilution zone (C).
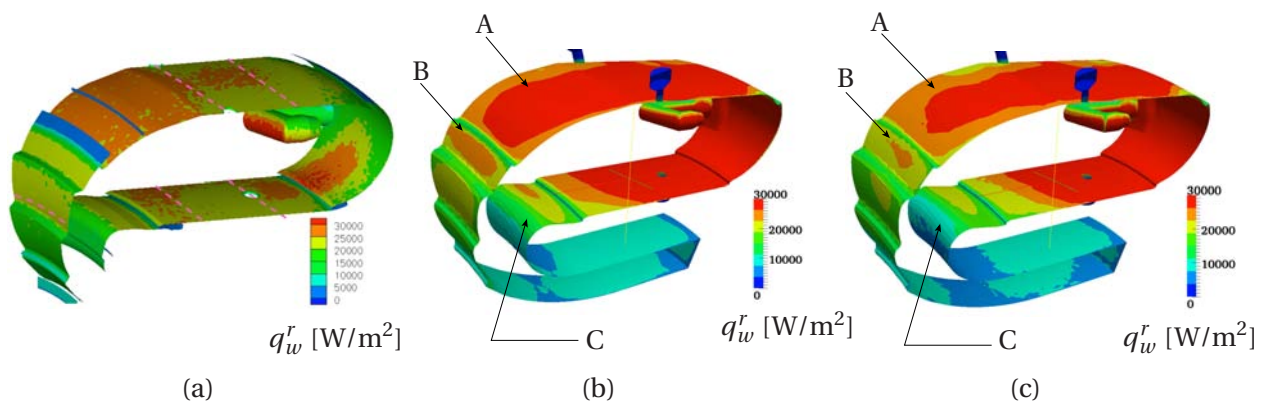

Figure 9.31: Wall radiative heat flux, q_w^r, obtained using: (a) a RANS solution and a Monte Carlo simulation performed by Turbomeca, (b) the RFTI coupled simulation, (c) one time-averaged solution from LES.

In Fig. 9.32 the results obtained from the coupled and the time-averaged simulations are shown. It can be observed that the maximum heat flux is 5 [kW/m^2] lower in the time-averaged simulation. The extension of the strong heat radiation zones show differences on the external wall (A) and on the internal wall between the cooling film and the primary holes (B). The strongest radiative heat flux is observed in the internal side of the dome (C) and below the injection cane.
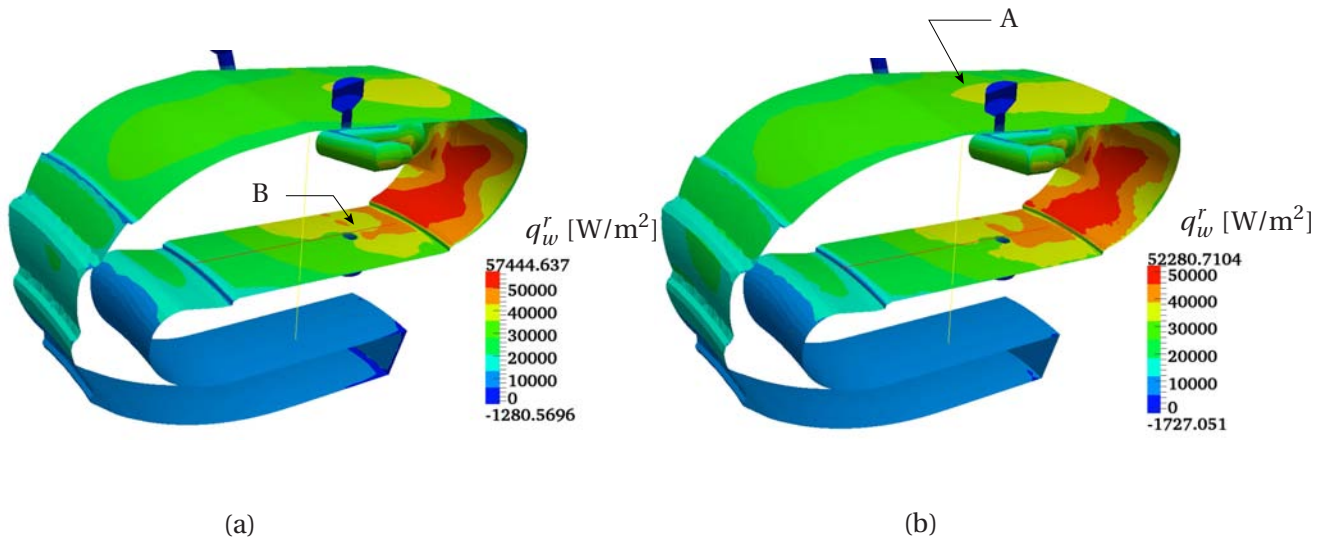

(a)   (b)

Figure 9.32: Wall radiative heat flux, q_w^r, obtained using: (a) the RFTI coupled simulation, (b) one time-averaged solution from LES.

9.4 Conclusions

Although the inclusion of radiation does not seem to modify the flame dynamics, the mean temperature distribution is different in the coupled and the uncoupled simulations. Including the radiation effects in the combustion chamber causes a change in the temperature fields. However, in the primary zone the total energy generated by the chemical reaction is many times stronger that the radiative source term. Adding radiation the the simulation redistributes energy in the domain but does not significantly change the energy content of the fluid.

To obtain an accurate prediction of the wall radiative heat fluxes in a combustion chamber it is necessary to perform coupled simulations, as taking into account only the mean temperature and mass fractions fields can lead to incorrect results. In addition, coupled RFTI simulations become extremely important in the study of TRI as each one of the terms of the correlations presented can be constructed and independently evaluated. The study of TRI using coupled simulation codes is a full subject on its own but the necessary tools to perform such work are now available.

In other combustion systems, like in piston engines, EGR (Efflux Gas Recirculation) is used in order

to lower the emission of pollutants and to lower the thermal stresses in the solid components. In this technique, combustion products are mixed with the fuel before entering into the combustion chamber. The injected gases are then composed of radiatively participant gases: in such systems the injected gases can be preheated by radiation, and can modify the flame dynamics.

10

Coupled FSTI simulation of a combustion chamber and a vaporizer injector

Contents

In this chapter a coupled Fluid-Solid Thermal Interaction (FSTI) simulation is performed between the combustion chamber presented in chapter 8.1 and the solid structure of the injection cane. The simulation is carried out using the coupling techniques developed in section 7.2.2.

As experimental data is extremely difficult to obtain in FSTI, most of the literature deals with model development mainly using DNS: Kasagi et al. [128] studied the CHT in the near-wall region using a deterministic turbulence model, Tiselj et al. [254] carried out DNS of anisothermal turbulent channel flows considering the heat conduction in the solid. In many cases these studies are used to build the simplified models commonly used in RANS or LES of industrial applications.

The main objective of this section is to present the feasibility of an unsteady coupled simulation applied to a real industrial case using the techniques discussed in section 7.2.2. In addition the effects of the thermal stresses on the solid cane and the impact of the inclusion of heat conduction in the injector are analyzed.

10.1   Study case

The coupled system consists of the combustion chamber presented in section 8.1 and the solid vaporizer presented in section 4.7. The numerical parameters of the LES are kept unchanged from the reference simulation.

In the preceding chapters the external walls of the vaporizer (the walls facing the hot gases in the combustion chamber) were considered adiabatic. The internal walls (facing the cold injection premixed fuel) heat the injected gas through a heat flux boundary condition with reference temperatures ranging from $T_{ref} = 1400$K to $T_{ref} = 2000$K, and a wall thermal resistance $R = e/\lambda^s = 5\,10^{-5}$ [m^{2}K/W], where e is the wall thickness and λ^s is the conductivity of the solid (Fig. 10.1). In this case heat transfer by convection at the surface is neglected from the thermal resistance term R.
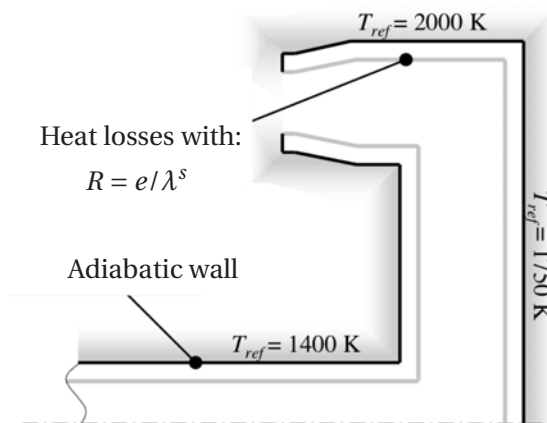

Figure 10.1: Thermal boundary conditions used in the cane in the reference LES, extracted from [19]

A strong thermal gradient is present between the interior and the exterior of the injector, so that the temperature of the solid can not be uniform all over the structure: it is piloted by the heat transported

from the exterior (hot gases) to the interior (cold gases) of the injector.

A coupled FSTI simulation presents two main advantages compared to non-coupled simulations:

- Including the solid structure, gives correct heat fluxes between the exterior and the interior of the vaporizer, so it imposes the correct boundary condition for the LES.

- The temperature distribution in the solid structure can be studied.

The numerical parameters used in AVBP are the same as presented in section 8.1. The code AVTP was used to solve the heat conduction problem in the solid injector, and the numerical parameters used are presented next.

10.2   Numerical parameters

The mesh used in the solid structure is presented in Fig. 10.2. The cells at the interface have a size comparable to the cells used in the neighboring LES mesh, but the nodes are non-coincident. At least five nodes are used between the internal and the external walls. No zone of the computational domain has any special refinement, therefore the shape of the elements of the mesh is very homogeneous. A total of 44 026 nodes and 210 191 cells compose the mesh. The value of the smallest volume is equal to $\Delta_{min} = 4.1391\, 10^{-12}$ [m^3].
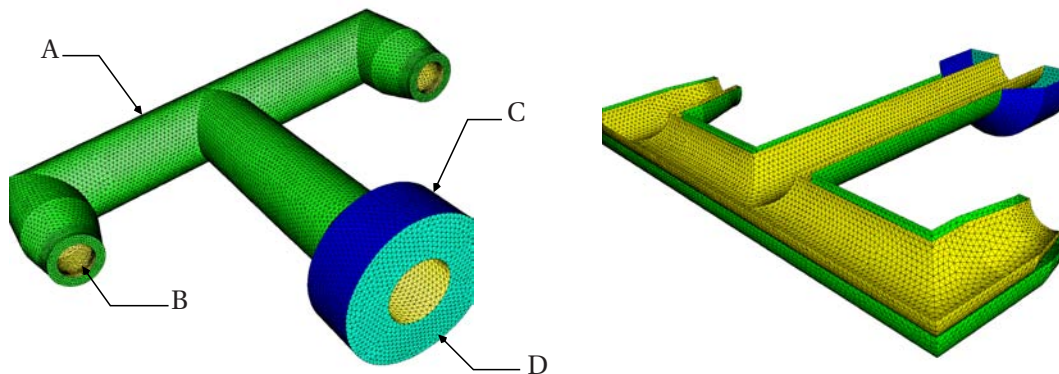

Figure 10.2: Surface mesh of the T-shaped cane vaporizer: (A) external wall, (B) internal wall, (C) base of the vaporizer, (D) fixation surface to the chamber wall. (right) cut showing the interior.

Three surfaces where chosen to study the interaction between the fluid and the solid. These correspond to the interior and the exterior wall, and to the cane base. The surface called "fixation" is not in direct contact with the flow, so a heat flux boundary condition was imposed, using a reference temperature $T_{ref} = 600$K and a convective heat transfer coefficient $h = 3000$ [Wm^{-2}K^{-1}] corresponding to the interaction between the solid and the cold air flowing in the annulus.

The external surfaces allow to test the effect of the coupling process in zones were the boundary is divided in two: the external wall (A) and the cane base (C) are both situated on the external surface, but belong to different boundary groups in both the LES and the solid conduction codes. This provides an insight into the stability of the coupling sequence and the continuity of the solution.

The material used corresponds to one specific type of stainless steel which shows an almost constant conductivity for different temperatures (see Fig. 4.10). This material has a melting point of $T = 1720$K, a density of $\rho = 7900$ [kg/m^3] and a conductivity of $\lambda = 18.9$ [Wm^{-1}K^{-1}] at high temperatures. The specific heat capacity of the material can also change with temperature, but has a mean value of $C = 586.15$ [JK^{-1}kg^{-1}]. The thermal diffusivity of the material can be calculated using Eq. (4.3): $a = 4.084\,10^{-6}$ [m^3 s^{-1}].

An approximation of the time step associated to solid conduction can be obtained from the Fourier condition (Eq. 4.18): $\Delta t_s \approx 1.7\,10^{-3}$. This time step is four orders of magnitude larger than the LES time step. The characteristic time of conduction in the studied configuration is based on the radius of the injector base:

$$\tau_s \approx 2.2 \text{ [s]} \tag{10.1}$$

The characteristic time associated to the heat transfer from the fluid to the solid can be calculated in different ways. In this work, the maximum interaction time between a fluid molecule and the solid can be associated to the convective time needed to go from the inlet to the exit of the vaporizer. Taking the mean distance of this path, $L = 7\,10^{-2}$ [m], and the mean injection velocity, $u_{\text{inj}} = 87.5$ [m/s], the characteristic thermal time is obtained:

$$\tau_f = \frac{L}{u_{\text{inj}}} = 8\,10^{-4} \text{ [s]} \tag{10.2}$$

10.3 Coupling strategy

The coupled FSTI simulation was carried out for $t_f = 40$ [ms] in the fluid solver and $t_s \approx 400$ [s] in the heat conduction code. In section 7.2.2 it was observed that the time and length scales associated to the fluid and the solid are different and coupled FSTI simulations are performed using the Asynchronous Coupled Simulation (ACS) strategy. This technique needs to be employed because a typical LES simulation computes at best a few hundred milliseconds of physical time, which is a period where the temperature of the solid structure can be considered constant. The reason why a coupled simulation is still necessary comes from the fact that the temperature distribution on the solid structure is not known in advance.

In the ACS the heat diffusion problem is scaled in time, in order to obtain similar characteristic times

in both codes. In this strategy, changes of the temperature field in the solid do not correspond to the real temporal evolution: only the final stable state to which the coupling converges has a physical meaning.

The convective heat fluxes in the LES are computed using the law of the wall developed in section 7.3.3, and data exchange between the codes is performed using the Neumann-Dirichlet approximation presented in section 7.2.2. The coupling was performed using the PCS presented in section 7.1.4.

Between two coupling points each code calculates a physical time equal to $\alpha_s \tau_s$ in the solid and $\alpha_f \tau_f$ in the fluid (see seection 7.5.2). Duchaine et al. [67] shows that, in a FSTI coupling using AVBP and AVTP, convergence speed increases for low values of α (Fig. 10.3). In the present work different values were tested, but only the simulation showing the best response was used to perform statistical analysis, and corresponds to the case where $\alpha_f = 0.1$ and $\alpha_s = 0.5$.
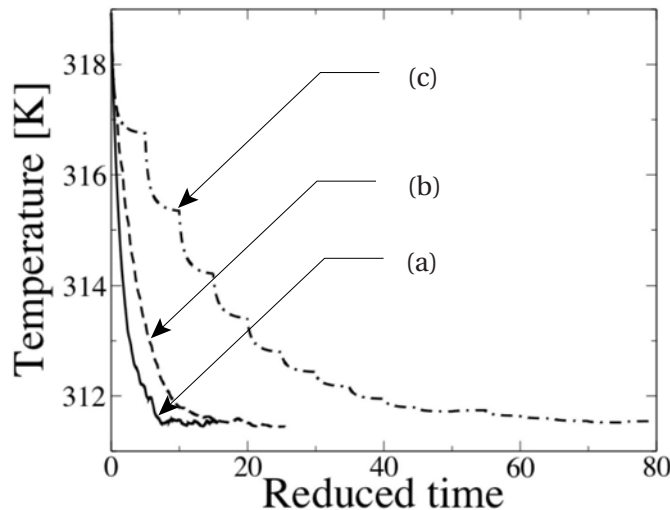

Figure 10.3: Evolution of the mean temperature on a coupled FSTI simulation on a turbine blade: (a) $\alpha = 0.1$, (b) $\alpha = 0.85$, (c) $\alpha = 5$. Extracted from [67]

From eqs. (7.43) and (7.44) the total number of iterations between two coupling points can be deduced: $n_f = 615$ and $n_s = 648$. The processor distribution is set up as described in section 7.2.2: the number of nodes in the fluid mesh is six times larger than in the solid mesh; in addition the computational cost is almost seven times larger for the LES than heat conduction. Consequently, for a total of $P = 30$ available processors, solid conduction needs $P_{\text{sol}} = 1$ processor, while LES requires the remaining $P_{\text{LES}} = 29$ processors.

All simulations were carried out on an IBM iDataPlex computer featuring "nehalem" processors at a clock-rate of 2.66 GHz. The restitution time of the coupled simulation is close to the uncoupled simulation, as the CPU cost of the simulation of solid heat conduction is small compared with LES.

10.3.1 Evolution of the coupled FSTI simulation

The initial solution used in the solid was extracted from the test calculated in section 4.7. During the first iterations data exchange between the codes pulls the temperature of the solid towards an steady state, as shown in Fig. 10.4 (left). It can be observed a drastic variation in the mean temperature of the solid going from $\langle T \rangle_{\text{vol}} = 977$ to $\langle T \rangle_{\text{vol}} \approx 915$. The response of the coupling algorithm and the codes is satisfactory, and the computation does not show any sign of divergence.

Adding all the heat fluxes crossing the walls of the injector an energy budget can be constructed: $[Q_w^s]_{\partial\Omega} = \int_{\partial\Omega} q_w^s dS$. This value permits to verify if the solid has reached a thermal equilibrium state. Figure 10.4 (right) shows that after 22 coupling points the solid reaches thermal equilibrium. It can be observed however that from one coupling cycle to the next the heat fluxes imposed by the fluid can have large variations.
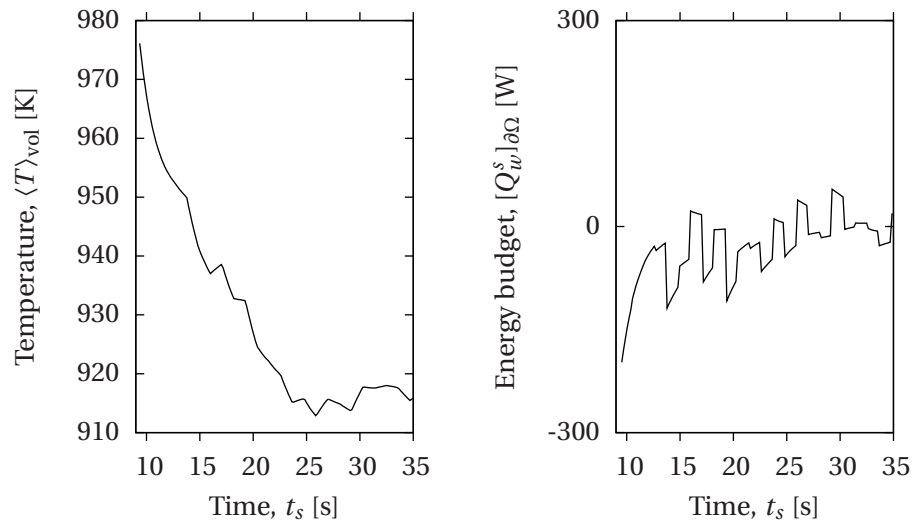

Figure 10.4: Evolution of the mean temperature $\langle T \rangle_{\text{vol}}$ (left) and the heat flux budget $[q_w^s]_{\partial\Omega}$ (right) during the first iterations.

Once the "converged" state is reached, the simulation is ran until $t_s = 400$ [s] in order to perform a proper statistical analysis. Figure 10.5 shows the evolution of the mean, maximum and minimum temperature inside the solid, the energy crossing the four walls of the injector and the energy budget. Temperature and energy values oscillate around the target solution of the coupled problem. This behavior corresponds to the oscillating convergent case presented in section 7.2.2.

To avoid oscillations around the solution, the analysis performed in section 7.2.2 shows that the ratio $H'(q_w^s) = -h_f/h_s$ must be as close to zero as possible. The use of Asynchronous Coupled Simulations (ACS) modifies the response of the solid to any external excitation by a factor of α_s, this value has shown in tests to influence the amplitude of the oscillations as shown in Fig. 10.6, where the value of
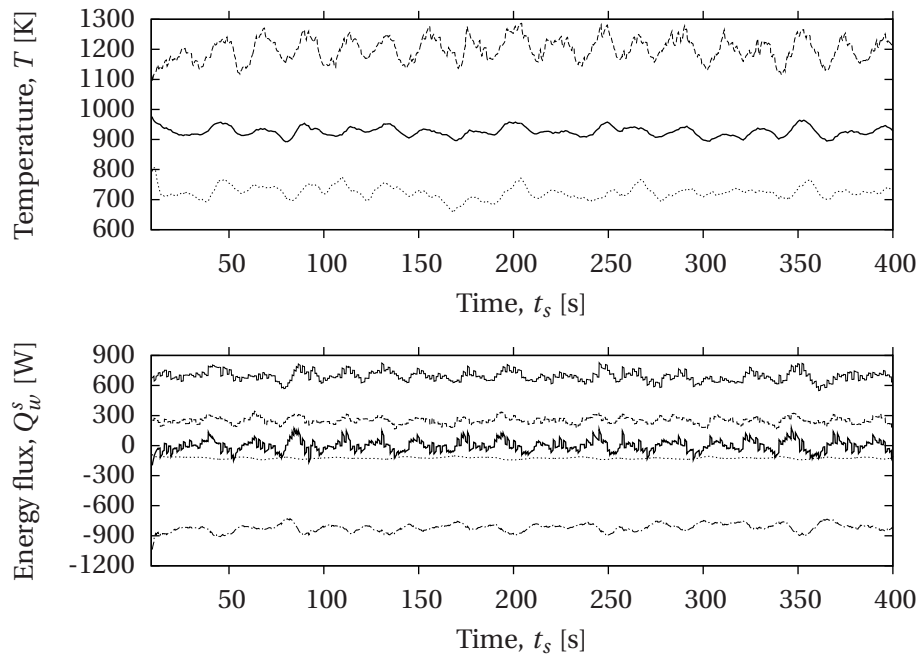
Figure 10.5: (top) Evolution of the temperature (maximum, minimum and mean) in the solid. (bottom) Heat flux crossing the four boundaries (— · — :internal wall; ——— :external wall; – – – – : base; ········ :fixation) and the heat flux balance (thick solid line ———).

$\alpha_s = 0.1$ was used: while higher oscillations of the heat flux are observed, temperature remains stable.

10.4   Effects on the solid injector

10.4.1   Instantaneous temperature fields

Figure 10.7 shows four views of an instantaneous temperature field of the injector. The colors represent the temperature of the structure. Iso-contour lines are used to better identify the hot and cold zones.

The most prominent feature in Fig. 10.7 is the hot spot situated on the bottom-half of the cane base (A), where the temperature reach $T = 1200K$. This high temperature penetrates into the solid structure and reaches the interior, as shown in the top right image of Fig. 10.7 (B). This zone of local high temperature may lead to a non-homogeneous heating of the injected premixed fuel.

Also in Fig. 10.7, iso-contour lines show a rapid temperature variation between the central cylinder and the injection tips (E). At the exit of the injector the structure reaches temperatures around $T =$
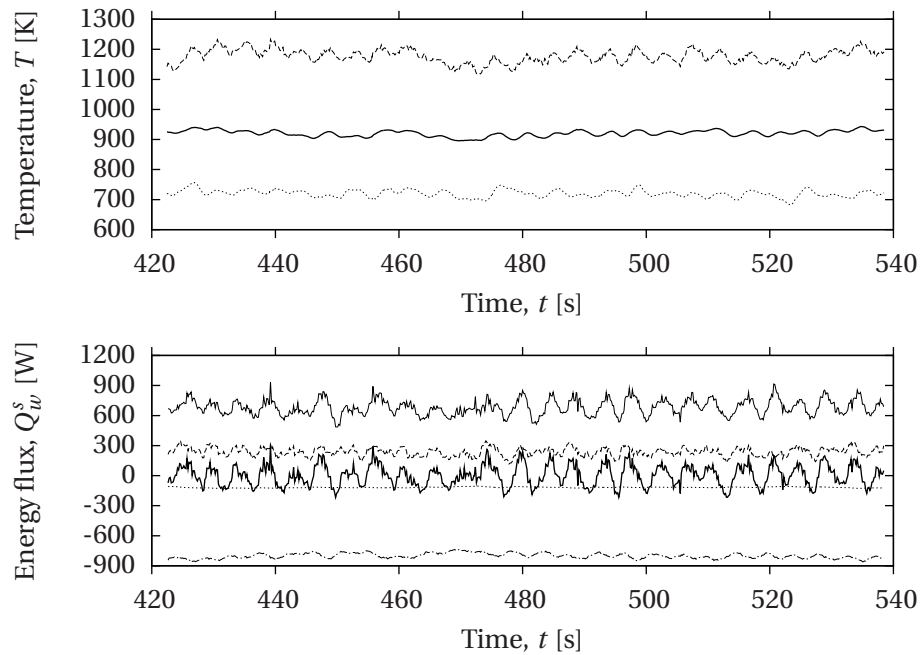
Figure 10.6: (top) Evolution of the temperature (maximum, minimum and mean) in the solid. (bottom) Heat flux crossing the four boundaries (— · — :internal wall; ——— :external wall; – – – – : base; ········ :fixation) and the heat flux balance (thick solid line ———).

1000K, while the top and the bottom views show that the outermost corners are exposed to a very high heat flux (D).

Finally, a "cold" spot can be observed in the external (top left image) and the internal (bottom right image) top half section of the solid (C), where the temperatures reaches $T = 750K$. This cold region extends from the base of the cane to the rear wall where the injected fuel impacts. A less extended but similar cold zone is visible on the bottom half of the solid (F).

The temperature on the internal surfaces of the structure is allays higher than the temperature of the injected gas, which is warmed up by the heat flux imposed by the solid. Note that the temperature of the solid never reaches its melting point. At the base of the cane the thickness of the solid helps to diffuse the temperature, however the strong temperature gradient in this zone may cause thermal fatigue.
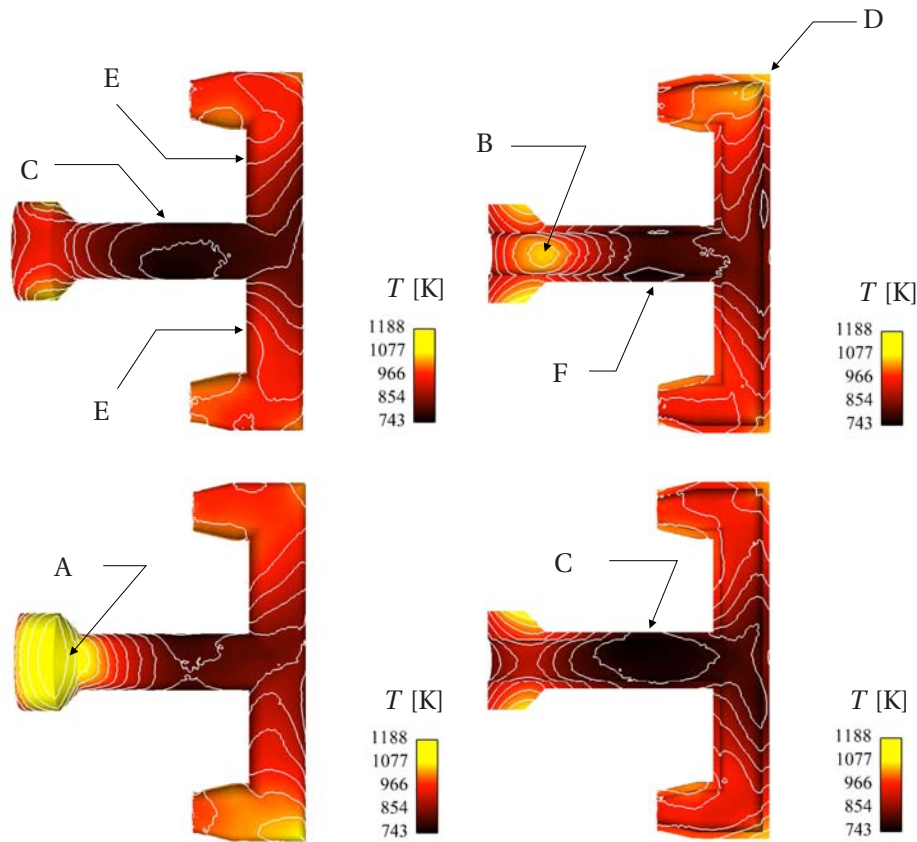
Figure 10.7: Temperature field on the cane solid surface: (top) top view, (bottom) bottom view, (left) exterior, (right) interior.

10.4.2   Time-averaged temperature fields

The time-average temperature field of the vaporizer was obtained using a sampling of the instantaneous temperature field every coupling iteration (in the present case every 648 iterations). Figure 10.8 shows the top-half (left) and the bottom-half (right) parts of the vaporizer and its surface temperature.

It can be observed that the maximum temperature is found at the base of the cane (A) near the hot combustion gases of the primary zone of the chamber. The "cold" region observed in the instantaneous temperature fields can also be observed in the central cylinder of the cane (B). A strong temperature gradient is present from the base of the cane to the "cold" spot, with temperatures varying from $\langle T \rangle = 1230K$ down to $\langle T \rangle = 700K$.

Another zone showing a temperature variation can be observed between the central cylinder and the tips of the injector (C). These gradients show temperature variations between $\langle T \rangle = 850K$ and $\langle T \rangle = 1000K$. The temperature is also high at the external corners of the injector tips (D), where the
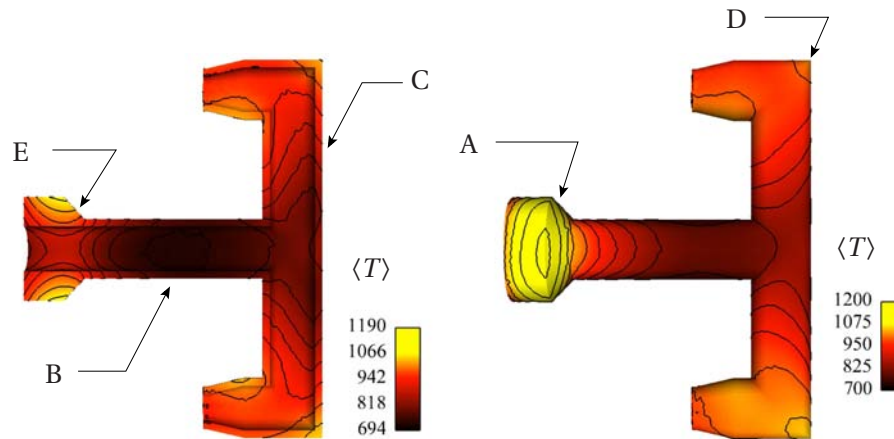
Figure 10.8: Time-averaged temperature field on the cane solid surface, bottom view: (left) interior of the top half of the cane, (right) exterior of the bottom half.

temperature reaches $\langle T \rangle = 1100\text{K}$.

Note how the temperature is diffused inside the base of the injector (E), where the gradients are the strongest: in this zone the thickness of the wall protects the internal surface from over-heating, thus avoiding heat transfer to the premixed fuel.

The time-averaged field at the internal surface of the injector is very symetric and shows little variations (temperature ranges from $\langle T \rangle = 700\text{K}$ to $\langle T \rangle = 980\text{K}$), whereas the external surface show a slight asymmetry in particular on the tips of the injector.

10.5 Effects on the fluid flow

10.5.1 Spectral analysis of the unsteady flow

Figure 10.9 shows the spectral analysis of the pressure signal recorded at probes 1 (left) and 2 (right). Results of the reference LES are also plotted for comparison. The overall shape of the plot is similar in both cases, but the peaks move by $f = 50$ [Hz] to $f = 100$ [Hz] towards lower frequencies, and the amplitude of the fluctuations at $f \approx 8600$ [Hz] are higher on probe 1. In the coupled simulation (dashed lines) the frequency peaks are located on a slightly broader frequency range.

Heat conduction slightly modifies the periodic phenomena detected by the spectral analysis. This frequencies are not related to any acoustic property of the chamber. The peaks are most probably related with some turbulent phenomena in the injector which, in this case, shows sensitivity to heat conduction.
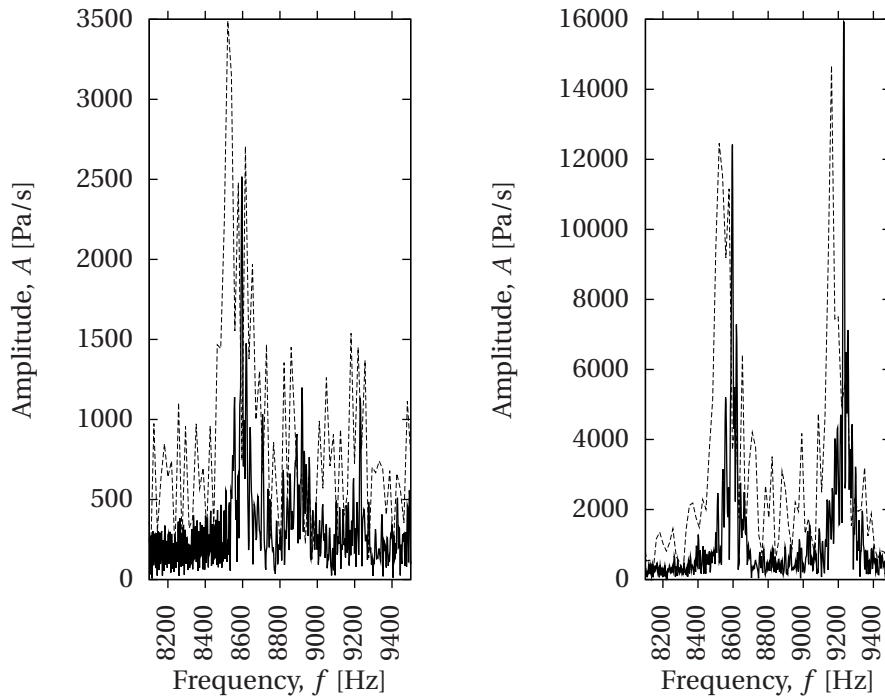
Figure 10.9: Spectral analysis of pressure at probe 1 (left) and probe 2 (right) Solid line: reference simulation. Dashed line: coupled FSTI.

10.5.2   Time-averaged flow inside the injector

Including heat conduction in the vaporizer, energy transfer from the external flow to the premixed fuel is more accurate than using the classical heat loss boundary condition of the reference LES. Figure 10.10 shows a comparison between the temperature fields of the fuel at the interior of the injector for the coupled and the reference simulations. The gray saturated scale used allows to better identify the differences between the fields: black zones correspond to cold fluid, clearly showing that the flow is cooler in the coupled simulation.

The thermal boundary layers are different in each case and the amount of energy injected in the premixed fuel is also different. This is caused by the heat flux model used in the reference simulation: the arbitrary choice of a reference temperature T_{ref} and a resistance R causes an over-estimation of the heat flux imposed on the flow at the interior of the injector. In addition in the reference LES the heat flux is imposed uniformly over each internal surface. On the contrary, in the previous sections it has been observed that in the coupled simulation the temperature of the internal surfaces can quickly change. As a consequence the temperature profiles at the exit of the injector are different in each simulation as shown in Fig. 10.11.

In both profiles presented in Fig. 10.11 it can be observed that the flow near the wall is warmer than
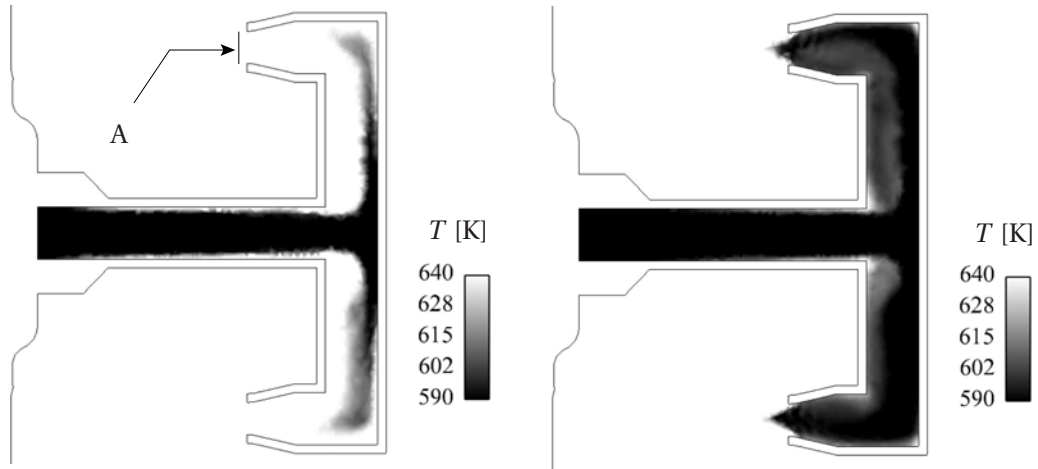
Figure 10.10: Temperature fields inside the injector: (left) reference, (right) coupled FSTI.

the fluid at the core of the jet. The differences can attain 200K in the reference simulation and 150K in the coupled FSTI simulation. The injection temperature of the reference LES is over-predicted, and this can lead to an inaccurate prediction of the final combustion temperature of the premixed flame.

10.5.3 Mean temperature and heat release fields

Figure 10.12 shows the relative difference field $\delta(T)$ (Eq. 9.7) and the absolute difference field $\Delta\langle\widetilde{T}\rangle$ (Eq. 9.8) between the coupled and the uncoupled simulations in cuts 2 and 3. Main differences appear at the point of injection into the combustion chamber (D) that engenders a reduction of the final combustion temperature of the premixed flame (E) in the coupled simulation, and consequently a temperature reduction of the combustion gases evacuated towards the dilution zone (B). A temperature reduction is also observed near the solid injector (F).

At the the base of the cane approaching the upper non-premixed flame (A), the remaining unburned fuel ejected from the premixed flame is at a lower temperature in the coupled case. At the intersection between the axi-symmetric boundaries and the dome (C) a local temperature reduction is also observed.

Figure 10.13 shows the absolute difference of the heat release between the coupled $\langle\widetilde{\dot{\omega}}_T\rangle_{\text{s-f}}$ and the uncoupled $\langle\widetilde{\dot{\omega}}_T\rangle_{\text{ref}}$ fields, calculated using:

$$\Delta\langle\widetilde{\dot{\omega}}_T\rangle = \langle\widetilde{\dot{\omega}}_T\rangle_{\text{s-f}} - \langle\widetilde{\dot{\omega}}_T\rangle_{\text{ref}} \tag{10.3}$$

Differences appear only around the premixed flame (A) and in particular at the holding point of the flame to the injector. This shows a clear modification of the combustion process most probably due

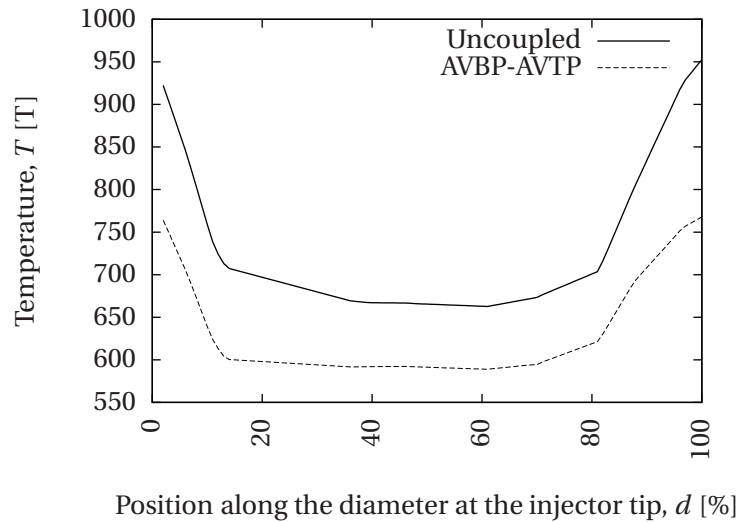Position along the diameter at the injector tip, d [%]

Figure 10.11: Temperature profile at the exit of the injector (marker A on Fig. 10.10). The center of the injected jet is colder than the flow near the walls.

to the reduction of the injection temperature of the fuel and the heat losses near the solid walls.

10.5.4   Radial Temperature Function

The temperature profile at the exit of the combustion chamber, described by the RTF (Eq. 9.9), is also affected in the coupled simulation. In Fig. 10.14, the profiles of both simulations show a close behavior, but a "hot point" is observed at the 40% radial position, as well as a temperature elevation near the internal wall (0% radial position). The mean temperature at the exit plane $\overline{\langle T \rangle}_{\text{exit}}$ is reduced by 1.3 % in the coupled case (corresponding to a total temperature difference of almost 16.3K).

10.5.5   The premixed combustion zone

To study the variations between the two simulations, temperature and heat release profiles are plotted along the three lines presented in Fig. 10.15, coplanar with cut 3. The first line (1) is placed in front of one of the exits of the injector in the axial direction. The second line (2) is oriented in the azimuthal direction, perpendicular to the injection. The third line (3) has been placed in the anchoring zone of the premixed flame.

Figure 10.16 shows the time-averaged heat release and temperature profiles along line 1. The plots show that in the coupled FSTI simulation the energy released by combustion is lower, and as a consequence the gas temperature is almost 100K lower. These profiles show that the temperature gap
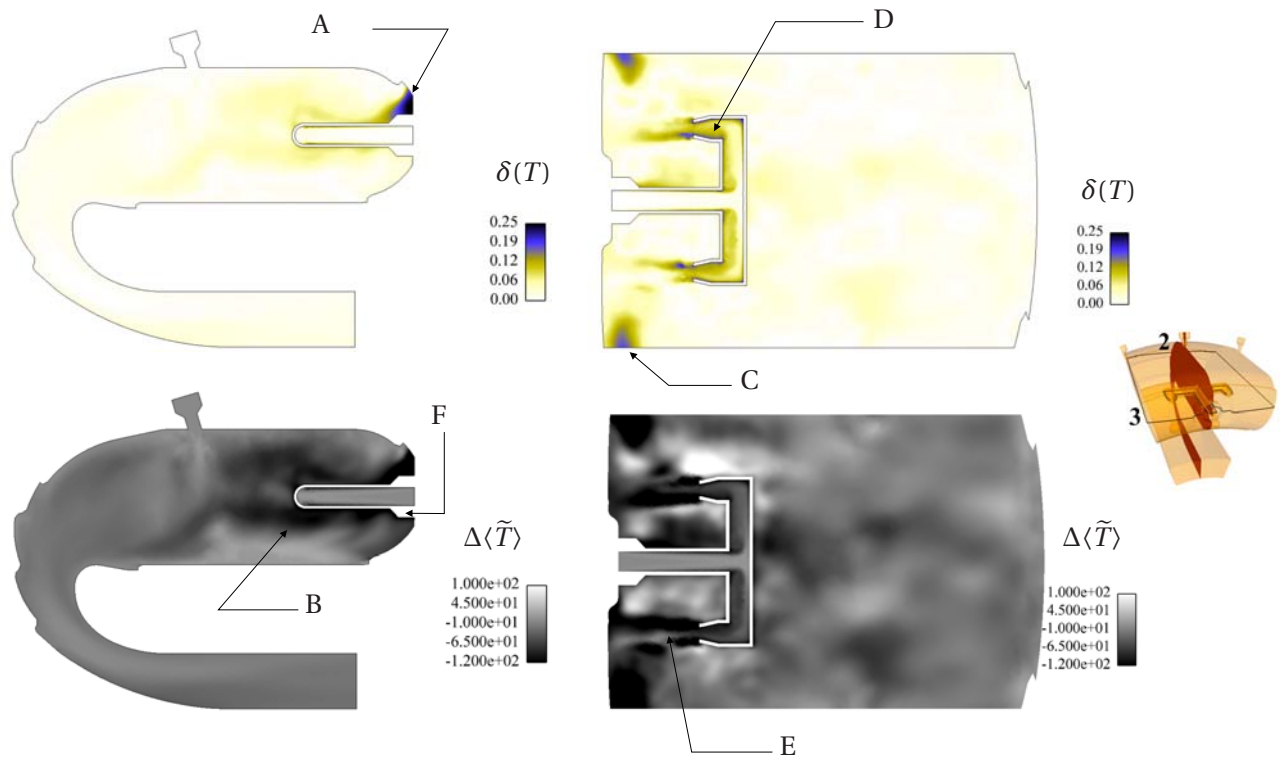
Figure 10.12: Relative difference field (top) and absolute difference field (bottom) between the coupled and the reference simulations in cuts 2 and 3.

present at the exit of the injector remains invariable along the line until the dome.

The temperature and heat release profiles shown in Fig. 10.17 correspond to the data obtained along line 2. In this azimuthal direction the profiles remain almost unchanged in both simulations. Note that in the Radiation-Fluid Thermal Interaction (RFTI) simulation performed in chapter 9, the temperature profiles show a broadening of the flame brush in this direction.

Finally, along the third line (3), the heat release an temperature profiles presented in Fig. 10.18 show significant differences between the two simulations. In this image the solid wall is located to the right of the graphs. The heat release in the coupled simulation drops down to almost half the value on the reference simulation. The temperature near the wall shows a strong variation of almost 250K, and the peak value is moved away from the wall.

These profiles indicate that the flame is no longer anchored to the tip of the injector in the coupled simulation. The heat losses associated with heat conduction in the injector cool down the flow near the wall engendering a local flame extinction. However the flame does not show any sign of destabilization in the FSTI simulation.
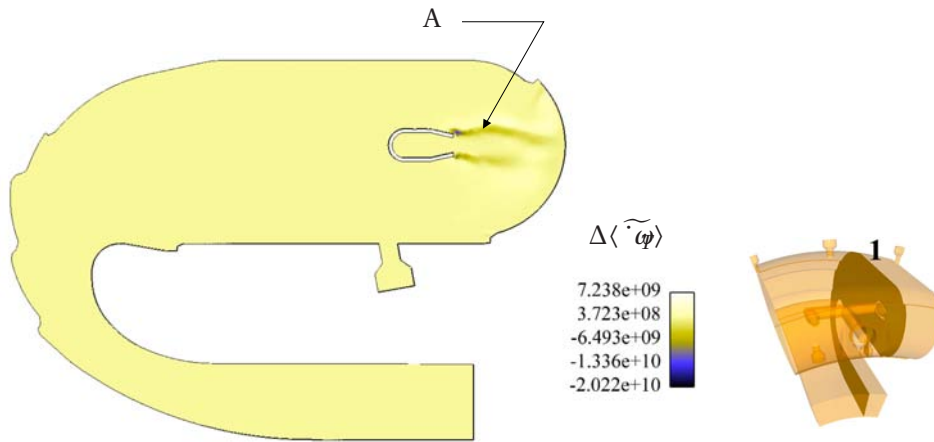
Figure 10.13: Absolute error field of heat release between the coupled and the uncoupled simulations.

10.6   Conclusions

The hypothesis used in the reference LES concerning the boundary conditions on the internal surfaces of the injector induces a strong heat flux to the internal fluid, which in consequence increases the injection temperature. Such variation changes the final temperature in the premixed flame modifying the mean temperature of the chamber. The main consequence of a bad prediction of the injection temperature is the modification of the RTF at the exit of the combustion chamber.

Heat loss at the external surfaces of the injector produces only a slight lifting of the premixed flame, but do not affect its stability. Finally, in the coupled simulation the spectral analysis of the unsteady flow suggests a correlation between the frequency peaks and the thermal conduction phenomena in the injector.
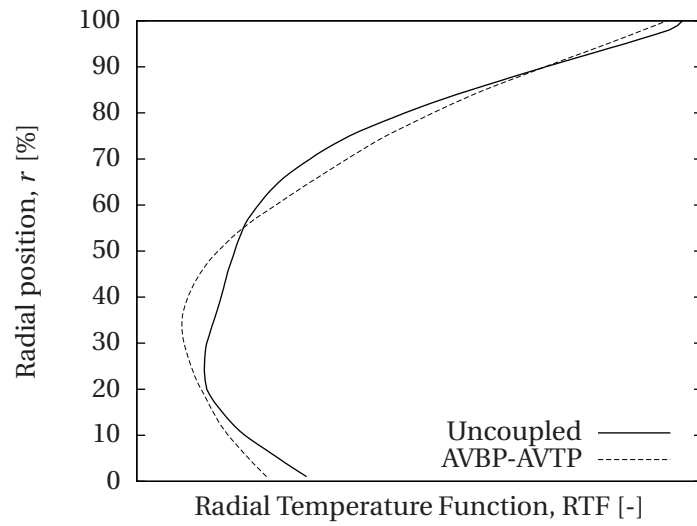
Figure 10.14: TRF of the combustion chamber in the reference LES simulation and the coupled Fluid-Solid simulation.
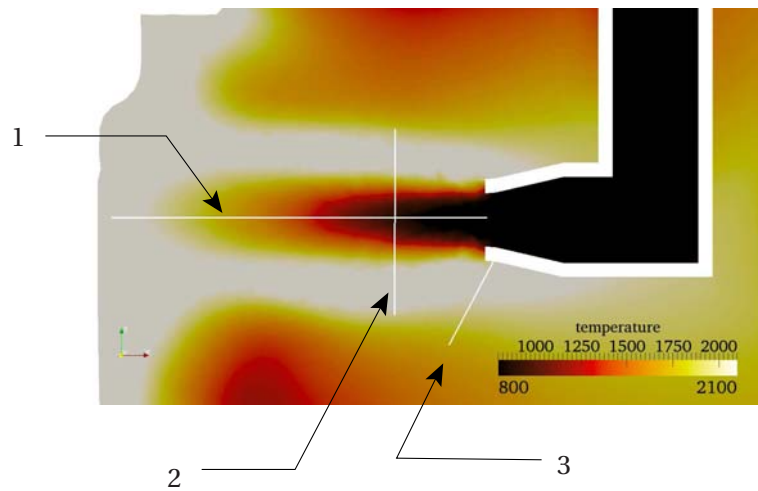
Figure 10.15: Location of the lines used to trace plots 10.16, 10.17 and 10.18, in cut 3. Time-averaged temperature field of the coupled simulation.
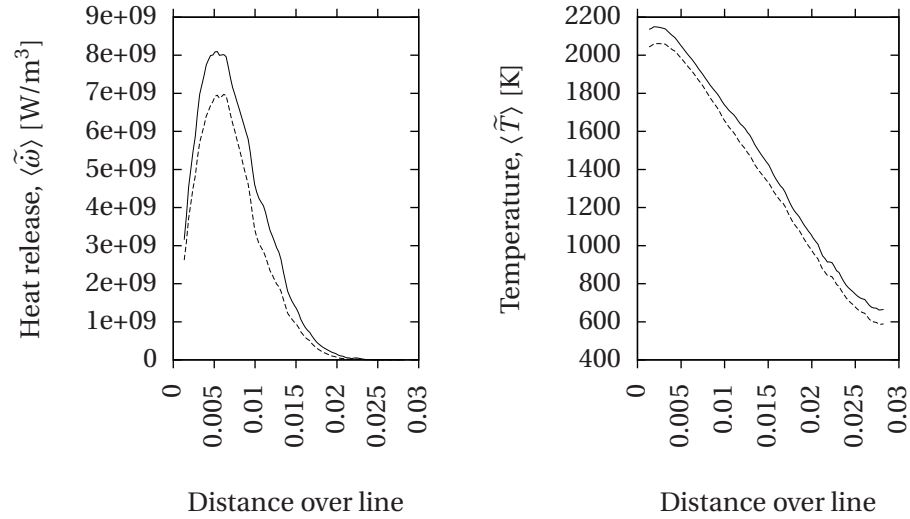
Figure 10.16: Profiles along line 1: (left) heat release, (right) temperature. Solid line: reference LES. Dashed line: coupled FSTI.
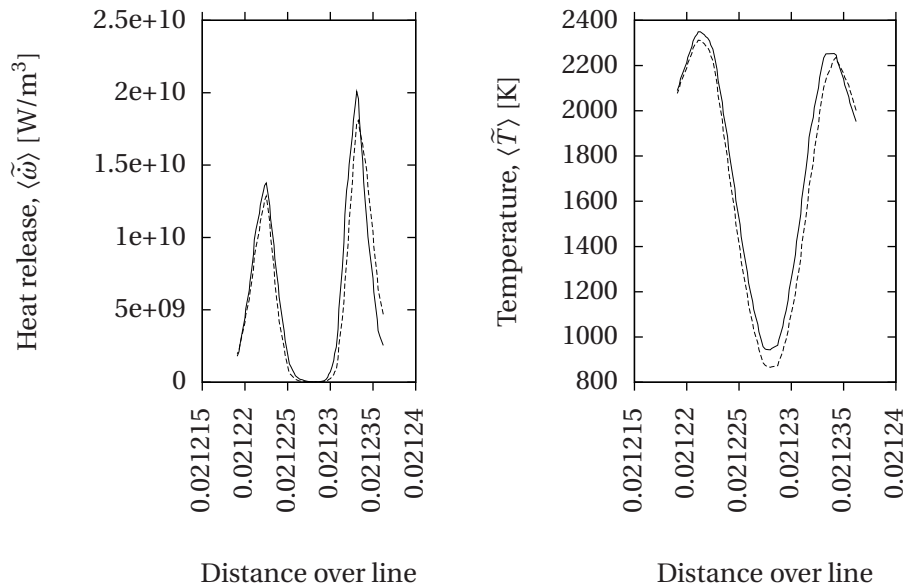
Figure 10.17: Profiles along line 2: (left) heat release, (right) temperature. Solid line: reference LES. Dashed line: coupled FSTI.
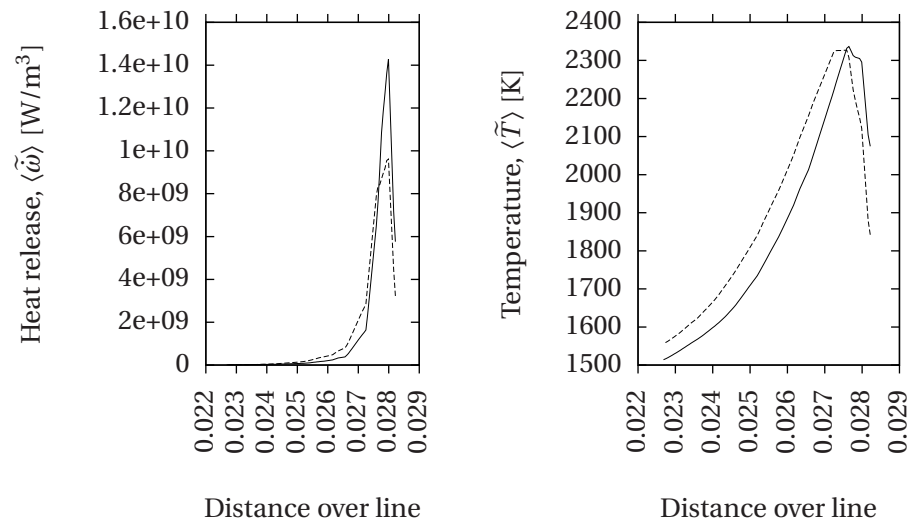
Figure 10.18: Profiles along line 3: (left) heat release, (right) temperature. Solid line: reference LES. Dashed line: coupled FSTI.

11

Towards multi-physics: LES-DOM-Solid heat conduction coupling in a combustion chamber with vaporizer

Contents

11.1 Introduction

The results of the coupled effects of heat transfer by conduction, convection and radiation in an aeronautical combustion chamber are presented in this chapter. To our knowledge, this is the first time that such coupled simulation is performed. Data is collected on the statistical properties of the combustion chamber and the solid vaporizer in the coupled simulation to be compared with the simulations performed in the three previous chapters. The coupling methodology consists on the overlaping of the RFTI and the FSTI couplings presented in chapters 9 and 10, using the technique introduced in section 7.5.2.

Coupled simulations including the three heat transfer modes (conduction, convection and radiation) are rarely reported in the literature: analytical studies of academic cases were presented by Bell [14], Siegel and Howell [236] and Modest [177], and numerical simulations of natural convection were performed by Balaji and Venkateshan [13] and Nouanegue et al. [188]. Fully coupled unsteady simulations of combustion chambers are not referenced in the literature. The primary goal of the present work is to show that such kind of simulations are currently feasible and that they bring valuable information to the motorists.

In the Multi-Physics Coupling (MPC) performed, the calculation domains are the same as in chapters 9 and 10, and the interaction between radiation and conduction is only taken into account at the interface between the fluid and the injector. This is however an small element of the combustion chamber, and this simulation is a first step towards a complete multi-physics simulation of a full combustion chamber. It is a good platform used to identify and solve possible difficulties and to evaluate the interest of such simulations.

11.2 Numerical approach

The simulation was carried out on an IBM iDataPlex server featuring Intel Xeon Nehalem processors at a clock speed of 2.66 GHz. The computation used a 32 processor configuration, where two processors where dedicated to the coupler and the two interfacing units and 30 processors where exclusively allocated to the three simulation codes.

The Mixed Coupling Strategy (MCS) presented in section 7.1.4 was employed. Using the approach presented in section 7.5.3, the processor distribution of a shared MCS is calculated: processor sharing is imposed on the two most performant[1] codes: AVBP and AVTP, leading to $P_{s\text{-}f} = 6$ processors for LES and conduction and $P_{rad} = 24$ processors for radiation. This processor distribution is the same as the

---

[1]Performance is based on computational speed of one iteration, memory management and code scalability. The DOM code remains the weak link in the coupling chain in particular due to the large amount of memory it requires.

one obtained for the RFTI coupling (chapter 9): thermal conduction is calculated so fast that sharing the processors with AVBP does not change the processor distribution obtained in the RFTI simulation.
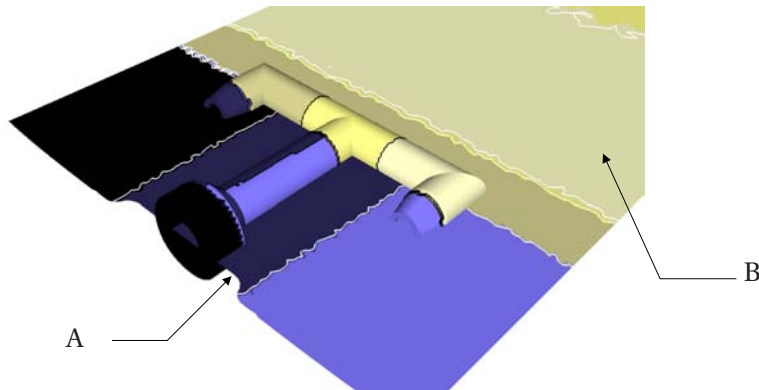
Figure 11.1: Parallel partitioning of the coupled domains: cut 3 is shown for the fluid, top half of the vaporizer is shown for the solid.

Figure 11.1 shows the partition obtained for the fluid and solid computational domains[2]. It shows that some LES processors communicate with many processors in the solid code (A), while others do not share any coupling surfaces (B). An upgraded partitioning algorithm will be developed to take into account the coupling surfaces, avoiding such unbalanced communications.

The coupling frequency used between the solid and the fluid correspond to the FSTI simulation, given in section 10.3, where $n_f = 615$ LES iterations and $n_s = 648$ solid iterations are performed between two coupling points. This high coupling frequency also explains the processor distribution: the solid code works two orders of magnitude faster than the LES code, so that the added cost of including heat conduction is comparable to adding one iteration of the LES code.

The coupling frequency between the LES and the radiation code remains the same as in chapter 9: $N_{it} = 80$ LES iterations are carrier out for one radiative calculation.

Boundary conditions, LES SGS models, radiation models, time steps and all other parameters for the three codes are the same as presented in the three previous chapters. This simulation was run for $t = 38$ [ms] which permits to record good statistics.

The effect of MPC is evaluated by comparing the radiation fields against the RFTI coupling, the temperature of the vaporizer against the FSTI coupling and the fluid temperature fields against the reference LES (uncoupled) simulation.

---

[2]No domain partitioning is done for the radiation code.

11.3 Instantaneous flame structure

Figure 11.2 shows the instantaneous temeprature field in cut 3, between the injector and the dome, with iso-lines of heat release colored with the Takeno index (Eq. 8.6): white lines correspond to pre-mixed combustion and black lines to non-premixed. The left image corresponds to an instantaneous solution of the reference simulation and the right image is an instantaneous screenshot of the MPC simulation. Notice that this is a zone where turbulent combustion is strong, however both solutions are representative of the general behavior of the flame.
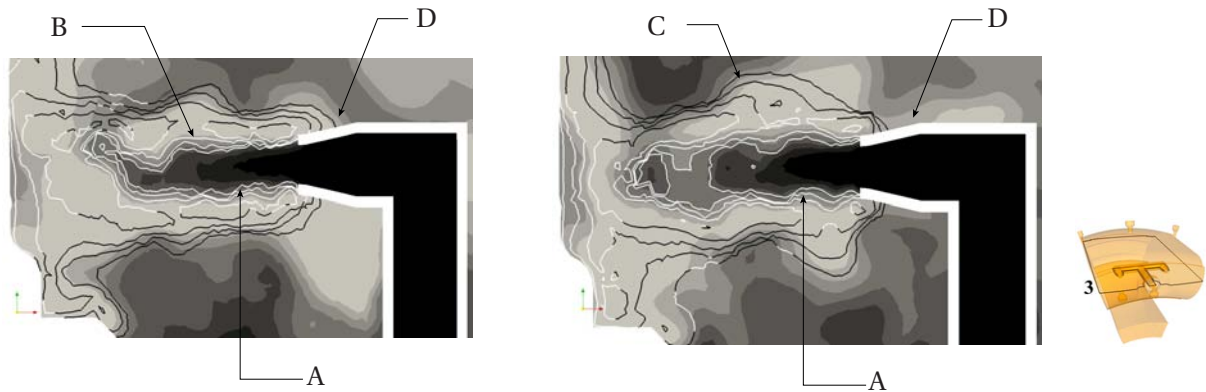
Figure 11.2: Instantaneous temperature field (the palette uses 8 levels) and iso-contours of heat release (5 levels: $5\,10^8$, $1.54\,10^9$, $4.77\,10^9$, $1.47\,10^{10}$ and $4.55\,10^{10}$.

As presented in chapter 10 the injection temperature is lower in the case where heat conduction in the vaporizer is included. The penetration distance of the cold fuel inside the combustion chamber is larger in the case of the MPC simulation (A). In both cases pockets of gases are detached from the premixed flame (B) and consumed a few millimeters downstream. The shape of the premixed flame is thicker in the MPC simulation: the fields shown here are instantaneous snapshots, however it was shown in chapter 9 that inclusion of radiation can produce this effect in the time-averaged temperature field. The same expansion of the combustion zone can be observed in the diffusion flame (C).

Finally, the zone of attachment of the flame to the injector is modified: the inclusion of heat loss through the vaporizer provokes a reduction of the reaction zone at the tip of the injector in the MPC simulation (D), but the flame does not show any sign of instability.

11.4 Impact on the time-averaged radiation

Poitou [204] and Gonçalves [65] have shown that the radiation code is sensitive to slight variations of the wall temperature and the wall emissivity: the temperature distribution on the wall determines

the energy flux repartition from the solid to the fluid. In MPC simulations this repartition is obtained from the heat conduction solver. The inclusion of the proper wall temperature on the radiation code modifies the emitted (an absorbed) energy on each coupled surface.

An evaluation of these effects can be performed by comparing the time-averaged radiative fields from the RFTI and the MPC simulations. Radiative heat flux differences can be observed using expression:

$$\Delta\langle q^r\rangle = \langle q^r\rangle_{\text{s-f-r}} - \langle q^r\rangle_{\text{f-r}} \tag{11.1}$$

where $\langle q^r\rangle_{\text{f-r}}$ and $\langle q^r\rangle_{\text{s-f-r}}$ are the time-averaged magnitudes of the radiative heat flux vector in the RFTI and the MPC simulations respectively.

It was shown in section 10.4 that with the inclusion of heat conduction the bottom of the cane base is heated by the combustion gases. Figure 11.3 shows that in this zone (C) the heat flux is increased in the MPC simulation. This increase in the heat flux can be also observed in cut 1 (Fig. 11.3-A), where most part of the primary zone shows a variation in the heat flux.
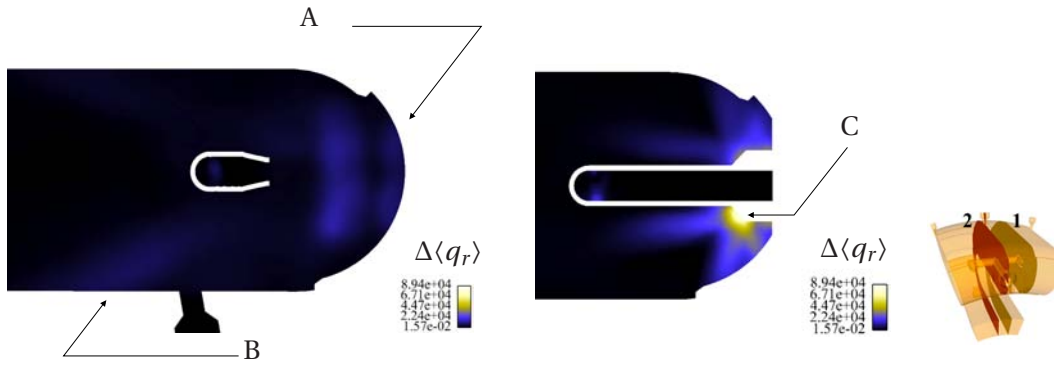
Figure 11.3: Difference on the the radiative heat fluxes $\langle q_r\rangle$ between the RFTI coupling of chapter 9 and the MPC simulation.

Another difference between both simulations can be observed in the internal side of the intermediate zone, behind the primary hole (B): a change in the temperature distribution inside the combustion chamber has been observed when heat conduction in the injector is included (chapter 10). Temperature variations in the intermediate zone provoke a variation in the radiative heat fluxes.

The differences between the RFTI and the MPC simulations can also be studied by analyzing the differences between the radiative source terms, using expression:

$$\Delta\langle \mathscr{S}_r\rangle = \langle \mathscr{S}_r\rangle_{\text{s-f-r}} - \langle \mathscr{S}_r\rangle_{\text{f-r}} \tag{11.2}$$

where $\langle \mathscr{S}_r\rangle_{\text{f-r}}$ and $\langle \mathscr{S}_r\rangle_{\text{s-f-r}}$ are the time-averaged radiative source terms in the RFTI and the MPC simulations respectively.

The broadening effect of the reaction zone described in section 11.3 is also visible in the radiative source term difference field displayed in Fig. 11.4. The energy reduction around the premixed flame (A) is compensated by an energy rise near the central cylinder of the injector (C): in this case the cause is attributed to the differences between the temperature fields in both simulations. In the corner zone (B) radiative power is strongly reduced in the MPC simulation.
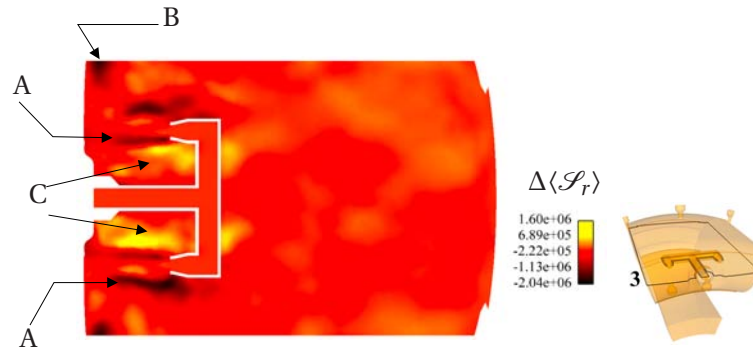
Figure 11.4: Difference on the mean radiative source term $\langle \mathcal{S}_r \rangle$ between the FSTI coupling and the MPC simulation.

The same comparison is made in Fig. 11.5 for cuts 1 and 2. On the left image (cut 1) a reduction of the radiative power is observed around the premixed flame (A) and on the fuel side of both non-premixed flames (B). These zones were previously identified as regions influenced by the diminution of the injected fuel temperature. The radiative source term is enhanced on the external side of the premixed flame (C). On the right image (cut 2) radiation is stronger near the internal perforated plate (D) and a reduction of the radiative source term is observed around the cane base (E).
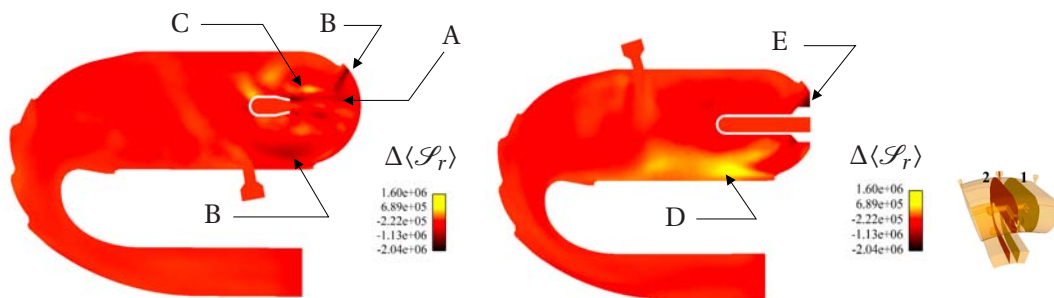

Figure 11.5: Difference fields between the mean radiative power fields $\langle \mathcal{S}_r \rangle$ of the Radiation-Fluid coupling of chapter 9 and the multiphysic coupling. (left) cuts 1 (right) cut 2.
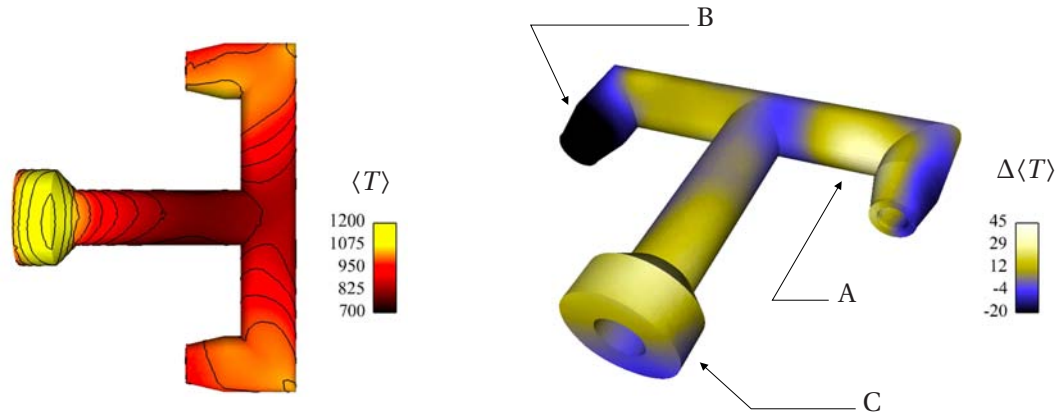
Figure 11.6: Solid vaporizer: (left) mean temperature $\langle T \rangle$ of the surface viewed from the bottom, (right) absolute difference field $\Delta\langle T \rangle$ between the FSTI and the MPC simulation.

11.5   Effects on the temperature of the solid

Comparing the left image of Fig. 11.6 with Fig. 10.8, the general aspect of the mean temperature of the surface of the vaporizer looks very similar in both cases (with and without radiation). The same features can be observed: a hot spot at the bottom of the base of the cane, a cold spot at the central cylinder, a temperature gradient on the back cylinder between the central zone an the hot injection tips and external corners at high temperature.

The differences between the FSTI simulation and the MPC simulation are presented in the right image of figure 11.6. A positive value implies that the surface of the solid is hotter in the multi-physics simulation, and a cold spot represent the zones where radiation evacuates energy from the solid. The most prominent feature on this image is the hot spot on the arms of the vaporizer (A): in this zone the temperature gradients are strong, and a small displacement of the temperature field causes an important effect on the temperature absolute error field.

The external side of the injection tips are cooled down by the inclusion of radiation in the simulation, but a strong temperature reduction is observed at the internal side of one of the injection tips (B). The origin of such temperature reduction is uncertain, however Fig. 9.25 has previously shown that the temperature of the fluid in the zone between this injection tip and the central cylinder is reduced by radiation, and can play a role in the temperature drop of this element of the solid.

The temperature is also higher on the top of the vaporizer at the cane base and the central cylinder (C), while the bottom shows a slightly lower value (not visible in the image): radiation is more effective on the (hot) internal zone than on the (cold) external side. The cold side of the solid is prone to absorb more energy from the hot surrounding gases in the MPC simulation, thus rising the temperature in this area.
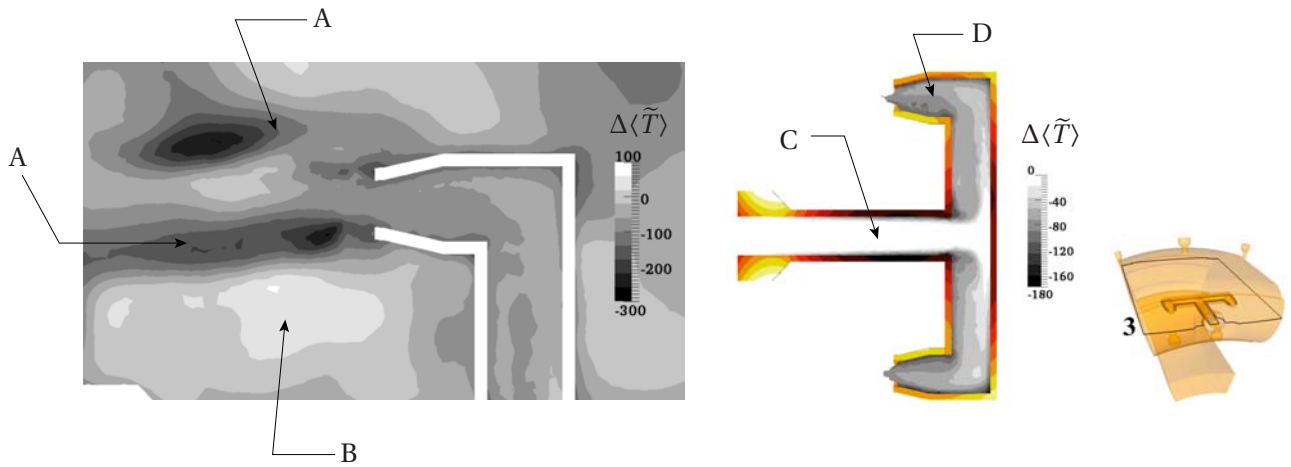
Figure 11.7: Temperature difference between the MPC simulation and the reference (uncoupled) LES in cut 3. (left) injection zone between the cane tip and the dome, (right) zone inside the injector, and temperature in the vaporizer (10 levels in the range [730K;1100K] are shown)

Radiation can modify the mean temperature of the solid structure, with a maximum variation around 40 K. Energy redistribution on the surface of the vaporizer may modify the flame and combustor behavior.

It will be interesting to explore the response of other solid components of the combustion chamber, e.g. the flame tube, where radiation can play an important role for the evacuation of energy to the annulus.

11.6   Impact on the time-averaged fluid temperature

11.6.1   Multi-physics vs. uncoupled LES

Temperature variations in the MPC simulation are the result of the addition of the effects observed in the RFTI and FSTI simulations. Figure 11.7 (left) shows the temperature difference, $\Delta\langle\widetilde{T}\rangle$, between the MPC simulation and the reference (uncoupled) LES simulation. A reduction of the final temperature of the premixed flame is evident in this image (A). In the MPC simulation the expansion of the flame brush caused by radiation is combined with the temperature drop caused by the use of heat conduction in the vaporizer (lower injection temperature), and a slight temperature rise, caused by the expansion effect of radiation, can be observed near the non-premixed flame (B).

The right image of Fig. 11.7 shows the temperature repartition in the solid cane, and the temperature differences between the MPC simulation and the reference LES inside the injector. The flow in the central cylinder (C) is essentialy the same in both simulations, but in the reference simulation the

(a) FRTI vs. MPC   (b) FSTI vs. MPC
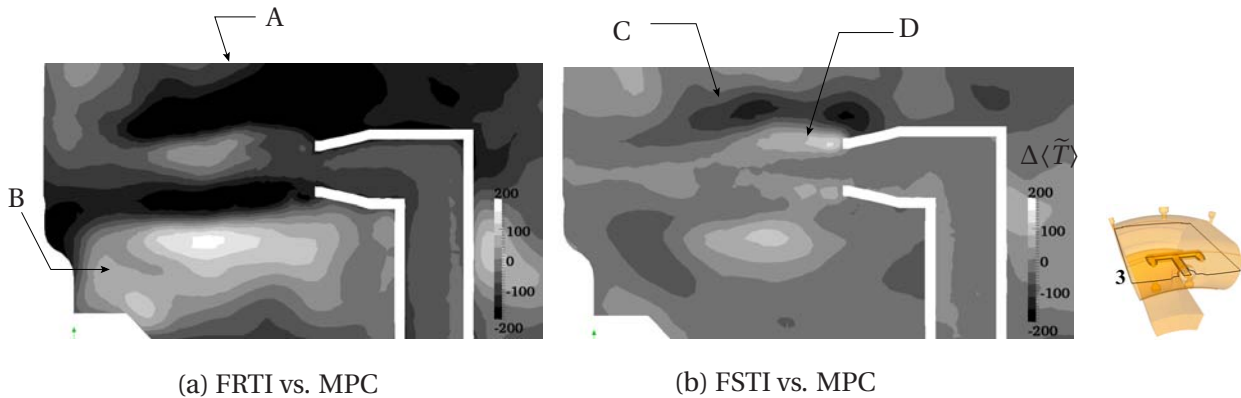
Figure 11.8: Temperature difference in the premixed flame region in cut 3.

fuel gets warmed faster than in the MPC simulation. As a result the temperature distribution at the exit of the injector (D) is lower in the coupled simulation. This result has been already observed in section 10.4 when the FSTI coupling was discussed.

11.6.2 Multi-physics vs. RFTI and FSTI

Figure 11.8 shows the temperature difference, $\Delta\langle\widetilde{T}\rangle$, observed in the primary zone of the chamber, in front of one of the injection tip in cut 3, between the MPC and the RFTI (left) and between the MPC and the FSTI (right) simulations.

Temperature differences are more important in the first case, as the injection temperature is over-predicted in the RFTI simulation (no heat conduction in the solid). The lower temperatures predicted in by the premixed flame in the MPC simulation can be observed (A), but it can also be observed that in the non-premixed flame zone (B) temperatures can be higher in the MPC simulation.

Figure 11.8 (right) shows that the temperature fields are closer between the MPC and the FSTI simulations. The expansion effect observed in chapter 9, when radiation is included, can be also observed in this figure causing a slight variation of the temperature around the premixed (D) and non-premixed (C) flames. Finally, ompared with the FSTI the MPC simulation shows temperature variations inside the injector of ±8K.

11.7   The RTF profiles

For all simulations the RTF has been plotted in Fig. 11.9. In the RFTI coupling the RTF radial profile is also different, showing a plateau and a temperature rise near the external (top) wall. The FSTI simulation shows a RTF with a peak around 40% of the radial position. This "hot spot" is different

from the one in the reference simulation at $r = 20\%$.

In the multi-physics simulation the mean temperature at the exit plane $\overline{\langle T \rangle}_{\text{exit}}$ is 20K lower than the mean temperature on the reference simulation. The combined effect obtained with the multi-physics coupling shows a temperature homogeneization of the RTF profile between $r = 25\%$ and $r = 65\%$, a temperature rise near the external wall ($r = 100\%$) and a temperature drop near the internal wall ($r = 0\%$). The temperature profile at the exit of the combustion chamber in this simulation shows a lower radial variation, suggesting that in a fully coupled simulation the radial repartition of temperature is more homogeneous.
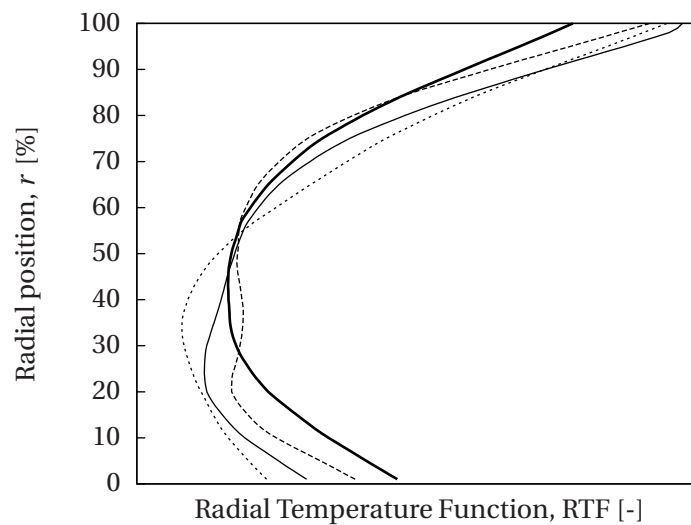
Figure 11.9: RTF of the combustion chamber. ——— : LES simulation; ⋯⋯⋯ : coupled FSTI; − − − − : coupled RFTI; ■■■■ : MPC simulation.

11.8   Conclusion

The results obtained in the Multi-Physics Coupling (MPC) simulation show that combining the different heat transfer modes can lead to different instantaneous and mean temperature fields compared against the reference calculation. Moreover, the MPC simulation is different from the two-code couplings, showing an integration of the properties observed in the RFTI and FSTI simulations: an expansion of the flame brush, a drop in the temperature inside the vaporizer and a redistribution of the temperature field.

A spatial averaging of the mean temperature fields, $\langle\langle \widetilde{T} \rangle\rangle_{\text{vol}}$, shows that the mean temperature of the chamber drops 0.2% in the RFTI simulation, 1,4% in the FSTI simulation and 1,9% in the MPC simulation compared with the mean temperature of the reference simulation. Although this variations

are small, the temperature repartition is not the same in each case and they have an impact on the temperature profiles at the exit of the chamber.

Note that the only structure where the coupled effect was evaluated is the injection cane. The effects of a MPC simulation can be more important when all the flame tube will be studied using the coupling techniques presented in this work, in particular the zones near the multi-perforated walls can show a significant temperature increment caused by radiation from the combustion gases in the intermediary zone.

12

Conclusions

We have demonstrated the feasibility and the impact of coupled multi-physics unsteady simulations in combustion applications. The necessary tools to perform such simulations where developed and important scientific and engineering results were obtained, showing that such multi-physics is a field that require special attention.

The analysis of the models used in the radiation code PRISSMA, showed that a careful selection of the spectral integration is important for the good prediction of the radiative fields. In particular it was observed that global models could lead to inaccurate results and that the optically thin gas model, which is the simplest way to introduce radiation into a CFD code, can lead to unrealistic modifications of the fluid dynamics. It was concluded that the spectral model is one of the key elements of a good radiation solver.

The interaction of radiation with the Turbulent Boundary Layer (TBL) was also discussed. Direct Numerical Simulations (DNS) performed with AVBP, were coupled with the radiation solver PRISSMA, to study the effects of radiation in the near-wall region. It was observed that the optical thickness of the TBL is very small and only absorbs a fraction of the emitted energy. However, the inclusion of radiation modifies the total heat flux to the wall in a non-negligible quantity. It was also observed that the fraction of heat transfer to the wall by radiation is lower in a TBL with strong temperature gradient than in a simulation with a weak temperature gradient. This conclusion is not necessarily true in applications involving ablating walls of pyrolysis, as the optical thickness in such applications could rapidly increase.

This results are consistent with the findings of Coelho, Roger and Poitou, who show that turbulence is

not affected by radiation at such small scales. However, in larger applications, as e.g. in a combustion chamber, an initial Turbulence-Radiation Interactions (TRI) study showed that the radiation fields obtained using the time-averaged fields (or RANS simulations) can lead to an inaccurate value of the wall radiative heat fluxes. This result alone shows the importance of coupled Radiation-Fluid Thermal Interaction (RFTI) simulations. It was also observed that radiation does not modify the flow or the flame dynamics, however the temperature distribution of the mean flow inside the combustion chamber is affected.

In the case of Fluid-Solid Thermal Interaction (FSTI) simulations, it was observed that using heat conduction in the injection cane of the combustion chamber can affect the combustion process: the good prediction of the fluxes crossing the vaporizer, causes a lower injection temperature, thus modifying the flame properties. A lower final temperature is obtained in the premixed flame, and a different temperature distribution is observed inside the chamber when compared to the reference uncoupled simulation. Conduction also causes a slight detachment of the flame from the injector and a decrease in the temperature and reaction rates near the wall.

The results obtained from the full multi-physics simulation of the combustion chamber correspond to a superposition of the effects observed in the FSTI and RFTI coupled simulations. Slight variations of the temperature repartition in the solid structure were observed, and differences in the Radial Temperature Function (RTF) at the exit of the chamber where observed in all simulations. These last result shows the importance of performing coupled simulations including all heat transfer modes.

12.1   Engineering accomplishments

In the engineering field many objectives were accomplished. The three codes were evaluated and optimized, and the strengths and weaknesses of each one are summarized here:

- It was observed that the code AVTP can perform very accurate transient simulations of heat conduction both in analytical studies and practical applications. It is however a tool that can be optimized using more robust numerical methods, as for example implicit time integration. AVTP is a derived code from AVBP, thus it contains several subroutines that are not optimized for heat conduction problems. In addition solid elastic deformation is not included in the code. But for unsteady coupled thermal simulations its computational speed and its accuracy are largely sufficient.

- Modifications have been included in the code AVBP in order to acknowledge the new heat sources coming from the solid and from the radiation solvers, and the new law of the wall that resolves the near-wall heat flux including radiation. This is a mature code that performed very well in all coupled simulations.

- The code PRISSMA was developed to calculate the radiative heat transfer in industrial applications. The code has been completed and optimized for its use on parallel architectures. New

spectral methods have been included, and in particular the TFS-SNBcK model showed a very good performance in coupled simulations without losing accuracy.

The code however presents some weaknesses: (1) memory use is high due to the need of keeping all mesh cells on every processor. New numerical techniques are now being developed to reduce memory use. (2) The code shows a speedup bottleneck for global spectral models that needs to be corrected using different parallel strategies. (3) For applications in aeronautical chambers it is necessary to add axi-periodic boundary conditions.

The tool developed is very easy to use and can be adapted to many different architectures and problems, from small scale Turbulence Radiation Interaction (TRI) using DNS data, to industrial glass and oil furnaces.

Coupled simulations were performed using the codes, AVBP, AVTP and PRISSMA, which were equipped with a communications platform based on the coupler PALM. It was observed during the development phase that two of the most important aspects of coupling corresponds to the synchronization in physical time (frequency of data exchange) and in CPU time (resource distribution).

Coupling combustion and radiation requires a good knowledge of each algorithm, their models and their structure. Data exchange between them is relatively simple to understand and requires only a few interventions. In this case most of the development was done on the improvement of the codes.

On the other hand, heat transfer between fluid and solid requires a more intense work on the coupling methodology. The characteristic time of each phenomena being very different, coupling between convection and conduction is asynchronous (Asynchronous Coupled Simulation, ACS). This approach allows the solid to evolve fast to a steady state, thus saving computational time, but can provoke instabilities or oscillations around the solution of the coupled system. It was shown that in the case of LES and heat conduction using a law of the wall at the interface, coupling can be stable but oscillatory. In was also exposed that better coupling techniques are available and should be implemented in the future.

12.2 Perspectives

The tools developed open a wide range of applications of scientific and engineering interest. One of the missing links in the thermal cycle of combustion is the formation and transport of soot particles. Luminous radiation by soot is one of the major contributors of heat transport inside a combustion chamber and needs to be included in future coupled simulations. One additional step in this direction is the inclusion of complex chemistry in combustion in order to predict pollutant concentration and the influence of radiation and conduction.

Coupled simulations using LES and detailed radiation will be used in the next months to identify and evaluate each one of the terms in the correlations found in Turbulence-Radiation Interaction (TRI).

This is one domain that will gain a great impulse with the use of unsteady coupled RFTI simulations, and will lead to interesting scientific and engineering applications.

Concerning the resolution of the Radiative Transfer Equation (RTE) one question remains open: is the Monte Carlo method ready to perform unsteady coupled simulations? The work performed by Zhang et al. [278] try to respond to this question. This methods are still too expensive for coupled simulations, but have a great potential for its implementation on massively parallel architectures.

Other domain that has been avoided in the present work is the elastic deformation of the solid structure caused by variations in the fluid pressure, or by pyrolysis and ablation of the walls. Research in this area is extensive, but literature on coupled applications including other heat transfer modes is still rare.

Engineering objectives that can be achieved as a continuation of the present work include: the parallelization of the radiation code in order to attain perfect scalability, and the realization of MPC simulations of a complete combustion chamber, including all the solid elements and the annulus.

In addition, technology in the domain of digital computers has shown great advances in Graphical Process Unit (GPU) architectures, that could be used to implement fast radiation solvers, computational fluid dynamic tools and heat conduction codes, eventually leading to scientific computation on personal computers. GPUs are a good alternative to reduce the restitution times of radiation.

Future research on combustion simulation should focus on the incorporation of all the different physical phenomena involved in energy production. Such project require the close collaboration of different scientists (and laboratories) which specialize in different areas of physics.

Each one of these points has been more or less treated during the past, but their interaction in a complex system is still a subject that will be treated in the next coming years. In a longterm vision of Computational Fluid Dynamics, the major goal is to develop a predicting numerical tool capable of performing a complete simulation of the unsteady flow inside a jet engine including combustion, heat conduction, structure deformation, radiation and pollutant formation.

A

The PALM environment

Contents

A.1   The software

A coupler is a software tool allowing the concurrent execution and the intercommunication of programs not having been especially designed for that. In addition to data exchange issues, the coupler takes care of a number of other services, such as intermediate computations on the exchanged data, grid to grid interpolations, parallel data redistribution. The couplings, therefore, span from simple sequential code assembling (chaining) to applications involving tens of models. The codes may run in parallel, especially if the coupling takes place in the inner iterative processes of the computational entities.

More generally, a component coupling approach often allows to split a system into elementary computational entities that can be handled and maintained more comfortably. This approach has proved to be very effective for the design, the management and the monitoring of large complex systems as, for instance, data assimilation suites.

The main qualities of the PALM coupler are its easy set-up, its flexibility, its performances, the simple updates and evolutions of the coupled application and the many side services and functions that it offers.

A.1.1   Dynamic coupling

With a static coupler, all the coupled programs have to start simultaneously at the beginning of the simulation. Therefore, they lock their memory and CPU resources from the beginning to the end of the application.

In PALM a coupled component can be launched and can release resources upon termination at any moment during the simulation. The originality of this coupler resides in the faculty of describing complex coupling algorithms. Programs, parallel or not, can be executed in loops or under logical conditions. Computing resources such as the required memory and the number of concurrent processors, are handled by the PALM coupler. A component of the coupled system starts only when it is active in the algorithm. For the rest of the time it can release memory and processors. Notice that the dynamic resource management is bound to a static allocation: the coupler never goes beyond the total amount of available resources set by the user.

A PALM application can be described as a set of computational units arranged in a coupling algorithm. The different units are controlled by conditional and iterative constructs and belong to algorithmic sequences called computational branches. A branch is structured like a program in a high level programming language: it allows the definition of sequential algorithms. Inside a branch, the coupled independent programs, the units, are invoked as if they were subroutines of the branch program. The transformation of computational independent code into a PALM unit is almost straightforward, provided that the user can access the code sources.

The exchange of information between the components take into account the volatility of the units: even if a program has ended, PALM grants that the data it produced remain accessible.

A.1.2 Parallelism

The PALM coupler handles two levels of parallelism:

- The first level concerns the components themselves. While managing the resources, PALM allocates the number of the processes which are necessary to any computational unit. These units can be parallel programs based on domain decomposition with MPI or applications multithreaded with OpenMP.

- The second level of parallelism is a task parallelism: when the algorithm is defined, two units appearing in different branches can be executed in parallel, whether the necessary processors are available. Coding parallelism in PALM is straightforward: through the graphical user interface. PALM thus offers a very high flexibility for testing different coupling techniques and for reaching the best load balance on a high performance computer.

A.1.3 End-point communications

PALM is based on the "end point" communication scheme. To keep the components fully independent, the production or the reception of the exchanged data (arrays of any kind) only depends on the unit itself. Vectors are uploaded and downloaded from a cloud that does not impose any restriction to the unit. The routing of information inside the cloud is handled by the coupler. In this scheme data production is never blocking: if the component in need of data is not ready, data is buffered. In addition, if data in the unit is decomposed over different processors PALM grants the management of data distribution.

The principle of the "end point" communications is simple: when a code produces a data potentially interesting for other components, it informs the coupler with an appeal to a PALM_Put primitive. In a similar way, a calculation code needing data tells the coupler, with a PALM_Get primitive, that it is waiting for information. This scheme allows total independence between the codes and authorises the replacement of a unit by another without interfering with the rest of the application.

The instrumentation of the source codes is restricted to calls to a few primitives: in this way it is very little intrusive. Various compiled languages (C, C++, Fortran) are supported. For time dependent or iterative processes, the coupler can manage many different temporal instances of the exchanged data. For instance, through this mechanism, the coupler can manage the temporal interpolation of the fields during the exchange.

A.1.4   Graphical user interface

PALM applications are implemented via a graphical user interface (GUI) called PrePALM. In this interface, the programmer initially defines the coupling algorithm: number of components, sequential and parallel sections, loops and conditional executions, resources management.

The actual communications between units can then be described. All synchronization, memory management and parallel computing options are set at this level.

A.2   Palmerization of the codes

A minimal instrumentation of the simulation codes is required to include them as computational units in PALM. Three steps are necessary to transform a simulation code in a fully palmerized code: unit identification, data manipulation and parallel distribution.

A.2.1   Unit identification

In this first non invasive step the size and shape of each object[1] is defined. Such vectors have been previously identified using the procedure presented in section 7.1.4. Using the PALM identification language a new file is added for each one of the simulation codes and to the interfacing units of the coupled simulations.

The delivery and reception of vectors from a parallel unit may require the set up of a data distribution protocol. Unit identification is then also used to designate the subroutines in charge of the distribution of each one of the vectors. Parallel distribution will be presented further in section A.2.3.

A.2.2   Data manipulation

Two communication methods can be carried up in PALM: the first involves communications by file exchange. In this case each unit must be able to read and process information via disk access. This communication technique is particularly useful in cases where there is no access to the source files of a simulation code.

However, if access to the source files is granted the most efficient way to communicate data is by using a memory-to-memory exchange. Entry and exit points must be identified in the codes: the best location where data can be extracted or inserted depends on the numerical method of each program and requires a fairly good knowledge of the code.

---

[1] In PALM an object is a vector or matrix exchanged between different units.
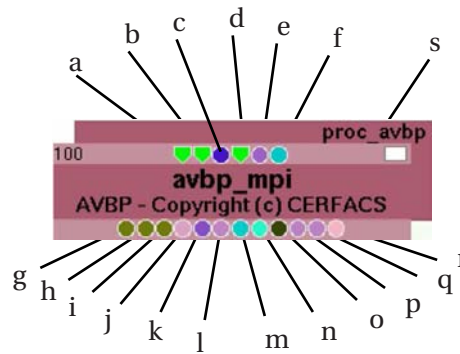
Figure A.1: Graphical representation of the unit AVBP.

Once the entry/exit points are identified subroutine calls are inserted, and the PALM_Get and PALM_Put primitives are added written.

A.2.3 Parallel distribution

Simulation codes and interfacing units use memory in different ways and run on different numbers of processors. In the present work, interfacing units run on only one processor while simulation codes run on several hundred cores. A communication protocol has been set up to identify the origin of the data and the memory position for each object (coupling control vectors or physical fields being communicated) transfered from one code to the other.

This step can be critical in the coupling set-up: indeed any debugging implies that all codes involved in the communication run simultaneously, which makes much more difficult for the developer to identify the source of a problem. A careful implementation of the parallel distribution subroutines is crucial.

A.3 The PALM units for multi-physics

A.3.1 The unit AVBP

In Fig. A.1 the unit AVBP is shown as it appears on the PrePALM GUI. Each circle in the unit represents a communication port, summarized in Table A.1.

This unit has been conceived in order to perform coupled simulations in conjunction with one code (AVTP or PRISSMA) or with both codes simultaneously. Activation flags are used to trigger or block coupling sections of the source code.

Table A.1: Communication ports for the unit AVBP

Port	Description
a	AVBP-PRISSMA coupling activation flag
b	Radiation-Fluid coupling iteration N_{it}
c	Radiation fields
d	AVBP-AVTP coupling activation flag
e	Fluid-Solid coupling parameters
f	Solid wall temperature
g	Number of nodes in the volume per processor
h	Number of cells in the volume per processor
i	Number of boundary faces limiting with a solid per processor
j	Node coordinates
k	Cell coordinates
l	Boundary face coordinates
m	Coupling fluid fields for the radiation simulation
n	Wall temperature: boundary condition for radiation
o	Number of nodes at the coupling interface with the solid
p	All surface node coordinates
q	Coupling surface node coordinates
r	Fourier heat flux, reference temperatures and exchange coefficients
s	Total number of processors for this unit
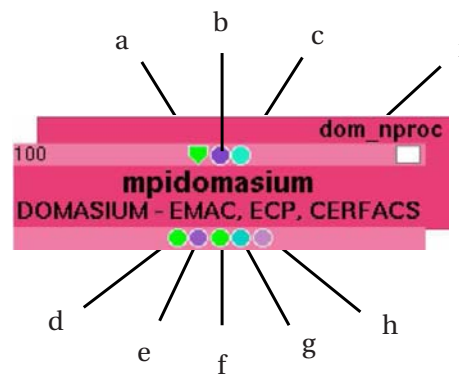
Figure A.2: Graphical representation of the unit PRISSMA.

A.3.2 The unit PRISSMA

Unit PRISSMA is presented in Fig. A.2. Table A.2 describes the possible communications in the unit.

In this unit no distribution subroutines were added: the information is equally distributed on all the processors. The reason is that currently no geometrical partitioning is used in the DOM code: all processors keep the full mesh and the data in memory.

Table A.2: Communication ports for the unit PRISSMA

Port	Description
a	Total number of iterations of the DOM code
b	Temperature, pressure and molar mass fraction fields
c	Wall temperatures
d	Total number of cells in the DOM mesh
e	Cell coordinates
f	Total number of boundary faces in the DOM solver
g	Boundary face coordinates
h	Radiation fields
i	Processors allowed to the DOM code

A.3.3 The unit AVTP

The PALM unit for the solid code is presented in Fig. A.3 and each one of the communication ports are detailed in Table A.3.
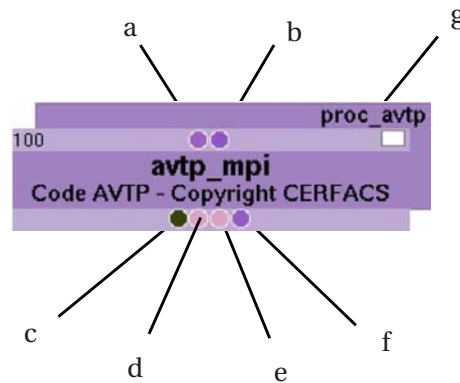
Figure A.3: Graphical representation of the unit AVTP.

Similar to the AVBP unit, the AVTP unit ports are coupled with distribution subroutines that sort the in/out data flux in the appropriate memory location for each processor.

Table A.3: Communication ports for the unit AVTP

Port	Description
a	Fluid-Solid coupling parameters
b	Fourier heat flux, reference temperatures and exchange coefficients
c	Number of nodes at each boundary per processor
d	Node coordinates at each boundary per processor
e	Node coordinates of the coupled boundaries per processor
f	Wall temperature at every boundary per processor
g	Total processors allowed to this unit

A.3.4   The interfacing units

The interfacing units basically perform two tasks: a) they create the connectivity between the nodes of the solvers, and b) transfer the data between the codes using this connectivity.

Both interfacing units (AVBP-PRISSMA and AVBP-AVTP) currently work on one single processor. This could eventually become a bottleneck and drop in the coupling performances. However, tests were performed using up to 800 processors showing no decrease in the efficiency.

Table A.4: Communication ports for the Radiation-Fluid interface unit.

Port	Description
a	Total number of coupling iterations
b	Number of cells in the DOM code
c	Cell coordinates from the DOM code
d	Number of nodes in the LES code per processor
e	Node coordinates of the LES mesh per processor
f	Number of cells in the LES code per processor
g	Cell coordinates of the LES mesh per processor
h	Number of boundary faces per processor in the LES code
i	Boundary face coordinates per processor in the LES code
j	Number of boundary faces in the DOM code
k	Boundary face coordinates in the DOM code
l	Fourier heat flux, reference temperatures and exchange coefficients from AVBP
m	Wall temperature from AVBP: boundary condition for radiation
n	Radiation fields from PRISSMA
o	Fluid fields from the LES code to the DOM code
p	Radiation fields from DOM to the LES code
q	Wall temperature: boundary conditions for the DOM code

Table A.5: Communication ports for the Fluid-Solid interface unit.

Port	Description
a	Number of boundary nodes per processor in the solid code
b	Boundary node coordinates per processor in the solid code
c	Coupling interface node coordinates in AVTP per processor
d	Number of boundary nodes per processor in the LES code
e	Boundary node coordinates per processor in the LES code
f	Coupling interface node coordinates in AVBP per processor
g	Solid wall temperature at the coupling interface
h	Fluid heat transfer data at the interface
i	Fluid-Solid coupling parameters
j	Fluid fields from the LES code to the solid code
k	Wall temperatures at the interface from AVTP to AVBP
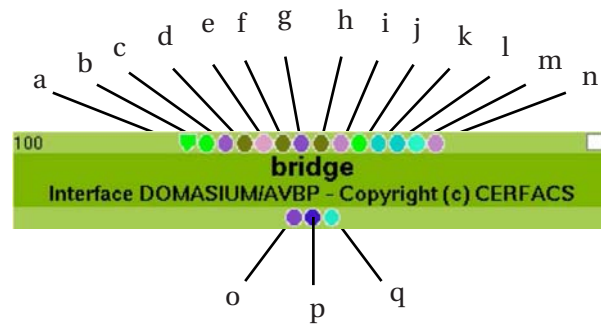
Figure A.4: Graphical representation of the interfacing unit for the Radiation-Combustion coupling.
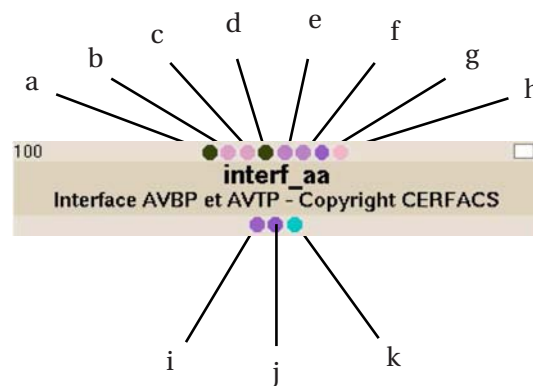
Figure A.5: Graphical representation of the interfacing unit for the Solid-Fluid coupling.

A.4   The PrePALM projects

In the Graphical User Interface PrePALM, communication paths between the units are set up. In this software the coupling parameters are imposed: vector sizes, processor distribution, coupling iterations, etc. Options for data debugging include verbose communications and units execution. Other coupler options were not included in this work, like temporal interpolation of data, scripted communications, unit loops, algebra units, etc.

Figure A.6 shows the unit interconnection for the RFTI project. This was the first coupled project prepared in this work, and it can be seen that the AVBP unit has input ports only for the radiation fields.

In order to develop a full thermal coupling project, the developments presented by Duchaine et al. [67] where added to the original RFTI coupling. Activation flags where added to decouple the radiative problem from the solid conduction problem when needed. In Fig. A.7 the PrePALM project for the FSTI coupling is presented. It can be seen that the ports involving communications with the radiation code are not used.
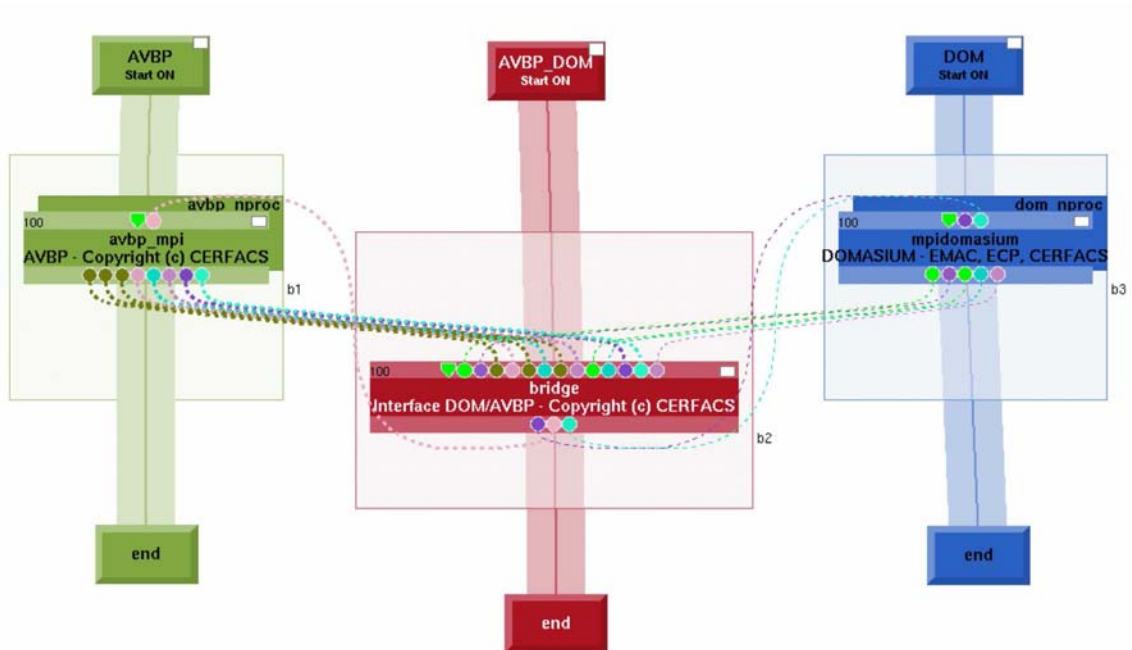
Figure A.6: Graphical representation of the PrePALM project for the RFTI coupled simulation.

Thick lines represent parallel distribution of data from the interface code to the multiple processors of the simulation codes. In the case of the DOM code, the lines are thin, which indicates that data is not distributed but copied on all processors (the same vectors are received by each processor).

The full thermal coupled simulation represented in Fig. A.8 is constructed by superposition of the two precedent projects. It can be seen that in the AVBP unit all communication ports are used and that no communication is made between the DOM code and AVTP. Information about solid boundary temperature and radiative heat loss to the walls is transfered via the unit AVBP.

A.5   Cost of coupling

It is a major concern for software developers to properly detect the cost in time efficiency of a simulation when a new module is added. In this section the two main sources of possible time consumption are isolated and evaluated.
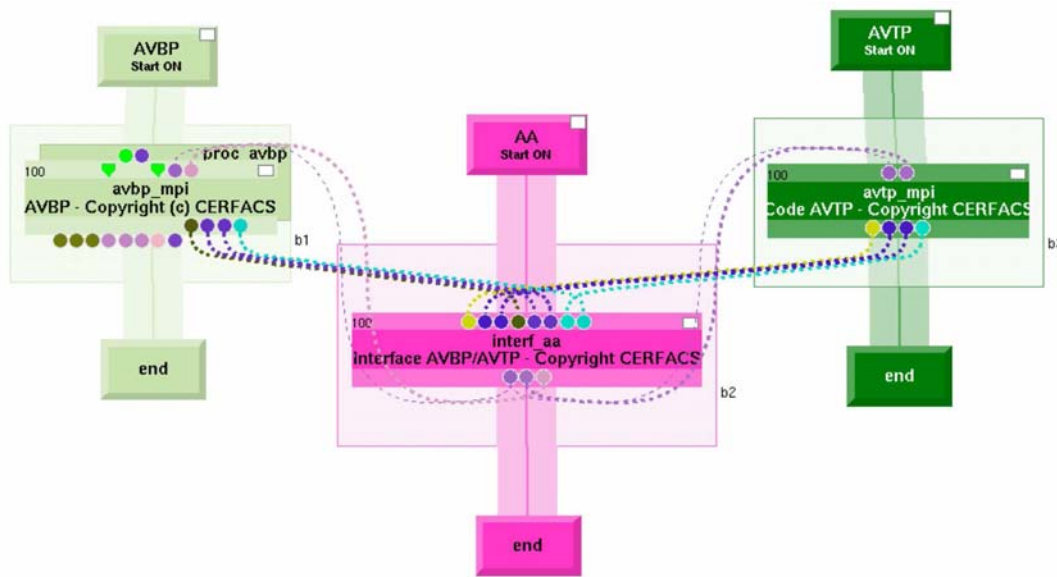
Figure A.7: Graphical representation of the PrePALM project for the FSTI coupled simulation.

A.5.1   Palmerized units without communications

For all simulation codes (AVBP, AVTP and PRISSMA) the palmerized unit was executed alone, without any communications with other codes. The objective of this exercise is to quantify the computational time loss due to the encapsulation of the code in a PALM unit. Although very minor modifications where done to the code, parallel communications are no longer independently handled by the simulation code but are mastered by the coupler.

Results showed that the computational speed is not altered by the encapsulation procedure. No difference could be detected between the units and the stand-alone codes.

A.5.2   Communications-only tests

One useful option included in PALM is to create a surrogate project in which the encapsulated codes are absent and only the coupling communications between units are saved. This permits to launch a simulation in which the total running time is a maximum value of the communications cost caused by the use of a coupling software.

Tests showed that the added computational time due to communications in PALM count for 2% to 4% of the computational time of the fully functional coupling project. This test clearly shows that a key point in code coupling is CPU synchronization: loss in computational time is mainly due to the
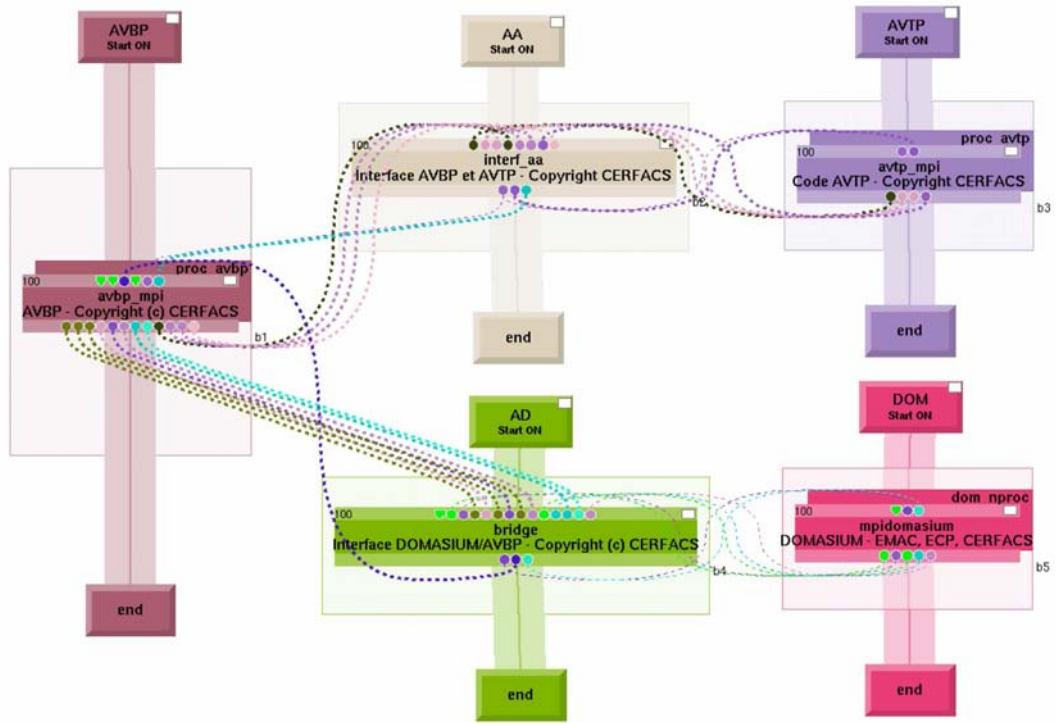
Figure A.8: Graphical representation of the PrePALM project for the MPC.

desynchronization of the unit communications.

Bibliography

[1] R. G. Abdel-Gayed and D. Bradley. Combustion regimes and the straining of turbulent premixed flames. *Combust. Flame*, 76:213–218, 1989.

[2] R. G. Abdel-Gayed, D. Bradley, M. N. Hamid, and M. Lawes. Lewis number effects on turbulent burning velocity. *Proc. Combust. Inst.*, 20:505–512, 1984.

[3] B. R. Adams and P. J Smith. Modeling effects of soot and Turbulence-Radiation coupling on radiative transfer in turbulent gaseous combustion. *Combustion Science and Technology*, 109(1):121 – 140, 1995.

[4] N.H. Afgan and J.M. Beer. *Heat Transfer in Flames*. John Wiley & Sons Inc, 99th edition, December 1974.

[5] J. Amaya, O. Cabrit, D. Poitou, B. Cuenot, and M. El Hafi. Unsteady coupling of Navier-Stokes and radiative heat transfer solvers applied to an anisothermal multicomponent turbulent channel flow. *Journal of Quantitative Spectroscopy and Radiative Transfer*, 111(2):295–301, 2010.

[6] J. Amaya and B. Cuenot. Combustion et rayonnement par sge. Rapport contractuel CR/CFD/08/136, CERFACS, Décembre 2008.

[7] P. S. Andersen, W. M. Kays, and R. J. Moffat. Experimental results for the transpired turbulent boundary layer in an adverse pressure gradient. *J. Fluid Mech.*, 69(2):353–375, 1975.

[8] Frédéric André and Rodolphe Vaillon. The k-moment method for the narrow band modeling of radiative properties of nonuniform gaseous media. *Journal of Quantitative Spectroscopy and Radiative Transfer*, 109(2):258–268, 2008.

[9] C. Angelberger, D. Veynante, F. Egolfopoulos, and T. Poinsot. Large eddy simulations of combustion instabilities in premixed flames. In *Proc. of the Summer Program*, pages 61–82. Center for Turbulence Research, NASA Ames/Stanford Univ., 1998.

[10] Albert Arking and Kenneth Grossman. The influence of line shape and band structure on temperatures in planetary atmospheres. *Journal of the Atmospheric Sciences*, 29(5):937–949, 1972.

[11] Vedat S. Arpaci, Shu-Hsin Kao, and Ahmet Selamet. *Introduction to heat transfer*. Prentice Hall, 1999.

[12] L. Artal. *Modélisation des flux de chaleur stationnaires pour un mélange multi-espece avec trans-fert de masse à la paroi.* Phd thesis, University Montpellier II, 2006.

[13] C. Balaji and S.P. Venkateshan. Combined conduction, convection and radiation in a slot. *International Journal of Heat and Fluid Flow*, 16(2):139–144, April 1995.

[14] Lon Edward Bell. *Energy transport by combined radiation and conduction.* Thesis, California Institute of Technology, 1968.

[15] Ryszard A. Bialecki and Gabriel Wecel. Solution of conjugate radiation convection problems by a BEM FVM technique. *Journal of Quantitative Spectroscopy and Radiative Transfer*, 84(4):539–550, April 2004.

[16] D. Bohn and J. Ren. Systematic investigation on conjugate heat transfer rates of film cooling configurations. In *The 10th Int, Symp on Transport Phenomena and Dynamics of Rotating Machinery*, 2004.

[17] M. Boileau, G. Staffelbach, B. Cuenot, T. Poinsot, and C. Bérat. LES of an ignition sequence in a gas turbine engine. *Combust. Flame* , 154(1-2):2–22, 2008.

[18] R. Borghi. Turbulent combustion modelling. *Prog. Energy Comb. Sci.* , 14(4):245–292, 1988.

[19] G. Boudier. *Application de la méthode LES à la combustion instationnaire dans les foyers d'hélicoptère.* PhD thesis, Institut National Polytechnique de Toulouse, France - Dynamique des fluides, 2007.

[20] G. Boudier, L. Y. M. Gicquel, T. Poinsot, D. Bissières, and C. Bérat. Effect of mesh resolution on large eddy simulation of reacting flows in complex geometry combustors. *Combust. Flame* , 155(1-2):196–214, 2008.

[21] G. Boudier, L.Y.M. Gicquel, T. Poinsot, D. Bissières, and C. Bérat. Comparison of LES, RANS and experiments in an aeronautical gas turbine combustion chamber. *Proc. of the Combustion Institute*, 31(2):3075–3082, 2007.

[22] G. Boudier, G. Staffelbach, L. Gicquel, and T. Poinsot. Mesh dependency of turbulent reacting large-eddy simulations in a gas turbine combustion chamber. In *QLES (Quality and reliability of LES) workshop*, Leuven, Belgium, october 2007. ERCOFTAC.

[23] Pierre Bouguer. *Essai d'optique sun la graduation de la lumière.* Jombert, 1729.

[24] J. Boussinesq. Théorie de l'écoulement tourbillant. *Mém. Présentés par Divers Savants. Acad. Sci. Inst. Fr.*, 23:46–50, 1877.

[25] K. N. C. Bray. The interaction between turbulence and combustion. In *17th Symp. (Int.) on Combustion*, pages 223–233. The Combustion Institute, Pittsburgh, 1979.

[26] Jr. Breene and Thornton Page. The shift and shape of spectral lines. *American Journal of Physics*, 31(3):224, March 1963.

[27] J. J. Brehm and W. J. Mullins. *Introduction to the Structure of Matter: A Course in Modern Physics.* January 1989.

[28] Jean-Louis Breton, Jean-Louis Joly, and Grandpeix Jean-Yves. Méthodologie des couplages et transferts thermiques. Cours Master Recherche DET, Université Paul Sabatier, December 2007.

[29] T. J. Bruno, M. L. Huber, A. Laesecke, E. W. Lemmon, and R. A. Perkins. Thermochemical and thermophysical properties of JP-10. Technical Report NISTIR 6640, Chemical science and technology laboratory, 325 Broadway Boulder, CO 80305, 2006.

[30] B W. Butler, M A. Finney, P L. Andrews, and F A. Albini. A radiation-driven model for crown fire spread : The international crown fire modelling experiment (icfme). *Canadian Journal of Forest Research*, 34(8):1588–1599, 2004.

[31] T. D Butler and P. J. O'Rourke. A numerical method for two dimensional unsteady reacting flows. In *Symposium on Combustion (International), 16th, Cambridge, Mass., August 15-20, 1976, Proceedings. (A77-48158 23-25) Pittsburgh, Pa., Combustion Institute, 1977, p. 1503-1513; Comments, p. 1513-1515. ERDA-Navy-supported research.*, pages 1503–1513, 1977.

[32] O. Cabrit and F. Nicoud. Direct simulations for wall modeling of multicomponent reacting compressible turbulent flows. *Phys. Fluids* , 21(5):055108, May 2009.

[33] S. M. Candel and T. Poinsot. Flame stretch and the balance equation for the flame surface area. *Combust. Sci. Tech.* , 70:1–15, 1990.

[34] B. G. Carlson. *Tables of equal weight quadrature eq over the unit sphere.* 1971.

[35] W. R. Catchpole, E. A. Catchpole, B. W. Butler, R. C. Rothermel, G. A. Morris, and D. J. Latham. Rate of spread of free-burning fires in woody fuels in a wind tunnel. *Combust. Sci. Tech.* , 131:1–37, 1998.

[36] Tuncer Cebeci and Jean Cousteix. *Modeling and computation of boundary-layer flows.* Springer, 2005.

[37] S. Chandrasekhar. *Radiative Transfer.* Dover, Mineola, NY, 1960.

[38] Patrick Chassaing. *Turbulence en mécanique des fluides, Analyse du phénomène dans une perspective de modélisation à l'usage de l'ingénieur.* Institut National Polytechnique de Toulouse, 2000.

[39] Alexandre Chatelain. *Simulation des Grandes Echelles d'écoulements turbulents avec transferts de chaleur.* PhD thesis, Institut National Polytechnique de Grenoble, September 2004.

[40] Sébastien Chemin. *Etude des interactions thermiques fluide-structure par un couplage de codes de calculs*. PhD thesis, Universitée Reims Champagne-Ardenne, 2006.

[41] Zheng Chen, Xiao Qin, Bo Xu, Yiguang Ju, and Fengshan Liu. Studies of radiation absorption on flame speed and flammability limit of CO2 diluted methane flames at elevated pressures. *Proceedings of the Combustion Institute*, 31(2):2693–2700, 2007.

[42] Lin Cheng, Mingtian Xu, and Liqiu Wang. From boltzmann transport equation to single-phase-lagging heat conduction. *International Journal of Heat and Mass Transfer*, 51:6018–6023, 2008.

[43] J. H. Chin, T. D. Panczak, and L. Fried. Spacecraft thermal modelling. *International Journal for Numerical Methods in Engineering*, 35:641–653, September 1992.

[44] K. H. Chu and R. Greif. Theoretical determination of band absorption for nonrigid rotation with applications to co, no, n2o, and co2. *ASME Transactions Journal of Heat Transfer*, 100:230–234, May 1978.

[45] P. J. Coelho. Numerical simulation of the interaction between turbulence and radiation in reactive flows. *Progress in Energy and Combustion Science*, 33(4):311–383, August 2007.

[46] P. J. Coelho. Approximate solutions of the filtered radiative transfer equation in large eddy simulations of turbulent reactive flows. *Combustion and Flame*, 156(5):1099–1110, May 2009.

[47] P. J. Coelho, P. Perez, and M. El Hafi. Benchmark numerical solutions for radiative heat transfer in two-dimensional axisymmetric enclosures with non-gray sooting media. *Numerical Heat Transfer, Part B: Fundamentals*, 43(5):425 – 444, 2003.

[48] P. J. Coelho, O. J. Teerling, and D. Roekaerts. Spectral radiative effects and turbulence/radiation interaction in a non-luminous turbulent jet diffusion flame. *Combustion and Flame*, 133(1-2):75 – 91, 2003.

[49] O. Colin, F. Ducros, D. Veynante, and T. Poinsot. A thickened flame model for large eddy simulations of turbulent premixed combustion. *Physics of Fluids*, 12(7):1843–1863, 2000.

[50] G. Cox. On radiant heat transfer in turbulent flames. *Combustion Science and Technology*, 17:75–78, 1977.

[51] P. I. Crumpton. An efficient cell vertex method for unstructured tetrahedral grids. Technical Report 95/19, Oxford University Computing Laboratory, 1995.

[52] P. I. Crumpton, J. A. Mackenzie, and K. W. Morton. Cell vertex algorithms for the compressible navier-stokes equations. *J. Comput. Phys.*, 109:1–15, 1993.

[53] N. Darabiha, V. Giovangigli, A. Trouvé, S. M. Candel, and E. Esposito. Coherent flame description of turbulent premixed ducted flames. In R. Borghi and S.N.B. Murthy, editors, *Turbulent Reacting Flows*, volume 40 of *Lecture Notes in Engineering*, page 591. Springer Verlag, 1989.

[54] A. de Boer, A.H. van Zuijlen, and H. Bijl. Comparison of conservative and consistent approaches for the coupling of non-matching meshes. *Computer Methods in Applied Mechanics and Engineering*, 197(49-50):4284 – 4297, 2008.

[55] J. W. Deardorff. A numerical study of three-dimensional turbulent channel flow at large reynolds numbers. *J. Fluid Mech.*, 41(2):453–480, 1970.

[56] M. K. Denison and B. W. Webb. A spectral line based weighted-sum-of-gray-gases model for arbitrary RTE solvers. *ASME Journal of Heat Transfer*, (115):1004–1012, 1993.

[57] M. K. Denison and B. W. Webb. The spectral-line-based weighted-sum-of-gray-gases model in nonisothermal nonhomogeneous media. *ASME Journal of Heat Transfer*, (117):359–365, 1995.

[58] K. V. Deshmukh, D. C. Haworth, and M. F. Modest. Direct numerical simulation of turbulence radiation interactions in homogeneous nonpremixed combustion systems. *Proceedings of the Combustion Institute*, 31(1):1641–1648, 2007.

[59] K.V. Deshmukh, M.F. Modest, and D.C. Haworth. Direct numerical simulation of turbulence-radiation interactions in a statistically one-dimensional nonpremixed system. *Journal of Quantitative Spectroscopy and Radiative Transfer*, 109(14):2391–2400, September 2008.

[60] P. E. Desjardin and S. H. Frankel. Two-dimensional large eddy simulation of soot formation in the near-field of a strongly radiating nonpremixed acetylene-air turbulent jet flame. *Combustion and flame*, 119(1-2):121–132, 1999.

[61] W.J. Dodds and D.W. Bahr. *Design of modern gas turbine combustors*, chapter Combustion system design, pages 343–476. Academic Press, 1990.

[62] G. A. Domoto. Frequency integration for radiative transfer problems involving homogeneous non-gray gases: The inverse transmission function. *Journal of Quantitative Spectroscopy and Radiative Transfer*, 14(9):935–942, September 1974.

[63] C. Dopazo. Recent developments in pdf methods. In P. A. Libby and F. A. Williams, editors, *Turbulent Reacting Flows*, pages 375 – 474. Academic, London, 1994.

[64] R. Goncalves dos Santos, M. Lecanu, S. Ducruix, O. Gicquel, E. Iacona, and D. Veynante. Coupled large eddy simulations of turbulent combustion and radiative heat transfer. *Combustion and Flame*, 152(3):387–400, February 2008.

[65] R. GonÁalves dos Santos. *Large Eddy Simulation of Turbulent Combustion Including Radiative Heat Transfer*. PhD thesis, EM2C, 2007.

[66] E. R. Van Driest. Turbulent boundary layer in compressible fluids. *J. Aeronaut. Sci.*, 18(3):145–160, 216, 1951.

[67] F. Duchaine, A. Corpron, L. Pons, V. Moureau, F. Nicoud, and T. Poinsot. Development and assessment of a coupled strategy for conjugate heat transfer with Large Eddy Simulation. application to a cooled turbine blade. *International Journal of Heat and Mass Transfer*, submitted, 2009.

[68] F. Duchaine, S. Mendez, F. Nicoud, A. Corpron, V. Moureau, and T. Poinsot. Conjugate heat transfer with large eddy simulation application to gas turbine components. *C. R. Acad. Sci. Mécanique*, 337(6-7):550–561, 2009.

[69] Jean-Louis Dufresne and Jean-Yves Grandpeix. Raccordement des modèles thermodynamiques de glace, d'océan et d'atmosphère. Note Interne 205, Laboratoire de Météorologie Dynamique, september 1996.

[70] D. K. Edwards. Molecular gas band radiation. In *Advances in heat transfer. Volume 12. New York, Academic Press, Inc., 1976, p. 115-193.*, volume 12, pages 115–193, 1976.

[71] D. K. Edwards and W. A. Menard. Comparison of models for correlation of total band absorption. *Appl. Opt.*, 3(5):621–625, 1964.

[72] W.M. Elsasser. *Heat transfer by infrared radiation in the atmosphere*. Harvard University Press, 1943.

[73] A. Ern and V. Giovangigli. *Multicomponent Transport Algorithms*. Lecture Notes in Physics. Springer Verlag, Heidelberg, 1994.

[74] M. Errera and S. Chemin. A fluid-solid thermal coupling applied to an effusion cooling system. In *34th AIAA Fluid Dynamics Conference and Exhibit*, Portland, Oregon, 2004.

[75] M.P. Errera, G. Chaineray, and S. Chemin. Etude du transitoire thermique dans un matériau via un couplage convection-conduction. In *Congrés français de thermique, SFT*, 2007.

[76] Michael Faraday. Experimental researches in electricity. *Philosophical Transactions of the Royal Society of London*, 128:1–40, 1838.

[77] Michael Faraday and William Crookes. *The chemical history of a candle : a course of lectures delivered before a juvenile audience at the Royal Institution / by Michael Faraday ; edited by William Crookes*. Chatto and Windus, London, 1861.

[78] C. A. Felippa and K. C. Park. Staggered transient analysis procedures for coupled mechanical systems: Formulation. *Computer Methods in Applied Mechanics and Engineering*, 24(1):61 – 111, 1980.

[79] Xiaobing Feng. Analysis of finite element methods and domain decomposition algorithms for a fluid-solid interaction problem. *SIAM Journal on Numerical Analysis*, 38(4):1312–1336, 2000.

[80] E. Fernandez-Tarrazo, A. Sanchez, A. Linan, and F. Williams. A simple one-step chemistry model for partially premixed hydrocarbon combustion. *Combust. Flame*, 147(1-2):32–38, 2006.

[81] W. A. Fiveland. *Discrete ordinate methods for radiative heat transfer in isotropically and anisotropically scattering media*. W. A. Babcock and Wilcox Research and Development Div., 1987.

[82] B. Franzelli, E. Riber, M. Sanjosé, and T. Poinsot. A two-step chemical scheme for kerosene-air premixed flames. *Combustion and Flame*, In Press, Corrected Proof:–, 2010.

[83] M. García. *Développement et validation du formalisme Euler-Lagrange dans un solveur parallèle et non-structuré pour la simulation aux grandes échelles - TH/CFD/09/1*. PhD thesis, Université de Toulouse - Ecole doctorale : Mécanique, Energétique, Génie civil, Procédés, 2009.

[84] Vijay K. Garg. Heat transfer research on gas turbine airfoils at NASA GRC. *International Journal of Heat and Fluid Flow*, 23(2):109–136, April 2002.

[85] M. Germano, U. Piomelli, P. Moin, and W. Cabot. A dynamic subgrid-scale eddy viscosity model. *Phys. Fluids*, 3(7):1760–1765, 1991.

[86] M. B. Giles. Stability analysis of numerical interface conditions in fluid-structure thermal analysis. *International Journal for Numerical Methods in Fluids*, 25:421–436, August 1997.

[87] P. Giordano and D. Lentini. Combustion-radiation-turbulence interaction modeling in absorbing/emitting nonpremixed flames. *Combust. Sci. Tech.*, 1:1–22, 2001.

[88] V. Giovangigli. *Multicomponent Flow Modeling*. Modeling and Simulation in Science, Engineering and Technology. Birkhäuser, Boston, 1999.

[89] W. L. Godson. The computation of infrared transmission by atmospheric water vapor, part ii. *Journal of the Atmospheric Sciences*, 12(6):533–535, December 1955.

[90] R. M. Goody. A statistical model for water-vapour absorption. *Quarterly Journal of the Royal Meteorological Society*, 78(336):165–169, 1952.

[91] Richard M. Goody and Y. L. Yung. *Atmospheric radiation*. Oxford University Press US, 1995.

[92] J.P. Gore, J. Lim, T. Takeno, and X.L. Zhu. A study of the effects of thermal radiation on the structure of methane/air counter-flow diffusion flames using detailed chemical kinetics. In *Proceedings of the Fifth ASME/ISME Joint Thermal Engineering Conference*, March 1999.

[93] F. C. Gouldin. Combustion intensity and burning rate integral of premixed flames. In *26th Symp. (Int.) on Combustion*, pages 381 – 388. The Combustion Institute, Pittsburgh, 1996.

[94] N Gourdain, L Gicquel, M Montagnac, O Vermorel, M Gazaix, G Staffelbach, M Garcia, J-F Boussuge, and T Poinsot. High performance parallel computing of flows in complex geometries: I. methods. *Computational Science & Discovery*, 2(1):015003, 2009.

[95] V. Goutière, A. Charette, and L. Kiss. Comparative performance of non-gray gas modeling techniques. *Numerical Heat Transfer Part B: Fundamentals*, 41:361–381, March 2002.

[96] V. Goutiere, F. Liu, and A. Charette. An assessment of real-gas modelling in 2D enclosures. *Journal of Quantitative Spectroscopy and Radiative Transfer*, 64:299–326, February 2000.

[97] G Grötzbach. Direct numerical and large eddy simulation of turbulent channel flows. *Encyclopedia of Fluid Mechanics*, 6:1337, 1987.

[98] O. Gulder. Turbulent premixed flame propagation models for different combustion regimes. In *23rd Symp. (Int.) on Comb.*, pages 743–835, Orleans, 1990. The Combustion Institute, Pittsburgh.

[99] Ankur Gupta, Michael F. Modest, and Daniel C. Haworth. Large-eddy simulation of turbulence-radiation interactions in a turbulent planar channel flow. *Journal of Heat Transfer*, 131(6):061704, 2009.

[100] J. O. Hinze. *Turbulence*. McGraw-Hill, New-York, 1975.

[101] C. Hirsch. *Numerical Computation of Internal and External Flows*, volume 2. John Wiley & Sons, New York, 1990.

[102] J. Hirschfelder, C. Curtis, and B. Bird. *Molecular Theory of Gases and Liquids*. John Wiley & Sons, 1954 edition, 1954.

[103] Guy Hoffmann and Carlo Benocci. Approximate wall boundary conditions for large eddy simulations. In *Proceedings of the 5th European Turbulence Conference*, pages 222–228, July 1994.

[104] N. Hoffmann and N. C. Markatos. Thermal radiation effects on fires in enclosures. *Applied Mathematical Modelling*, 12(2):129 – 140, 1988.

[105] H. C. Hottel and E. S. Cohen. Radiant heat exchange in a gas-filled enclosure: Allowance for nonuniformity of gas temperature. *AIChE Journal*, 4(1):3–14, 1958.

[106] H.C. Hottel and A.F. Sarofim. *Radiative Transfer*. McGraw-Hill, New York, 1976.

[107] S. Hoyas and J. Jiménez. Scaling the velocity fluctuations in turbulent channel up to $Re_\tau = 2003$. *Phys. Fluids* , 18(011702):18–21, 2006.

[108] T.C Hsieh and R Greif. Theoretical determination of the absorption coefficient and the total band absorptance including a specific application to carbon monoxide. *International Journal of Heat and Mass Transfer*, 15(8):1477 – 1487, 1972.

[109] Christian Huygens. *Traité de la lunière*. 1690.

[110] Frank P. Incropera and David P. DeWitt. *Fundamentals of heat and mass transfer*. John Wiley, 2007.

[111] Internal. Thermique dans une chambre de combustion. Technical report, Turbomeca, 2009.

[112] F. Jaegle, O. Cabrit, S. Mendez, and T. Poinsot. Implementation methods of wall functions in cell-vertex numerical solvers. *Flow, Turbulence and Combustion*, Submitted, 2010.

[113] R.K. Jaiman, X. Jiao, P.H. Geubelle, and E. Loth. Conservative load transfer along curved fluid-solid interface with non-matching meshes. *Journal of Computational Physics*, 218(1):372 – 397, 2006.

[114] William S. Janna. *Engineering heat transfer*. CRC Press, 2000.

[115] J.H. Jeans. The equations of radiative transfer of energy. *Monthly Notices Royal Astronomical Society*, 78:28–36, 1917.

[116] C.L. Jensen. Thermal radiation analysis system. Trasys-ii user's manual, Martin Marietta Corp., Denver, CO, February 1987.

[117] K. A. Jensen, J.F. Ripoll, A. Wray, D. Joseph, and M El Hafi. On various modeling approaches to radiative heat transfer in pool fires. *Combustion and Flame*, 148(4):263–279, March 2007.

[118] J. Jiménez and P. Moin. The minimal flow unit in near-wall turbulence. *J. Fluid Mech.*, 225:213–240, 1991.

[119] Richard W. Johnson. *The handbook of fluid dynamics*. Springer, 1998.

[120] W.P. Jones and M.C. Paul. Combination of DOM with LES in a gas turbine combustor. *International Journal of Engineering Science*, 43(5-6):379–397, March 2005.

[121] D. Joseph. *Modélisation des transferts radiatifs en combustion par méthode aux ordonnées discrètes sur des maillages non structurés tridimensionnels*. PhD thesis, Institut National Polytechnique de Toulouse, 2004.

[122] D. Joseph, P. Perez, M. El Hafi, and B. Cuenot. Discrete ordinates and monte carlo methods for radiative transfer simulation applied to computational fluid dynamics combustion modeling. *Journal of Heat Transfer*, 131(5):052701–9, May 2009.

[123] V.P. Kabashnikov and G.I. Kmit. Influence of turbulent fluctuations on thermal radiation. *Journal Applied Spectroscopy*, 31(2):963–967, 1979.

[124] V.P. Kabashnikov and G.I. Myasiwkova. Thermal radiation in turbulent flows - temperature and concentration fluctuations. *Heat Transfer - Soviet Research*, 17(6):116–125, 1985.

[125] B. A. Kader. Temperature and concentration profiles in fully turbulent boundary layers. *Int. J. Heat and Mass Transfer*, 24(9):1541–1544, 1981.

[126] B. A. Kader. Heat and mass transfer in pressure-gradient boundary layers. *Int. J. Heat and Mass Transfer*, 34(11):2837–2857, November 1991.

[127] V. Karpov, A. Lipatnikov, and V. Zimont. A test of an engineering model of premixed turbulent combustion. In *26th Symp. (Int.) on Combustion*, pages 249–257. The Combustion Institute, Pittsburgh, 1996.

[128] N. Kasagi, A. Kuroda, and M. Hirata. Numerical investigation of near-wall turbulent heat transfer taking into account the unsteady heat conduction in the solid wall. *Journal of Heat Transfer*, 111(2):385–392, 1989.

[129] A. Kassab, E. Divo, J. Heidmann, E. Steinthorsson, and F. Rodriguez. BEM/FVM conjugate heat transfer analysis of a three-dimensional film cooled turbine blade. *International Journal of Numerical Methods for Heat & Fluid Flow*, 13(5):581 – 610, 2003.

[130] Nuray Kayakol, Nevin Selçuk, Ian Campbell, and Ömer L. Gülder. Performance of discrete ordinates method in a gas turbine combustor simulator. *Experimental Thermal and Fluid Science*, 21(1-3):134 – 141, 2000.

[131] K.C. Kays. Turbulent Prandtl number. Where are we ? *J. Heat Trans.*, 116:284–295, May 1994.

[132] W.M. Kays, M.E. Crawford, and B. Weigand. *Convective Heat and Mass Transfer*. McGraw-Hill, 2004.

[133] A. R. Kerstein, W. Ashurst, and F. A. Williams. Field equation for interface propagation in an unsteady homogeneous flow field. *Phys. Rev. A*, 37(7):2728–2731, 1988.

[134] J. Kim, P. Moin, and R. Moser. Turbulence statistics in fully developed channel flow at low Reynolds number. *J. Fluid Mech.*, 177:133–166, 1987.

[135] Gustav Kirchhoff. über das verhältnis zwischen dem emissionsvermöogen und dem absorptionsvermögen. der körper für wärme und licht. *Poggendorfs Annalen der Physik und Chemie*, 109:275–301, 1860. English translation: On the relation between the radiating and the absorbing powers of different bodies for light and heat. Phil. Mag., 1860, ser. 4, v. 20, 1-21.

[136] Rainer Koch and Ralf Becker. Evaluation of quadrature schemes for the discrete ordinates method. *Journal of Quantitative Spectroscopy and Radiative Transfer*, 84(4):423 – 435, 2004. Eurotherm Seminar 73 - Computational Thermal Radiation in Participating Media.

[137] A. N. Kolmogorov. The local structure of turbulence in incompressible viscous fluid for very large reynolds numbers. *C. R. Acad. Sci.*, USSR, 30:301, 1941.

[138] K. Y. Kondratyev. *Radiation in the atmosphere*. 1969.

[139] M. E. Kounalakis, J. P. Gore, and G. M. Faeth. Turbulence/radiation interactions in nonpremixed hydrogen/air flames. *Symposium (International) on Combustion*, 22(1):1281–1290, 1988.

[140] U.O. Köylü and G. M. Faeth. Spectral extinction coefficients of soot aggregates from turbulent diffusion flames. *Journal of Heat Transfer*, 118(2):415–421, 1996.

[141] Sunil Kumar and Kunal Mitra. Microscale aspects of thermal radiation transport and laser applications. volume 33 of *Advances in Heat Transfer*, pages 187 – 294. Elsevier, 1999.

[142] Kenneth K. Kuo. *Principles of combustion*. Wiley, 1986.

[143] N. Lamarque. *Schémas numériques et conditions limites pour la simulation aux grandes échelles de la combustion diphasique dans les foyers d'hélicoptère*. Phd thesis, INP Toulouse, 2007.

[144] P. D. Lax and B. Wendroff. Systems of conservation laws. *Commun. Pure Appl. Math.* , 13:217–237, 1960.

[145] M. Leacanu. *Couplage milti-physique combustion turbulent - rayonnement - cinétique chimique*. PhD thesis, Ecole centrale Paris, 2005.

[146] A. H. Lefebvre. *Gas Turbines Combustion*. Taylor & Francis, 1999.

[147] Arthur H. Lefebvre. Flame radiation in gas turbine combustion chambers. *International Journal of Heat and Mass Transfer*, 27(9):1493 – 1510, 1984.

[148] J.-Ph. Légier. *Simulations numériques des instabilités de combustion dans les foyers aéronautiques - TH/CFD/01/86*. PhD thesis, Institut National Polytechnique de Toulouse, France - Mécanique des fluides, 2001.

[149] Marcel Lesieur. *Turbulence in fluids*. Springer, 4th. edition, 2008.

[150] Genong Li and Michael F. Modest. Importance of turbulence-radiation interactions in turbulent diffusion jet flames. *Journal of Heat Transfer*, 125(5):831–838, 2003.

[151] S. C. Li, B. Varatharajan, and F. A. Williams. Chemistry of jp-10 ignition. *Am. Inst. Aeronaut. Astronaut. J.* , 39(12):2351–2356, 2001.

[152] John H. Lienhard. *A heat transfer textbook*. Phlogiston Press, August 2003.

[153] D. K. Lilly. A proposed modification of the germano sub-grid closure method. *Phys. Fluids* , 4(3):633–635, 1992.

[154] F. Liu, H. Guo, G. J. Smallwood, and M. El Hafi. Effects of gas and soot radiation on soot formation in counterflow ethylene diffusion flames. *Journal of Quantitative Spectroscopy and Radiative Transfer*, 84(4):501–511, April 2004.

[155] F. Liu and G. J. Smallwood. An efficient approach for the implementation of the SNB based correlated-k method and its evaluation. *Journal of Quantitative Spectroscopy and Radiative Transfer*, 84(4):465–475, April 2004.

[156] F. Liu, G. J. Smallwood, and O. L. G̦lder. Application of the statistical narrow-band correlated-k method to non-grey gas radiation in $CO_2 - H_2O$ mixtures: approximate treatments of overlapping bands. *Journal of Quantitative Spectroscopy and Radiative Transfer*, 68(4):401–417, February 2001.

[157] F. Liu, M. Yang, G.J. Smallwood, and H. Zhang. Evaluation of the snb based full-spectrum ck method for thermal radiation calculations in $CO_2 - H_2O$ mixtures. In *Proceedings of ICHMT*, 2004.

[158] R. S. Longhurst. *Geometrical and physical optics [by] R. S. Longhurst.* Longman [London], 3d ed. edition, 1973.

[159] J. A. Mackenzie. *Cell vertex finite volume methods for the solution of the compressible Navier-Stokes equations.* Phd thesis, Oxford University Computing Laboratory, 1991.

[160] B. F. Magnussen and B. H. Mjertager. On mathematical modeling of turbulent combustion. In *16th Symp. (Int.) on Combustion*, pages 719–727. The Combustion Institute, Pittsburgh, 1976.

[161] S. Manabe. A global ocean-atmosphere climate model with seasonal variation for future studies of climate sensitivity. *Dynamics of Atmospheres and Oceans*, 3:393–426, July 1979.

[162] Syukuro Manabe and Kirk Bryan. Climate calculations with a combined ocean-atmosphere model. *Journal of the Atmospheric Sciences*, 26(4):786–789, 1969.

[163] F. E. Marble and J. E. Broadwell. The coherent flame model for turbulent chemical reactions. Technical Report Tech. Rep. TRW-9-PU, Project Squid, 1977.

[164] J. D. Mattingly. *Elements of gas turbine propulsion.* AIAA, 2nd edition, 2005.

[165] J. C. Maxwell. *A treatise on electricity and magnetism*, volume 1 and 2. Clarendon Press, Oxford, 1873.

[166] J. Clerk Maxwell. A dynamical theory of the electromagnetic field. *Philosophical Transactions of the Royal Society of London*, 155:459–512, 1865.

[167] Zdzislaw Mazur, Alejandro Hernńdez-Rossette, Rafael García-Illescas, and Alberto Luna-Ramírez. Analysis of conjugate heat transfer of a gas turbine first stage nozzle. *Applied Thermal Engineering*, 26(16):1796–1806, November 2006.

[168] Bonnie J. Mcbride, Sanford Gordon, and Martin A. Reno. Coefficients for calculating thermodynamic and transport properties of individual species. Technical Report E-7981; NAS 1.15:4513; NASA-TM-4513, Glenn Research Center, October 1993.

[169] Gerald A. Meehl. *Climate system modeling*, chapter Global coupled models: atmosphere, ocean, sea ice, pages 555–581. Cambridge University Press, 1995.

[170] S. Mendez and F. Nicoud. Large-eddy simulation of a bi-periodic turbulent flow with effusion. *J. Fluid Mech.* , 598:27–65, 2008.

[171] M.P. Mengüç, W. G. Cummings, and R. Viskanta. Radiative transfer in a gas turbine combustor. *Journal of Propulsion and Power*, 2:241–247, 1986.

[172] Nicholas Metropolis. The beginning of the monte carlo metod. *Los Alamos Science*, pages 125–130, 1987.

[173] Anthony F. Mills. *Heat transfer*. Irwin, 1992.

[174] Subhash C. Mishra, Bittagopal Mondal, Tuanuj Kush, and B. Silva Rama Krishnan. Solving transient heat conduction problems on uniform and non-uniform lattices using the lattice boltzmann method. *International Communications in Heat and Mass Transfer*, 36:322–328, 2009.

[175] M. F. Modest. The weighted-sum-of-gray-gases model for arbitrary solution methods in radiative transfer. *ASME Transactions Journal of Heat Transfer*, 113:650–656, August 1991.

[176] M. F. Modest and H. Zhang. The full-spectrum correlated-k distribution for thermal radiation from molecular gas-particulate mixtures. *Journal of Heat Transfer*, 124(1):30–38, 2002.

[177] Michael F. Modest. *Radiative heat transfer*. Academic Press, 2003.

[178] B. Mohammadi and G. Puigt. Wall functions in computational fluid mechanics. *Combust. Flame*, 35(10):1108–1115, 2006.

[179] P. Moin and J. Kim. Numerical investigation of turbulent channel flow. *J. Fluid Mech.*, 118:341–377, 1982.

[180] P. Moin, T.-H. Shih, D. Driver, and N. N. Mansour. Direct numerical simulation of a three-dimensional turbulent boundary layer. *Physics of Fluids A: Fluid Dynamics*, 2(10):1846–1853, 1990.

[181] P. Moin, K. D. Squires, W. Cabot, and S. Lee. A dynamic subgrid-scale model for compressible turbulence and scalar transport. *Phys. Fluids*, A 3(11):2746–2757, 1991.

[182] Parry Moon. *The scientific basis of illuminating engineering*. 1936.

[183] Tegan Morrison. Radiative gas properties. Private communication, 2003.

[184] R.D. Moser, J Kim, and N.N. Mansour. Direct numerical simulation of turbulent channel flow up to R$e_\tau = 590$. *Phys. Fluids*, 11(4):943–945, 1999.

[185] Praveen Narayanan and Arnaud Trouvé. Radiation-driven flame weakening effects in sooting turbulent diffusion flames. *Proceedings of the Combustion Institute*, 32(1):1481 – 1489, 2009.

[186] Sir Isaac Newton, I. Bernard Cohen, Albert Einstein, and Sir Edmund Whittaker. *Opticks: Or a Treatise of the Reflections, Refractions, Inflections & Colours of Light-Based on the Fourth Edition London, 1730*. Dover Publications, June 1952.

[187] F. Nicoud and F. Ducros. Subgrid-scale stress modelling based on the square of the velocity gradient tensor. *Flow, Turbulence and Combustion*, 62(3):183–200, 1999.

[188] H.F. Nouanegue, A. Muftuoglu, and E. Bilgen. Heat transfer by natural convection, conduction and radiation in an inclined square enclosure bounded with a solid wall. *International Journal of Thermal Sciences*, 48(5):871–880, May 2009.

[189] Benoît Olsommer, Michael von Spakovsky, and Daniel Favrat. Transfert de chaleur par rayonnement dans un four d'incinération industriel: application de la méthode des zones. radiative heat transfer in an industrial waste incinerator : application of the zone method. *Revue Generale de Thermique*, 36(2):125 – 134, 1997.

[190] Alan V Oppenheim, Alan S Willsky, and S Hamid Nawab. *Señales y sistemas*. Prentice-Hall, 2nd. edition, 1997.

[191] J. M. Østerlund, A. V. Johansson, H. M. Nagib, and M. H. Hites. A note on the overlap region in turbulent boundary layers. *Phys. Fluids* , 12(1):1–4, January 2000.

[192] S. V. Patankar and D. B. Spalding. *Heat and mass transfer in boundary layers*. Morgan-Grampian, London, 1967.

[193] R.W. Patch. Effective absorption coefficients for radiant energy transport in nongrey, nonscattering gases. *Journal of Quantitative Spectroscopy and Radiative Transfer*, 7(4):611 – 637, 1967.

[194] S.C. Paul and M.C. Paul. Radiative heat transfer during turbulent combustion process. *International Communications in Heat and Mass Transfer*, 37(1):1–6, 2010.

[195] L. Pierrot, P. Rivière, A. Soufiani, and J. Taine. A fictitious-gas-based absorption distribution function global model for radiative transfer in hot gases. *Journal of Quantitative Spectroscopy and Radiative Transfer*, 62(5):609 – 624, 1999.

[196] L. Pierrot, A. Soufiani, and J. Taine J. Accuracy of narrow-band and global models for radiative transfer in H_2O, CO_2 and $H_2O - CO_2$ mixtures at high temperature. *Journal of Quantitative Spectroscopy and Radiative Transfer*, 62:523–548, July 1999.

[197] U. Piomelli. Wall-layer models for large-eddy simulations. *Prog. Aerospace Sci.* , 44(6):437–446, 2008.

[198] U. Piomelli and E. Balaras. Wall-layer models for large-eddy simulations. *Ann. Rev. Fluid Mech.* , 34:349–374, 2002.

[199] J. Piquet. *Turbulent flows, models and physics*. Springer-Verlag, 1999.

[200] Max Planck. Distribution of energy in the spectrum. *Annalen der Physik*, 4(3):553–563, 1901.

[201] T. Poinsot, C. Angelberger, F. Egolfopoulos, and D. Veynante. Large eddy simulations of combustion instabilities. In *1st Int. Symp. On Turbulence and Shear Flow Phenomena*, pages 1–6, Santa Barbara, Sept 12-15., 1999.

[202] T. Poinsot and S. Lele. Boundary conditions for direct simulations of compressible viscous flows. *J. Comput. Phys.* , 101(1):104–129, 1992.

[203] T. Poinsot and D. Veynante. *Theorical and Numerical Combustion*. Edwards, 2001.

[204] D. Poitou. *Modélisation du rayonnement dans la simulation aux grandes échelles de la combustion turbulente*. PhD thesis, Institut National Polytechnique de Toulouse, Décembre 2009.

[205] D. Poitou, J. Amaya, Bushan Singh C., D. Joseph, M. El Hafi, and B. Cuenot. Validity limits for the global model FS-SNBcK for combustion applications. In *Proceedings of Eurotherm83 – Computational Thermal Radiation in Participating Media III*, 2009.

[206] D. Poitou, M. El Hafi, and B. Cuenot. Diagnosis of Turbulence Radiation Interaction in turbulent flames and implications for modeling in Large Eddy Simulation. *Turkish Journal of Engineering and Environmental Sciences*, 31:371–381, 2007.

[207] S. Pope. The evolution of surfaces in turbulence. *Int. J. Engng. Sci.*, 26(5):445–469, 1988.

[208] S. B. Pope. Pdf methods for turbulent reactive flows. *Prog. Energy Comb. Sci.* , 19(11):119–192, 1985.

[209] S. B. Pope. *Turbulent flows*. Cambridge University Press, 2000.

[210] S. B. Pope. Ten questions concerning the large-eddy simulation of turbulent flows. *New Journal of Physics*, 6:35, 2004.

[211] M. Porta. *Développement, vérification et validation des outils LES pour l'étude du bruit de combustion et de l'interaction combustion/acoustique/turbulence - TH/CFD/07/46*. PhD thesis, Institut National Polytechnique de Toulouse, France - Dynamique des Fluides, 2007.

[212] Jacek Pozorski and Jean-Pierre Minier. Stochastic modelling of conjugate heat transfer in Near-Wall turbulence. In *Engineering Turbulence Modelling and Experiments 6*, pages 803–812. Elsevier Science B.V., Amsterdam, 2005.

[213] L. Prandtl. Über Flussigkeitsbewegung bei sehr kleiner Reibung. In Teubner, editor, *Verhandlungen des dritten internationalen Mathematiker-Kongresses*, pages 484–491, Leipzig, Germany, 1905.

[214] L. Prandtl. Investigations on turbulent flow. *Zeitschrift fur angewandte Mathematik und Mechanik*, 5:136, 1925.

[215] B. Roe, R. Jaiman, A. Haselbacher, and P. H. Geubelle. Combined interface boundary condition method for coupled thermal simulations. *International Journal for Numerical Methods in Fluids*, 57:329–354, May 2008.

[216] M. Roger, S. Blanco, M. El Hafi, and R. Fournier. Monte carlo estimates of Domain-Deformation sensitivities. *Physical Review Letters*, 95(18):180601, October 2005. Copyright (C) 2009 The American Physical Society; Please report any problems to prola@aps.org.

[217] M. Roger, C. B. Da Silva, and P. J. Coelho. Analysis of the turbulence-radiation interactions for large eddy simulations of turbulent flows. *International Journal of Heat and Mass Transfer*, 52(9-10):2243 – 2254, 2009.

[218] Maxime Roger, Pedro J. Coelho, and Carlos B. da Silva. The influence of the non-resolved scales of thermal radiation in large eddy simulation of turbulent flows: A fundamental study. *International Journal of Heat and Mass Transfer*, In Press, Corrected Proof.

[219] Colin Ronan. *The Cambridge illustrated history of the world's science*. Newness Books, 1983.

[220] L.S. Rothman, D. Jacquemart, A. Barbe, D. Chris Benner, M. Birk, L.R. Brown, M.R. Carleer, C. Chackerian, Jr., K. Chance, L.H. Coudert, V. Dana, V.M. Devi, J.-M. Flaud, R.R. Gamache, A. Goldman, J.-M. Hartmann, K.W. Jucks, A.G. Maki, J.-Y. Mandin, S.T. Massie, J. Orphal, A. Perrin, C.P. Rinsland, M.A.H. Smith, J. Tennyson, R.N. Tolchenov, R.A. Toth, J. Vander Auwera, P. Varanasi, and G. Wagner. The hitran 2004 molecular spectroscopic database. *Journal of Quantitative Spectroscopy and Radiative Transfer*, 96(2):139 – 204, 2005.

[221] François-Xavier Roux, Frédéric Magoulès, Stéphanie Salmon, and Laurent Series. Optimization of interface operator based on algebraic approach. In Ismael Herrera, David E. Keyes, Olof B. Widlund, and Robert Yates, editors, *Fourteenth International Conference on Domain Decomposition Methods*, 2003.

[222] M. A. Rudgyard. *Cell Vertex methods for compressible gas flows*. Phd thesis, Oxford University Computing Laboratory, 1990.

[223] Carl Sagan. *Cosmos*. Ballantine Books, 1993.

[224] P. Sagaut. *Large Eddy Simulation for incompressible flows*. Scientific computation series. Springer-Verlag, 2000.

[225] M. Sakami, A. Charette, and V. Le Dez. Radiative heat transfer in three-dimensional enclosures of complex geometry by using the discrete-ordinates method. *Journal of Quantitative Spectroscopy and Radiative Transfer*, 59(1-2):117 – 136, 1998.

[226] Mohamed Sakami and André Charette. A new differencing scheme for the discrete-ordinates method in complex geometries. *Revue Générale de Thermique*, 37(6):440 – 449, 1998.

[227] H. Schlichting and K. Gersten. *Boundary layer theory*. Springer-Verlag, 8th rev. edition, 2000.

[228] Fran¡ois G. Schmitt. About boussinesq's turbulent viscosity hypothesis: historical remarks and a direct evaluation of its validity. *Comptes Rendus Mécanique*, 335(9-10):617 – 627, 2007. Joseph Boussinesq, a Scientist of bygone days and present times.

[229] P. Schmitt. *Simulation aux grandes échelles de la combustion étagée dans les turbines à gaz et son interaction stabilité-polluants-thermique*. Phd thesis, INP Toulouse, 2005.

[230] P. Schmitt, T. Poinsot, B. Schuermans, and K. P. Geigle. Large-eddy simulation and experimental study of heat transfer, nitric oxide emissions and combustion instability in a swirled turbulent high-pressure burner. *J. Fluid Mech.* , 570:17–46, 2007.

[231] T. Schønfeld and T. Poinsot. Influence of boundary conditions in LES of premixed combustion instabilities. In *Annual Research Briefs* , pages 73–84. Center for Turbulence Research, NASA Ames/Stanford Univ., 1999.

[232] E. Schrödinger. An undulatory theory of the mechanics of atoms and molecules. *Physical Review*, 28(6):1049–1070, 1926.

[233] U. Schumann. Subgrid scale model for finite difference simulations of turbulent flows in plane channels and annuli. *J. Comput. Phys.* , 18:376–404, 1975.

[234] R.G. Siddall and I.A. McGrath. The emissivity of luminous flames. *Symposium (International) on Combustion*, 9(1):102 – 110, 1963.

[235] R. Siegel. Radiative behavior of a gas layer seeded with soot. *NASA STI/Recon Technical Report N*, 76:28512–+, July 1976.

[236] Robert Siegel and John R. Howell. *Thermal radiation heat transfer*. Taylor & Francis, 2002.

[237] C. V. Silva, F. H. R. França, and H. A. Vielmo. Analysis of the turbulent, non-premixed combustion of natural gas in a cylindrical chamber with and without thermal radiation. *Combustion Science and Technology*, 179(8):1605, 2007.

[238] J. Smagorinsky. General circulation experiments with the primitive equations: 1. the basic experiment. *Mon. Weather Rev.* , 91:99–164, 1963.

[239] George Smith. *The Chaldean account of Genesis*. 1879.

[240] A. Yu. Snegirev. Statistical modeling of thermal radiation transfer in buoyant turbulent diffusion flames. *Combustion and Flame*, 136(1-2):51–71, 2004.

[241] A. Soufiani and E. Djavdan. A comparison between weighted sum of gray gases and statistical narrow-band radiation models for combustion applications. *Combustion and Flame*, 97(2):240 – 250, 1994.

[242] A. Soufiani, P. Mignon, and J. Taine. Radiation-turbulence interaction in channel flows of infrared active gases. In *Proceedings of the Ninth International Heat Transfer Conference*, volume 6, pages 403–408, Washington, DC, 1990. Hemisphere.

[243] A. Soufiani and J. Taine. High temperature gas radiative propriety parameters of statistical narrow-band model for H_2O, CO_2 and CO and correlated-k model for H_2O and CO_2. *Technical note in International Journal of Heat and mass transfer*, 40:987–991, 1997.

[244] D. B. Spalding. Mixing and chemical reaction in steady confined turbulent flames. In *13th Symp. (Int.) on Combustion*, pages 649–657. The Combustion Institute, Pittsburgh, 1971.

[245] D. B. Spalding. Development of the eddy-break-up model of turbulent combustion. In *16th Symp. (Int.) on Combustion*, pages 1657–1663. The Combustion Institute, 1976.

[246] G. Staffelbach, L.Y.M. Gicquel, G. Boudier, and T. Poinsot. Large eddy simulation of self-excited azimuthal modes in annular combustors. *Proc. Combust. Inst.* , 32:2909–2916, 2009.

[247] J. Strˆhle, U. Schnell, and K. Hein. A mean flux discrete ordinate interplolation scheme for general coordinates. In *3rd Internationnal Conference on Heat Transfer*, Antalya, 2001.

[248] D. R. Stull and H. Prophet. Janaf thermochemical tables, 2nd edition. Technical Report NSRDS-NBS 37, US National Bureau of Standards, 1971.

[249] S. Succi. *The lattice Boltzmann equation for fluid dynamics and beyond.* 2 edition, 2001.

[250] J. Taine and A. Soufiani. Gas ir radiatives properties: From spectroscopic data to approximate models. *Advanced Heat Transfer*, 33:296–414, 1999.

[251] Jean Taine and Jean-Pierre Petit. *Heat transfer.* Prentice Hall, 1993.

[252] C. K. M. Tam and J. C. Webb. Dispersion-relation-preserving finite difference schemes for computational acoustics. *J. Comput. Phys.* , 107:262–281, 1993.

[253] J. Thiévin, R. Georges, S. Carles, A. Benidar, B., R., and J.P. Champion. High-temperature emission spectroscopy of methane. *Journal of Quantitative Spectroscopy and Radiative Transfer*, 109(11):2027–2036, July 2008.

[254] I. Tiselj, R. Bergant, F. Mavko, I. Bajsic, and G. Hetsroni. Dns of turbulent heat transfer in channel flow with heat conduction in the solid wall. *J. Heat Trans.* , 123:849–857, 2001.

[255] S. C. Traugott. On grey absorption coefficients in radiative transfer. *Journal of Quantitative Spectroscopy and Radiative Transfer*, 8(3):971 – 999, 1968.

[256] Kevin E. Trenberth. *Climate system modeling.* Cambridge University Press, 1995.

[257] A. Trouvé and T. Poinsot. The evolution equation for the flame surface density. *J. Fluid Mech.* , 278:1–31, 1994.

[258] J. S. Truelove. *Discrete-ordinate solutions of the radiation transport equation.* 1987.

[259] L. Vervisch, E. Bidaux, K. N. C. Bray, and W. Kollmann. Surface density function in premixed turbulent combustion modeling, similarities between probability density function and flame surface approaches. *Phys. Fluids A*, (7):2496, 1995.

[260] L. Vervisch, R. Hauguel, P. Domingo, and M. Rullaud. Three facets of turbulent combustion modelling: Dns of premixed v-flame, les of lifted nonpremixed flame and rans of jet flame. *J. Turb.* , 5:004, 2004.

[261] L. Vervisch and D. Veynante. Interlinks between approaches for modeling turbulent flames. *Proc. Combust. Inst.* , 28:175–183, 2000.

[262] D. Veynante and T. Poinsot. Reynolds averaged and large eddy simulation modeling for turbulent combustion. In J. Ferziger O. Metais, editor, *New tools in turbulence modelling. Lecture 5*, pages 105–135. Les editions de Physique, Springer, 1997.

[263] R. Viskanta and M. P. Mengüç. Radiation heat transfer in combustion systems. *Progress in Energy and Combustion Science*, 13(2):97–160, 1987.

[264] L. Wang, M.F. Modest, D.C. Haworth, and S.R. Turns. Modelling nongrey gas-phase and soot radiation in luminous turbulent nonpremixed jet flames. *Combust. Theory and Modelling* , 9:479–498, 2005.

[265] Y. Wang. *Direct Numerical Simulation of non-premixed combustion with soot and thermal radiation*. PhD thesis, University of Maryland, 2005.

[266] Zhenfeng Wang, Peigang Yan, Zhaoyuan Guo, and Wanjin Han. BEM/FDM conjugate heat transfer analysis of a two-dimensional air-cooled turbine blade boundary layer. *Journal of Thermal Science*, 17(3):199–206, 2008.

[267] Warren M. Washington, Albert J. Semtner, Gerald A. Meehl, David J. Knight, and Thomas A. Mayer. A general circulation experiment with a coupled atmosphere, ocean and sea ice model. *Journal of Physical Oceanography*, 10(12):1887–1908, 1980.

[268] Hiroaki Watanabe, Ryoichi Kurose, Satoru Komori, and Heinz Pitsch. Effects of radiation on spray flame characteristics and soot formation. *Combustion and Flame*, 152(1-2):2 – 13, 2008.

[269] R.O. Weber. Analytical models for fire spread due to radiation. *Combustion and Flame*, 78(3-4):398 – 408, 1989.

[270] F. A. Williams. *Combustion Theory*. Benjamin Cummings, Menlo Park, CA, 1985.

[271] P. Wolf, G. Staffelbach, A. Roux, L. Gicquel, T. Poinsot, and V. Moureau. Massively parallel les of azimuthal thermo-acoustic instabilities in annular gas turbines. *C. R. Acad. Sci. Mécanique*, 337(6-7):385–394, 2009.

[272] Y. Wu, D.C. Haworth, M.F. Modest, and B. Cuenot. Direct numerical simulation of turbulence/radiation interaction in premixed combustion systems. *Proceedings of the Combustion Institute*, 30(1):639–646, 2005.

[273] Y. Wu, M. F. Modest, and D. C. Haworth. A high-order photon monte carlo method for radiative transfer in direct numerical simulation. *J. Comput. Phys.*, 223(2):898–922, 2007.

[274] V. Yakhot, C. G. Orszag, S. Thangam, T. B. Gatski, and C. G. Speziale. Development of turbulence models for shear flows by a double expansion technique. *Phys. Fluids*, 4(7):1510, 1992.

[275] H. Yamashita, M. Shimada, and T. Takeno. A numerical study on flame stability at the transition point of jet diffusion flame. In *26th Symp. (Int.) on Combustion*, pages 27 – 34. The Combustion Institute, Pittsburgh, 1996.

[276] G. H. Yeoh, R. K. K. Yuen, S. C. P. Chueng, and W. K. Kwok. On modelling combustion, radiation and soot processes in compartment fires. *Building and Environment*, 38(6):771 – 785, 2003.

[277] Thomas Young. Experimental demonstration of the general law of the interference of light. *Philosophical Transactions of the Royal Society of London*, 94, 1804.

[278] Jin Zhang, Olivier Gicquel, Denis Veynante, and Jean Taine. Monte carlo method of radiative transfer applied to a turbulent flame modeling with LES. *Comptes Rendus Mécanique*, 337(6-7):539–549.